Vol. 38 • No. 1 • 2017

Chemical and Process Engineering

Inżynieria Chemiczna i Procesowa

Polish Academy of Sciences
Committee of Chemical and Process Engineering

The Journal is supported by the Ministry of Science and Higher Education

Editorial Board

Andrzej Burghardt (Chairman), Polish Academy of Sciences, Gliwice, Poland
Jerzy Bałdyga, Warsaw University of Technology, Poland
Andrzej Górak, T.U. Dortmund, Germany
Leon Gradoń, Warsaw University of Technology, Poland
Andrzej Jarzębski, Silesian University of Technology, Poland
Zdzisław Jaworski, West Pomeranian University of Technology, Szczecin, Poland
Władysław Kamiński, Technical University of Łódź, Poland
Stefan Kowalski, Poznań University of Technology, Poland
Andrzej Kraslawski, Lappeenranta University of Technology, Finland
Stanisław Ledakowicz, Technical University of Łódź, Poland
Eugeniusz Molga, Warsaw University of Technology, Poland
Alvin W. Nienow, University of Birmingham, United Kingdom
Andrzej Noworyta, Wrocław University of Technology, Poland
Ryszard Pohorecki, Warsaw University of Technology, Poland
Andrzej Stankiewicz, Delft University of Technology, The Netherlands
Czesław Strumiłło, Technical University of Łódź, Poland
Stanisław Sieniutycz, Warsaw University of Technology, Poland
Krzysztof Warmuziński, Polish Academy of Sciences, Gliwice, Poland
Laurence R. Weatherley, University of Kansas Lawrence, United States
Günter Wozny, T.U. Berlin, Germany
Ireneusz Zbiciński, Technical University of Łódź, Poland

Editorial Office

Andrzej K. Biń (Editor-in-Chief)
Barbara Zakrzewska (Technical Editor)
Marek Stelmaszczyk (Language Editor)

Address

ul. Waryńskiego 1
00-645 Warszawa
cpe.czasopisma.pan.pl; degruyter.com/view/j/cpe

Printed in Poland
Print run: 100 copies

Printing/binding:
Centrum Poligrafii Sp. z o.o.
ul. Łopuszańska 53
02-232 Warszawa

Chemical and Process Engineering 2017, 38 (1), 3-4
DOI: 10.1515/cpe-2017-0001

EDITOR'S NOTES

IN HONOUR OF PROFESSOR LEON GRADOŃ ON THE OCCASION OF HIS 70TH BIRTHDAY

Professor Leon Gradoń is one of the most prominent Polish scientists working in the field of chemical engineering. Leon Gradoń studied chemical engineering at Warsaw University of Technology (WUT) and mathematics at University of Warsaw. He received his PhD on the mechanisms of evaporation of superheated droplets in emulsions (1976) under supervision of Professor Anatol Selecki. In 1978-79 Leon Gradoń was a postdoc fellow at University of Houston (TX), where he worked with several distinguished scientists (prof. Payatakes, Amundson, Luss, Bailey) and started his scientific work on dispersed systems and aerosols. Upon return to Warsaw he continued this research which led him to the second degree (DSc - *'habilitation'*) received in 1982 with the thesis entitled *'The mechanism of dendrite formation from submicron aerosols'*. In 1984-85 and 1987 he was a visiting professor at the SUNY at Buffalo where he worked on modeling of fibrous particle deposition in lungs. After his return to Poland he became the head of the Division of Fundamental Processes at the Faculty of Chemical and Process Engineering, Warsaw University of Technology. In 1990 he became the full Professor of chemical engineering at WUT. In 1993-94 he was a visiting professor at University of Cincinnati (OH) as a recipient of Fulbright Foundation Award (cooperation with prof. Pratsinis). Later on he also stayed for some weeks at University of Hiroshima (17 years of cooperation with prof. Okuyama), University of Vienna, Technical University of Delft, University of Lund and University of Salzburg.

During the years of his work at WUT he significantly contributed to the development of new areas of research and teaching. He established the world-recognized Polish scientific school in aerosol science. Together with his younger collaborators he advanced the research on aerosol filtration (theory and applications), physicochemical effects of inhalation, powder particle engineering and liquid filtration. He also introduced new teaching areas at the Faculty (*Environmental Protection Process Engineering, Polymer Processing and Biomedical Processes & Products*), with many new lectures and laboratories. During 1999-2005 Professor Gradoń was the dean of the Faculty of Chemical and Process Engineering. Since 2013 he has been a head of the Chair of Integrated Processes Engineering.

Currently Professor Gradoń is a head of the executive board of the Foundation for Polish Science (FNP), a member of the National Science Council (NRN), the Committee of Chemical Engineering Polish Academy of Sciences and several scientific boards of international and domestic institutions, scientific organizations and journals. In 2006 Professor Leon Gradoń received the main award of Foundation for Polish Science (known as '*Polish Nobel Prize*') for his research and application/industrial achievements in filtration of dispersed systems. He was also a recipient of Marian Smoluchowski Award (1989, Vienna) and Rockefeller Foundation Award (1995) for his achievements in aerosol science. Prof. Gradoń was a recipient of the Japan Society for Promotion of Science Award (2001) and was distinguished as Doshisha University Fellow (Kyoto, 2011-2014). He holds a title of the *'Distinguished Cummins Professor in Filtration'* obtained from Cummins Filtration, Inc. (Cummins Endowed Professor) as a mark of excellence in the development of a Diesel engine exhaust filter which had been applied by this company.

The main scientific activities of Professor Leon Gradoń have been related to (to name the few):

- Design of filtering structures for separation of micro- and nanoparticles from fluids
- Design of coalescing filters for mists and emulsions
- Physicochemical and transport phenomena of inhaled aerosol particles in the lungs
- Particle formation by controlled spray-drying
- Design of inhaling devices and systems

In all these fields he published significant papers. He has (co-) authored over 150 scientific papers, 4 books and 65 patents. He supervised 11 PhD theses and was the co-advisor of 4 PhD students in USA and Japan. For his achievements in the field of science and engineering, Professor Gradoń was awarded with Commander's Cross of Polonia Restituta Order (2014).

Professor Leon Gradoń significantly contributed to the international scientific community as a Board Member of GeAF (*Gesselschaft für Aerosolforschung*) and a regular member of ISAM (*International Society for Aerosols in Medicine*) and *American Filtration Society*. He has been a member of Editorial Boards of the scientific journals: *Journal of Aerosol Science*, *Journal of Aerosol Medicine*, *Advanced Powder Technology*, *KONA – Particle and Powder Journal*, and *Chemical & Process Engineering*.

All the contributors to this issue wish Professor Gradoń further scientific achievements and good health in the coming years.

Eugeniusz Molga (Dean of the Faculty) and
Tomasz Sosnowski

Faculty of Chemical and Process Engineering
Warsaw University of Technology

Warsaw, 2017

DE GRUYTER OPEN
Chemical and Process Engineering 2017, 38 (1), 5-18
DOI: 10.1515/cpe-2017-0002

ROLE OF ACETONE IN THE FORMATION OF HIGHLY DISPERSED CATIONIC POLYSTYRENE NANOPARTICLES

Lusi Ernawati[1], Ratna Balgis[1], Takashi Ogi*[1], Kikuo Okuyama[1], Tomonori Takada[2]

[1]Hiroshima University, Department of Chemical Engineering, 1-4-1 Kagamiyama, Hiroshima 739-8527, Japan

[2]Fuso Chemical Company Co., Ltd., 4-3-1-0 Koreibashi, Chuo-ku, Osaka 5410043, Japan

Dedicated to Prof. Leon Gradoń on the occasion of his 70th birthday

A modified emulsion polymerisation synthesis route for preparing highly dispersed cationic polystyrene (PS) nanoparticles is reported. The combined use of 2,2′-azobis[2-(2-imidazolin-2-yl)propane] di-hydrochloride (VA-044) as the initiator and acetone/water as the solvent medium afforded successful synthesis of cationic PS particles as small as 31 nm in diameter. A formation mechanism for the preparation of PS nanoparticles was proposed, whereby the occurrence of rapid acetone diffusion caused spontaneous rupture of emulsion droplets into smaller droplets. Additionally, acetone helped to reduce the surface tension and increase the solubility of styrene, thus inhibiting aggregation and coagulation among the particles. In contrast, VA-044 initiator could effectively regulate the stability of the PS nanoparticles including both the surface charge and size. Other reaction parameters i.e. VA-044 concentration and reaction time were examined to establish the optimum polymerisation conditions.

Keywords: diffusion, emulsion, nanoparticle, polystyrene, solubility

1. INTRODUCTION

Polystyrene (PS) nanoparticles, both anionic and cationic, have attracted much interest owing to their excellent properties such as low density, high hydrophobicity, large specific surface area, good mechanical and chemical stability (Ernawati et al., 2016; Liu et al., 2012; Nandiyanto et al., 2008; Nandiyanto et al., 2012). They have many potential applications as templates, calibration standards, film coatings, ink toners, or polymer fillers, or in chromatographic separation and drug delivery (Chou et al., 2014; Li et al., 2011; Shibuya et al., 2014; Tadros, 2013). The size and distribution of PS particle are considered to be the most important parameters that succeeded in these applications (Abadi et al., 2015; Camli et al., 2010). Hence, how to synthesize and control highly dispersed PS particles with the size around 50 nm or less becomes a critical issue.

Numerous polymerisation methods, including dispersion, suspension, miniemulsion, microemulsion, and living radical polymerisation, have been used for preparing PS nanoparticles (Liu et al., 2014; Rao and Geckeler, 2011; Sood, 2004). Among these methods, the emulsion method is widely used because of its rapid polymerisation rate, high conversion, and environmental friendly and readily scalable characteristics (Chou and Chiu, 2013; Liu et al., 2014). In an emulsion system, to control the stability and to reduce the size of PS particle, high amount of surfactant (up to 20 wt%) and/or emulsifier are often required (Ishii et al., 2014; Maiti and Mc Grother, 2004). It is because of the adsorbed surfactant

---

*Corresponding author, e-mail: ogit@hiroshima-u.ac.jp

molecules at the oil-water (O/W) interface which can effectively reduce the O/W interfacial tension, further against the droplet coalescence and increase the emulsion stability. However, the use of high level amount of surfactant is often not acceptable as it leaves uncommon residues in products and contaminants in the reaction medium which have to be removed. Moreover, particle coagulation also readily occurs during the emulsion process and becomes the major drawback of this method.
The addition of co-solvents such as alcohols, acetone and some organic solvents into emulsion system also played an important role in controlling formation and size of PS particle (Kim et al., 2010). For instance, the synthesis of anionic PS nanoparticles using potassium persulfate as the initiator and acetone/water as the mixture solvent medium was reported for the first time by Okubo and co-workers (Okubo et al., 1981). Acetone was used to increase the solubility of styrene in the aqueous-phase system. This approach could effectively prevent particle coagulation and generate small PS particles. Subsequent research has enabled the successful preparation of smaller anionic PS particles (50 nm) via a microwave-assisted emulsion polymerisation process (Ngai and Wu, 2005). Additionally, a detailed study of the nucleation and growth mechanism of anionic PS particles has been reported (Li et al., 2012). Besides anionic PS nanoparticles, cationic PS particles are as important, particularly as a template material in the design of nanostructures (Balgis et al., 2012; Balgis et al., 2014; Ogi et al., 2014). However, to our knowledge, the synthesis of cationic PS particles with controllable size of less than 50 nm is rarely reported.

The present study reports an improved synthesis route for the preparation of highly dispersed cationic PS nanoparticles as small as 31 nm in diameter by the combined use of acetone/water as the mixture solvent medium and 2,2′-azobis[2-(2-imidazolin-2-yl)propane] dihydrochloride as the cationic initiator. Acetone was selected as a co-solvent because of its rapid diffusion characteristic and ability to promote the formation of small droplets in an emulsion system. 2,2′-Azobis[2-(2-imidazolin-2-yl)propane] dihydrochloride was used to control both the surface charge and size of the particles.

2. EXPERIMENTAL

2.1. Materials

Monomer styrene (99%, Kanto Chemical Co., Inc., Japan) was purified using sodium hydroxide (NaOH) prior to use. Cationic initiator 2,2′-azobis[2-(2-imidazolin-2-yl)propane] dihydrochloride (VA-044; 99%) was obtained from Wako Pure Chemical Industries, Ltd. (Japan). Acetone (99%, Kanto Chemical Co., Inc.) and ultra-pure water were used as a mixture solvent medium without further purification.

2.2. Preparation of cationic PS particles

The reaction set-up consisted of a 300-mL three-neck round-bottom flask equipped with a stirrer (the rotation speed was adjusted to 700 rpm), a reflux condenser, a heating jacket to control the temperature, a temperature controller, and a nitrogen (N_2) gas source. The polymerisation process was performed as follows. Ultra-pure water and acetone at known compositions were introduced into the reactor vessel and heated at 60°C under N_2 atmosphere for 30 min. After the reaction temperature and oxygen-free conditions were attained, styrene and VA-044 were added simultaneously. The acetone-to-water mass ratio and VA-044 concentration were varied from 0 to 2.33 and 0.0048 to 0.0193 mol L^{-1}, respectively. The reaction time was varied from 2 to 14 h. Other parameters i.e., styrene concentration and reaction temperature were maintained at 9.24 mol L^{-1} and 60°C, respectively. The polymerisation conditions are given in Table 1. After polymerisation, acetone was removed by heating at 60 °C for 3 h. The samples were then dried in a vacuum oven at 60 °C overnight prior to calculating total solid content (TSC).

2.3. Characterisation

The morphology of the prepared particles was observed by scanning electron microscopy (SEM; Hitachi S-5000, Japan; operating at 20 kV) and transmission electron microscopy (TEM; JEM-3000F, JEOL, Japan; operating at 300 kV). To obtain the average diameter and size distribution of the particles, more than 200 particles ($\Sigma n_i = 200$) were statistically examined. The hydrodynamic diameter (D_h) distribution of the PS particles was determined using dynamic light scattering (DLS). For the measurement, colloidal PS particle suspensions were diluted with deionised water and sonicated for 1 h at room temperature. The zeta potential (ζ) of the particles was measured on a Zetasizer (Malvern Instruments, Nano ZS, UK). The surface tension of PS particles in colloidal solution was measured using a surface tensiometer (KF14001139, Japan; operating at 100 V). Hence, for the measurement of surface tension, the use of VA-044 initiator was negligible.

3. RESULTS AND DISCUSSION

3.1. Influence of acetone-to-water mass ratio on PS particle size

The effect of the acetone-to-water mass ratio on the surface charge of the PS nanoparticles was examined by measuring the zeta potential of the PS samples. Positively charged PS particles, with zeta potentials of approximately +43 to +47 mV, were obtained for the PS samples prepared with varying acetone-to-water mass ratios as given in Table 1. No significant changes in the zeta potential values of the PS samples were obtained with increasing acetone-to-water mass ratios.

Table 1. Polymerisation conditions employed for the synthesis of the cationic polystyrene particles

Sample	$C_{VA\text{-}044}$[a] (mol L^{-1})	Acetone/ water mass ratio	VA-044/ styrene mass ratio (g/g)	Reaction time (h)	R_h (DLS) (nm)	D_p (SEM) (nm)	Zeta potential (ζ) (mV)	TSC [b] (wt.%)
CPS1	0.0064	0	0.055	8	330	272	+43	7.4
CPS2	0.0064	0.28	0.055	8	192	163	+45	6.4
CPS3	0.0064	0.67	0.055	8	101	88	+46	4.1
CPS4	0.0064	1.04	0.055	8	47	35	+47	3.6
CPS5	0.0064	1.50	0.055	8	44	31	+48	2.4
CPS6	0.0064	1.86	0.055	8	-	coagulated	+46	-
CPS7	0.0064	2.33	0.055	8	-	coagulated	+47	-
CPS8	0.0064	> 2.33	0.055	8	-	no particle	+47	-
CPS9	0.0064	1.04	0.055	2	41	32	+45	0.6
CPS10	0.0064	1.04	0.055	4	43	33	+46	1.5
CPS11	0.0064	1.04	0.055	6	44	34	+48	3.2
CPS12	0.0064	1.04	0.055	10	46	42	+47	3.7
CPS13	0.0064	1.04	0.055	12	48	45	+48	3.8
CPS14	0.0064	1.04	0.055	14	55	48	+49	3.9
CPS15	0.0048	1.50	0.041	8	coagulated	coagulated	+41	-
CPS16	0.0091	1.50	0.077	8	46	33	+46	2.2
CPS17	0.0128	1.50	0.112	8	47	35	+48	2.3
CPS18	0.0193	1.50	0.167	8	48	37	+49	2.4

The concentration of styrene was kept constant at 9.24 mol L^{-1}.

[a] Initial concentration of VA-044 initiator in mixture solution system.

[b] TSC was determined using a gravimetric method and calculated as follows

Additionally, the effect of varying the acetone-to-water mass ratio from 0 to 2.33 on the average diameter of the PS particles was examined. (Other parameters namely, the concentration of styrene and VA-044 initiator, reaction time, and reaction temperature were kept constant.). The results are shown in Fig. 1 and summarised in Table 1.

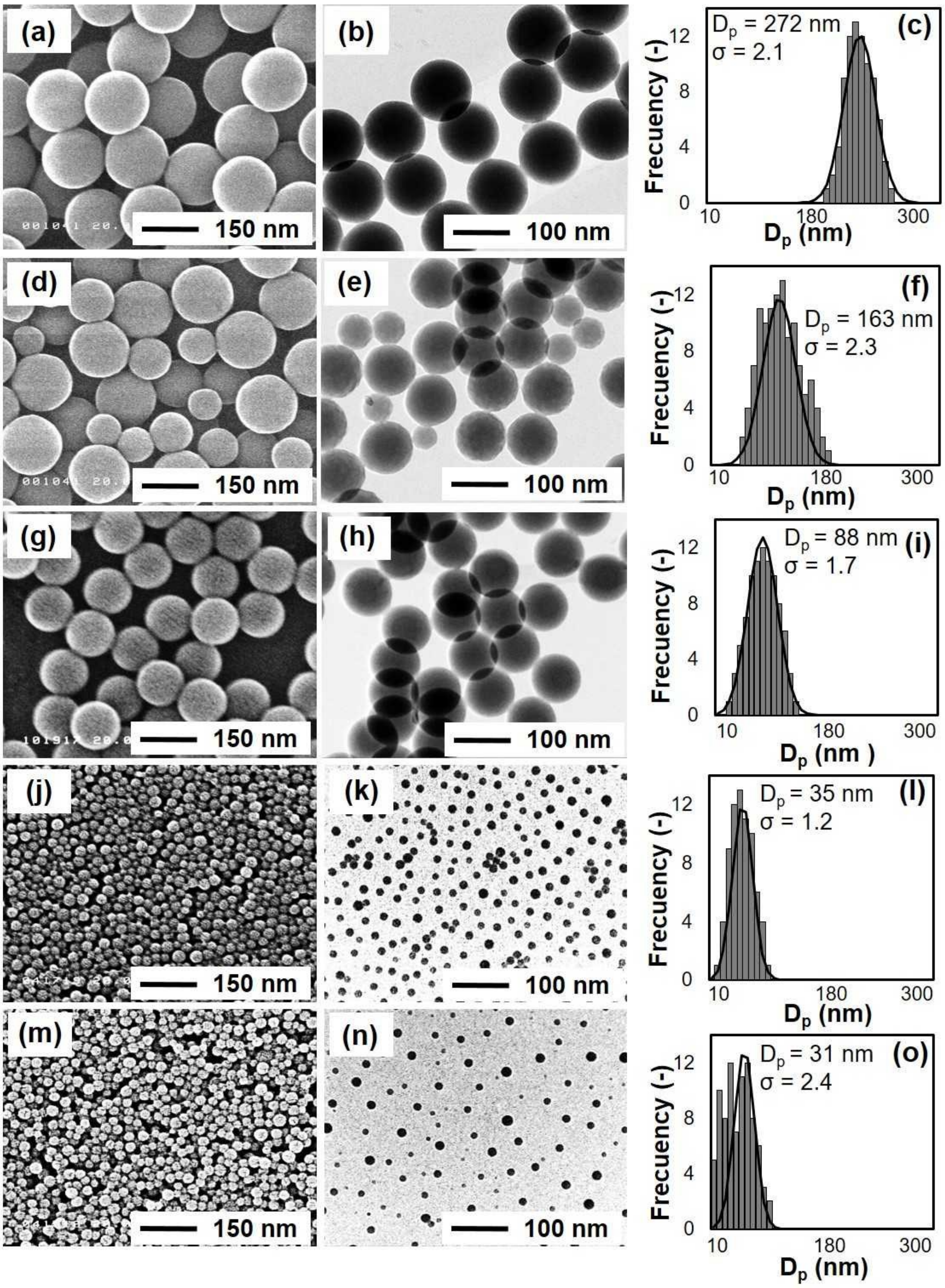

Fig. 1. SEM and TEM images, and size distribution profiles of the PS particles prepared at different acetone-to-water mass ratios of (a, b, c) 0, (d, e, f) 0.28, (g, h, i) 0.67, (j, k, l) 1.04, and (m, n, o) 1.50. Other parameters were kept constant: VA-044 initiator-to-styrene mass ratio, 0.055; reaction temperature, 60 °C; and reaction time, 8 h

$$S(wt\%) = \left(\frac{W_1}{W_2}\right) \tag{1}$$

where W_1 and W_2 are the weights of the dried and wet PS samples, respectively.

Large cationic PS particles of ~272 nm were obtained in the absence of acetone (Fig. 1(a)). The particle size could be significantly reduced to 31 nm when the acetone-to-water mass ratio was increased to 1.50. It is well known that high-polarity solvents, such as acetone, can form small droplets owing to rapid diffusion of the solvent (Ganachaud and Katz, 2005; Horn and Rieger, 2001; Legrand et al., 2007). The emulsion droplets formed upon addition of the styrene monomer to the acetone/water mixture solvent medium. Acetone quickly diffused and spread into the styrene monomer, subsequently leading to rupture of styrene into small droplets. By assuming that one PS particle is formed in each emulsion droplet, the particles shrink after evaporation of acetone, resulting in the formation of PS nanoparticles (Gradon et al., 2004). Thus, a good correlation between the initial droplet size and final size of the PS particles can be expected. According to this concept, the role of acetone on the formation of the cationic PS nanoparticle is illustrated in Fig. 2.

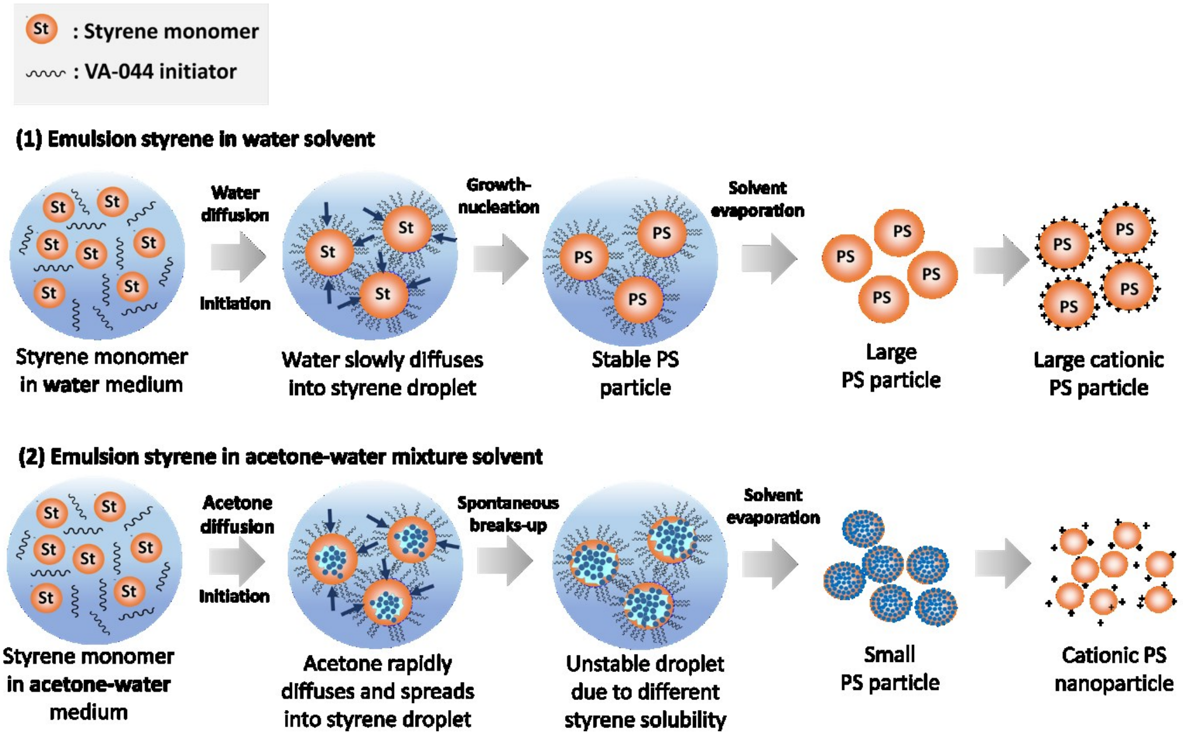

Fig. 2. Schematic of the formation of the cationic PS nanoparticles influenced by differences in the diffusion rate of acetone in the emulsion system

The solvent diffusion phenomenon, which causes spontaneous rupture of droplets, depends on the mass ratio of acetone to water. In the presence of water medium only, droplet rupture is slower owing to the slower diffusion rate of water (when compared with that of acetone), thereby resulting in the formation of large droplets. In contrast, when acetone is added to the emulsion system, emulsion droplets can readily break into small droplets owing to rapid diffusion of acetone.

Based on the proposed mechanism in Fig. 2, rapid diffusion of acetone, which promotes the formation of small cationic PS particles, was successfully attained when the mass ratio of acetone to water was 1.50 (Fig. 1(m, n, o)). In contrast, when the mass ratio of acetone to water was greater than 1.50, particle coagulation occurred (Fig. A.1(a, b), *APPENDICES*); the results are summarised in Table 1. Particle coagulation, observed at acetone-to-water mass ratios of 1.86 and 2.33, occurred because the equilibrium solubility of styrene was surpassed. Furthermore, the increase in the diffusion of acetone, while the amount of styrene monomer was constant, likely led to increased particle collision events and gelling effects. Further increases in the acetone-to-water mass ratios to above 2.33 did not generate any PS nanoparticles. Styrene monomers tend to dissolve in acetone rather than in aqueous phase, thereby accelerating the diffusion process. Consequently, the formation of particle nuclei becomes difficult because of the imbalance in the hydrophobic and hydrophilic properties of the different solvents involved in the system.

As noted, the droplet size was mainly influenced by the acetone/water composition, diffusion and shrinkage processes. The size of PS particles could be adjusted by controlling the mass ratio of the acetone/water mixture solvent. With increasing acetone contents, the diffusion of acetone becomes rapid and the extent of shrinkage of the particle becomes greater owing to the evaporation of more acetone molecules. Both processes synergistically reduce the diameter of PS particles.

In the present system, the rapid diffusion of acetone has important roles in instigating spontaneous droplet break-up and preventing particle re-coalescence, thereby generating PS nanoparticles. However, the balanced mass ratio between acetone and water should be properly maintained; excessive amounts of acetone will result in increased supersaturation of styrene, thus impeding the subsequent growth and nucleation of emulsion droplets, consequently impeding the formation of PS nanoparticles.

Moreover, as previously reported, the effect of interfacial phenomena during diffusion contributes to the formation of nanoparticles (Natu et al., 2015). In this work, a similar trend was observed as represented by the effect of increasing acetone-to-water mass ratios on the solubility of styrene and the reduction of surface tension (Figs. 3 and 4).

Figure 3 shows that a high acetone content reduced the surface tension of the emulsion system, consequently inducing a reduction in the particle size. (The surface tension of acetone is lower than that of water). Specifically, when the acetone-to-water mass ratio was 1.50, a low interfacial tension of 32.73 N m^{-1} was attained. As the interfacial tension of the aqueous phase was decreased further by increasing the content of acetone, the affinity and/or electrostatic force between the initiator and the PS particle surface was not as high as the affinity among the initiator molecules. Consequently, the initiator molecules were loosely packed on the PS particle surface, and the degree of particle dispersion become high owing to the enhanced solubility of styrene, thereby promoting the formation of PS nanoparticles.

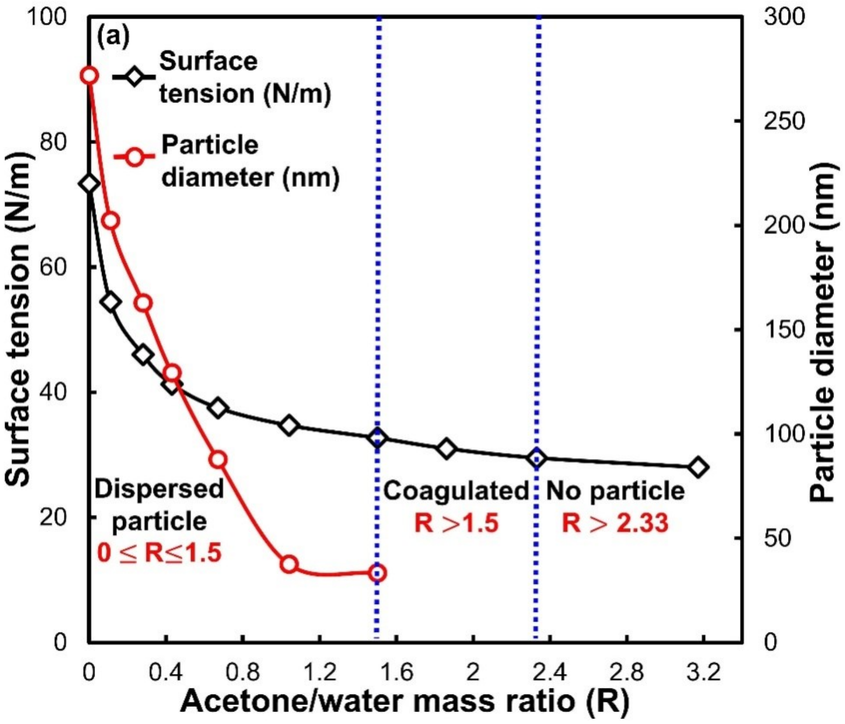

Fig. 3. Influence of the acetone/water composition on the average diameter of the PS particles and surface tension of the emulsion system

Figure 4 shows the relationship between the acetone/water composition and the surface tension and the solubility parameter of styrene in the mixture solvent system, which was evaluated by using the model established by Beerbower et al. (1971):

$$\sum \delta^2 = \delta_{\mathrm{d}}^2 + 0.632\,\delta_{\mathrm{p}}^2 + 0.632\,\delta_{\mathrm{h}}^2 = 13.9\left(\frac{1}{V_{\mathrm{m}}}\right)^{1/3} \gamma_{\mathrm{L}}\ \text{(for non-alcohols)} \tag{2}$$

The experimental data were then linearly fitted using the model established by Koenhen and Smolders (1975):

$$\sum \delta^2 = \delta_{\mathrm{d}}^2 + \delta_{\mathrm{p}}^2 = 13.5\left(\frac{1}{V_{\mathrm{m}}}\right)^{1/3} \gamma_{\mathrm{L}}\ \text{(for all substances)} \tag{3}$$

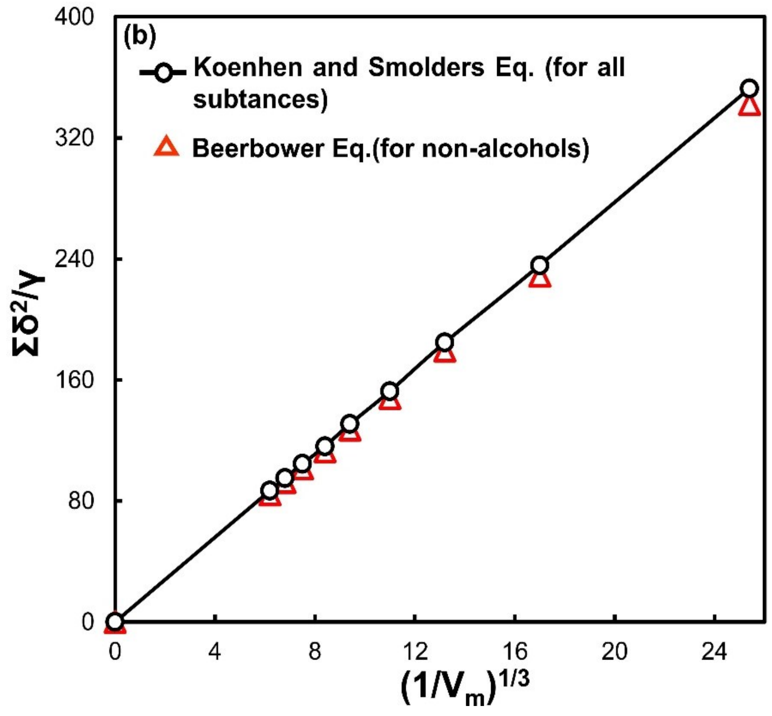

Fig. 4. Correlation between the acetone-water composition to the surface tension and the solubility parameter of styrene in the mixture solvent system calculated using the Beerbower model (1971) and fitted using the Koenhen-Smolders equation model (1975)

As deduced from these calculations, increasing the acetone-to-water mass ratio increased the solubility of styrene and reduced the interfacial tension of the solution system simultaneously. Furthermore, it enabled the formation of a homogenous mixture emulsion system and an increased number of particle nuclei, while preventing aggregation and coagulation among the particles, consequently leading to the formation of small PS particles.

3.2. Influence of VA-044 initiator concentration on PS particles size and zeta potential

The effect of VA-044 concentration on the average size and zeta potential of the prepared PS particles was evaluated. The polymerisation process was performed at varying VA-044 concentrations from 0.0048 to 0.0193 mol L^{-1}, while other parameters i.e., styrene concentration, acetone-to-water mass ratio, reaction time, and reaction temperature were kept constant. The results are given in Fig. 5 and summarised in Table 1.

As observed from the SEM and TEM images in Fig. 5, the VA-044 concentration had a slight effect on the particle size. The size of PS particles increased slightly from 33 from 37 nm with increasing VA-044 concentrations from 0.0091 to 0.0193 mol L^{-1}. As reported, the formation of considerably larger PS particles is expected by increasing the VA-044 concentration (Lee et al., 2010; Nandiyanto et al., 2014). However, the trend obtained herein differed from that previously reported using excessively high VA-044 concentrations and did not have a significant effect on the size of the particles; only a small difference in the particle size was observed. This result indicated that when a high VA-044 concentration was used, both the consumption and initiation rates of the styrene monomers increased simultaneously.

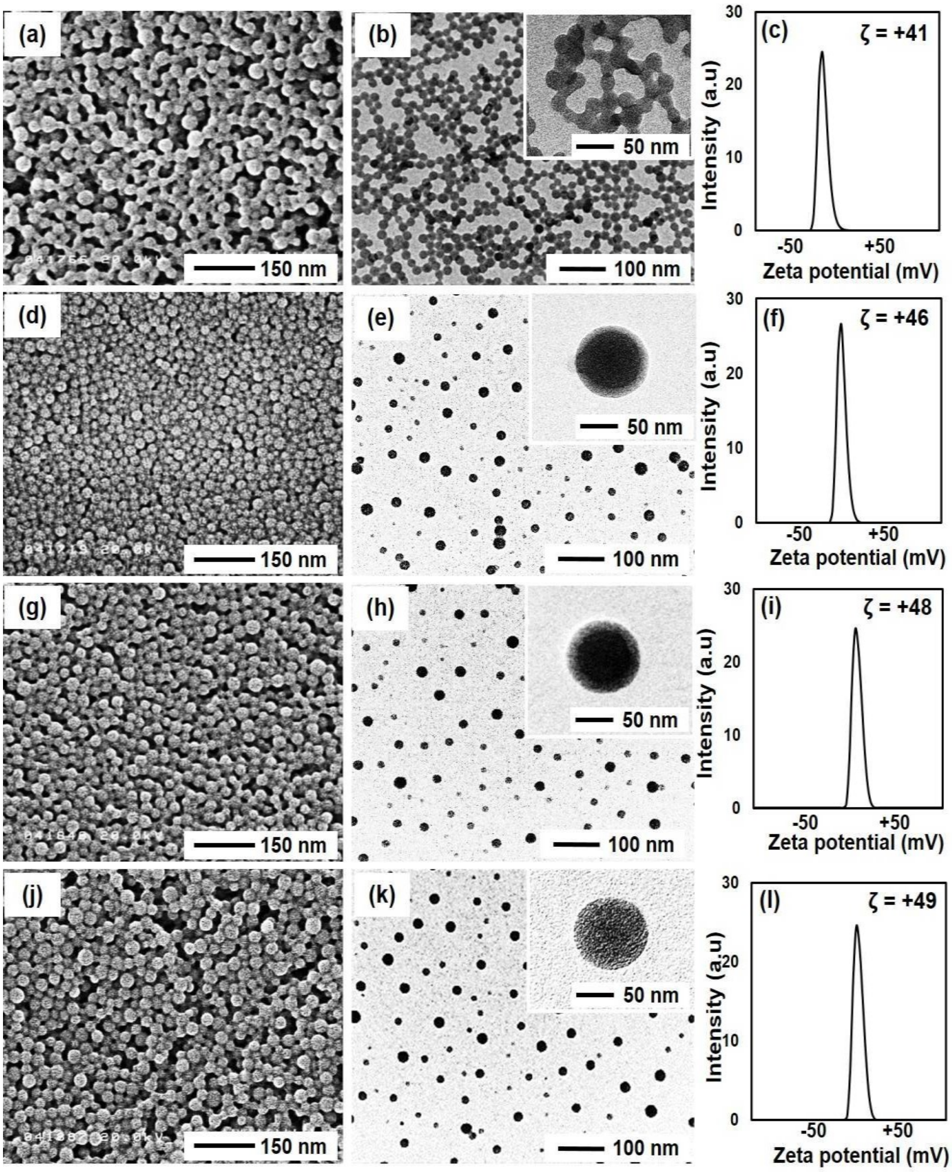

Fig. 5. SEM and TEM images, and zeta potential distribution (ζ) of the PS particles prepared at various VA-044 concentrations of (a, b, c) 0.0048, (d, e, f) 0.0091, (g, h, i) 0.0129, and (j, k, l) 0.0193 mol L^{-1}. Other parameters were kept constant: acetone-to-water mass ratio, 1.50; styrene, 9.24 mol L^{-1}; reaction temperature, 60 °C; and reaction time, 8 h

As the amount of styrene monomers was constant, the number of styrene units that could be attacked by the initiator was limited by the solubility of the monomer itself. This promoted the uncontrolled formation of free-radical initiators, thereby generating particle nuclei. In contrast, using excessively low VA-044 concentrations did not impact on the formation of PS particles as shown in Fig. 5(a). This is due to the low initiation and consumption rates of the styrene monomers in the emulsion system.

Likewise, the zeta potential of PS particles increased slightly from +41 to +50 mV with increasing VA-044 concentrations. This result implied that the presence of VA-044 initiator stabilised the emulsion system by a combined electrostatic and attractive force mechanism. To investigate the effect of increasing VA-044 concentrations on the stability of PS particles, D_h of PS particles in aqueous medium was evaluated as shown in Fig. 6.

Figure 6(a) shows that the D_h of cationic PS nanoparticles, as measured by DLS, was ~50 nm. The diameter of the particles, as measured by SEM, was 30 nm. The smaller size determined by SEM was related to the shrinkage of the particles upon drying for the measurement.

The principle of DLS for D_h particle measurement depends on the measuring of fluctuation intensity caused by interference of laser light that is scattered by diffusing particles. The evolution time of these fluctuations depends on the particle movement caused by Brownian motion, as well as the size of particle (Hirschle et al.,2016). Hence, it is possible to observe the correlation between the force at distance, Ģ(г), of colloidal PS particles and lag time, (г).

Force at distance is also called as the first-order autocorrelation function Ģ(г). This parameter describes temporal aggregated formation and/or coagulation of particles in a particular orientation within scattering light. At short time, the system is nearly stationary and the value of the correlation function is approximately equal to unity (1). Due to the random nature (i.e., Brownian motion effect), at longer time, the force appeared in the system, meaning that the system with the initial state approaches zero. On the other hand, lag time (г) describes the required time to reach a steady-state of particle size distribution (PSD) which is determined as a function of the relative rates of coagulation (Holthoff et al., 1996). Herein, the intensity of Ģ(г) represents the degree of interaction between interfacial PS particles in the colloidal system that is controlled by regulating the VA-044 concentration. As observed in Fig. 6(b), at short lag times (<50 μs), the Ģ(г) intensity changed slightly with increasing VA-044 concentrations from 0.0048 to 0.0193 mol L^{-1} (inset of Fig. 6(b)). This result revealed that by using VA-044 initiator, the nucleation and growth rates of particles could be greatly suppressed, thereby affording control over the formation of smaller PS particles without any coagulation. This result agreed with the results of previous reports (Ito et al., 2002; Shibuya et al., 2014). The authors reported high electron density and strong hydration capabilities of VA-044 initiator that resulted in weak adsorption between particle interfaces. Thus, VA-044 initiator has potential in preventing the formation of large particles through coagulation.

3.3. Influence of reaction time on the yield and PS particles size

The effect of reaction time on the size of PS particles was evaluated, and the results are shown in Fig. 7.

Figure 7 shows that the size of PS particles increased slightly from 32 to 48 nm when the reaction time increased from 2 to 14 h. The PS particles grew continuously during the early stages of the reaction (2–8 h), after which the growth rate became steady. These results revealed that as the reaction time increased, the monomer concentration in the emulsion system decreased continually as it was converted into an oligomer and a polymer. The growth of PS particles decreased slowly, and then stopped. Using a short reaction time of 2 h produced small PS particles of ~32 nm in size. PS nanoparticles with controllable sizes of <50 nm were also obtained when the reaction time was increased from 8 to 14 h (Table 1). This result shows that the reaction time is important for controlling the size of PS particles. The effect of the reaction time on D_h of PS particles was also evaluated by DLS, and the results are shown in Fig. S2. Based on the DLS results, the size of PS particles could be controlled to less than 60 nm even under prolonged polymerization ($t = 14$ h).

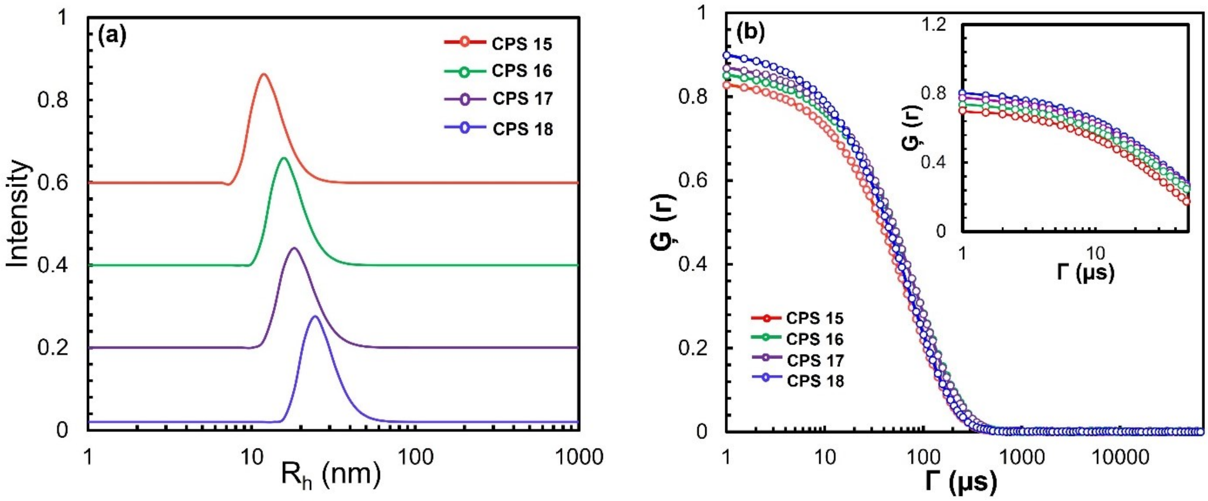

Fig. 6. (a) Hydrodynamic diameter (R_h) distributions of the colloidal PS particles measured by DLS. (b) Force at distance, Ģ(ᴦ), of the colloidal PS particles as a function of lag time, (ᴦ). The inset shows an enlarged view at the shorter lag-time intervals. The synthesis condition of representative PS sample was summarised in Table 1

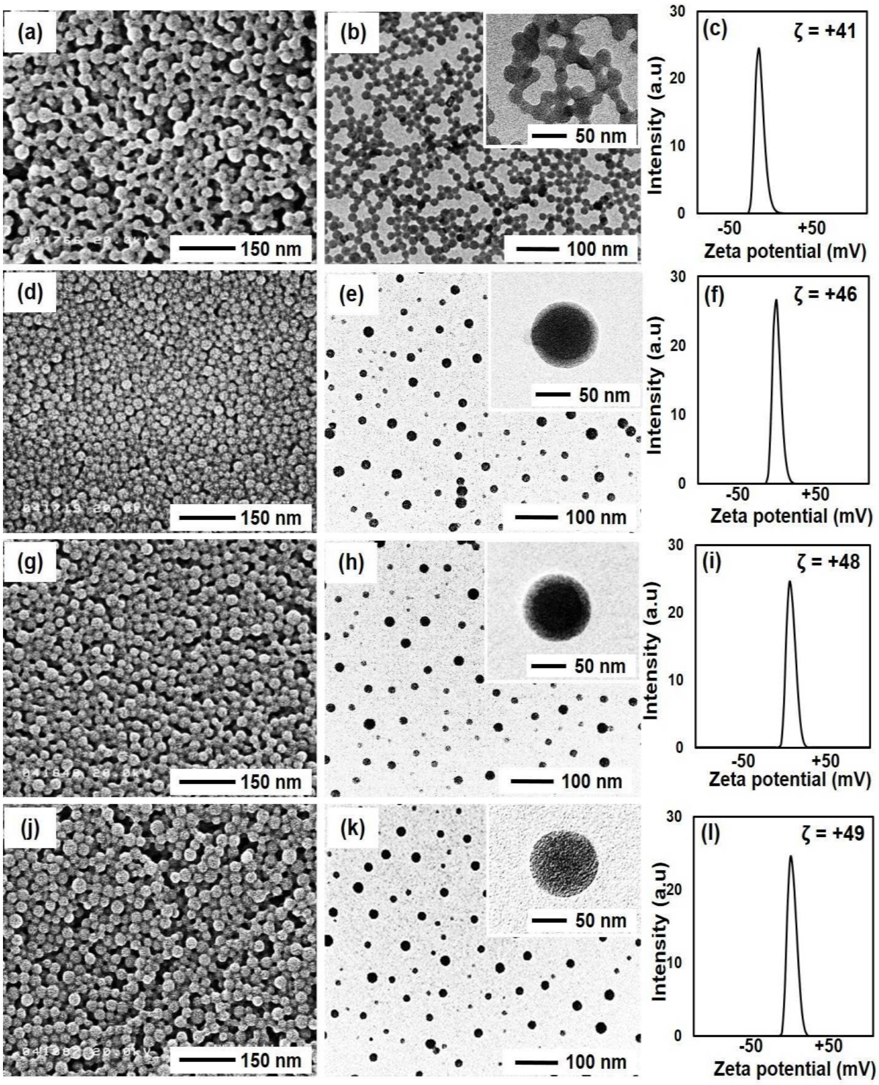

Fig. 7. SEM images and associated size distribution profiles of the PS particles prepared under different reaction times of (a, b) 2, (c, d) 4, (e, f) 10, (g, h) 12, and (i, j) 14 h. Other reaction parameters were kept in constant: acetone-to-water and VA-044 initiator-to-styrene mass ratio, 1.04 and 0.055, respectively; reaction temperature, 60 °C

3. CONCLUSIONS

Highly dispersed cationic PS nanoparticles were successfully synthesised via a modified emulsion polymerisation method. Specifically, the combined use of VA-044 initiator and acetone/water mixture solvent enabled the preparation of cationic PS nanoparticles with enhanced stability and controllable sizes of ~31 nm. Moreover, highly dispersed cationic PS nanoparticles could be obtained using high styrene concentrations without any added surfactant. The optimum polymerisation condition was achieved by using VA-044 initiator concentration of 0.0064 mol L^{-1}, acetone-to-water mass ratio of 1.50, reaction time of 8 h, styrene concentration of 9.24 mol L^{-1}, and reaction temperature of 60 °C. The addition of acetone increased the solubility of styrene and reduced the surface tension between the PS particle surface and aqueous phase. Additionally, rapid diffusion of acetone contributed to the formation of small droplets in the emulsion system, further enabling the formation of PS nanoparticles. The VA-044 initiator could effectively control the stability of both the surface charge and size of PS particles. This study provides important insights and a new methodology for further research and application, especially for preparing polymer nanoparticles via a convenient, low-temperature, and chemical handling process.

This work was supported by the Japan Society for the promotion of Science (JSPS) KAKENHI Grant Number 26709061 and Grant-in-Aid for Scientific Research (B) Grant Number 15K182570A. A scholarship was provided to L.E. by the Ministry of Education, Culture, Sports, Science and Technology (MEXT) of Japan. The authors thank Dr. Makoto Maeda of Natural Science Center for Basic Research and Development (N-BARD) at Hiroshima University for helpful discussion and help with the TEM studies.

SYMBOLS

D_h	hydrodynamic diameter
Ģ(г)	first-order autocorrelation function (force at distance of the colloidal PS particle)
Σn_i	total number of PS particles counted from SEM results
t	reaction time
V_m	average molar volume of styrene based on the mole fraction of acetone to water
Z	zeta potential of colloidal PS particles

Greek symbols

γ_L	gradient surface tension between the PS surface and acetone in aqueous phase system
Γ	lag time
δ_d	solubility parameter owing to dispersion forces
δ_p	solubility parameter owing to polarity
δ_h	solubility parameter owing to hydrogen bonding (donor–acceptor interactions)
$\sum \delta^2$	total solubility of styrene in acetone-water mixture medium

REFERENCES

Abadi A.R.S., Darabi A., Jessop P.G. Cunningham M.F., 2015. Preparation of redispersible polymer latexes using cationic stabilizers based on 2-dimethylaminoethyl methacrylate hydrochloride 2,2′-azobis[2-(2-imidazolin-2 yl)propane]dihydrochloride. *J. Polym.*, 60, 18. DOI:10.1016/j.polymer.2015.01.017.

Balgis R., Anilkumar G.M., Sago S., Ogi T., Okuyama K., 2012. Nanostructured design of electrocatalyst support materials for high-performance PEM fuel cell application. *J. Power Sources*, 203, 26-33. DOI: 10.1016/j.jpowsour.2011.11.064.

Balgis R., Ogi T., Wang W. N., Anilkumar G. M., Sago S., Okuyama K., 2014. Aerosol synthesis of self-organized nanostructured hollow and porous carbon particles using a dual polymer system. *Langmuir*, 30, 11257-11262. DOI: 10.1021/la502545d.

Beerbower A., 1971. Surface free energy: A new relationship to bulk energies. *J. Colloid Interface Sci.* 35, 126-132. DOI: 10.1016/0021-9797(71)90192-5.

Camli S.T., Buyukserin F., Balci O., Budak G.G., 2010. Size controlled synthesis of sub-100 nm monodisperse poly(methylmethacrylate) nanoparticles using surfactant-free emulsion polymerization. *J. Colloid Interface Sci.*, 344(2), 528-532, DOI: 10.1016/j.jcis.2010.01.041.

Chou C., Chiu W.Y., 2013. Novel Synthesis of Multi-Scaled, surfactant-free monodisperse latexes via alcoholic dispersion polymerization in a mixed ionic-nonionic initiation system. *Macromolecules*, 46, 3561-3569. DOI: 10.1021/ma400277s.

Chou I. C., Chen S. I., Chiu W. Y., 2014. Surfactant-free dispersion polymerization as an efficient synthesis route to a successful encapsulation of nanoparticles. *RSC Adv.*, 4, 47436-47447. DOI: 10.1039/C4RA07475K.

Ernawati, L., Ogi T., Balgis R., Okuyama K., Stucki M., Hess S. C., Stark W.J., 2016. Hollow silica as an optically transparent and thermally insulating polymer additive. *Langmuir*, 32, 338-345. DOI: 10.1021/acs.langmuir.5b04063.

Ganachaud F., Katz J.L., 2005. Nanoparticles and nanocapsules created using the ouzo effect: spontaneous emulsification as an alternative to ultrasonic and high-shear devices. *Chem. PhysChem*, 6, 209-216. DOI: 10.1002/cphc.200400527.

Gradon L., Janeczko S., Abdullah M., Iskandar F., Okuyama K., 2004. Self-organization kinetics of mesoporous nanostructured particle. *AIChE J.,* 50, 2583-2593. DOI:10.1002/aic.10257.

Hansen C.M., 1969. The universality of the solubility parameter. *Ind. Eng. Chem. Prod. Res. Dev.*, 8, 2-11. DOI: 10.1021/i360029a002.

Hirschle P., Prei T., Auras F., Pick A., Völkner J., Valdepérez D., Witte G., Parak W. J., Rädler J. O., Wuttke S., 2016. Exploration of MOF nanoparticle sizes using various physical characterization methods is what you measure what you get. *Cryst. Eng. Comm.*, 18, 4359-4368. DOI: 10.1039/c6ce00198j.

Horn D., Rieger J., 2001. Organic nanoparticles in the aqueous phase-theory, experiment, and use. *Angew. Chem. Int. Ed.*, 40, 4330-4361. DOI: 10.1002/1521-3773(20011203)40:23.

Ishii H., Ishii M., Nagao D., Konno M., 2014. Advanced synthesis for monodisperse polymer nanoparticles in aqueous media with sub-millimolar surfactants. *Polymer*, 55, 2772-2779. DOI: 10.1016/j.polymer.2014.04.011.

Ito F., Ma G., Nagai M., Omi S., 2002. Study of particle growth by seeded emulsion polymerization accompanied by electrostatic coagulation. *Colloids Surf. Physicochem. Eng. Asp.* 201, 131-142. DOI: 10.1016/S0927-7757(01)01030-5.

Kim, G., Lim, S., Lee, B.H., Shim, S.E., Choe, S., 2010. Effect of homogeneity of methanol/water/monomer mixture on the mode of polymerization of MMA: Soap-free emulsion polymerization versus dispersion polymerization. *Polymer*, 51, 1197-1205. DOI:10.1016/j.polymer.2009.12.038.

Lee S.Y., Gradon L., Janeczko S., Iskandar F., Okuyama K., 2010. Formation of highly ordered nanostructures by drying micrometer colloidal droplets. *ACS Nano*, 4, 4717-4724. DOI: 10.1021/nn101297c15.

Legrand P., Lesieur S., Bochot A., Gref R., Raatjes W., Barratt G., 2007. Influence of polymer behaviour in organic solution on the production of polylactide nanoparticles by nanoprecipitation. *Int. J. Pharm.*, 344, 33-43. DOI: 10.1016/j.ijpharm.2007.05.054.

Li Zh., Cheng Z., Han H.C. C., 2012. Mechanism of narrowly dispersed latex formation in a surfactant-free emulsion polymerization of styrene in acetone-water mixture, *Macromolecules*, 45, 3231-3239. DOI: 10.1021/ma202535j.

Li L., Zhai T., Zeng H., Fang X., Bando Y., Golberg D., 2011. Polystyrene sphere-assisted one-dimensional nanostructure arrays: synthesis and applications. *J Mater. Chem.*, 21, 40-56. DOI: 10.1039/C0JM02230F.

Liu B., Zhang M., Cheng H., Fu Z., Zhou T., Chi H., Zhang H., 2014. Large-scale and narrow dispersed latex formation in batch emulsion polymerization of styrene in methanol-water solution. *Colloid Polym. Sci.*, 292, 519-525. DOI: 10.1007/s00396-013-3113-8.

Liu B., Sun S., Zhang M., Ren L., Zhang H., 2015. Facile synthesis of large scale and narrow particle size distribution polymer particles via control particle coagulation during one-step emulsion polymerization. *Colloids Surf. Physicochem. Eng. Asp.*, 484, 81-88. DOI: 10.1016/j.colsurfa.2015.07.050.

Liu Q., Li Y., Duan Y., Zhou H., 2012. Research progress on the preparation and application of monodisperse cationic polymer latex particles. *Polym. Int.*, 61, 1593-1602. DOI: 10.1002/pi.4347.

Liu Q., Tang Z., Zhou Z., Zhou H., Liao B., Shen S., Chen L., 2014. A novel route to prepare cationic polystyrene latex particles with monodispersity, *J. Macromol. Sci.* 51, 271-278. DOI:10.1080/10601325.2014.882683.

Maiti A., Mc Grother S., 2004. Bead-bead interaction parameters in dissipative particle dynamics: Relation to bead-size, solubility parameter, and surface tension. *J. Chem. Phys.*, 120, 1594. DOI: 10.1063/1.1630294.

Nandiyanto A.B.D., Iskandar F., Okuyama. K., 2008. Nanosized polymer particle-facilitated preparation of mesoporous silica particles using a spray method. *Chem. Lett.*, 37, 1040-1041. DOI:10.1246/cl.2008.1040.

Nandiyanto A.B.D., Suhendi A., Ogi T., Iwaki T., Okuyama K., 2012. Synthesis of additive-free cationic polystyrene particles with controllable size for hollow template applications. *Colloids Surf. Physicochem. Eng. Asp.*, 396, 96-105. DOI: 10.1063/1.1630294.

Nandiyanto A.B.D., Suhendi A., Ogi T., Umemoto R., Okuyama K., 2014. Size and charge controllable polystyrene spheres for templates in the preparation of porous silica particle with tunable internal hole configurations. *Chem. Eng. J.*, 256, 421-430. DOI:10.1016/j.cej.2014.07.005.

Natu A.M., Wiggins M., Van De Mark M.R., 2015. Synthesis and characterization of cationic colloidal unimolecular polymer (CUP) particles. *Colloid Polym. Sci.*, 293, 1191-1204. DOI: 10.1007/s00396-015-3508-9.

Ngai T., Wu C., 2005. Double roles of stabilization and destabilization of initiator potassium persulfate in surfactant-free emulsion polymerization of styrene under microwave irradiation, *Langmuir*, 21, 8520-8525. DOI: 10.1021/la0506630.

Ogi T., Nandiyanto, A. B. D., Okuyama, K., 2014. Nanostructuring strategies in functional fine-particle synthesis towards resource and energy saving applications. *Adv. Powder. Technol.* 25, 3-17. DOI: 10.1016/j.apt.2013.11.005.

Okubo M., Yamada A., Shibao S., Nakamae K., Matsumoto T., 1981**.** Studies on suspension and emulsion. XLVI. Emulsifier-free emulsion polymerization of styrene in acetone-water. *J. Appl. Polym. Sci.*, 26, 1675-1679. DOI: 10.1002/app.1981.070260522.

Koenhen D. M., Smolders C. A., 1975. The determination of solubility parameters of solvents and polymers by means of correlations with other physical quantities. *J. Appl. Polym. Sci.*, 19, 1163-1179. DOI: 10.1002/app.1975.070190423.

Rao J. P., Geckeler K. E., 2011. Preparation techniques and size-control parameters. Prog.Polym. Sci., 36, 887-913. DOI:10.1016/j.apt.2013.11.005.

Shibuya D., Nagao H., Ishii., Konno M., 2014. Advanced soap-free emulsion polymerization for highly pure, micron-sized, monodisperse polymer particles. *Polymer*, 55, 535-539. DOI:10.1016/j.polymer.2013.12.039.

Sood A., 2004. Particle size distribution control in emulsion polymerization. *J. Appl. Polym. Sci.*, 92, 2884-2902. DOI: 10.1002/app.20231.

Tadros T. F., 2013. *Emulsion formation and stability*. John Wiley & Sons.

Received 21 April 2016
Received in revised form 31 August 2016
Accepted 13 September 2016

APPENDICES

A1. Influence of high acetone-to-water mass ratio on the formation of PS particles

SEM images of the PS nanoparticles prepared at high acetone-to-water mass ratios and R_h distribution profiles evaluated by DLS.

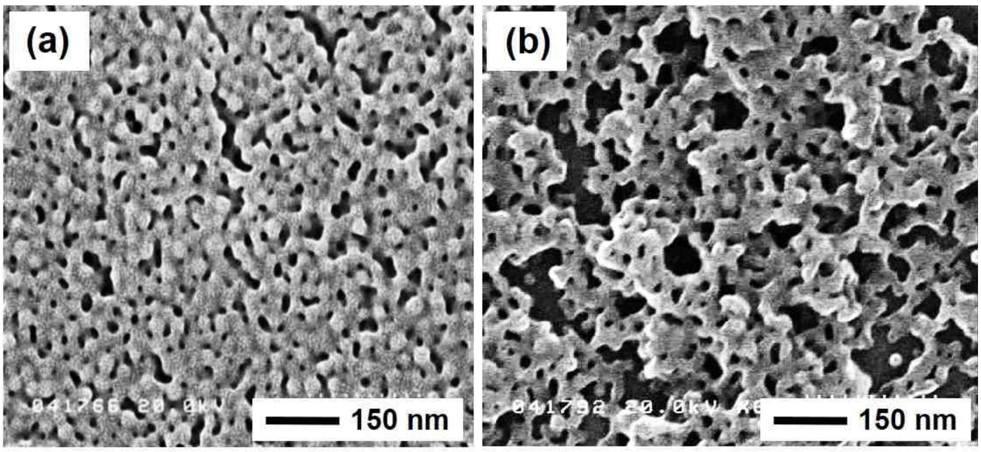

Fig. A.1. SEM images of the PS particles prepared at different acetone-to-water mass ratios of (a) 1.86 and (b) 2.33. Other parameters were kept constant: VA-044 initiator-to-styrene mass ratio, 0.055; reaction temperature, 60 °C; and reaction time, 8 h

A2. Hydrodynamic diameter (D_h) distribution of the prepared PS particles as a function of reaction time

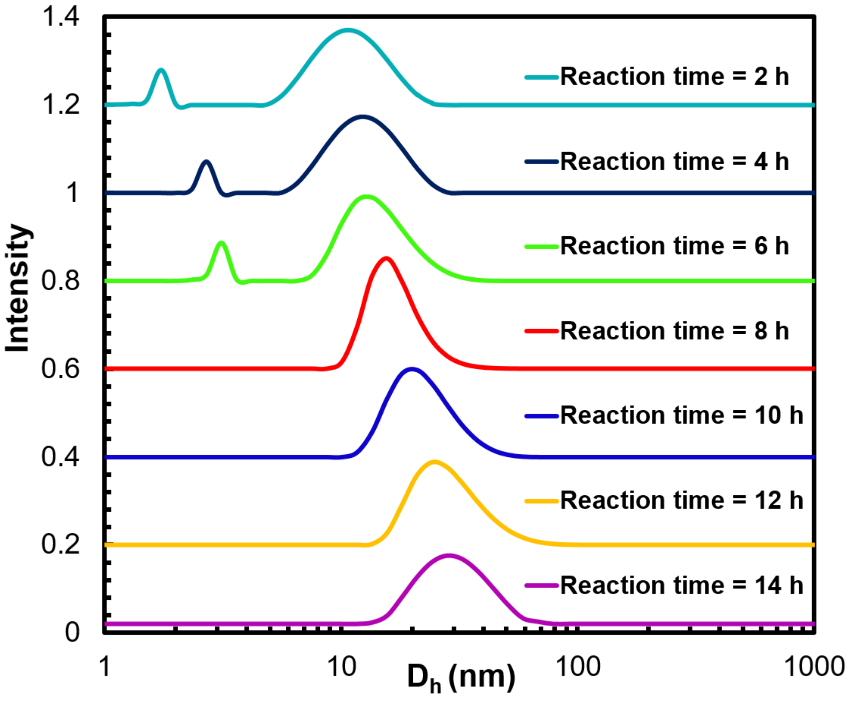

Fig. A.2. Hydrodynamic diameter (D_h) distribution profiles of the PS particles in aqueous medium measured by DLS. The colloidal PS samples were diluted in ultra-pure water prior to characterisation.

DE GRUYTER OPEN
Chemical and Process Engineering 2017, 38 (1), 19-30
DOI: 10.1515/cpe-2017-0003

PREDICTION OF GAS SOLUBILITY IN IONIC LIQUIDS USING THE COSMO-SAC MODEL

Manfred Jaschik, Daniel Piech, Krzysztof Warmuzinski, Jolanta Jaschik*

Polish Academy of Sciences, Institute of Chemical Engineering, ul. Baltycka 5, Gliwice, Poland

Dedicated to Prof. Leon Gradoń on the occasion of his 70th birthday

Thermodynamic principles for the dissolution of gases in ionic liquids (ILs) and the COSMO-SAC model are presented. Extensive experimental data of Henry's law constants for CO_2, N_2 and O_2 in ionic liquids at temperatures of 280-363 K are compared with numerical predictions to evaluate the accuracy of the COSMO-SAC model. It is found that Henry's law constants for CO_2 are predicted with an average relative deviation of 13%. Both numerical predictions and experimental data reveal that the solubility of carbon dioxide in ILs increases with an increase in the molar mass of ionic liquids, and is visibly more affected by the anion than by the cation. The calculations also show that the highest solubilities are obtained for $[Tf_2N]^-$. Thus, the model can be regarded as a useful tool for the screening of ILs that offer the most favourable CO_2 solubilities. The predictions of the COSMO-SAC model for N_2 and O_2 in ILs differ from the pertinent experimental data. In its present form the COSMO-SAC model is not suitable for the estimation of N_2 and O_2 solubilities in ionic liquids.

Keywords: vapour-liquid equilibrium, ionic liquids, Henry's constant, solubility, carbon dioxide capture, COSMO-SAC model

1. INTRODUCTION

Due to the environmental effect of CO_2 emissions generated by power plants and energy-intensive industrial sectors such as the chemical industry, the necessity to develop effective CO_2 capture technologies is obvious. In recent years it has been concluded that, most probably, conventional chemical scrubbing will not be widely applicable on a large scale due to its high operating costs. There is thus an urgent need for highly efficient novel technologies that will compete with or complete established capture methods.

Ionic liquids have shown high selectivity towards CO_2 and have recently been considered as very promising reversible absorbents for CO_2 separation (Privalova et al., 2012). Ionic liquids are chemically inert, stable, and nonvolatile liquid organic salts at temperatures below 100 °C. CO_2 solubility in ionic liquids depends on their chemical composition, i.e. on the proper combination of cations, anions and substituents. Ionic liquids (ILs) offer an almost unlimited number of cation and anion combinations and their chemical structures. The problem of finding the best IL for the removal of carbon dioxide from flue gas is a challenging task, with experimental studies time-consuming and expensive. Therefore, the tool for predicting CO_2 solubilities in ILs may optimise the screening process and suggest a vast array of novel cation-anion configurations although, at some point, the predictions have to undergo a carefully planned verification procedure.

---

*Corresponding author, e-mail: jjaschik@iich.gliwice.pl

In the present study the parameters needed for COSMO-SAC calculations are presented and discussed. This quantum mechanics model makes it possible to determine the data required for the estimation of Henry's law constants for a gas dissolved in ionic liquids (Lee et al., 2015). Henry's law constants for CO_2, N_2 and O_2 in ILs are estimated using the COSMO-SAC model and compared with the relevant experimental data.

2. THEORETICAL BACKGROUND

The description of phase equilibria is necessary for the design and optimisation of a number of processes at the core of chemical engineering, e.g. absorption, desorption, distillation, adsorption and crystallisation. The term "description" signifies, essentially, the concentrations of all the species of a system in thermodynamic equilibrium. These concentrations can be determined experimentally or predicted based on fundamental principles governing phase equilibria.

2.1. Vapour-liquid equilibrium

The solubility of gases in liquids can be described by an equation that relates the fugacity of a component in the gas phase with that in the liquid. At equilibrium we have (Lee et al., 2015):

$$y_i P\overline{\phi_i} = p_i \overline{\phi_i} = x_i \gamma_i f_i \tag{1}$$

At low pressures it may be assumed that the gas phase is an ideal gas mixture, and Eq. (1) becomes:

$$P y_i = p_i = x_i \gamma_i f_i \tag{2}$$

For low gas solubilities the concentration of the solute *i* in the liquid phase can be calculated using Henry's law:

$$\frac{p_i}{x_i} = H_i \tag{3}$$

with

$$H_i = \gamma_i^{\infty} f_i \tag{4}$$

It may be noted that at low pressures the fugacity of a pure gas in the liquid state corresponds to its saturated vapour pressure (Lee et al., 2015; Sandler, 1994):

$$f_i = p_i^0 \tag{5}$$

Saturated vapour pressures above a pure species can be determined experimentally (National Institute of Standards and Technology, 2016) or, alternatively, calculated from the relevant equations which relate the saturation pressure to temperature. To predict Henry's constant we also have to know the activity coefficient for the dissolved gas. This may be done using the COSMO-SAC model which makes it possible to estimate the activity coefficient of a gas dissolved in ionic liquids (ILs) (Lee et al., 2015; Shimoyama et al., 2010).

2.2. Segment activity coefficient (COSMO-SAC) model

There are a number of methods to calculate thermodynamic data for gaseous and liquid mixtures (e.g., the activity coefficients can be estimated using NRTL, UNIFAC, UNIQUAC or COSMO-SAC models, to mention but a few). A major advantage of the COSMO-SAC approach lies in its relative simplicity compared with the other models – the calculations only require the knowledge of a structural formula and certain parameters commonly available in the relevant literature (Firaha et al., 2013; Mullins et al., 2006; Shah et al., 2012; Shah et al., 2013; Shimoyama et al., 2010).

In the COSMO-SAC model it is assumed that the molecule in a solution is surrounded by a sphere called molecular cavity. The solvent outside this cavity is treated as a continuum of a constant relative permittivity (Klamt et al., 1998). The shape of the cavity results from the overlapping of atomic spheres, and its surface is divided into small circles of similar dimensions. The radii of the atomic spheres for various elements are given as empirical parameters. (In the present study the values of these parameters are taken from the paper of Mullins et al. (2006)). Then, using quantum chemistry methods, the surface charge density σ_n^* is estimated over the n-th segment of the cavity, the probability distribution of surface charge density (the so-called sigma profile) is calculated, and the activity coefficient for gas i in a solution is determined.

In the COSMO-SAC model the activity coefficient of i in a mixture is expressed as a sum of two contributions, namely combinatorial (comb) and residual (res):

$$\ln \gamma_i = \ln \gamma_i^{comb} + \ln \gamma_i^{res} \tag{6}$$

The combinatorial term reflects differences in the size and structure of the molecules and is given as:

$$\ln \gamma_i^{comb} = \ln\left(\frac{\phi_i}{x_i}\right) + \frac{z}{2} q_i \ln\left(\frac{\theta_i}{\phi_i}\right) + l_i - \frac{\phi_i}{x_i}\sum_i x_i l_i \tag{7}$$

where:

$$\theta_i = \frac{x_i q_i}{\sum_i x_i q_i} \tag{8}$$

$$\phi_i = \frac{x_i r_i}{\sum_i x_i r_i} \tag{9}$$

$$l_i = (\frac{z}{2})(r_i - q_i) - (r_i - 1) \tag{10}$$

$$r_i = \frac{V_i}{r} \tag{11}$$

$$q_i = \frac{A_i}{q} \tag{12}$$

The procedure for calculating the total volume, V_i, and the total surface area of the molecular cavity, A_i, is given in reference (Mullins et al., 2006); the other parameters are shown in Table 1.

The residual term results from molecular interactions. It can be predicted using the following relationship:

$$\ln \gamma_i^{res} = \frac{1}{a_{eff}} \sum_{\sigma_m} p'_i(\sigma_m)[\ln(\Gamma_s(\sigma_m)) - \ln(\Gamma_i(\sigma_m))] \tag{13}$$

where:

$$p'(\sigma) = p(\sigma) A_i \tag{14}$$

$$\ln \Gamma_s(\sigma_m) = -\ln\left[\sum_i \frac{p'_s(\sigma_n)}{A_i}\Gamma_s(\sigma_n)\exp\left(-\frac{\Delta W(\sigma_m,\sigma_n)}{RT}\right)\right] \tag{15}$$

$$\ln \Gamma_i(\sigma_m) = -\ln\left[\sum_i \frac{p'_i(\sigma_n)}{A_i}\Gamma_i(\sigma_n)\exp\left(-\frac{\Delta W(\sigma_m,\sigma_n)}{RT}\right)\right] \tag{16}$$

$$\Delta W(\sigma_m,\sigma_n) = \left(\frac{\alpha'}{2}\right)(\sigma_m+\sigma_n)^2 + c_{hb}\max\left[0,\sigma_{acc}-\sigma_{hb}\right]\min\left[0,\sigma_{don}-\sigma_{hb}\right] \tag{17}$$

The sigma profiles for the pure species *i*, $p'_i(\sigma_m)$, and for the solution, $p'_s(\sigma_m)$, were calculated based on the approach proposed in reference (Mullins et al., 2006), with numerical values of the relevant parameters based on literature data (Mullins et al., 2006).

Table 1. Values of the parameters in the COSMO-SAC model

Parameter	Symbol	Value	Unit
effective surface area of a segment	a_{eff}	7.5	Å^2
hydrogen bonding constant	c_{hb}	85580.0	kcal·Å^4·mol^{-1}·e^{-2}
surface area normalization constant	q	79.53	Å^2
volume normalization constant	r	66.69	Å^3
average radius of a cavity fragment	r_{av}	0.81764	Å
gas constant	R	0.001987	kcal·mol^{-1}·K^{-1}
coordination number	z	10	–
dislocation energy constant	α'	9034.97	kcal·Å^4·mol^{-1}·e^{-2}
hydrogen bonding correction	σ_{hb}	0.0084	e·Å^{-2}

3. COMPUTATIONAL DETAILS

A number of studies have been devoted to the prediction of gas solubilities in ionic liquids using the COSMO-SAC model. In their most recent paper Lee et al. (2015) calculate Henry's constants for several thousand systems consisting of gas (CO_2, N_2, H_2, CH_4) – ionic liquid. It has to be noted, though, that the numerical results concerning Henry's law constant were compared with only 53 sets of experimental data, and even a cursory examination shows that some results may be affected by a considerable error.

In Lee et al.'s (2015) method the optimisation of the molecular geometry was performed separately for cations and anions. Similarly, sigma profiles were obtained separately for cations and anions. In some studies, however, a different approach is proposed – the cation and the anion are treated as a whole (Palomar et al., 2007). In the present paper a combination of the two approaches was employed. The optimisation of the molecular geometry is based on Lee et al. (2015) method, whereas the sigma profile is obtained for the ionic liquid molecule treated as a single entity.

The COSMO-SAC model provided the core element of the procedure whereby activity coefficients, γ_i^∞, were predicted for ideally dilute solutions of CO_2, N_2 or O_2 and ILs. The calculations were done using a software package (Materials Studio 5.5) and following the procedure described by Mullins et al. (2006).

Ionic liquids include an organic cation and an inorganic or organic anion. The simulation is started by drafting the three-dimensional structure of the cation, the anion and the gas, thus creating the initial geometry. This geometry is then optimised for each of the species to find the most stable configuration. The optimisation is based on minimising the total energy of the molecule by altering the individual angles and bond lengths, and employs the density functional theory (DFT) as implemented in the software package used.

The complex structures of ionic liquids lead to a number of different conformations for which the energy may exhibit several local minima. Since optimisation results depend on the initial geometry, for larger molecules several conformation isomers were selected and the one most energetically favourable was eventually chosen.

In the next step the electron density for the optimised molecule is computed using the DFT method and the COSMO-SAC proper calculations are done. A dedicated algorithm draws a sphere around each atom, and then creates a molecular cavity surrounding the molecule. Klamt et al. (1998) suggest that in most cases the radius of the sphere should be assumed as equal to around 120% of the van der Waals radius. The values of these radii and the other parameters of the COSMO-SAC model are given in literature (Mullins et al., 2006).

The molecular cavity is divided into several smaller segments. For each segment the surface density charge, σ_n^*, is estimated based on the electron density of the molecule. Using the number of segments of the molecular cavity, the coordinates defining its shape, surface areas and surface charge densities for the segments, the charge distribution over the surface of the cavity (the sigma profile), $p(\sigma_m)$, is determined for the pure components (a gas and an ionic liquid) following the procedure proposed by Mullins et al. (2006). As already mentioned, it is assumed in the calculations that the cation and the anion form a single molecule.

The sigma profiles thus obtained were used to predict the activity coefficients, γ_i^∞, of CO_2, N_2 and O_2 dissolved in an ionic liquid. The prediction employs the COSMO-SAC-VT-2005 program (Eqs. (6) – (17)) and constitutes the final stage of the COSMO-SAC procedure. It is assumed that for an ideally dilute solution the mole fraction of the solvent (IL) is at least 99.5%. In the present paper the concentration of the solvent was fixed at 0.995. The programs *Sigma-average.exe* and *COSMO-SAC-VT-2005.exe* are written in Fortran 90 and are available on the Internet (Virginia Polytechnic Institute and State University, 2006).

The estimation of the Henry's constant for a gas−IL system (Eq. (4)) requires the knowledge of the pure gas fugacity in its hypothetical liquid state. This was done using the following equation:

$$p_i^0 \approx \exp\left(A_i + \frac{B_i}{T} + C_i \ln T + D_i T^{E_i}\right) \tag{18}$$

The coefficients in Eq. (18) were estimated by Lee et al. (2015) using the relevant experimental data (saturated vapour pressure for pure species below the critical temperature and solubility in the supercritical region). In the present study it has been found, however, that Eq. (18) yields incorrect saturated vapour pressures for nitrogen. If this quantity is calculated using Eq. (18) and the coefficients given in Lee et al. (2015) (Table 1), the numerical results are an order of magnitude larger than the experimental data at $T < T_C$. Closer scrutiny reveals that the discrepancy is due to the erroneous value of the coefficient D, which should be 3.7676×10^{-3} rather than 3.7676×10^{-2} originally proposed in Lee et al. (2015).

Next the coefficients of Eq. (18) for oxygen were estimated using the experimental saturated vapour pressures for the pure gas, published by the National Institute of Standards and Technology (2016). The coefficients for the three gases (with the corrected value of D for N_2) are given in Table 2.

An important advantage of Eq. (18) results from the wide range of temperatures over which it may be used with appreciable accuracy. Below the critical temperature the fugacities agree very well with the experimental data. Above T_C Eq. (18) may also be used; this is of special importance in the case of nitrogen and oxygen, as their critical temperatures are by far lower than those at which N_2/O_2 solubilities in ILs are studied.

Table 2. Coefficients in Eq. (18)

Gas	T	A	B	C	D	E
CO_2	217 – 340	140.54	-4735	-21.268	0.040909	1
N_2	64 – 343	30.895	-847.518	-1.999	0.0037676	1
O_2	63 – 153	69.7277	-1426.2836	-10.3129	0.0447	1

4. RESULTS AND DISCUSSION

4.1. CO_2 – ionic liquid systems

To validate the parameter values and the principal assumptions extensive COSMO-SAC calculations were done concerning Henry's constants for a range of CO_2 – IL systems. The results were then compared with the pertinent experimental data. The ionic liquids analysed were composed of a number of different cation – anion combinations. The cations were C_nMIM^+, C_nDMIM^+ and C_nMpyrr^+ (for the full names see the Appendix). The cations contained different alkyl groups, e.g. ethyl (*n* = 2), propyl (*n* = 3), butyl (*n* = 4), etc. ILs also contain inorganic (e.g. BF_4^-, $B[(CN)_4]^-$, PF_6^-, DCA^-) and organic (e.g. Tf_2N^-, OTf^-) anions. The structural formulae of these cations and anions are shown in Fig. 1.

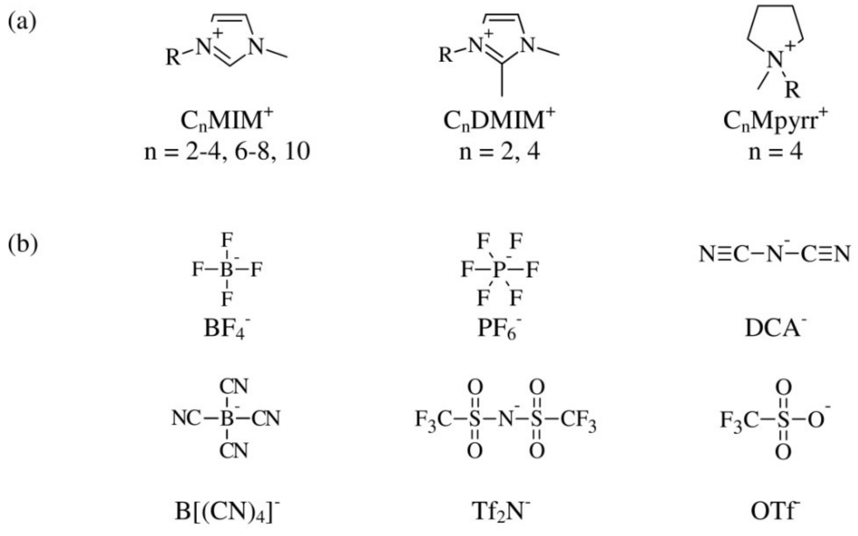

Fig. 1. Structural formulae of cations (a) and anions (b) analysed in this study

The comparison between the model predictions and experimental data for the system CO_2 – IL is presented in Fig. 2.

It may be seen from Fig. 2 that the model proposed in this work agrees better with the experiment. For 37 systems examined, only 4 deviate by more than 20% from the respective experimental data, and the average relative error is 10.3%. In the case of Lee et. al.'s (2015) calculations these numbers are, respectively, 13 and 16.7%; also, in a number of cases their results are visibly lower than the experimental values. This may be due to the fact that, in the present work, cations and anions were assumed to form a single compound, whereas Lee et al. (2015) determined the sigma profiles separately for these two moieties. Moreover, a different equation was employed to calculate the energy of interaction between two surface segments, $\Delta W(\sigma_m, \sigma_n)$, Eq. (17).

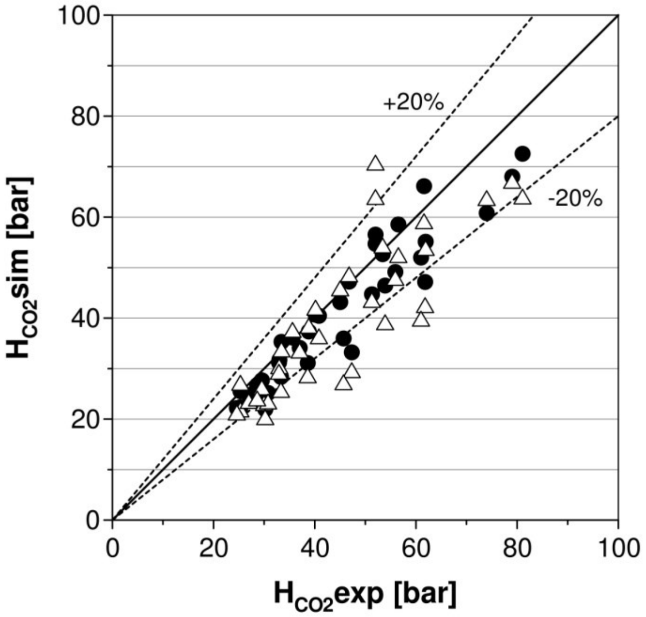

Fig. 2. Comparison of the experimental Henry's constants for CO_2 in ionic liquids with the COSMO-SAC predictions (circles – present study, triangles – results of Lee et al., 2015)

The average relative deviation is defined as:

$$ARD = \frac{1}{n}\sum\frac{|H_{sim} - H_{\exp}|}{H_{\exp}} \cdot 100\ \% \tag{19}$$

In Fig. 3 142 values of Henry's constant are shown for CO_2 in 18 different ionic liquids at temperatures between 280 K and 363 K. These values are compared with the experimental data obtained by various authors (Lei et al., 2014).

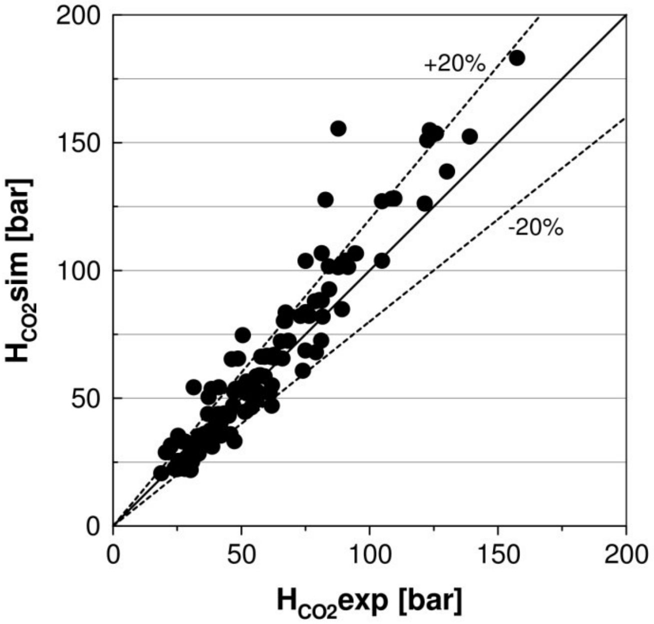

Fig. 3. Experimental Henry's constants for CO_2 in ILs vs. results of the COSMO-SAC model obtained in this work

It may be seen from Fig. 3 that most of the results are predicted with reasonable accuracy (deviation < 20%). However, there are 28 systems which deviate by more than 20% from the experimental values, especially for larger values of Henry's constants. The ARD is 13.2%.

It has to be noted that the coefficients in Eq. (18) were estimated based on experimental data measured mainly below the critical temperature for CO_2, while Fig. 3 includes 77 points close to or above T_C (31 °C) for CO_2. For these cases 18 points differ by more than 20% from their measured counterparts, and the average relative error is 16.0%. It may thus be concluded that the COSMO-SAC model can be employed for the prediction of Henry's constants over a wide range of temperatures.

Once the model has been validated the Henry's law constants for a range of CO_2 – IL systems at a specified temperature (say, 25°C) may be calculated. The results are shown in Fig. 4, where the ILs are grouped according to the type of the anion. The individual points for the same anion differ only in the nature of the cation (cf. Fig. 1).

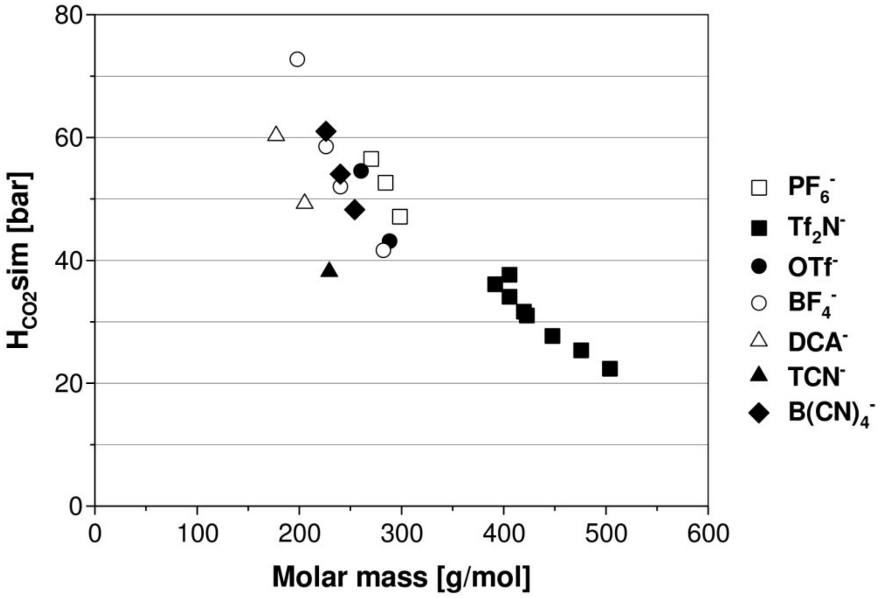

Fig. 4. Henry's constants for CO_2 in ionic liquids predicted by the COSMO-SAC model as a function of the IL molar mass

It may be seen from Fig. 4 that with an increase in the molar mass of ILs, Henry's constants tend to decrease (i.e., the solubility expressed in CO_2 mole fractions increases). Further, H_{CO_2} also depends on the anion and cation type, with anions having a more pronounced effect on H_{CO_2} than cations. It may also be noted that, at a constant temperature, for the three anions exhibiting the most obvious pattern, CO_2 solubility increases as the anions change in the following order: $BF_4^- < PF_6^- < Tf_2N^-$. These results agree well with the data quoted in the literature (Anthony et al., 2005; Ramdin et al., 2012; Shimoyama et al., 2010).

4.2. N_2 – ionic liquid and O_2 – ionic liquid systems

The usefulness of the COSMO-SAC model in predicting the solubility of nitrogen in ionic liquids was examined. 32 Henry's constants were calculated for eight N_2 – IL systems over a range of temperatures (283 – 343 K). The results are shown in Fig. 5.

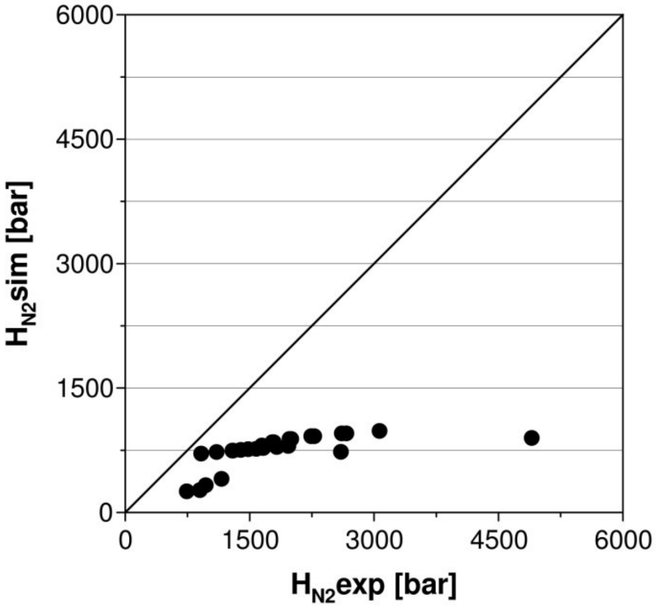

Fig. 5. Experimental Henry's constants for N_2 in ILs vs. results of the COSMO-SAC model obtained in this work

The results for nitrogen are far from satisfactory. A considerable discrepancy may be seen between the COSMO-SAC predictions and the experimental data, with the values obtained in the present study situated visibly lower. Unfortunately, the activity coefficients used, $\gamma_{N_2}^{\infty}$, cannot be verified with reasonable accuracy based on the available data.

Similar calculations were carried out for oxygen at temperatures between 283 K and 323 K. Again, in a number of cases the error exceeded 100%, thus limiting the usefulness of the model in this particular instance. Substantial errors for nitrogen and oxygen are reported in other studies (cf. e.g. Lei et al., 2014). This may be due to N_2 and O_2 solubilities being an order of magnitude smaller than that of CO_2; consequently, the relevant measurements are associated with a larger experimental error. Second, the calculations were performed using certain thermodynamic properties extrapolated well above the critical temperatures for N_2 and O_2, i.e. beyond their rigorous range of validity. Finally, the discrepancy may have resulted from the inherent deficiencies of the model itself.

Further studies will focus on using the COSMO-SAC model to predict the solubility of carbon dioxide in polyionic liquids (PILs). It is suggested that activity coefficients predicted for gas – IL systems may, under certain conditions, be extrapolated onto gas – PIL mixtures (Kuo et al., 2013). Based on the activity coefficient thus calculated it is possible to estimate the respective Henry’s constant.

5. CONCLUSIONS

The COSMO-SAC model may successfully be employed to predict Henry’s law constants for the CO_2 – IL system. The model may thus be useful in selecting the best candidate for the absorption of carbon dioxide. As the parameters required by the COSMO-SAC model are rather general, the examination of any new IL does not necessitate tedious experimental studies. Of the ILs so far investigated, the best CO_2 solubility is offered by those containing Tf_2N^-. The effect of the anion on CO_2 absorption is more pronounced than that of the cation. Finally, in its present form the COSMO-SAC model is not suitable for the estimation of N_2 and O_2 solubilities in ionic liquids.

SYMBOLS

A_i	total cavity surface area, Å^2
ARD	average absolute relative deviation, %
a_{eff}	effective surface area of a standard surface segment, Å^2
c_{hb}	constant for hydrogen bonding, kcal·Å^4·mol^{-1}·e^{-2}
f_i	fugacity of pure gas in the hypothetical liquid state, bar
H_i	Henry's law constant of component *i,* bar
P	total pressure, bar
p_i	vapour pressure of gas *i* above the solution, bar
p_i^0	vapour pressure of pure component *i*, bar
$p'_i\ (\sigma_m)$	modified sigma profile of pure component, Å^2
$p'_s\ (\sigma_m)$	modified sigma profile for a mixture, Å^2
q	surface area normalisation constant, Å^2
q_i	normalised surface area parameter
R	ideal gas constant, kcal·mol^{-1}·K^{-1}
r	volume normalisation constant, Å^3
r_i	normalised volume parameter
T	temperature, K
T_C	critical temperature, K
V_i	total cavity volume, Å^3
$\Delta W(\sigma_m,\sigma_n)$	exchange energy, kcal·mol^{-1}
x_i	mole fraction of gas *i* in the liquid phase
y_i	mole fraction of gas *i* in the gas phase
z	coordination number

Greek symbols

α'	constant for the misfit energy, kcal·Å^4·mol^{-1}·e^{-2}
γ_i	activity coefficient of component *i* in the liquid phase
γ_i^∞	infinite dilution activity coefficient of component *i*
γ_i^{comb}	combinatorial contribution to the activity coefficient of component *i* in solution
γ_i^{res}	residual contribution to the activity coefficient of component *i* in solution
$\Gamma_i(\sigma_m)$	segment activity coefficient of the solute
$\Gamma_s(\sigma_m)$	segment activity coefficient of the solvent
σ_{acc}	maximum of a set of σ_m and σ_n
σ_{don}	minimum of a set of σ_m and σ_n
σ_m	effective surface charge density on segment *m,* e·Å^{-2}
σ_n^*	surface charge density on segment *n,* e·Å^{-2}
$\bar{\phi}_i$	fugacity coefficient of gas *i* in the gas phase

Subscripts and superscripts

exp	experimental
sim	calculation

APPENDIX

Anion full names:

BF_4^-	tetrafluoroborate
$B(CN)_4^-$	tetracyanoborate
DCA^-	dicyanamide
PF_6^-	heksafluorophosphate
Tf_2N^-	bis(trifluoromethylsulfonyl)imide
OTf^-	trifluoromethanesulfonate; also triflate

Cation full names:

C_nMIM^+	1-alkyl-3-methylimidazolium; e.g.:
C_3MIM^+	1-propyl-3-methylimidazolium
C_6MIM^+	1-hexyl-3-methylimidazolium
C_8MIM^+	1-octyl-3-methylimidazolium
C_2DMIM^+	1-ethyl-2,3-dimethylimidazolium
C_4DMIM^+	1-butyl-2,3-dimethylimidazolium
C_4Mpyrr^+	N-butyl-N-methylpyrrolidinium

REFERENCES

Anthony J.L., Anderson J.L., Maginn E.J., Brennecke J.F., 2005. Anion effects on gas solubility in ionic liquids. *J. Phys. Chem. B*, 109, 6366-6374. DOI: 10.1021/jp0464041.

Firaha D.Z., Paulechka Y.U., 2013. Kinetics of the synthesis of 1-alkyl-3-methylimidazolium ionic liquids in dilute and concentrated solutions. *Int. J. Chem. Kinet*., 45, 771-779. DOI: 10.1002/kin.20812.

Klamt A., Jonas V., Bürger T., Lohrenz J.C.W., 1998. Refinement and parametrization of COSMO-RS. *J. Phys. Chem. A*, 102, 5074-5085. DOI: 10.1021/jp980017s.

Kuo Y.C., Hsu C.C., Lin S.T., 2013. Prediction of phase behaviors of polymer − solvent mixtures from the COSMO-SAC activity coefficient model. *Ind. Eng. Chem. Res*., 52, 13505-13515. DOI: 10.1021/ie402175k.

Lee B.S., Lin S.T., 2015. Screening of ionic liquids for CO_2 capture using the COSMO-SAC model. *Chem. Eng. Sci*., 121, 157-168. DOI: 10.1016/j.ces.2014.08.017.

Lei Z., Dai C., Chen B., 2014. Gas solubility in ionic liquids. *Chem. Rev*., 114, 1289-1326. DOI: 10.1021/cr300497a.

Mullins E., Oldland R., Liu Y.A., Wang S., Sandler S.I., Chen C.C., Zwolak M., Seavey K.C., 2006. Sigma-Profile Database for Using COSMO-Based Thermodynamic Methods. *Ind. Eng. Chem. Res*., 45, 4389-4415. DOI: 10.1021/ie060370h.

National Institute of Standards and Technology, 2016. Thermophysical Properties of Fluid Systems. NIST Standard Reference Data website: http://webbook.nist.gov/chemistry/fluid/.

Palomar J., Fero V.R., Torrecilla J.S., Rodriguez F., 2007. Density and molar volume predictions using COSMO-RS for ionic liquids. An approach to solvent design. *Ind. Eng. Chem. Res*., 46, 6041-6048. DOI: 10.1021/ie070445x.

Privalova E.I., Mäki-Arvela P., Yu Murzin D., Mikkhola J.P., 2012. Capturing CO_2: conventional versus ionic-liquid based technologies. *Russ. Chem. Rev*., 81, 435-457. DOI: 10.1070/RC2012v081n05ABEH004288.

Ramdin M., de Loos T.W., Vlugt T.J.H., 2012. State-of-the-art of CO_2 capture with ionic liquids. *Ind. Eng. Chem. Res*., 51, 8149-8177. DOI: 10.1021/ie3003705.

Sandler S.I. (ed.), 1994. *Models for thermodynamic and phase equilibria calculations*. Marcel Dekker, Inc., New York.

Shah M.R., Anantharaj R., Banerjee T., Yadav G.D., 2013. Quaternary (liquid + liquid) equilibria for systems of imidazolium based ionic liquid + thiophene + pyridine + cyclohexane at 298.15 K: Experiments and quantum chemical predictions. *J. Chem. Thermodynamics*, 62, 142-150. DOI: 10.1016/j.jct.2013.02.020.

Shah M.R., Yadav G.D., 2012. Prediction of liquid−liquid equilibria of (aromatic + aliphatic + ionic liquid) systems using the Cosmo-SAC model. *J. Chem. Thermodynamics*, 49, 62-69. DOI: 10.1016/j.jct.2012.01.012.

Shimoyama Y., Ito A., 2010. Predictions of cation and anion effects on solubilities, selectivities and permeabilities for CO_2 in ionic liquid using COSMO based activity coefficient model. *Fluid Phase Equilib*., 297, 178-182. DOI: 10.106/j.fluid.2010.03.026.

Virginia Polytechnik Institute and State University, 2006. VT Sigma Profile Databases, Virginia Tech website: http://www.design.che.vt.edu/VT-Databases.html

Received 20 September 2016
Received in revised form 26 October 2016
Accepted 29 December 2016

DE GRUYTER OPEN
Chemical and Process Engineering 2017, 38 (1), 31-50
DOI: 10.1515/cpe-2017-0004

ESTIMATION OF FILTRATION EFFICIENCY – FROM SIMPLE CORRELATIONS TO DIGITAL FLUID DYNAMICS

Rafał Przekop*

Warsaw University of Technology, Faculty of Chemical and Process Engineering, ul. Waryńskiego 1, 00-645 Warsaw, Poland

Dedicated to Prof. Leon Gradoń on the occasion of his 70th birthday

Aerosol filtration in fibrous filters is one of the principal methods of accurate removal of particulate matter from a stream of gas. The classical theory of depth filtration of aerosol particles in fibrous structures is based on the assumption of existing single fibre efficiency, which may be used to recalculate the overall efficiency of entire filter. Using "classical theory" of filtration one may introduce some errors, leading finally to a discrepancy between theory and experiment. There are several reasons for inappropriate estimation of the single fibre efficiency: i) neglecting of short-range interactions, ii) separation of inertial and Brownian effects, ii) perfect adhesion of particles to the fibre, iv) assumption of perfect mixing of aerosol particles in the gas stream, v) assumption of negligible effect of the presence of neighbouring fibres and vi) assumption of perpendicular orientation of homogenous fibres in the filtration structure. Generally speaking, "classical theory" of filtration was used for characterization of the steady – state filtration process (filtration in a clean filter, at the beginning of the process) without deeper investigation of the influence of the nternal structure of the filter on its performance. The aim of this review is to outline and discuss the progress of deep-bed filtration modelling from the use of simple empirical correlations to advanced techniques of Computational Fluid Dynamics and Digital Fluid Dynamics.

Keywords: filtration, lattice Boltzmann, Brownian dynamics, multi-phase flows, porous media

1. INTRODUCTION

A collection of aerosol particles in the particular steps of their production, and purification of the air at the workplace and atmospheric environment requires an efficient separation method of particulate matter from the carrier gas. Filtration is one of the most effective methods of particle removal from an aerosol stream. New fibrous structures could provide a promising tool for the development of highly efficient filters. A fibrous material operates by capturing an aerosol particle on fibre surface within the filter depth. Its effectiveness depends on the particle and fibre size, filter porosity and material properties of particle and filter media. Performance of a filter can be defined by its efficiency, pressure drop, and dust capacity. The basic principle of deep bed filtration is that solid particles suspended in a fluid are typically smaller than the pores of the filtering medium and as they deposit on fibres they become evenly distributed in the entire volume of the filter. As the fluid-solid suspension flows through the filter, particles present in the suspension deposit at various depths within the bed, that is, on solid walls bordering pore spaces. This leads to progressive clogging of a filter and a subsequent increase of pressure drop across it. Thus, it is usual to divide the filtration process into two stages: initial and aging. In the initial stage, the deposition of particles inside the filter is relatively small. Its effect on the

---

*Corresponding author, e-mail: r.przekop@ichip.pw.edu.pl properties of the filter is negligible, and the performance of the filter can be regarded as that of a clean filter.

However, to produce the optimal filter structure for the given application, it is necessary to know not only the characteristic of a clean filter but also its behaviour during loading. The presence of previously deposited particles causes an increase of both – filtration efficiency and pressure drop. It is worth noting that not only the total amount of deposited particles but also their spatial distribution and structure affect filter performance. When pressure drop approaches the maximum acceptable value that corresponds to the clogging of the media the filter has to be regenerated or changed.

The application of the "classical theory" of filtration for description of filter performance may introduce some errors for the realistic filter behaviour. There are several reasons for inappropriate estimation of the single fibre efficiency: neglecting of short-range interactions, separation of inertial and Brownian effects in description of particle motion, assumption of perfect adhesion of particles to the fibre and perfect mixing of aerosol particles in the gas stream, assumption of negligible effect of the presence of neighbouring fibres and their perpendicular orientation in the filtered structure.

The aim of this review is to outline and discuss the progress of deep-bed filtration modelling from the use of simple empirical correlations to advanced techniques of Computational Fluid Dynamics and Digital Fluid Dynamics.

2. CLASSICAL THEORY OF DEEP BED FILTRATION

The main assumptions of "classical theory" can be summarised as follows (Podgórski, 2002):

- Initial penetration of aerosol particles through a filter is calculated as:

$$1-\eta = exp(-\lambda L) \tag{1}$$

- The filter coefficient is related to single fibre efficiency as:

$$\lambda = \frac{4E}{\pi d_F}\left(\frac{1-\varepsilon}{\varepsilon}\right) \tag{2}$$

- The single fibre efficiency (defined as a ratio of the flux of particles depositing onto the fibre to the flux of particles passing a surface being projection of the fibre onto a plane perpendicular to the direction of mean motion) is calculated assuming that the deposition efficiency due to deterministic mechanisms (inertial impaction, sedimentation, electrostatic force) and stochastic mechanism (Brownian diffusion) are independent:

$$E = 1-(1-E_{det})(1-E_{diff}) \tag{3}$$

- E_{det} may be obtained using limiting trajectory concept and solving the deterministic, Lagrangian equation of motion for a particle, neglecting Brownian motion, E_{diff} is calculated solving Eulerian (convective-diffusion) equation for a weightless particle in the absence of external forces.
- Both, E_{det} and E_{diff} are calculated for an assumed model of gas flow around a single circular fibre.
- The perfect adhesion. No rebound of a particle colliding with fibre surface may occur.

3. GAS FLOW MODELS

3.1. Isolated fibre models

The existing models of gas flow in fibrous filters were developed in most instances for the 2D case. For isolated fibre models, the gas flow field near a collector in a fibrous filter is estimated solving the governing equations for the simplest geometrical system of a single, circular cylinder in unbounded space. Consequently, the effect of neighbouring fibres on the gas flow pattern around the fibre considered is completely neglected.

The potential flow was the first model ever used to investigate aerosol filtration in fibrous filters theoretically (Albrecht, 1931; Sell, 1931). The potential flow is the model of a steady state, vorticity-free flow of an inviscid, incompressible fluid. The major drawbacks of the potential flow model are related to the neglect of the fluid viscosity and the assumption of zero vorticity due to which the tangential component of the gas velocity does not vanish at the fibre surface. Consequently, gas velocities are much too high near the fibre and hence the efficiency of aerosol particle deposition calculated using this model is expected to be significantly overestimated.

As most fibrous filters operate at low Reynolds numbers defined as $Re = U\, d_f / \nu_f$, the model of creeping flow seems to be a much better alternative than that of potential flow. This approximation assumes predomination of the viscous forces over the inertial ones. Unfortunately, it is impossible to match the constants of integration in order to satisfy exactly all the boundary conditions (fixed velocity in infinity and vanishing gas velocity at the fibre surface).

The validity of the creeping flow approximation that neglects the inertial effects of the fluid motion is restricted to the values of the Reynolds number below about 0.5; losing a bit more accuracy it could be extended to $Re = 1$. An approximate method of approach to this issue enabling an analytical solution to the problem was suggested by Oseen (1927). The first approximate solution to that problem for the transverse flow past a circular cylinder was given by Lamb (1932). Two important features of the Lamb model should be outlined: being formally a solution to the Oseen problem, it still retains the downstream-upstream symmetry, so that the inertial effects of the fluid flow are not accounted for properly, and although the gas velocity vanishes at the fibre surface, both components of the velocity tend to infinity far from the fibre. It means that the Lamb model is still limited to very low values of the Reynolds number. But in addition, the Lamb model might have a high degree of error if used in the modelling of filters with extremely high porosity, when the mean inter-fibre distances are very large compared to the fibre diameter and one has to compute the trajectories of aerosol particles beginning very far from the fibre.

The next, more successful trial to improve the Lamb solution, was undertaken by Tomotika and Aoi (1950) who employed a different kind of expansion to obtain the stream function as a sum of the stream function given by Lamb plus a correction term proportional to the Reynolds number. Tomotika and Aoi’s solution is a first order (with respect to Re) correction to the Lamb model, hence it also possesses an undesirable property of diverging gas velocity to infinity at an infinite distance from the fibre, though, like for the Lamb model, the non-slip conditions at the fibre surface are fulfilled exactly. Podgórski (1993) has shown a very accurate solution to the Oseen problem using Imai’s (1951) method of a complex disturbance velocity. A comprehensive comparison of the various flow models past an isolated fibre and an analysis of their applicability in the modelling of aerosol filtration in fibrous filters was presented by Lastow and Podgórski (1998).

3.2. Fibre in cell models

In contrast to isolated fibre models, fibre-in-cell models also describe one fibre but it placed centrally in a finite volume of fluid, called the unit cell. For the most popular, Kuwabara (1959) and Happel (1959) models, this unit cell is a cylinder (coaxial with a fibre) of radius R_K , such that $R_K = R_c / \alpha^{1/2}$, Kuwabara (1959) derived a formula for the stream function for the creeping flow assuming non-slip conditions on the fibre surface and normal velocity and vorticity at the border of the unit cell to be zero. Happel (1959) obtained a similar solution assuming the tangential stress instead of vorticity to be zero at the cell border.

Kirsch and Fuchs (1967) measured fluid velocities in a system of parallel cylinders and concluded that the Kuwabara formula fits the experimental data better than the Happel solution. The Kuwabara model was extended by Pich (1966), Yeh and Liu (1974) and Henry and Ariman (1981) to allow for possible gas slip on the surface of an ultrathin fibre. In practice, this extension is important for fibres with a diameter below one micrometer. A disadvantage of the Kuwabara and Happel models is related to the fact that it is impossible to compose a filter structure as a set of circular unit cells (without the cells overlapping or empty spaces between them). Marshall et al. (1994) derived an approximate analytical solution for a fibre in a square cell that obeys periodic boundary conditions; the resulting formula for the stream function is much more complex than the Kuwabara solution. The authors reported that deposition efficiency predicted by the rectangular cell model is higher than that for the original Kuwabara model. Banks and Kurowski (1990) extended the 2D Kuwabara model for the case of gas flow past a fibre inclined with respect to the main direction of the gas flow.

3.3. Analytical solution of flow around two fibres

Przekop and Podgórski (2004) have proposed a solution to the Oseen problem for the case of two cylindrical fibres. The authors noticed that an approximate analytical solution can easily be obtained using Imai's (1951) method of complex disturbance velocity, which was used earlier by Podgórski (1993) to obtain a solution to the Oseen problem in case of a single fibre. Let us introduce two Cartesian coordinate systems Ox_1y_1- and Ox_2y_2- engaged in the centre of the second fibre, oriented such that axes Ox_1 and Ox_2 overlap the main direction of gas flow. Similarly, let us introduce two cylindrical coordinate systems engaged in the centre of both fibres, $Or_1\theta_1$ and $Or_2\theta_2$, where angles θ_1 and θ_2 are measured from axes Ox_1 and Ox_2, respectively, counter-wise to the main direction of the gas flow (Fig. 1).

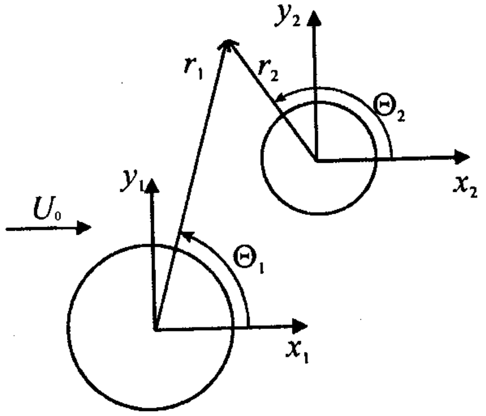

Fig. 1. Definition of the co-ordinates systems for flow past two fibres

Following the Imai's scheme one may introduce a complex coordinate $z = x + iy$, where $i = \sqrt{-1}$ is an imaginary unit and a complex disturbance velocity U, such that $U{+}u_0{=}u_x{-}iu_y$. A general solution to the Oseen problem in cylindrical coordinate system has the following form if one decomposes U into harmonic, U_h, and non-harmonic, U_u, components:

$$\begin{aligned} U = U_h + U_u = \sum_{i=1}^{\infty} \frac{A_n}{r_n} exp(-in\theta) + \\ + exp(k^* x) \sum_{i=1}^{\infty} [B_n K_{n-1}(k^* r) exp[i(n-1)\theta] + \overline{B}_n K_n(k^* r) exp(-in\theta)] \end{aligned} \tag{4}$$

where

$$k^{*}=\frac{U}{2\nu} \tag{5}$$

Let us define:

$$\begin{aligned} A_n &= a_n + i\alpha_n \\ B_n &= b_n + i\beta_n \\ \overline{B}_n &= b_n - i\beta_n \end{aligned} \tag{6}$$

In view of $u_x = u_0 + Re(U)$ and $u_y = Im(U)$, where $Re(U)$ and $Im(U)$ denote the real and imaginary parts, respectively, we can calculate their values as:

$$\begin{aligned} u_x = u_0 &+ \sum_{n=1}^{N}\frac{a_n^{(1)}\cos n\theta_1 + a_n^{(1)}\sin n\theta_1}{r_1^{\,n}} + \sum_{n=1}^{N}\frac{a_n^{(2)}\cos n\theta_2 + a_n^{(2)}\sin n\theta_2}{r_2^{\,n}} + \\ &+ exp(k^{*}x_1)\sum_{n=1}^{N} b_n^{(1)}[K_{n-1}(k^{*}r_1)cos(n-1)\theta_1 + K_n(k^{*}r_1)\cos n\theta_1] + \\ &- exp(k^{*}x_1)\sum_{n=1}^{N} \beta_n^{(1)}[K_{n-1}(k^{*}r_1)sin(n-1)\theta_1 + K_n(k^{*}r_1)\sin n\theta_1] + \\ &+ exp(k^{*}x_2)\sum_{n=1}^{N} b_n^{(2)}[K_{n-1}(k^{*}r_2)cos(n-1)\theta_2 + K_n(k^{*}r_2)\cos n\theta_2] + \\ &- exp(k^{*}x_2)\sum_{n=1}^{N} \beta_n^{(2)}[K_{n-1}(k^{*}r_2)cos(n-1)\theta_2 + K_n(k^{*}r_2)\cos n\theta_2] \end{aligned} \tag{7}$$

$$\begin{aligned} -u_y = &\sum_{n=1}^{N}\frac{a_n^{(1)}\cos n\theta_1 - a_n^{(1)}\sin n\theta_1}{r_1^{\,n}} + \sum_{n=1}^{N}\frac{a_n^{(2)}\cos n\theta_2 - a_n^{(2)}\sin n\theta_2}{r_2^{\,n}} + \\ &+ exp(k^{*}x_1)\sum_{n=1}^{N} b_n^{(1)}[K_{n-1}(k^{*}r_1)sin(n-1)\theta_1 - K_n(k^{*}r_1)\sin n\theta_1] + \\ &+ exp(k^{*}x_1)\sum_{n=1}^{N} \beta_n^{(1)}[K_{n-1}(k^{*}r_1)cos(n-1)\theta_1 - K_n(k^{*}r_1)\cos n\theta_1] + \\ &+ exp(k^{*}x_2)\sum_{n=1}^{N} b_n^{(2)}[K_{n-1}(k^{*}r_2)sin(n-1)\theta_2 - K_n(k^{*}r_2)\sin n\theta_2] + \\ &+ exp(k^{*}x_2)\sum_{n=1}^{N} \beta_n^{(2)}[K_{n-1}(k^{*}r_2)cos(n-1)\theta_2 - K_n(k^{*}r_2)\cos n\theta_2] \end{aligned} \tag{8}$$

To obtain $8N$ constants of integration ($a_n^{(1)}$, $b_n^{(1)}$, $a_n^{(2)}$, $b_n^{(2)}$, $\alpha_n^{(1)}$, $\beta_n^{(2)}$, $n = 1,\ldots, N$) one uses the zero-velocity condition for both components on both fibre surfaces and expands the exponential components into Fourier-Bessel series which leads to a system of $8N$ linear equations, from which the necessary constants may be derived.

Similary to Podgórski (1993) solution for the case of a single fibre, the method fulfils the condition of steady gas velocity away from the fibre surface.

The results obtained by Przekop and Podgórski (2004) have shown a strong influence of mutual fibre orientation on filtration efficiency and spatial distribution of deposits, which suggests that mesoscale inhomogeneity of filter structures may influence the overall filtration efficiency. This problem will be discussed later in this review.

3.4. Multi fibre models

No exact analytical solution to the problem of gas flow in a system consisting of many fibres exists. However, some analytical approximate solutions can be obtained for assumed regular arrangements of fibres. There are two popular models of a fibrous filter: channel structure (rectangular array) and staggered model (hexagonal array). The basic element of such structures is a row of parallel cylinders. General solutions of the problem of creeping flow past a row of fibres were obtained by Tamada and Fujikawa (1957) and Miyagi (1958) in the form of an infinite series. Explicit expressions for gas velocity components taking into account only the first terms of the series were first presented by Kirsch and Stechkina (1977). However, such a description was not sufficiently accurate (for typical values of the filter porosity, that solution gave the velocity on the fibre surface of the order of 10% of the mean gas velocity). Expansions for two terms of the series were given by Podgórski and Gradoń (1992), and an even more accurate solution for three terms was presented by Podgórski et al. (1998).

4. THE COUPLING OF DETERMINISTIC AND STOCHASTIC MECHANISMS

Particle collection by interception occurs when a particle follows a gas streamline that happens to come within a particle radius to the surface of a fibre. The particle hits the fibre and is captured due to its finite size. The single fibre deposition efficiency due to interception depends on the dimensionless parameter, R, defined as

$$R = \frac{d_p}{d_F} \tag{9}$$

The single fibre efficiency due to interception was given by Lee and Ramamurthi (1993) as:

$$E_R = \frac{(1-\alpha)R^2}{Ku(1+R)} \tag{10}$$

where Kuwabara factor, Ku, is defined as:

$$Ku = -\frac{ln\,\alpha}{2} - \frac{3}{4} + \alpha - \frac{\alpha}{4} \tag{11}$$

Inertial impaction occurs when the particle, because of its inertia, is unable to adjust quickly to the abruptly changing streamlines near the fibre and crosses those streamlines to hit the fibre. The parameter that governs this mechanism is Stokes number

$$Stk = \frac{\rho_p d_p C_c U}{18\mu d_F} \tag{12}$$

The single fibre efficiency for inertia was given by Yeh and Liu (1974)

$$E_I = \frac{Stk\ J}{Ku^2} \tag{13}$$

where:

$$J = \left(29.6 - 28\alpha^{0.62}\right)R^2 - 27.5R^{2.8} \qquad \text{for } R < 0.4$$

$$J = 2.0 \qquad \text{for } R > 0.4 \tag{14}$$

Impaction is the most important mechanism for large particles. But such particles reveal significant collection by direct interception as well. The sum of E_I and E_R may not exceed the theoretical value of R+1.

The Brownian motion of small particles is sufficient to greatly enhance the probability of their hitting a fibre while travelling past it on a non-intercepting streamline. The single fibre efficiency is a function of dimensionless Peclet number, Pe

$$Pe = \frac{d_F U}{D} \tag{15}$$

The single fibre efficiency due to diffusion was empirically determined by Kirsch and Fuchs (1968) as

$$E_{diff} = 2Pe^{-2/3} \tag{16}$$

Theoretical expression for E_{diff} including the effect of Ku was presented by Brown (1993)

$$E_{diff} = 2.9\left(\frac{1-\alpha}{Ku}\right)^{1/3} Pe^{-2/3} + 0.62Pe^{-1} \tag{17}$$

In estimating the deposition efficiency near the size of minimum efficiency Hinds (1999) reported the necessity to include the interaction term for enhanced collection due to the interception of diffusing particles

$$E_{BD} = \frac{1.24R^{2/3}}{(KuPe)^{1/2}} \tag{18}$$

Generalised Brownian dynamics algorithm accounting simultaneously for particle inertia, random walk, convection in a moving fluid and influence of external forces was derived by Podgórski (2002) from Chandrasekhar's (1943) method. Particle trajectory is calculated for the generalised Besset-Boussinesqu-Ossen equation, which in a simplified form is reduced to the following expression:

$$m\frac{dv}{dt} = F^{(D)} + F^{(ext)} + F^{(R)} \tag{19}$$

Integration of Eq. (19) for the time interval Δt, small enough that the host fluid velocity u_i and the external force $F_i^{(ext)}$ may be assumed constant over $(t, t + \Delta t)$, gives the following bivariate normal density probability distribution functions $\varphi_i(\Delta v_i, \Delta L_i)$ that during time interval Δt the particle will change its i^{th} component of velocity by Δv_i and it will be displaced by a distance ΔL_i in i^{th} direction.

$$\begin{aligned}\varphi_i(\Delta v_i, \Delta L_i) = {} & \frac{1}{2\pi\sigma_{vi}\sigma_{Li}\sqrt{1-\rho_c^{\,2}}}\, exp\left\{-\frac{1}{2(1-\rho_c)^2}\left[\left(\frac{\Delta v_i - <\Delta v_i>}{\sigma_{Li}}\right) - \right.\right. \\ & \left.\left. - \frac{2\rho_c(\Delta v_i - <\Delta v_i>)(\Delta L_i - <\Delta L_i>)}{\sigma_{vi}\sigma_{Li}} + \left(\frac{\Delta L_i - <\Delta L_i>}{\sigma_{Li}}\right)^2\right]\right\}\end{aligned} \tag{20}$$

The generalised algorithm for the Brownian dynamics can be formulated as follows. For a given initial particle position and its initial velocity components, v_i, at a moment t, we calculate the local fluid velocity, u_i, the external forces, $F_i^{(ext)}$, then, one calculates the expected values $<\Delta v_i>$ and $<\Delta L_i>$ and the correlation coefficient, ρ_c. Next, we generate two independent random values G_{Li}, G_{vi}, having Gaussian distribution with zero mean and a unit variance. Finally, we calculate the change of particle velocity, Δv_i, and the particle linear displacement, ΔL_i, during time step Δt from the expressions accounting for deterministic and stochastic motion:

$$\Delta v_i = <\Delta v_i> + G_{vi}\sigma_{vi} \tag{21}$$

$$\Delta L_i = <\Delta L_i> + \rho_c G_{vi}\sigma_{Li} + \left(1-\rho_c^{\,2}\right)G_{Li}\sigma_{Li} \tag{22}$$

All the steps are repeated for each co-ordinate $i = 1, 2, 3$. Having determined the increments Δv_i and ΔL_i the new particle velocity at the moment $t + \Delta t$ is obtained as $v_i(t+\Delta t) = v_i+\Delta v_i$, and in the same manner the new particle's position is calculated. After completing one time-step of simulations, the next step is performed in the same way.

Based on comparison of Brownian dynamics calculations of a single fibre efficiency and "classical theory" estimations of deterministic and diffusive deposition, Sztuk et al. (2012) have reported the enhancement term in a similar form to Eq. (18).

5. THERMAL REBOUND AND RESUSPENSION

5.1. Empirical correlations

Most theories of aerosol filtration in fibrous filters assume that the particle is captured when it collides with a fibre. However, the particle may bounce-off the collector if its kinetic energy is high enough to overcome the energy of adhesion. Maus and Umhauer (1997) observed experimentally that the collection efficiency of particle drops for values of the Stokes number above 2. The authors suggested the following empirical correlation for the adhesion efficiency (defined as the ratio of the actually measured collection efficiency to that calculated with the particle rebound neglected):

$$AE = (1.76Stk)/\left(1+Stk^2\right) \tag{23}$$

Another formula was proposed by Ptak and Jaroszczyk (1990):

$$AE = 190/\left[190+\left(18\ Stk^2 d_F/d_p\right)^{0.68}\right] \tag{24}$$

Using the data collected by Brown (1993), Podgórski et al. (1998) derived another correlation:

$$AE = 1.8\times10^{-4}E_{kp}^{\,-0.24} \tag{25}$$

Kasper et al. (2010) have introduced bounce parameter $\beta \sim Stk/R$. The authors concluded that compact, forward facing deposit structures dominate in case of significant particle bounce ($\beta > \beta^*$ where β^* represents the critical conditions for the onset bounce on the bare fibre). For smaller values of bounce parameter, dendritic structures with pronounced sideways branching are formed. The critical bounce parameter is defined as $\beta^* = d_p U^*$. The critical fluid velocity, U^*, is defined as fluid velocity above which particles start to bound. Critical fluid velocity depends on particle size and material (Wang and John, 1987).

5.2. Molecular Dynamics

Moskal and Przekop (2002) have used Molecular Dynamics method to model particle deposition on surfaces. In this method the motion of each particle is computed by Newton's law. The standard pair-wise potential in Molecular Dynamics simulations is the Lennard-Jones potential

$$\phi = -4\varepsilon_b\left[\left(\frac{\sigma}{r_a}\right)^6 - \left(\frac{\sigma}{r_a}\right)^{12}\right] \tag{26}$$

Molecular dynamics can be used to calculate, both, static and dynamic properties of the system. The method briefly described above was used to simulate the impact of a particle with collector surface. Particle deformations during the impact were observed. Also, the possibility of particle rebound from surface was theoretically confirmed. The method allows to predict forces acting between the particle and surface during the impact.

5.3. Energy-balanced oscillatory model

Energy-balanced oscillatory model of particle rebound and resuspension was introduced by Przekop et al. (2004). The model is based on adhesion theory. There are two dominating models of particle adhesion proposed by Johnson et al. (1971), known as JKR theory, and by Derjaguin et al. (1975), referred to as DMT theory. The JKR model assumes that adhesion-induced deformations are entirely elastic. Deformations could be calculated from three terms: the elastically stored energy from creating the contact zone, the mechanical potential energy, and the surface energy. The JKR theory assumes that interaction forces exist at the contact area only. When the applied load is negative, the contact area decreases. This means that the force of adhesion may be defined as the opposite of the force required to separate two bodies:

$$F_a = \frac{3}{2}\pi\gamma d_p \tag{27}$$

The contact area corresponding to this force is not zero. However, it jumps to zero as the surfaces spontaneously separate. The DMT theory does not approach the problem of particle adhesion from a contact mechanism perspective. It takes into account the molecular attraction in the noncontact zone. The analysis consists of two steps: determination of a shape of a particle near the contact surface and calculation of the sticking force. The applied load causes a pressure distribution over the contact area. The DMT model assumes that this distribution is given by Hertz equations (Hertz, 1896). The theory considers the generalised force of particle attraction, F_s, the elastic reaction force, F_e, and the adhesion force, $F_a = F_s - F_e$. When the sphere just touches the plane ("point contact"), there is no deformation and the adhesion force has the maximum value:

$$F_a = 2\pi\gamma d_p \tag{28}$$

Muller et al. (1980) proposed a model, later called MYD, in which the surface forces were calculated by doing a pairwise summation of interaction potentials between atoms. The basic assumption is that atoms in a particle are interacting with those in the substrate via a Lennard-Jones potential (Lennard-Jones, 1924) and the motion of one atom does not affect the position of neighbouring atoms. According to MYD theory, both the JKR and DMT models are its subsets and have their ranges of validity. The JKR model is proper for compliant materials, large particles, and high values of work of adhesion, whereas the DMT model is valid for small particles, more rigid materials, and lower surface energies.

The resuspension model is based on works by Reeks et al. (1988) and Ziskind et al. (2000). The authors assumed that the adhesion force and elastic reaction force considered in the JKR theory can be described by an equation of harmonic movement with dumping effect. Extending this approach, one can assume that the interactions between particles also have an oscillatory character. The displacement of a particle at the cluster attached to the neighbouring particles can be expressed as follows:

$$-kx - b\frac{dx}{dt} = m\frac{d^2x}{dt^2} \tag{29}$$

The coefficient of stiffness can be calculated from the expression:

$$k = 2.4\left(\gamma\kappa^2 \frac{d_p{}^2}{4}\right)^{1/3} \tag{30}$$

The elastic constant κ is given by:

$$\kappa = \frac{4}{3}\left(\frac{1-\nu_1}{E_{Y1}} + \frac{1-\nu_2}{E_{Y2}}\right)^{-1} \tag{31}$$

The coefficient of dumping $b = b_f + b_m$, where

$$b_f = \frac{3\pi d_p{}^2 \mu}{2m}\left(\frac{\sqrt{k}}{2\nu}\right) \tag{32}$$

$$b_m = \frac{2.4}{\pi}\frac{mk^2}{\rho_2 (E_{Y2}/\rho_2)^{3/2}} \tag{33}$$

The process of resuspension is caused by external forces, but the transmission of stress by interactions between particles is also important. Interaction between particles (or particle and collector) vanishes when the distance between their surfaces is larger than y_b.

$$y_b = 0.437\left(\frac{\pi^2\gamma^2 d_p/2}{\kappa^2}\right)^{1/3} \tag{34}$$

6. MESOSCALE INHOMOGENEITY

The first approach to modelling of mesoscale in homogeneity were purely empirical correction factors, derived to obtain agreement between theory and experiment (Benarie, 1969). These correction factors (called filter inhomogeneity factors) are defined as:

$$\Lambda_P = \frac{\Delta P}{\Delta P_{hom}} \tag{35}$$

$$\Lambda_E = \frac{ln(1-\eta)}{ln(1-\eta)_{hom}} \tag{36}$$

Cai (1992) reported the following expressions:

$$\Lambda_P = \exp\left(-3\sigma_p{}^2\right) + \frac{0.4\sigma_p{}^3}{0.8+\sigma_p{}^3} \tag{37}$$

$$\Lambda_E = \exp\left(-2\sigma_p{}^2\right) + \frac{0.8\sigma_p{}^3}{1.3+\sigma_p{}^3} \tag{38}$$

Shweers and Löffler (1994) subdivided a filter into a series of cubical elements with different local permeabilities and then used the known correlations for the single fibre deposition efficiency for each element. The distribution of local packing densities was assumed to be log-normal. The overall filter efficiency was then calculated element by element. A similar approach was used by Dhaniyala and Liu (2001). The authors also assumed log-normal distribution of local packing densities and used well known correlations to calculate single fibre efficiency as a function of the local packing density. The filter efficiency was then obtained computing the integral-mean of the deposition efficiency averaged over the assumed distribution of the packing density. An even simpler model was proposed by Clement and Dunnett (2000). The authors used the standard equation of the "classical theory", Eq. (1), assuming that for a non-uniform filter the parameter is a random variable (along various paths through a filter) having Gaussian distribution.

All these models can predict a lower pressure drop and a higher penetration than results from the "classical theory" for homogeneous structures. Neither of them, however, seems to be realistic, since they are based on the concept of the single fibre efficiency and averaging over an assumed distribution. Thus, the effect of neighbouring fibres is in practice neglected. Moreover, as the transport of aerosol in a porous space between many fibres is not considered in these models, the fundamental phenomena related to the filter non-uniformity (namely, a preferential "channelling" of flow through regions of a higher local porosity and the "shadowing" of fibres by preceding ones in zones of a lower local porosity) are not taken into consideration. Podgórski and Moskal (2001) and Podgórski (2002) have performed the analysis for a representative volume of a filter, which contains a small enough number of fibres to enable a numerical solution of microscopic transport equations, and simultaneously large enough to assure that the results obtained are statistically significant.

The model calculations consisted of the following steps: a) generation of a filtering structure consisting of 100 fibres placed in space in an assumed way (completely random distribution, perfectly regular arrangement of fibres, or a slightly disturbed ordered structure); b) characterisation of the degree of the structure inhomogeneity by dividing it into smaller parts, determination of the local packing densities and the standard deviation of the packing density distribution; c) calculation of the microscopic flow pattern in the entire structure by numerical solution of Navier-Stokes equation (using Fluent CFD package) and determination of the pressure drop; d) solution of Lagrangian transport equations (Brownian dynamics method) for a cloud of 10.000 particles injected into the filter and direct determination of the overall penetration by counting the number of particles leaving the filter; due to the stochastic nature of Brownian motion, step d) is repeated several times and results are averaged. Such simulations allow the relationships between the filter penetration, pressure drop, standard deviation of the local packing density and particle residence time to be established.

It may be concluded that classical theories of homogeneous filter media always overestimate pressure drop in real, more or less random fibrous filters. The pressure drop in a filter with a random arrangement of fibres is well correlated with the degree of filter inhomogeneity measured by the standard deviation of the local mesoscale packing density and this relationship seems to be linear.

Too high variability of the local filter porosity causes very strong channelling of the aerosol stream resulting in a drop of filtration efficiency. On the other hand when the structure becomes too regular, the shadowing effect (also lowering filtration efficiency) may be the predominant phenomenon so an optimum level of filter inhomogeneity might be expected. From the practical point of view, it seems that the bypass effect is most important for real fibrous filter structures.

Similar results were obtained by Przekop and Jackiewicz (2016). The authors studied the influence of filter inhomogeneity and fibre size distribution on deposition efficiency and pressure drop using 3D lattice-Boltzmann hydrodynamics combined with Brownian Dynamics model of particle displacement. The assumption of polydispersity of fibre sizes increased the predicted values of filtration efficiency. It was probably related to the presence of small fibres in the filter structure.

Przekop and Gradoń (2008) analysed the time evolution of quality factor defined as:

$$QF = -\frac{ln(1-\eta)}{\Delta P} \tag{39}$$

for homogenous and inhomogeneous filter structures. It was shown that for inhomogeneous structures the time of filter clogging can be significantly longer than that of regular ones, so some optimum level of polydispersity not only for initial filter performance, as mentioned above, but also for its time evolution is expected.

7. DEPOSITION OF NON-SPHERICAL PARTICLES

When the transport of spherical particle is considered, it is usually sufficient to take into account only the translation of the particle mass centre. However aerosol aggregates composed of many solid particles are of great concern in most environmental issues (Wichmann and Peters, 2000). Real aggregates may undergo modifications of structure owing to the fluid–structure interaction during their movement in fluid. This fact has explicit importance in estimating aggregate deposition ratios on filter fibre. In order to establish deposition efficiencies for fractal-like aggregates, one should include interactions between primary particles which are often not stiff. Aggregate deposition efficiency is determined largely by the deformation of their structure. A flexible or rigid structure of aggregate gives different values of deposition efficiency (Podgórski et al., 1995). With the increasing power of the computers, research into the dynamics of fractal-like aggregates has been enhanced by their more complex and accurate mathematical models. There are two ways to model fractal-like aggregates. The first is to model an aggregate structure as a rigid body, which does not undergo deformation. An example of this approach can be followed in the work of Moskal and Payatakes (2006). The algorithm for the random displacement of small aggregates, whose deposition is controlled by diffusion, can be found in Bałazy and Podgórski (2007). The most important fact in this approach is that the structure and accurate shape of the aggregate are included, in order to find the real movement of the structure. The second approach allows the modelling of aggregates as flexible structures. Aggregates can be modelled with different elasticity. A common way to model an aggregate as a flexible structure is to apply interactions between primary particles, which are modelled by harmonic oscillator equation. Harmonic oscillator has been used to study the adhesion of particles on soft and rough surfaces (Reeks et al., 1988), or to model the re-entrainment of aggregates from the surface of the filter fibre (Przekop et al., 2004). This enables to go forward and use this approach to model movement of flexible aggregates in fluid. Flexible structures of aggregates, which undergo deformation under fluid interaction, are often modelled by joining together particles connected through springs or ball–socket systems. There are few examples of models of flexible aggregate structures that have been used for different tasks. Yamamoto and Matsuoka (1992) designed a flexible model consisting of connected rigid spheres, and established a new method called particle simulation method. Forces and torques acting on particles are obtained from previously calculated components of a mobility matrix. Interaction between particles is modelled by functions which mimic stretching, bending and twisting. Various structures can be analysed, such as rod-like or plate-like particles, with different abilities to deform under shear flow (Yamamoto and Matsuoka, 1999). Ross and Klingenberg (1996) used a flexible fibre model based on Yamamoto and Matsuoka's (1992) equations, where a structure is made up of rigid prolate spheroids connected through a ball and socket system. Switzer and Klingenberg (2004) developed a particle-level flexible chain fibre model, consisting of a number of cylinders connected with a ball and socket system, which has been used to investigate flocculation in the system of fibres interacting with each other. Wang et al. (2006) established a rod-chain-like fibre model, which can simulate long fibre chains with a relatively small amount of elements, which can speed up the calculations. Yamanoi and Maia (2011) analysed flexible and rigid fibres by implementing the particle simulation model approach, in order to investigate rheological properties under shear flow. In Żywczyk and Moskal (2015) model a flexible fractal-like aggregate is composed of N identical spherical primary particles. Interactions between particles are modelled by imposing equations of potential energy functions, which control stiffness of a structure. Aggregate structure is submitted to stochastic Brownian force, causing the modification of structure during its movement in fluid. The model was used to find the deposition efficiency of aggregates with different fractal dimensions, composed of various numbers of primary particles. Aggregates are conveyed towards the fibre's surface for various values of air velocity. More or less flexible structures of aggregates were analysed. It was shown that interactions between primary particles and the modifications of structure influence the efficiency of deposition of fractal-like aggregates.

8. NON-STEADY STATE FILTRATION

During an initial period of filtration, aerosol particles deposits on the collector surfaces forming chainlike agglomerates – dendrites. This phenomenon and its consequences were analysed originally for the case of submicron particles deposited on the micronsize fibres, by Payatakes and Gradoń (1980a) and then extended by Payatakes and Gradoń (1980b). The presence of previously deposited particles produces the increase of both – filtration efficiency and pressure drop. It is worth noting that not only the total amount of deposited particles, but also their spatial distribution and structure affect filter performance (Przekop and Gradoń, 2008). Most recently published papers (Karadimos and Ocone, 2003; Przekop and Podgórski, 2004; Przekop et al., 2004; Wang et al., 2006; Sztuk et al., 2012) consider particle deposition on the collector using the classical continuum approach. This approach can be efficiently used only for the initial stage of filtration, when previously deposited particles have not as yet significantly changed the fluid flow field and surface open for deposition. Some papers (Dunnett and Clement, 2006; Dunnett and Clement, 2012) take into account deposit growth, but the approach requires making assumptions of deposit structure. The important advantage in deep bed filtration modelling was the introduction of lattice gas automata (Biggs et al., 2003) and lattice-Boltzmann method (Long and Hilpert, 2009), that allows to take into account the geometry of flow change due to deposition of suspended particles. Biggs et al. (2003) have studied particle deposition in a 2D constriction unit cell and a random 2D porous medium. Long and Hilpert (2009) have studied filtration in sphere packings, using advection-diffusion equation for particle transport. By performing a set of numerical experiments the authors have developed a correlation for diffusional efficiency, but interception and sedimentation efficiency could be only obtained by employing terms from unit cell correlations. The authors have also reported numerical instabilities for fluid velocities higher than those of μm/s order.

The growth of deposits causes the decrease of local porosity and thus the increase of local fluid velocity and shear stress that may lead to the re-entrainment of single particles or aggregates. The phenomenon is not necessarily negative as resuspended particles may redeposit at the deeper layers of a filter structure, which results in a more uniform distribution of deposits through the filter and prevents the filter from clogging which boosts the filter lifetime. The combination of lattice-Boltzmann hydrodynamics, Brownian dynamics method for particle displacement and energy balanced model of adhesion, may be found as comprehensive model that may predict the nonsteady-state performance of a filter e.g. deposition efficiency, volume distribution of deposits or pressure drop (Przekop and Gradoń, 2008).

The concept of lattice applied to fluid dynamics is based on the Ulam's works on cellular automata, Ulam (1952). Fluid dynamics is especially a sufficiently large system for a cellular automaton formulation because there are two rich and complementary ways to picture fluid motion. The kinetic picture, in which many simple atomic elements rapidly collide with simple interactions, is in good agreement with the infinitive picture of dynamics in a cellular space.

The classical approach to the flow phenomena is through partial differential equations (Navier–Stokes equations) that describe collective motion in a dissipative fluid. The kinetic theory models a fluid by using an atomic picture and imposing Newtonian mechanics on the motion of the atoms.

Complete information on the statistical description of a fluid at, or near, its thermal equilibrium is assumed to be contained in the one-particle phase-space distribution function $f\ (x,\ t,\ □)$ for atomic constituents of the system. The variables x and t are the space and time coordinates of the atoms and □ stands for all other phase-space coordinates e.g. momentum, momentum flux. Since collisions preserve conservation laws, by integration of Boltzmann equation over the continuity equation and momentum tensor, an equation describing the macrodynamics of a system can be derived. To build a cellular-space picture with collective motion dynamics predicted by Navier-Stokes equation, a lattice on which particles move, collision rules and other restrictions characteristic for a chosen model should be defined. The evolution of the system is described by the expression:

$$f\left(\bar{x}+e_i,\bar{t}+1\right)-f\left(\bar{x},\bar{t}\right)=\Omega\left(f\right) \tag{40}$$

The outcome of a collision can be approximated by assuming that the momentum of interacting particles will be redistributed at some constant rate toward an equilibrium distribution $f_i^{eq}(x,t)$ (Qian et al., 1992). This simplification is called the single-time-relaxation approximation or lattice-BGK (Bhatnagar-Gross-Krook) and can be given by:

$$\Omega_i=\frac{1}{\bar{\tau}}\left(f_{i\,eq}\left(\bar{x},\bar{t}\right)-f_i\left(\bar{x},\bar{t}\right)\right) \tag{41}$$

In the single-time-relaxation approximation, the momentum distribution at each lattice site is forced toward the equilibrium distribution at each time step. In the absence of external forces, the equilibrium distribution of a state with zero net momentum is just equal to momentum in each direction. The rate of change toward equilibrium is $1/\bar{\tau}$, the inverse of relaxation time, and is chosen to produce the desired value of fluid viscosity.

$$\bar{\nu}=\frac{\bar{c}_s^{\,2}}{2}\left(2\bar{\tau}-1\right) \tag{42}$$

The equilibrium distribution $f_i^{eq}(x,t)$ is given as follows:

$$f_i^{eq}=\bar{\rho}\,\alpha_i\left(1+\frac{e_i\bar{u}}{\bar{c}_s^{\,2}}+\frac{1}{2}\left(\frac{e_i\bar{u}}{\bar{c}_s^{\,2}}\right)^2-\frac{\bar{u}^2}{2\bar{c}_s^{\,2}}\right) \tag{43}$$

where a_i are the model dependent constants. The values of parameters in Eq. (43) for different lattice geometries can be found in Masselot (2000). The equation of state for a discrete space has the following form:

$$\bar{P}=\bar{c}_s^{\,2}\bar{\rho} \tag{44}$$

In traditional (continuum) flow analysis, a no-slip velocity constraint is enforced along all solid-fluid interfaces. The notion behind the no-slip condition arises from the fact that there should be no discontinuities in the velocity field within the fluid as this would give rise to infinite velocity gradients and therefore infinite shear stresses. A similar argument can be employed for conditions at the wall. However, the no-slip constraint is strictly only valid if the fluid adjacent to the surface is in local thermodynamic equilibrium; a condition which requires a very high frequency of molecular collisions with the wall. In practice, the no-slip condition is found to be appropriately provided by the Knudsen number, $Kn < 10^{-2}$. If the Knudsen number is increased beyond this value, rarefaction effects start to influence the flow and the molecular collision frequency per unit area becomes too small to ensure thermodynamic equilibrium. Under such conditions, a discontinuity in the tangential velocity will form at any solid-fluid interface.

In continuum regime the bounce-back boundary condition is used on the solid level. This means that when a fluid particle enters the solid site, it changes its moving direction for the opposite one. This method naturally leads to zero-velocity at the solid level.

The model involves two parameters r, s, representing the probability for a particle to be bounced back and slipped forward, respectively. The boundary kernel takes the form, Succi (2002):

$$\mathbf{K} = \begin{pmatrix} r & 0 & s \\ 0 & r+s & 0 \\ s & 0 & r \end{pmatrix} \tag{45}$$

Obviously, the two parameters are not independent and must be chosen such that $r + s = 1$. Assuming second order slip velocity, one can write.

$$\bar{u}_{wall} = AKn\left|\frac{\partial \bar{u}_x}{\partial n}\right|_{wall} + BKn^2\left|\frac{\partial^2 \bar{u}_x}{\partial n^2}\right|_{wall} \tag{46}$$

$$A = \frac{e}{\bar{c}_s}\frac{1-r}{r}, \qquad B = \frac{e^2}{\bar{c}_s{}^2} \tag{47}$$

Knudsen number for lattice is given by

$$Kn = \frac{\bar{\nu}}{\bar{c}_s \bar{d}_F} \tag{48}$$

Przekop and Gradoń (2014) have used lattice Boltzmann algorithm combined with Brownian Dynamics method for calculations of non-steady state filter performance. Aerosol particles, moving with the superficial gas velocity, were uniformly distributed at the inlet. The particles passing through the outflow surface were lost from the computational domain; while on the sides, periodic boundary conditions were applied.

The procedure of calculating numerical, dimensionless values for lattice Boltzmann model was as follows. Having assumed physical values of air velocity and fibre size, we were able to calculate Knudsen and Reynolds numbers from the definition equations. Subsequently, the value of viscosity in the attice model and then relaxation time were calculated. After that, the formula for the Reynolds number enables to calculate a dimensionless superficial velocity for lattice-Boltzmann model. The interaction between lattice-Boltzmann and Brownian dynamics may be modelled as follows. Initially, the fluid velocity profile for a clean fibre was calculated. Then, the trajectories of aerosol particles with an assumed time step were tracked. The fluid velocity in a point of space, necessary to calculate drag forces acting on a particle, was determined as a superposition from the neighbouring nodes. Obviously, the relation between dimensionless velocity in lattice Boltzmann scheme and physical one, used in Brownian Dynamics calculations, was linear. When the deposition of particle occurred, the geometry of the computational domain was changed and a new velocity profile was calculated. The similar procedure was used earlier by Filippova and Hannel (1997) and Przekop et al. (2003) for the calculation of particle deposition on single fibre or in small fibre systems.

9. SUMMARY AND OUTLOOK

A collection of aerosol particles in the particular steps of the technology of their production, and purification of the air at the workplace and atmospheric environment, requires the efficient method of separation of particulate matter from the carrier gas. Filtration is one of the effective methods for the removal of particles from an aerosol stream. The developments in the formation of specific fibrous structures promises the construction of highly efficient filters for the collection of both micro and nanoparticles. Over the last fifty years many studies on modelling of filter performance have been done. With increasing computational power of computers it became possible to overcome all the limitations of "classical theory" of filtration. Many phenomena initially predicted about filter performance were successfully explained and described at the basic level. Today, comprehensive models of deep bed filtration enable to predict filter performance evolution over time taking into account its inhomogeneous structure, particle rebound and resuspension or changes of local velocity profile due to particle deposition and dendrite growth.

SYMBOLS

A_n	complex constant of integration
AE	adhesion efficiency
b	dumping coefficient, kg/s
b_f	fluid dumping coefficient, kg/s
b_m	mechanical dumping coefficient, kg/s
B_n	complex constant of integration
$\overline{B}_n$	coupled constant of integration
C_C	Cunningham factor
$\overline{c}_s$	dimensionless sound speed
D	diffusion coefficient, m^2/s
d_F	fibre diameter, m
d_p	particle diameter, m
e	unit vector
E	single fibre efficiency
E_{BD}	single fibre efficiency interaction term
E_{det}	deterministic single fibre efficiency
E_{diff}	diffusional single fibre efficiency
E_{kp}	particle kinetic energy, J
E_R	interception single fibre efficiency
E_I	inertial single fibre efficiency
E_Y	Young's modulus, Pa
F_a	adhesion force, N
$F^{(D)}$	drag force, N
$F^{(ext)}$	external force, N
$F^{(R)}$	random Brownian force, N
G_{vi}	random number
G_{Li}	random number
J	interception coefficient
k	stiffness coefficient, kg/s^2
K_n	modified Bessel function of n-th order
Kn	Knudsen number
Ku	Kuwabara factor
L	filter thickness, m
m	mass, kg
P	pressure, Pa
$\overline{P}$	dimensionless pressure
Pe	Peclet number

QF	quality factor, Pa^{-1}
r	reflection parameter
r_a	distance between atoms, m
R	interception parameter
R_K	Kuwabata cell diameter,
Re	Reynolds number
s	slip parameter
Stk	Stokes number
t	time, s
$\bar{t}$	dimensionless time
U	fluid velocity, m/s
U^*	critical fluid velocity, m/s
$\bar{u}$	dimensionless fluid velocity
v	particle velocity, m/s
x	position, m
$\bar{x}$	dimensionless position
y_b	distance between surfaces, m

Greek symbols

α	packing density
β	bounce parameter, m^2/s
β^*	critical bounce parameter, m^2/s
γ	work of adhesion, J/m^2
ε	porosity
ε_b	binding energy, J/mol
κ	elastic constant, Pa^{-1}
η	filter efficiency
Θ	angle, deg
λ	filter coefficient, m^{-1}
μ	viscosity, Pa*s
ν	Poisson’s ratio
ν_f	fluid dynamic viscosity, m^2/s
$\bar{\nu}$	dimensionless viscosity
ρ_c	correlation coefficient
ρ_p	particle density, kg/m^3
$\bar{\rho}$	dimensionless density
σ	spacing between atoms at which inter-particle potential is zero, m
σ_{Li}	standard deviation of displacement, m
σ_{vi}	standard deviation of velocity, m/s
σ_p	relative standard deviation of pore size distribution
$\bar{\tau}$	dimensionless relaxation time
φ_i	distribution function
ϕ	Lennard-Jones potential, J/mol
Ω	collision term

REFERENCES

Albrecht F., 1931. Theoretische Untersuchungen über die Ablagerung von Staub aus der Luft und ihre Anwendung auf die Theorie der Staubfilter. *Physik. Zeits*., 32, 48-68.

Bałazy A., Podgórski A., 2007. Deposition efficiency of fractal-like aggregates in fibrous filters calculated using Brownian dynamics method. *J. Colloid Interface Sci.*, 311, 323–337. DOI: 10.1016/j.jcis.2007.03.008.

Banks D.O., Kurowski G.J., 1990. Electrical enhancement of filters with randomly oriented fibres. *Aerosol. Sci. Tech.*, 12, 256-269. DOI: 10.1080/02786829008959344.

Benarie M., 1969. Einfluss der Porenstruktur auf den Abscheidegrad in Faserfiltern. *Staub-Reinhalt. Luft*, 29, 74-78.

Biggs M.J., Humby S.J., Buts A., Tuzun U., 2003. Explicit numerical simulation of suspension flow with deposition in porous media; influence of local flow field on deposition processes predicted by trajectory methods. *Chem. Eng. Sci*., 58, 1271-1288. DOI: 10.1016/S0009-2509(02)00103-3.

Brown R.C., 1993. *Air filtration: An integrated approach to the theory and applications of fibrous filters.* Pergamon Press, Oxford.

Cai J., 1992. *Fibrous filters with non-ideal conditions*. PhD Thesis, The Royal Institute of Technology, Stockholm.

Chandrasekhar S., 1943. Stochastic problems in physics and astronomy. *Rev. Mod. Phys*., 15, 1-89. DOI: 10.1103/RevModPhys.15.1.

Clement C.F., Dunnett. S.J., 2000. The use of random variables in fibrous filtration theory. *J. Aerosol. Sci.*, 31 (*Suppl. 1*), 200-201. DOI: 10.1016/S0021-8502(00)90207-6.

Derjaguin B.V., Muller V.M., Toporov Y.P., 1975. Effect of contact deformations on the adhesion of particles. *J. Colloid Interface Sci.* 53, 314-326. DOI: 10.1016/0021-9797(75)90018-1.

Dhaniyala S., Liu B.Y.H., 2001. Theoretical modeling of filtration by non-uniform fibrous filters. *Aerosl. Sci. Technol.* 34, 161-169. DOI: 10.1080/027868201300034763.

Dunnett S.J., Clement C.F., 2006. A numerical study of the effects of loading from diffusive deposition on the efficiency of fibrous filters. *J. Aerosol Sci*., 37, 1116-1139. DOI: 10.1016/j.jaerosci.2005.08.001.

Dunnett S.J., Clement C.F., 2012. Numerical investigation into the loading behaviour of filters operating in the diffusional and interception deposition regimes. *J. Aerosol Sci.*, 53, 85-99. DOI: 1016/j.jaerosci.2012.06.008.

Filippova O., Hänel D., 1997. Lattice-Boltzmann simulation of gas-particle flow in filters. *Comp. Fluids,* 26, 697-712. DOI: 10.1016/S0045-7930(97)00009-1.

Happel J., 1959. Viscous flow relative to arrays of cylinders. *AIChE J.*, 5, 174-177. DOI: 10.1002/aic.690050211.

Henry F., Ariman T., 1981. Cell model of aerosol collection by fibrous filters in an electrostatic field. *J. Aerosol Sci*. 12, 91-103. DOI: 10.1016/0021-8502(81)90041-0.

Hertz H., 1896. *Miscellaneous Papers.* Macmillan, London.

Hinds W.C., 1999. *Aerosol Technology.* Wiley & Sons, New York.

Imai I., 1951. On the asymptotic behaviour of viscous fluid flow at a great distance from a cylindrical body, with special reference to Filon's paradox. *Proc. Roy. Soc. London. Ser. A.,* 208, 487–516. DOI: 10.1098/rspa.1951.0176.

Johnson K.L., Kendall K., Roberts A.D., 1971. Surface energy and the contact of elastic solids. *Proc. R. Soc. London Ser. A,* 324, 301-313. DOI: 10.1098/rspa.1971.0141.

Karadimos A., Ocone R., 2003. The effect of the flow field recalculation on fibrous filter loading: a numerical simulation. *Powder Techn.*, 137, 109-119. DOI: 10.1016/S0032-5910(03)00132-3.

Kasper, G., Schollmeier, S., Meyer, J., 2010. Structure and density of deposits formed on filter fibers by inertial particle deposition and bounce. *J. Aerosol Sci*., 41, 1167-1182. DOI: 10.1016/j.aerosci.2010.08.006

Kirsch A.A., Fuchs N.A., 1967. Studies on fibrous aerosol filters. II. Pressure drops in systems of parallel cylinders. *Ann. Occup. Hyg*., 10, 23-30. DOI: 10.1093/annhyg/10.1.23.

Kirsch A.A., Fuchs N.A., 1968. Studies on fibrous aerosol filters. III. Diffusional deposition of aerosols in fibrous filters. *Ann. Occup. Hyg*. 11, 299-304. DOI: 10.1093/annhyg/11.4.299.

Kirsch A.A., Stechkina I.B., 1977. Inertial deposition of aerosol particles in model filters at low Reynolds numbers. *J. Aerosol Sci.*, 8, 301-307. DOI: 10.1016/0021-8502(77)90016-7.

Kuwabara S., 1959. The forces experienced by randomly distributed parallel circular cylinders or spheres in viscous flow at small Reynolds number. *J. Phys. Soc. Jpn.,* 14, 527-532. DOI: 10.1143/JPSJ.14.527.

Lamb H., 1932. *Hydrodynamics.* Cambridge University Press, Cambridge.

Lastow O., Podgórski A., 1998. Single fibre collection efficiency. In: Spurny K.R. (Ed.), *Advances in Aerosol Filtration*. Lewis Publishers, Boca Raton, 25-52.

Lee K.W., Ramamurthi M., 1993. Filter collection. In: Willeke K., Baron M. (Eds.) *Aerosol Measurements: Principles, Techniques and Applications*. Van Nostrand Reinhold, New York, 188.

Lennard-Jones J.E., 1924. On the determination of molecular fields. II. from the equation of state of a gas. *Proc. Royal Soc. London A*, 106, 463-477. DOI: 10.1098/rspa.1924.0082.

Long W., Hilpert M., 2009. A correlation for the collection efficiency of Brownian particles in clean bed filtration in sphere packings by a lattice-Boltzmann method. *Eniornm. Sci. Techn.*, 35, 205-218. DOI: 10.1021/es8024275.

Marshall H.; Sahraoui M.; Kaviany M., 1994. An improved analytic solution for analysis of particle trajectories in fibrous, two-dimensional filters. *Phys. Fluids,* 6, 507-520. DOI: 10.1063/1.868346.

Masselot A., 2000. *A new numerical approach to snow transport and deposition by wind: A parallel lattice gas model*. PhD Thesis, Geneve University, 2000.

Maus R., Umhauer H., 1997. Single fibre collection and adhesion efficiency for biological particles. *Part. Part. Syst. Charact*., 14, 250-256.

Moskal A., Payatakes A.C., 2006. Estimation of the diffusion coefficient of aerosol particle aggregates using Brownian simulation in the continuum regime. *J. Aerosol Sci.*, 37, 1081–1101. DOI: 10.1016/j.jaerosci.2005.10.005.

Muller V.M., Yushchenko B.V. Toporov Y.P., 1980. On the influence of molecular forces on the deformation of an elastic sphere and its sticking to a rigid plane. *J. Colloid Interface Sci.* 77, 91-101. DOI: 10.1016/0021-9797(80)90419-1.

Oseen C.W., 1927. *Neuere Methoden und Ergebnisse in der Hydrodynamik.* Akademische Verlagsgesellschaft, Leipzig.

Payatakes A.C., Gradoń L., 1980a. Dendritic deposition of aerosols by convective Brownian motion diffusion for small, intermediate and large Knudsen numbers. *AIChE J.*, 26, 443-454. DOI: 10.1002/aic.690260316.

Payatakes A.C., Gradoń L., 1980b. Dendritic deposition of aerosol particles in fibrous media by inertial impaction and interception. *Chem. Eng. Sci.*, **35**, 1083-1096. DOI: 10.1016/0009-2509(80)85097-4.

Pich J.,1966. Theory of aerosol filtration by fibrous and membrane filters. In: Davies C.N. (Ed.) *Aerosol Science*, Academic Press, London, 223-285.

Podgórski A., Gradoń L., 1992. Shadow and ordering effects in fibrous electret filters. *J. Aersol Sci.,* 23 (*Suppl. 1*), 753-756. DOI: 10.1016/0021-8502(92)90521-V.

Podgórski A., 1993. Analytical description of gas flow around a fibre for modelling of aerosol filtration. *J. Aersol Sci*., 24 (*Suppl. 1*), S277-S278. DOI: 10.1016/0021-8502(93)90231-W.

Podgórski A., Gradoń L., Grzybowski P., 1995. Theoretical study on deposition of flexible and stiff fibrous aerosol particles on a cylindrical collector. *Chem. Eng. J.,* 58, 109–121.

Podgórski A., Luckner H.J., Gradoń L., Wertejuk Z., 1998. Aerosol particle filtration in the fibrous filters at the presence of external electric field I. Theoretical model. *Chem. Process Eng.*, 19, 865-889.

Podgórski A., Moskal A., 2001. Dispersion of submicron aerosol particles in fibrous filters. *Chem. Process Eng*., 22, 1139-1144.

Podgórski A., 2002. *On the transport, deposition and filtration of aerosol particles in fibrous filters: Selected problems*. Oficyna Wydawnicza Politechniki Warszawskiej, Warsaw.

Przekop R., Moskal A., Gradoń L., 2003. Lattice-Boltzmann approach for description of the structure of deposited particulate matter in fibrous filters. *J. Aerosol Sci.,* 34, 133-147. DOI: 10.1016/S0021-8502(02)00153-2.

Przekop R., Grzybowski K., Gradoń L., 2004. Energy-balanced oscillatory model for description of particles deposition and reentrainment on fibre collector. *Aerosol Sci. Techn.*, 38, 330-337. DOI: 10.1080/02786820490427669.

Przekop R., Podgórski A., 2004. Effect of shadowing on deposition efficiency and dendrites morphology in fibrous filters. *Chem. Proc. Eng.*, 25, 1563-1568.

Przekop R., Gradoń L., 2008. Deposition and filtration of nanoparticles in the composites of nano- and microsized fibres. *Aerosol Sci. Technol.*, 42, 483-493. DOI: 10.1080/02786820802187077.

Przekop R., Gradoń L., 2014. Effect of particle and fibre size on the morphology of deposits in fibrous filters. *Int. J. Num. Meth. Fluids*, 76, 779-788. DOI: 10.1002/fld.3952.

Przekop R., Jackiewicz A., 2016. Effect of filter inhomogenity on deep bed filtration process. *22nd Polish Conference of Chemical Engineering*, Spała, Poland, 5-9 September 2016, 1152-1159.

Qian Y.H., d'Humieres D., Lallemand P., 1992. Lattice-BGK models for Navier-Stokes equation. *EPL*, 17, 479–484. DOI: 10.1209/0295-5075/17/6/001.

Reeks M.W., Reed J., Hall D., 1988. On the resuspension of small particles by turbulent flow. *J. Phys. D: Appl. Phys.*, 21, 574-589. DOI: 10.1088/0022-3727/21/4/006.

Ross R.F., Klingenberg D.J., 1996. Dynamic simulation of flexible fibres composed of linked rigid bodies. *J. Chem. Phys.*, 106, 2949–2960. DOI: 10.1063/1.473067.

Schweers E., Löffler F., 1994. Realistic modelling of the behaviour of fibrous filters through consideration of filter structure. *Powder Technol.*, 80, 191-206. DOI: 10.1016/0032-5910(94)02850-8.

Sell W., 1931. Staubabscheidung an einfachen Körpern und Luftfiltren. *VDI Forschungs Heft.*, 347, 1-14.

Switzer L.H., Klingenberg, D.J., 2004. Flocculation in simulations of sheared fibre suspensions. *International J. Multiphase Flow*, 30, 67–87. DOI: 10.1016/j.ijmultiphaseflow.2003.10.005.

Succi S., 2002. Mesoscopic modelling of slip motion at solid-fluid interfaces with heterogeneous catalysis. *Phys. Rev. Lett.,* 89, 64502. DOI: 10.1103/PhysRevLett.89.064502.

Sztuk E., Przekop R., Gradoń L., 2012. Brownian dynamics for calculation of the single fibre deposition efficiency of submicron particles. *Chem. Process Eng.*, 33, 279-290. DOI: 10.2478/v10176-012-0025-y.

Tamada K., Fujikawa H., 1957. The steady two-dimensional flow of viscous fluid At low Reynolds number passing through an infinite row of equal parallel circular cylinders. *Q. J. Mech. Appl. Math.*, 10, 425-432. DOI: 10.1093/qjmam/10.4.425.

Tomotika S., Aoi T., 1950. The steady flow of viscous fluid past a sphere and circular cylinder at small Reynolds numbers. *Q. J. Mechanics Appl. Math.*, 3, 141–161. DOI: 10.1093/qjmam/3.2.141.

Ulam S., 1952. Random processes and transformations. In: *Proceedings of the International Congress of Mathematicians (Cambridge, Massachusetts, August30-September 6, 1950),* American Mathematical Society, Providence, Rhode Island, 264-275.

Wang H.C., John W., 1987. Comparative bounce properties of particle materials. *Aerosol Sci. Technol.*, 7, 285-299. DOI: 10.1080/02786828708959165.

Wang G., Yu W., Zhou Ch., 2006. Optimization of the rod chain model to simulate the motions of long flexible in a simple shear flows. *Euro. J. Mech. B/Fluids*, 25, 337–347. DOI: 10.1016/j.euromechflu.2005.09.004.

Yamamoto S., Matsuoka T., 1992. A method for dynamic simulation of rigid and flexible fibres in a flow field. *J. Chem. Phys*., 98, 644–650. DOI: 10.1063/1.464607.

Yamamoto S., Matsuoka T., 1999. Dynamic simulation of rod-like and plate-like particle dispersed systems. *Comp. Materials Sci*., 14, 169–176. DOI: 10.1016/S0927-0256(98)00103-7.

Yamanoi M., Maia J.M., 2011. Stokesian dynamics simulations of the role of hydrodynamics interactions on the behaviour of a single particle suspending in a Newtonian fluid. Part 1. 1D flexible and rigid fibres. *J. Non-Newtonian Fluid Mech.*, 166, 457–468. DOI: 10.1016/j.jnnfm.2011.02.001.

Yeh H.C., Liu B.Y.H., 1974. Aerosol filtration by fibrous filters - I. Theoretical. *Aerosol Sci.,* 5, 191-204. DOI: 10.1016/0021-8502(74)90049-4.

Ziskind G., Fichman M., Gutfinger C., 2000. Particle behavior on surfaces subjected to external excitations. *J. Aerosol Sci*., 26, 703-720. DOI: 10.1016/S0021-8502(99)00554-6.

Żywczyk Ł., Moskal A., 2015. Modelling of deposition of flexible fractal-like aggregates on cylindrical fibre in continuum regime. *J. Aerosol Sci*., 81, 75-89. DOI: 10.1016/j.jaerosci.2014.12.002.

Received 30 November 2016
Received in revised form 10 February 2017
Accepted 11 February 2017

DE GRUYTER OPEN
www.czasopisma.pan.pl Chemical and Process Engineering 2017, 38 (1), 51-66 www.journals.pan.pl
DOI: 10.1515/cpe-2017-0005

PROCESS DESIGN FOR SIZE-CONTROLLED FLAME SPRAY SYNTHESIS OF $Li_4Ti_5O_{12}$ AND ELECTROCHEMICAL PERFORMANCE

Oliver Waser[1], Oliver Brenner[1], Arto J. Groehn[2], Sotiris E. Pratsinis*[1]

[1]Particle Technology Laboratory, Department of Mechanical and Process Engineering, ETH Zurich, Sonneggstrasse 3, CH-8092 Zurich, Switzerland

[2]Department of Chemical and Biological Engineering, University of Colorado, Boulder, 80309 CO, USA

Dedicated to Prof. Leon Gradoń on the occasion of his 70th birthday

Inexpensive synthesis of electroceramic materials is required for efficient energy storage. Here the design of a scalable process, flame spray pyrolysis (FSP), for synthesis of size-controlled nanomaterials is investigated focusing on understanding the role of air entrainment (*AE*) during their aerosol synthesis with emphasis on battery materials. The *AE* into the enclosed FSP reactor is analysed quantitatively by computational fluid dynamics (CFD) and calculated temperatures are verified by Fourier transform infrared spectroscopy (FTIR). Various $Li_4Ti_5O_{12}$ (LTO) particle compositions are made and characterized by N_2 adsorption, electron microscopy and X-ray diffraction while the electrochemical performance of LTO is tested at various charging rates. Increasing *AE* decreases recirculation in the enclosing tube leading to lower reactor temperatures and particle concentrations by air dilution as well as shorter and narrower residence time distributions. As a result, particle growth by coagulation – coalescence decreases leading to smaller primary particles that are mostly pure LTO exhibiting high C-rate performance with more than 120 mAh/g galvanostatic specific charge at 40C, outperforming commercial LTO. The effect of *AE* on FSP-made particle characteristics is demonstrated also in combustion synthesis of $LiFePO_4$ and ZrO_2.

Keywords: Li-ion battery, $Li_4Ti_5O_{12}$, size control, residence time distribution, computational fluid dynamics, flame synthesis of electroceramics

1. INTRODUCTION

With the spread of electric-mobility and renewable energy applications the need for inexpensive, safe and long-lasting energy-storage systems arises (Poullikkas, 2013). Batteries are well suited for this task (Armand and Tarascon, 2008) with the inherently safe LTO anode (Ferg et al., 1994) and LFP cathode materials (Padhi et al., 1997). Both are promising due to their low cost, abundant raw materials and environmental friendliness as well as performance in Li-ion batteries and novel hybrid supercapacitors made of LTO (Naoi et al., 2013) or LFP (Vlad et al., 2014). Furthermore, the negligible volume change of LTO during charging – discharging, zero-strain insertion (Ohzuku et al., 1995), results in outstanding cycle stability (Du Pasquier et al., 2009). Furthermore, LTO anode electrodes can be built with about three times lighter aluminium current collectors compared to the typically required Cu since the LTO insertion potential vs. Li/Li^+ is relatively high (> 1.2 V) and Li alloying of aluminium can be excluded (Hudak and Huber, 2012). A challenge of both materials, however, is their poor Li diffusion,

---

*Corresponding author, e-mail: sotiris.pratsinis@ptl.mavt.ethz.ch

10^{-12} cm^2/s for LTO (Wagemaker et al., 2009) and less than 10^{-9} cm^2/s for LFP (Gaberscek et al., 2007), hindering Li-ion transport during fast charge - discharge. Nanosizing LFP (Gaberscek et al., 2007) and LTO (Bresser et al., 2012), however, has shown distinct performance improvement by shortening the diffusion path lengths.

To take advantage of nanosize, economic synthesis methods are needed to preserve the benefit of low cost raw materials for LTO and LFP. Flame aerosol reactors have high potential in that front since they already produce several tons per hour of nanostructured carbon blacks for tire reinforcing and inks, TiO_2 for white pigments and catalysis or fumed SiO_2 as flowing aid and excipient for drugs (Pratsinis, 1998, Wegner and Pratsinis, 2003). These, typically gas-fed, flame aerosol reactors have limited precursor selection where the liquid-fed flame spray pyrolysis (FSP) (Madler et al., 2002) offers wide precursor flexibility (Teoh et al., 2010) for multi-component nanoparticles and close control over particle size and phase resulting in an array of functional materials (Strobel and Pratsinis, 2007).

More specifically, FSP has been applied for synthesis of nanosized battery active $LiMn_2O_4$, LTO and $LiFe_5O_8$ (Ernst et al., 2007) as well as LFP after annealing of amorphous precursor nanoparticles under reducing conditions (Waser et al., 2011) and very high charging rate (C-rate) capable LTO nanoparticles (Bresser et al., 2012). This FSP process is scalable (Mueller et al., 2003) to, at least, 10 metric tons per year production rate (Wegner et al., 2011) as it is similar to the furnace process for manufacture of carbon blacks (Strobel and Pratsinis, 2007). For such scale-up, however, process design by computational fluid dynamics (CFD) (Johannessen et al., 2000) is essential for understanding the effect of process variables to product particle characteristics as with FSP production of ZrO_2 (Groehn et al., 2012, Groehn et al., 2014).

Tube-enclosed FSP (Teleki et al., 2006) allows better control of the combustion environment to produce, for example, metallic nanoparticles (Athanassiou et al., 2006), select the product composition between maghemite, magnetite or wustite iron oxides (Strobel and Pratsinis, 2009), or anatase and rutile TiO_2 (Kho et al., 2011). Tube enclosing also allows in-situ SiO_2 coating on TiO_2 (Teleki et al., 2008), or Ag (Sotiriou et al., 2010) and carbon-coating of LFP nanoparticles (Waser et al., 2011). Recent in-situ XRD & microscopy (Krumeich et al., 2016) has shown that crystallization of the initially glassy carbon-coated LFP starts at about 400 °C, forming single crystals inside the confinement of the carbon shell. At about 700 °C, LFP starts to diffuse through the carbon shell creating cavities inside the shell. At 800 °C, the initial core-shell morphology converts into open carbon shells (flakes and cenospheres) and rather bulky LFP particles (300–400 nm in diameter) (Krumeich et al., 2016), in agreement with ex-situ experiments (Waser et al., 2011).

Particles made by enclosed FSP are typically 3-4 times larger than those made by open FSP under identical reactant flows and compositions as has been shown with TiO_2 and iron oxides above as well as CuO (Waser et al., 2013). Particle size control in tube-enclosed FSP can be accomplished also quite inexpensively by selectively allowing ambient air entrainment into the FSP unit as has been shown recently for CuO (Waser et al., 2014).

Here we generalize this method for primary particle size control during synthesis of nanosized battery active LTO and amorphous LFP precursor as well as ZrO_2 by tube-enclosed FSP. The spatial distributions of temperature and residence time in the reactor are elucidated by CFD and the particle size dependent electrochemical performance of LTO is evaluated in Li-ion test cells.

2. EXPERIMENTAL

2.1. Particle Synthesis

Nano-sized LTO, amorphous LFP precursor and ZrO_2 particles were made by FSP of precursor solutions in open (Madler et al., 2002) and tube-enclosed configurations (Waser et al., 2014). For the latter, a 20-cm long quartz glass tube of 4.7 cm inner diameter (ID) and 0.25 cm wall thickness was used. The (forced) air entrainment into this tube was controlled by a mass flow controller (MFC, Bronkhorst, Netherlands) through a stainless steel drum of 15 cm ID and 8 cm inner height surrounding the 1.0 cm gap between the FSP burner surface and the enclosing tube (Waser et al., 2014).

The LTO precursor solution (1.0 M total metal concentration) consisted of Li-acetylacetonate (Li-acac 97 %, Sigma-Aldrich, Switzerland) and Ti(IV)-isopropoxide (TTIP $\geq$ 97 %, Sigma-Aldrich, Switzerland) in stoichiometric molar ratio of Li / Ti = 4 / 5, diluted with a 1 / 3 (by volume) mixture of 2-ethylhexanoic acid (2-EHA, Sigma-Aldrich, Switzerland) and xylene (Sigma-Aldrich, Switzerland) solvents. For the FTIR temperature measurements and CFD calculations a metal-free solvent mixture was used where the TTIP is equivolumetrically replaced by isopropyl alcohol (2-propanol $\geq$ 99.5 %, Sigma-Aldrich, Switzerland) resulting in a volume-ratio of 1 / 3 / 0.787 of 2-EHA / xylene / 2-propanol and thus in approximately the same enthalpy density of 33 MJ/L (< 1 % deviation) as the above metal-containing precursor solution.

Similarly, the LFP precursor solution (0.24 M total metal concentration) consisted of Li-acetylacetonate (Li-acac $\geq$ 97 %, Sigma-Aldrich, Switzerland), iron (III) - acetylacetonate (Fe-acac $\geq$99%, Fluka, Switzerland) and tributyl phosphate ($\geq$99 %, Fluka, Switzerland) in stoichiometric molar ratio of Li / Fe / P = 1 / 1 /1, diluted with an equivolumetric mixture of 2-EHA, toluene (Sigma-Aldrich, Switzerland), diethylene glycol monobutyl ether (purum $\geq$98%, Fluka, Switzerland) and ethanol (98 %, Alcosuisse, Switzerland) (Waser et al., 2011). The ZrO_2 precursor solution (1.0 M Zr concentration) consisted of zirconium 2-ethylhexanoate (Valirex, 18 wt % Zr, Umicore) in xylene (Sigma-Aldrich, Switzerland) (Groehn et al., 2014). These solutions were fed to the FSP burner capillary at P = 5 mL/min and dispersed into a spray by D = 5 L/min O_2 (PanGas > 99.95 %) at 180 kPa (gauge) pressure drop resulting in nominal LTO, LFP and ZrO_2 production rates of 15.3, 3.9 and 37 g/h, respectively. The spray was ignited and supported by a stoichiometrically premixed pilot flame of 1.25 L/min CH_4 (PanGas > 99.5 %) and 2.5 L/min O_2 surrounding the dispersion O_2 annulus. In all experiments S = 10 L/min of sheath O_2 was introduced through 32 holes (0.06 cm *ID*) surrounding the pilot flame to ensure full oxidation of the precursor (Rudin et al., 2011). All gas flow rates are given at STP. The product particles were collected on glass-fibre filters (ALBET GF6, 25.7 cm in diameter) by a vacuum pump (Busch Mink MM 1324AV).

2.2. CFD Simulations

Commercial ANSYS Fluent v.12.1.4 was used on a two-dimensional (rotation symmetric) rectangular computational grid (height 35 cm, width 10 cm, approx. 10^5 cells) based on Groehn et al. (2012) with the difference of having a tube enclosure and adapted solvent mixture composition (without metal precursors) and flows to simulate synthesis of LTO. Radiation heat transfer was accounted for by the Fluent's built-in discrete ordinate model complemented with a weighted-sum-of-gray-gases model and user-specified gas mean beam length L^0 = 4.3 cm (Olfe, 1961). Furthermore, the dissociation energy of CH_4, CO_2, N_2, H_2O and O_2 was accounted for and a transition shear stress transport turbulence model was used instead of the classic k-ε since laminar flow patterns are present within the tube.

The residence time distributions were simulated by introducing a 10 ms pulse of 2 L/min Ne tracer along with 8 L/min O_2 sheath (to maintain the total of 10 L/min sheath gas flow). The pulse response was evaluated 0.5 cm above the tube exit (Octave, 1999). This was done after convergence of the actual (steady state) simulations by a separate transient simulation (Gamba et al., 2012) of the Ne concentration (Waser et al., 2014) by solving only the Ne transport equation with a time step size of 10^{-4} s. For details about the CFD boundary conditions please refer to Table A1 and Fig. A1 of the Appendix.

2.3. Temperature measurements

The line-of-sight tube exit temperature of the FSP gases during LTO synthesis was measured 0.5 cm above the tube exit by Fourier transform infrared spectroscopy (FTIR) by emission / transmission analysis (Morrison et al., 1997). Thereby, a metal precursor-free solvent mixture (2-EHA / xylene / 2-propanol = 1 / 3 / 0.787) was combusted with P = 5 ml/min and D = 10 L/min O_2, accompanied by S = 10 L/min O_2 sheath. The shaded area (Fig. 2) represents the difference between FTIR emission / transmission and normrad analysis spectra (Madler et al., 2002) while the solid red line is their average.

2.4. Particle and electrochemical characterization

Product powders were characterized by X-ray diffraction (XRD) for crystallinity (Bruker D8, Germany) and N_2 adsorption (5-point isotherm) for specific surface area, SSA (Micromeritics, Tristar 30000). The Brunauer–Emmett–Teller (BET) diameter is used as the average primary particle diameter, $d_{\mathrm{BET}} = 6 / (\mathrm{SSA} \times \rho)$, with bulk densities ρ of LTO: 3.48 (Deschanvres et al., 1971), LFP: 3.60 (Streltsov et al., 1993), CuO: 6.52 (Asbrink and Norrby, 1970) and ZrO_2: 5.72 g/cm^3 (Whitney, 1994), respectively.

The electrochemical performance of the LTO particles is evaluated in Li-ion battery half-cells vs. Li/Li$^+$. As-prepared LTO nanoparticles from open and enclosed FSP with AE = 50, 100, 200 and 300 L/min, respectively, are used as active material (AM). Carbon black (CB; Super P, TIMCAL SA, SSA = 62 m^2/g) was used as a conductive additive. Polyvinylidene fluoride (PVDF; SOLEF 5130, Solvay) dissolved in N-methylpyrrolidinone (NMP; Fluka) was used as binder. Since electrode mass loading and CB content strongly influence the high C-rate performance of Li-ion electrodes (Zheng et al., 2012) two sets of electrodes were made to benchmark the LTO performance. One set of electrodes was made with an electrode mass-ratio (after drying) of AM / CB / PVDF of 80 / 10 / 10 (Nowack et al., 2013) and a second one with 70 / 15 / 15 (Bresser et al., 2012). The suspensions were prepared by mixing all constituents in NMP with an ultrasonic stirrer (Vibra-Cell VCX 500, Sonics, USA) for about 2 min at 100 W and 20 kHz using a micro-tip.

To prepare test electrodes, suspensions were doctor-bladed at a ‘‘wet’’ thickness of 250 µm (80 / 10 / 10 composition) and 150 µm (70 / 15 / 15 composition) onto a 20 µm thick conductive carbon-coated aluminium current collector foil (EQ-CC-Al-20u-260, MTI, USA) and dried at 110 °C under vacuum overnight. Afterwards, disk electrodes of diameter 1.3 cm were punched out and dried again under vacuum at 110 °C overnight. The AM mass loading was 2.8 ± 0.1 mg/cm^2 for the 80 / 10 / 10 composition and 1.5 ± 0.15 mg/cm^2 for the 70 / 15 / 15 composition of the FSP-made LTO. The AM mass loading of commercial LTO was 2.0 ± 0.3 mg/cm^2 for both compositions. Coin-type test cells were assembled in an argon-filled glove box with less than 1 ppm of O_2, N_2, and H_2O. Lithium metal (99.9 %, Aldrich) served as both reference and counter electrode. A fiberglass separator (1 mm thick) was soaked with 500 µl of standard electrolyte 1 M LiPF6 in ethylene carbonate (EC) / dimethyl carbonate (DMC), 1:1 by mass (Selectilyte LP 30, BASF, Germany).

All electrochemical measurements (MPG-2, Bio-Logic, France) were performed at 25 °C and specific current corresponding to 0.1 – 50 C (1 C = 175 mA/g of LTO). For the rate capability measurements, the LTO electrodes were galvanostatically lithiated at the specified C-rate and delithiated at 1 C between 1.2 and 2.2 V vs. Li/Li^+. To promote complete lithiation / delithiation at the respective potential limits, a potentiostatic step was included until the specific current decreased to 17.5 mA/g (0.1 C). All electrochemical results are the average of three cells and error bars show the standard deviation.

3. RESULTS AND DISCUSSION

3.1. Temperature Distribution and Flow Streamlines

Figure 1 depicts the temperature distribution by CFD above the FSP burner as a function of air entrainment (*AE*) flow rate into the tube enclosure (from a to e) in comparison to open FSP (g) with overlaid streamlines. At low *AE* (< 100 L/min), a recirculation zone forms that is typical for bounded jets with limited co-flow (Curtet, 1958). The recirculation mass flow, m_r (fluid flow with negative velocity), relative to the net mass flow, m_0, (f) is shown as a function of height above the burner (HAB). Increasing the *AE* reduces the m_r / m_0 to practically zero for $AE \geq 100$ L/min (Fig. 1f).

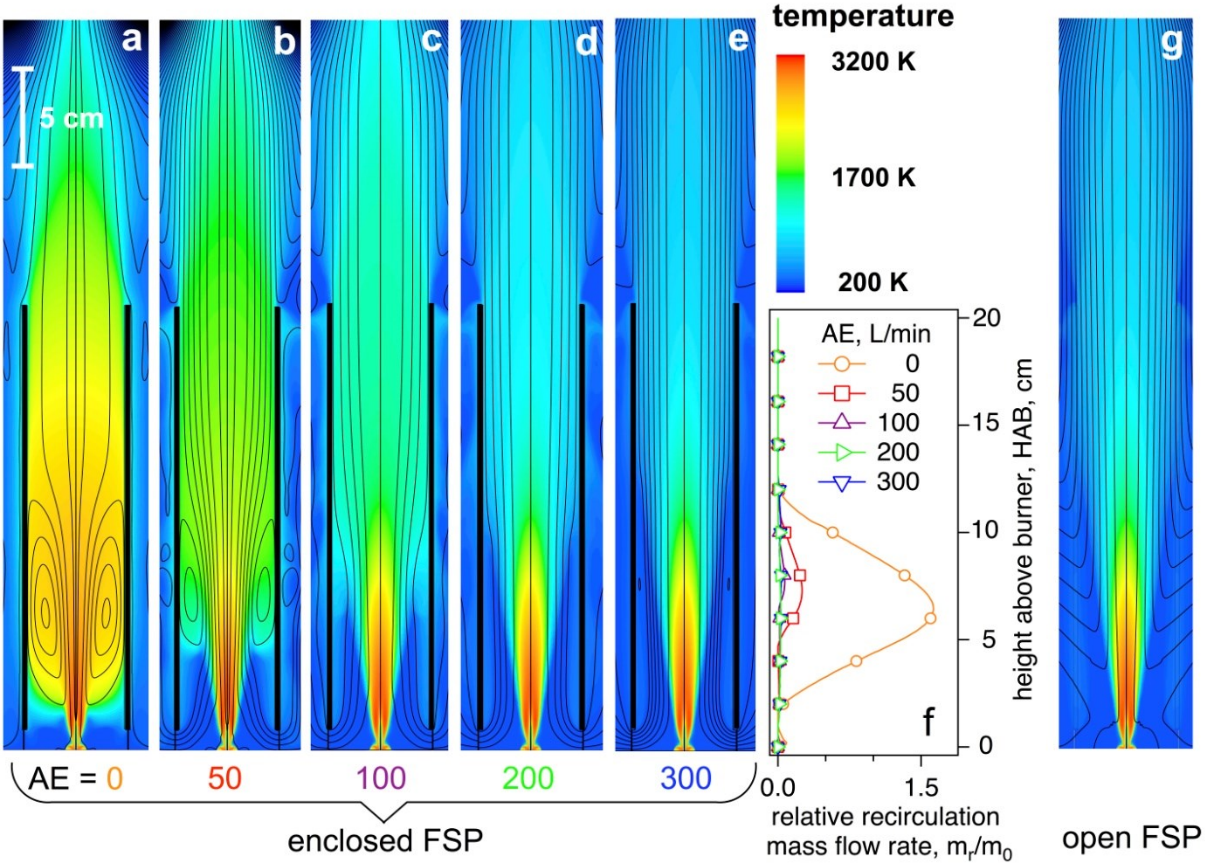

Fig. 1. Temperatures and flow streamlines by computational fluid dynamics (CFD) at air entrainment flow rate *AE* = 0, 50, 100, 200, 300 L/min into the enclosing tube for flame spray pyrolysis (FSP) of a solvent mixture (a to e), simulating $Li_4Ti_5O_{12}$ production, in comparison to open FSP (g). The relative recirculation mass flow (m_r/m_0) as a function of height above burner (f) is defined as the backflow (m_r) relative to the net mass flow (m_0) in the tube cross section and shows that up to about 150 % the net mass flow recirculates in the lower half of the tube (circles) in the absence of air entrainment (*AE* = 0 L/min). This recirculation decreases markedly with increasing *AE* to about 20 wt% of the net mass flow rate at *AE* = 50 L/min and practically ceases at $AE \geq 100$ L/min

Figure 1 illustrates also that the overall temperature within the tube decreases with increasing *AE* due to dilution, in agreement with such measurements at the tube exit for CuO synthesis (Waser et al., 2014). In the absence of entrained air (*AE* = 0 L/min, Fig 1a), the recirculation vortex and the extended high temperature zone in the reactor impose prolonged particle residence time at high temperature that typically leads to extended particle growth. In contrast, for increasing *AE* (50 – 100 L/min), that vortex shrinks and the overall temperature in the tube drops reducing particle growth. For *AE* ≥ 200 L/min, the temperature distribution and flow pattern are similar to those of the open FSP (Fig. 1g), consistent with similar product particle primary diameters from both FSP configurations for CuO (Waser et al., 2014) and as will be shown in Fig. 4.

Figure 2 shows the measured (circles) and CFD-calculated (diamonds) line-of-sight averaged temperature at the tube exit as a function of *AE*. The emission / transmission and normrad analyses of the FTIR spectra only deviate (shaded area in Fig. 2) at the completely enclosed configuration (*AE* = 0 L/min) due to strong IR absorption of CO_2 in such un-diluted off-gas. The aerosol temperature at 21.5 cm HAB of the open FSP configuration is shown to the right of Fig. 2. This HAB corresponds to the tube exit temperature above the enclosed FSP (1 cm tube lift-off from the FSP burner plus 20 cm tube length and 0.5 cm distance above the tube). As expected, the tube exit temperature decreases with increasing *AE* due to air dilution and cooling in agreement with temperature measurements during CuO synthesis by FSP (Waser et al., 2014).

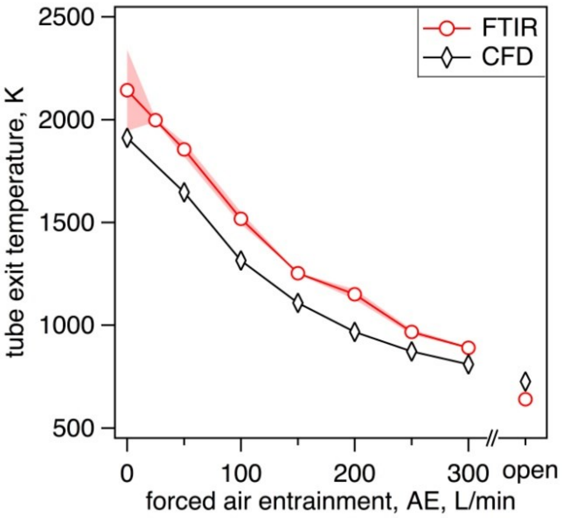

Fig. 2. Tube exit temperature at 0.5 cm height above the enclosing tube (HAT) exit during combustion of solvent mixture simulating LTO production by FTIR (red circles) and line-of sight averaged CFD temperature profile (black diamonds). As comparison, the temperatures for open FSP at 21.5cm (1 cm gap + 20 cm tube + 0.5 cm HAT) above FSP burner level are displayed to the right.

3.2. Aerosol Residence Time Distribution

Reasonably good agreement is obtained between temperature measurements and CFD simulations, however, with a consistent underprediction of about 50 - 200 K by CFD. This might be due to the rather simple eddy dissipation model (Magnussen and Hjertager, 1977) employed by CFD or the relatively simple discrete ordinate radiation model and assumptions for the gas radiative properties (Olfe, 1961). No significant differences in the FTIR spectra of effluent gases at various AE flow rates were observed indicating that chemical reactions had been completed at the tube exit regardless of AE flow rate (Mueller et al., 2004).

At low *AE* flow rates (< 100 L/min, Fig.1), vortices are formed that greatly influence the aerosol residence time distribution (RTD) within the tube und thus the time available for particle growth.

Figure 3a depicts such CFD calculated RTD's for various *AE* flow rates. The mean residence time, τ (triangles) and geometric standard deviation, σ_g, (diamonds) of these RTDs are presented in Fig. 3b. For no *AE* (0 L/min), strong recirculation is present (Fig. 1) resulting in the longest and broadest RTD (Fig. 3a, solid line) compared to higher *AE* of 50 – 300 L/min. Increasing the *AE* to 50 L/min reduces the mean residence time, τ, (Fig. 3b, triangles) by a factor of 3.5 from about 300 to 90 ms where further increasing the AE from 50 to 300 L/min gradually decreases τ to 40 ms. The spread of the RTD, given by σ_g (Fig. 3b, diamonds), shows also a distinct narrowing from $\sigma_g = 2.1$ at $AE = 0$ to $\sigma_g = 1.4$ at $AE = 50$ L/min in agreement with the disappearance of the recirculation zone (Fig.1). Upon further increasing the AE, the spread of the RTD remains largely invariant around $\sigma_g = 1.5$. So, increasing the *AE* clearly reduces the average high temperature residence time as both τ and *T* (Fig. 2) decrease by air dilution along with the precursor concentration. In combination, this results in smaller primary particles as shown for CuO (Waser et al., 2014).

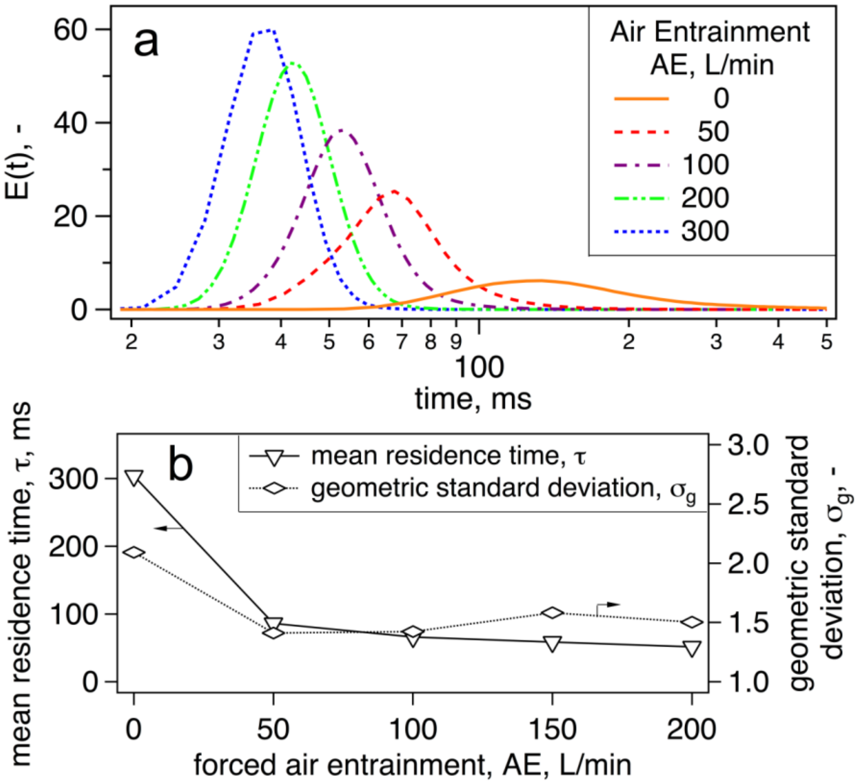

Fig. 3. (a) CFD-calculated aerosol residence time distributions within the enclosing tube at various airentrainment (*AE*) flow rates. At *AE* = 0 the RTD is longest and exceptionally wide, typical for recirculating flows (Fig.5.1) resulting in high particle deposition on tube walls. (b) Mean residence time (τ, triangles) & geometric standard deviation (σ_g, diamonds). The, τ decreases with increasing *AE* due to higher volume flow and reduced recirculation that narrow σ_g

Figure 4 presents the average primary particle diameter (d_{BET}) as a function of *AE* flow rate into the enclosed FSP unit for synthesis of LTO (open squares), LFP (diamonds) and ZrO_2 (circles) in comparison to CuO (triangles (Waser et al., 2014)) as well as the average LTO crystallite size (filled squares) by XRD (Fig. 5). The particle sizes from open FSP are shown to the right while selected images of LTO (a-c), ZrO_2 (d, e) and CuO (f) are presented as insets. Clearly, the largest primary particles are obtained at *AE* = 0 L/min for all materials as expected from their longest residence time (Fig. 3b) and highest aerosol concentration and temperature (Figs. 1 and 2) in the tube. For increasing *AE*, the d_{BET} of LTO, LFP and ZrO_2 decrease consistent with CuO (Waser et al., 2014) shown here also for convenience.

The individual materials, however, show a different d_{BET} evolution as a function of *AE* that depends on precursor solution concentration (Table 1) and material properties. High *AE* rapidly quenches the hot aerosol resulting in short high temperature residence time (Fig. 1e,g) similar to open FSP (Madler et al., 2002). In contrast, at low *AE* the high temperature region is greatly increased (Fig. 1a,b) and shows a smoother temperature decay compared to open FSP or high-*AE* enclosed FSP (Figs. 1a,b vs. 1e,g). So, decreasing the *AE* prolongs the residence time for primary particle growth by sintering or coalescence. This generally favours low-melting-point compounds (Table 1) to grow larger than high-melting-point ones. Furthermore, particle morphology depends on the interplay of sintering and collision rate: Monolithic particles are formed if sintering is faster than collision rate and aggregates if collision is faster than sintering rate (Pratsinis, 1998). So, at *AE* = 0 L/min (Fig. 4), the average LTO primary particles grow to rather spherical and non-aggregated ones having the largest d_{BET} = 63 nm (squares) as seen by microscopy (Fig. 4a). This indicates collision-limited growth of the comparatively low melting point LTO (m_p = 1290 K, Table 1).

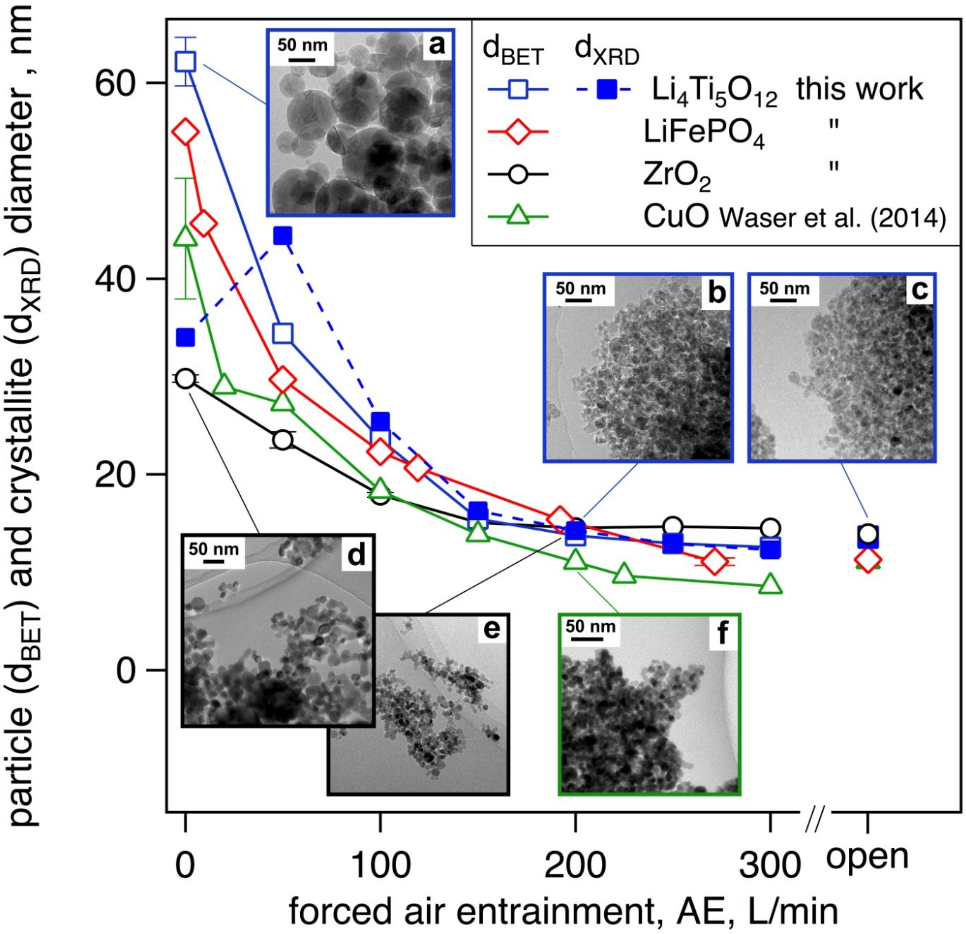

Fig. 4. Primary particle (d_{BET}, open symbols) and LTO crystallite diameter (filled squares) as a function of *AE* of LTO (squares) and LFP (diamonds), ZrO_2 (circles) and CuO (triangles, Waser et al. 2014) made by tube-enclosed FSP. As comparison, the d_{BET} from open FSP are displayed to the right. Insets show selected TEM images of LTO made at *AE* of (a) 0, (b) 200 L/min and (c) open FSP, ZrO_2 made at *AE* of (d) 0 and (e) 200 L/min as well as CuO made at *AE* of (f) 200 L/min

The LTO is further analysed by XRD and electrochemistry, as it is highly crystalline as-prepared. Figure 5 shows the XRD patterns (inset) of LTO made in open and tube-enclosed FSP at *AE* from 0 to 300 L/min along with the corresponding phase composition in terms of LTO (squares, ICSD 015787) and impurities: $Li_{0.14}TiO_2$ (stars, ICSD 075178), anatase (circles, ICSD 063711) and rutile TiO_2 (triangles, ICSD 080843). For *AE* = 0 L/min (orange pattern), the particles have a high impurity content of about 38 wt% $Li_{0.14}TiO_2$, 30 wt% rutile and 3 wt% anatase TiO_2 but only 29 wt% of the desired

LTO. This indicates suboptimal synthesis conditions with reactor temperatures (Fig. 2) approximately twice as high as usually applied for LTO production via solid-state reaction (Ferg et al., 1994), accompanied also by wide particle size distributions and poor yield due to long and broad RTD and deposition wall losses. For $AE \geq 50$ L/min, however, more than 95 wt% pure LTO is obtained with only minor impurities of anatase and rutile TiO_2. This appears superior to as-prepared LTO by open FSP (Ernst et al., 2007) with 87 wt% LTO content and d_{BET} of 20 nm and FSP-made nano LTO by Bresser et al. (2012) but similar to that by Karhunen et al. (2011).

Table 1. Precursor solution molarity & enthalpy with nominal production rate & melting temperature

Material	Metal concentration, mol/L	Combustion enthalpy, MJ/L	Production rate, g/h	Bulk melting temperature, K
LTO	1	33.1	15.3	1290
LFP	0.24	30.3	3.9	1320
CuO	0.25	31.8	6.0	1510
ZrO_2	1	33.6	37.0	2990

The LTO crystallite size d_{XRD} = 34 nm (Fig. 4, filled squares), determined from the peak with the Miller indices hkl = 111, at AE = 0 L/min is significantly smaller than its d_{BET} = 62 nm, as expected by its large impurity content (Birozzi et al., 2015). For AE = 50 L/min, however, the LTO average crystallite size (d_{XRD} = 44 nm) is larger than the average grain size (d_{BET} = 34 nm). This might indicate a rather broad LTO particle size distribution as shown by Rudin et al. (2011) for B_2O_3 nanoparticles and can occur by recirculation within the tube enclosure (Fig. 1b,f). For AE > 50 L/min the LTO crystallite size then continuously decreases from d_{XRD} = 26 to 14 nm, practically overlapping with d_{BET}. This indicates monocrystalline LTO.

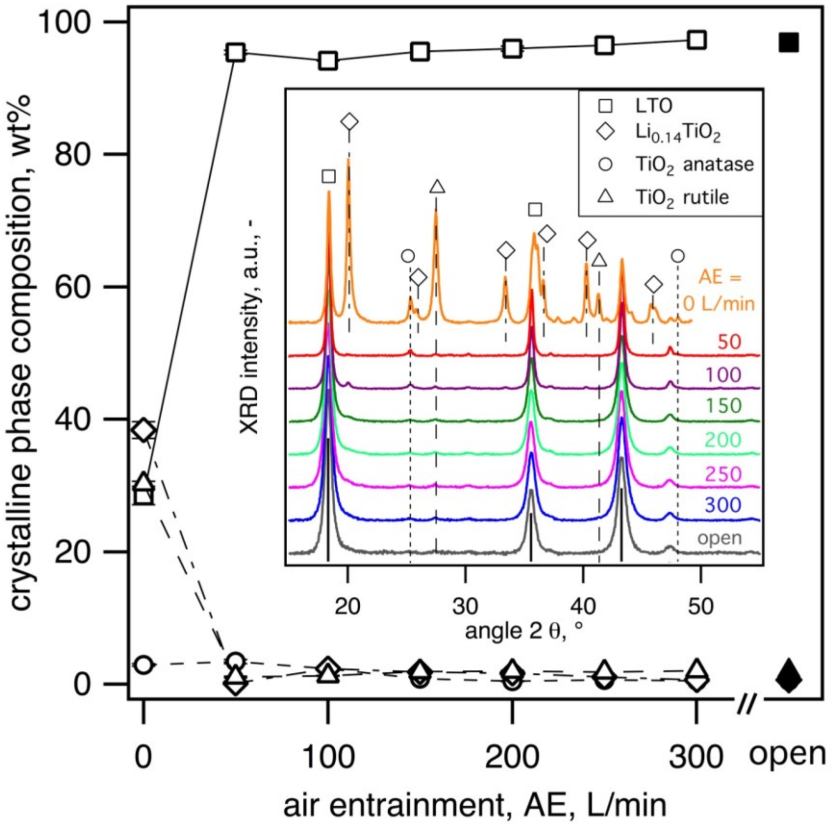

Fig. 5. XRD phase composition and patterns (inset) of as-prepared LTO particles made in tube-enclosed-FSP (open symbols) as a function of air entrainment (AE) in comparison to particles made in open- FSP (filled symbols)

It should be noted that the d_{BET} is larger than d_{XRD}. This is an intrinsic effect of the applied measurement techniques of d_{BET} (surface area derived particle diameter) and d_{XRD} (crystallite size derived particle diameter). So, if a particle contains a crystallite of LTO surrounded by other crystalline impurity or even amorphous phases the d_{BET} measures the whole particle and thus becomes larger than the d_{XRD}. The XRD, however, measures the core LTO crystallite diameter only.

3.3. Electrochemical performance

Figure 6 shows the specific charge of the thicker (2.8 mg/cm^2) electrodes upon the first lithiation (solid line) and the following delithiation (dotted line) of as-prepared LTO with average primary particle sizes of d_{BET} = 13, 14, 23 and 34 nm corresponding to those made at *AE* of 300, 200, 100 and 50 L/min (Fig. 4 squares). The theoretical specific charge of $Li_{4+x}Ti_5O_{12}$ $(0 < x \leq 3)$ is depicted as horizontal dashed line. The initial specific charge for the smallest LTO particles of d_{BET} = 13 and 14 nm is higher than the theoretical limit of 175 mAh/g (Ohzuku et al., 1995). It seems also to scale with increasing particle surface area exposed to the electrolyte since larger FSP-made (d_{BET} = 23 and 35 nm) and commercial LTO (d_{BET} = 177 nm) show specific charges below the theoretical limit.

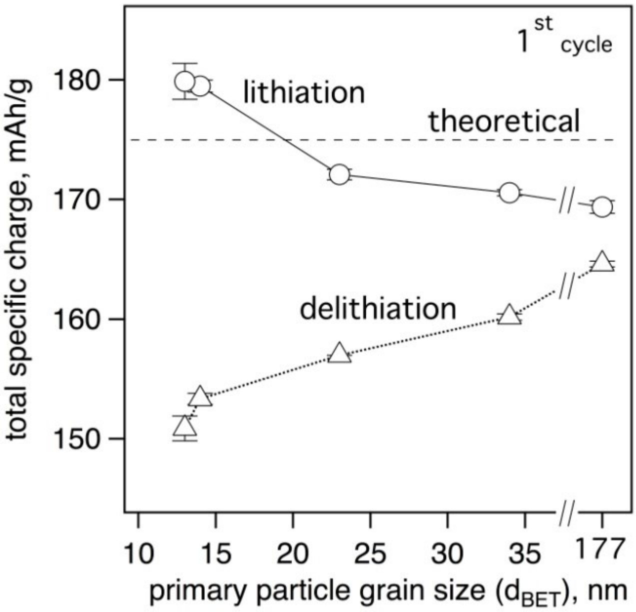

Fig. 6. Total specific charge upon first lithiation (solid line, circle) and following delithiation (dotted line, triangles) of electrodes made with as-prepared LTO nanoparticles as a function of primary particle size. The performance of commercial LTO (d_{BET}= 177 nm) is shown to the right for comparison. The horizontal dashed line indicates the LTO's theoretical specific charge of 175 mAh/g. The specific charge upon initial lithiation inversely scales with primary particle size due to irreversible surface reactions with the electrolyte. This results in higher lithiation specific charges than theoretically expected for the smallest LTO particles of d_{BET}=13 and 14 nm while the delithiation charges remain below the theoretical limit

A similar effect was observed for nanosized, FSP-made CuO particles used as conversion reaction battery material (Waser et al., 2013) where solid-electrolyte-interface (SEI) formation consumed Li (Laruelle et al., 2002). Here the extra specific charge might also be attributed to the formation of LiF, Li_2CO_3 and TiO_2 on the lithiated particle surfaces (Jiang et al., 2004). A more recent study shows approximately 3 nm thick surface layers containing anatase phase TiO_2 after immersion of the originally pure LTO particles in electrolyte solution (He et al., 2012). These reactions seem irreversible since the specific charge upon the following delithiation remains below the theoretical limit of

175 mAh/g, regardless of primary particle diameter. The trend of low specific charge upon delithiation of small LTO particles may be attributed to more pronounced LTO lattice defects in small particles (Kavan et al., 2003) resulting in lower specific charge. This results in 1st cycle coulombic efficiencies of 84, 85, 91, 94, and 97 % for d_{BET} = 13, 14, 23, 34, and commercial 177 nm LTO particles, respectively. This is in good agreement with FSP-made nano LTO (Bresser et al., 2012) also having lower columbic efficiencies of about 77 % for nanosized LTO (d_{BET} = 19 nm) compared to 94 % for micron sized particles.

Figure 7 depicts the galvanostatic specific charge upon lithiation at gradually increasing C-rates of the FSP-made LTO (Fig. 4, squares). The data in Fig. 7a are obtained from electrodes of 2.8 mg/cm^2 loading and 10 wt% conducting CB content. The data in Fig.7b are obtained from thinner electrodes of 1.5 mg/cm^2 loading and higher CB content of 15 wt%.

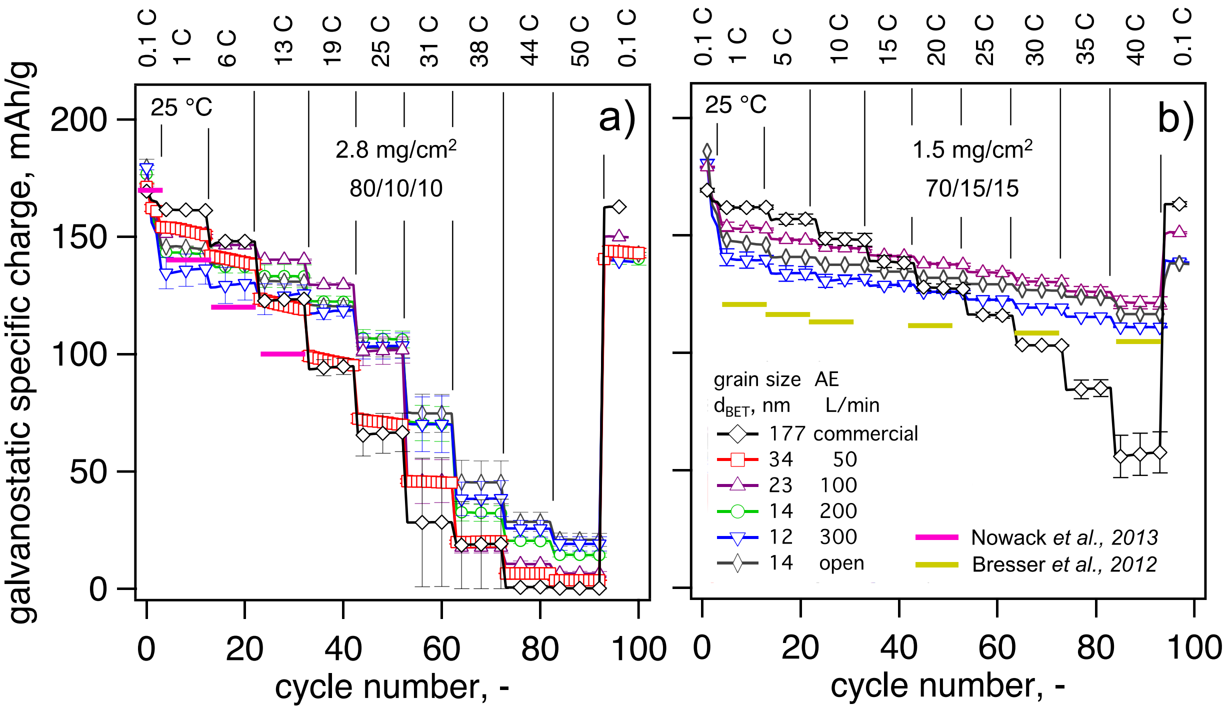

Fig. 7. Galvanostatic specific charge upon lithiation at various C-rates of electrodes made from as-synthesized LTO nanoparticles in comparison to commercial battery grade LTO. Superior high-C-rate electrochemical performance is obtained for the smallest FSP-made particles of d_{BET}= 12 to 14 where the larger ones of d_{BET} =23 and 34 nm as well as commercial LTO of d_{BET} = 177 nm shows relatively lower specific charge at high C-rates

For comparison, relatively large commercial LTO (d_{BET} = 177 nm) was processed and tested similarly (diamonds). The high but irreversible specific charge of small LTO during initial lithiation (Fig. 6) is seen also here, followed by a rapid charge decay within the first 3-4 cycles. This effect, however, is not seen for the relatively large (177 nm) commercial LTO particles that provide near theoretical specific charge of about 170 mAh/g.

Also in the subsequent cycles at low C-rates (less than 6C in Fig. 7a and 10C in Fig. 7b) the electrodes containing the largest particles (diamonds) provide the highest specific charge of 150 to 160 mAh/g where the smallest (d_{BET} = 12 nm, triangles down) deliver only 130 to 140 mAh/g for both electrode compositions. For particle sizes in between, the specific charge scales with LTO particle size as more pronounced LTO lattice defects in small particles reduce specific charge (Kavan et al., 2003). At these relatively low C-rates approximately the same performance is obtained from both electrode weight loadings and compositions for identical LTO particle size. This is expected since charge transfer resistance (diffusion limitation in electrode) and Ohmic resistance are not critical at low C-rates.

For higher C-rates (above 13C in Fig. 7a and 25C in Fig. 7b), however, the smaller particles of $d_{\mathrm{BET}} = 23$ (triangles up), 14 (open & filled circles) and 12 nm (triangles down) deliver superior specific charge compared to the larger ones of $d_{\mathrm{BET}} = 177$ nm (diamonds) due to their shorter Li-diffusion path length. They also show higher performance than, for example, microwave-assisted wet-made porous LTO particles (Nowack et al., 2013) (pink lines in Fig. 7a) as well as spray-dried porous ones (Hsiao et al., 2008). Both materials consist of nanosized primary particles of about 150 and 36 nm, respectively, consolidated in micron-sized secondary particles. The high C-rate performance of FSP-made LTO presented here is also higher than that of nano LTO (Bresser et al., 2012) ($d_{\mathrm{BET}} = 19$ nm) made by FSP (yellow lines in Fig. 7b) at similar electrode weight loading and identical electrode composition. This difference may be attributed to the improved purity of LTO (less TiO_2 impurity) obtained here (Fig. 5) by a scalable, single step process.

4. CONCLUSIONS

Air entrainment (*AE*) controls the product primary particle diameter during particle synthesis in scalable, tube-enclosed FSP. Here the underlying phenomena to this size-tuning operation are elucidated by computational fluid dynamics (CFD). At low *AE*, the tube temperature increases by minimal dilution with entrained air prolonging and broadening the aerosol residence time distribution by recirculation. These effects lead to the typically larger primary particles made in enclosed than open FSP configurations. This versatile and low cost technique is applied for size-controlled synthesis of battery active LTO (d_{BET} = 60 - 13 nm) and LFP (d_{BET} = 55 - 12 nm) as well as ZrO_2 (d_{BET} = 30 - 15 nm) by varying *AE* (0-300 L/min) into a 20 cm long enclosing tube in good agreement with literature for CuO (d_{BET} = 45 - 10 nm). As prepared, battery-active LTO particles are crystalline and quite pure resulting in high C-rate performance with more than 120 mAh/g galvanostatic specific charge at 40C outperforming commercial LTO. Tube-enclosed FSP thus offers a fast, scalable and size-controlled method to produce the intrinsically safe LTO with superior performance at high C-rate.

The research leading to these results has received funding from the European Research Council under the European Union's Seventh Framework Program (FP7 / 2007-2013) / ERC grant agreement n° 247283. We thank Dr. F. Krumeich (ETHZ) and the Electron Microscopy Center of ETH Zurich (EMEZ) for TEM.

SYMBOLS

AE	air entrainment, L/min
D	dispersion gas flow rate, L/min
d_{BET}	Brunauer–Emmett–Teller (primary particle) diameter, nm
d_{XRD}	x-ray diffraction (crystallite) diameter, nm
F	pilot flame gas flow rate, L/min
ID	inner tube diameter, cm
L	mean beam length, cm
m_0	net mass flow, kg/s
m_p	melting point, K
m_r	recirculation mass flow, kg/s
P	precursor flow rate, mL/min
S	sheath gas flow rate, L/min
SEI	solid electrolyte interphase

Greek symbols

σ_g	geometric standard deviation
τ	mean residence time, ms

REFERENCES

Armand M., Tarascon J.M., 2008. Building better batteries. *Nature*, 451, 652-657. DOI: 10.1038/451652a.

Asbrink S., Norrby L.J., 1970. A refinement of crystal structure of copper(2) oxide with a discussion of some exceptional E.s.d.'s. *Acta Crystall. B-Stru.*, B 26, 8-15. DOI: 10.1107/S0567740870001838.

Athanassiou E.K., Grass R.N., Stark W.J., 2006. Large-scale production of carbon-coated copper nanoparticles for sensor applications. *Nanotechnology*, 17, 1668-1673. DOI: 10.1088/0957-4484/17/6/022.

Birozzi A., Copley M., von Zamory J., Pasqualini M., Calcaterra S., Nobili F., Di Cicco A. Rajantie H., Briceno M., Bilbé E., Cabo-Fernandez L., Hardwick L.J., Bresser D. Passerini St., 2015. Scaling up "nano" $Li_4Ti_5O_{12}$ for high-power lithium-ion anodes using large flame spray pyrolysis. *J. Electrochem. Soc.*, 162, A2331-A2338. DOI: 10.1149/2.0711512jes.

Bresser D., Paillard E., Copley M., Bishop P., Winter M., Passerini S., 2012. The importance of "going nano" for high power battery materials. *J. Power Sources*, 219, 217-222. DOI: 10.1016/J.Jpowsour.2012.07.035.

Curtet R., 1958. Confined jets and recirculation phenomena with cold air. *Combust Flame*, 2, 383-411. DOI: 10.1016/0010-2180(58)90032-4.

Deschanvres A., Raveau B., Sekkal Z., 1971. Synthesis and crystallographic study of new solid solution of spinelle $Li_{1+x}Ti_{2-x}O_4$ less than or equal to x less than or equal to 0,333. *Mater. Res. Bull.*, 6, 699-704. DOI: 10.1016/0025-5408(71)90103-6.

Du Pasquier A., Huang C.C., Spitler T., 2009. Nano $Li_4Ti_5O_{12}$-$LiMn_2O_4$ batteries with high power capability and improved cycle-life. *J. Power Sources*, 186, 508-514. DOI: 10.1016/J.Jpowsour.2008.10.018.

Ernst F.O., Kammler H.K., Roessler A., Pratsinis S.E., Stark W.J., Ufheil J., Novák P., 2007. Electrochemically active flame-made nanosized spinels: $LiMn_2O_4$, $Li_4Ti_5O_{12}$ and $LiFe_5O_8$. *Mater. Chem. Phys.*, 101, 372-378. DOI: 10.1016/j.matchemphys.2006.06.014.

Ferg E., Gummow R.J., de Kock A., Thackeray M.M., 1994. Spinel anodes for lithium-ion batteries. *J. Elchem Soc.*, 141, L147-L150. DOI: 10.1149/1.2059324.

Gaberscek M., Dominko R., Jamnik J., 2007. Is small particle size more important than carbon coating? An example study on $LiFePO_4$ cathodes. *Electrochem. Commun.*, 9, 2778-2783. DOI: 10.1016/J.Elecom.2007.09.020.

Gamba I.L., Damian S.M., Estenoz D.A., Nigro N., Storti M.A., Knoeppel D., 2012. Residence time distribution determination of a continuous stirred tank reactor using computational fluid dynamics and its application on the mathematical modeling of styrene polymerization. *Int. J. Chem. React. Eng.*, 10, 1-32. DOI: 10.1515/1542-6580.3057.

Groehn A.J., Pratsinis S.E., Sanchez-Ferrer A., Mezzenga R., Wegner K., 2014. Scale-up of nanoparticle synthesis by flame spray pyrolysis: The high-temperature particle residence time. *Ind. Eng. Chem. Res.*, 53, 10734-10742. DOI: 10.1021/Ie501709s.

Groehn A.J., Pratsinis S.E., Wegner K., 2012. Fluid-particle dynamics during combustion spray aerosol synthesis of ZrO_2. *Chem. Eng. J.*, 191, 491-502. DOI: 10.1016/J.Cej.2012.02.093.

He Y.B., Li B., Liu M., Zhang C., Lv W., Yang C., Li J., Du H., Zhang B., Yang Q.H., Kim J.K., Kang F., 2012. Gassing in $Li_4Ti_5O_{12}$-based batteries and its remedy. *Scientific Reports*, 2, 1-9. DOI: 10.1038/srep00913.

Hsiao K.C., Liao S.C., Chen J.M., 2008. Microstructure effect on the electrochemical property of $Li_4Ti_5O_{12}$ as an anode material for lithium-ion batteries. *Electrochim. Acta*, 53, 7242-7247. DOI: 10.1016/J.Electacta.2008.05.002.

Hudak N.S., Huber D.L., 2012. Size effects in the electrochemical alloying and cycling of electrodeposited aluminum with lithium. *J. Electrochem. Soc.*, 159, A688-A695. DOI: 10.1149/2.023206jes.

Jiang J.W., Chen J., Dahn J.R., 2004. Comparison of the reactions between $Li_{7/3}Ti_{5/3}O_4$ or LiC_6 and nonaqueous solvents or electrolytes using accelerating rate calorimetry. *J. Electrochem. Soc.*, 151, A2082-A2087. DOI: 10.1149/1.1817698.

Johannessen T., Pratsinis S.E., Livbjerg H., 2000. Computational fluid-particle dynamics for the flame synthesis of alumina particles. *Chem. Eng. Sci.*, 55, 177-191. DOI: 10.1016/S0009-2509(99)00183-9.

Karhunen T., Lähde A., Leskinen J., Büchel R., Waser O., Tapper U., Jokiniemi J., 2011. Transition metal-doped lithium titanium oxide nanoparticles made using flame spray pyrolysis. *ISRN Nanotechnology*, 2011, 1-6. DOI: 10.5402/2011/180821.

Kavan L., Prochazka J., Spitler T.M., Kalbac M., Zukalova M.T., Drezen T., Gratzel M., 2003. Li insertion into $Li_4Ti_5O_{12}$ (Spinel) - Charge capability vs. particle size in thin-film electrodes. *J. Electrochem. Soc.*, 150, A1000-A1007. DOI: 10.1149/1.1581262.

Kho Y.K., Teoh W.Y., Madler L., Amal R., 2011. Dopant-free, polymorphic design of TiO_2 nanocrystals by flame aerosol synthesis. *Chem. Eng. Sci.*, 66, 2409-2416. DOI: 10.1016/J.Ces.2011.02.058.

Krumeich F., Waser O., Pratsinis S.E. 2016. Thermal annealing dynamics of carbon-coated $LiFePO_4$ nanoparticles studied by in-situ analysis. *J. Solid State Chem.* 242, 96-102. DOI: 10.1016/j.jssc.2016.07.002

Laruelle S., Grugeon S., Poizot P., Dolle M., Dupont L., Tarascon J.M., 2002. On the origin of the extra electrochemical capacity displayed by MO/Li cells at low potential. *J. Electrochem. Soc.*, 149, A627-A634. DOI: 10.1149/1.1467947.

Levenspiel O., 1999. *Chemical reaction engineering*. Wiley, New York.

Madler L., Kammler H.K., Mueller R., Pratsinis S.E., 2002. Controlled synthesis of nanostructured particles by flame spray pyrolysis. *J. Aerosol Sci.*, 33, 369-389. DOI: 10.1016/S0021-8502(01)00159-8.

Madler L., Stark W.J., Pratsinis S.E., 2002. Flame-made ceria nanoparticles. *J. Mater. Res.*, 17, 1356-1362. DOI: 10.1557/jmr.2002.0202.

Magnussen B.F., Hjertager B.H., 1977. On mathematical modeling of turbulent combustion with special emphasis on soot formation and combustion. *Symp. Int. Combust.*, 16, 719-729. DOI: 10.1016/S0082-0784(77)80366-4.

Morrison P.W., Raghavan R., Timpone A.J., Artelt C.P., Pratsinis S.E., 1997. In situ Fourier transform infrared characterization of the effect of electrical fields on the flame synthesis of TiO_2 particles. *Chem. Mater.*, 9, 2702-2708. DOI: 10.1021/cm960508u.

Mueller R., Kammler H.K., Pratsinis S.E., Vital A., Beaucage G., Burtscher P., 2004. Non-agglomerated dry silica nanoparticles. *Powder Technol.*, 140, 40-48. DOI: 10.1016/J.Powtec.2004.01.004\.

Mueller R., Madler L., Pratsinis S.E., 2003. Nanoparticle synthesis at high production rates by flame spray pyrolysis. *Chem. Eng. Sci.*, 58, 1969-1976. DOI: 10.1016/s0009-2509(03)00022-8

Naoi K., Naoi W., Aoyagi S., Miyamoto J., Kamino T., 2013. New generation "nanohybrid supercapacitor". *Accounts Chem. Res.*, 46, 1075-1083. DOI: 10.1021/Ar200308h.

Nowack L.V., Waser O., Yarema O., Wood V., 2013. Rapid, microwave-assisted synthesis of battery-grade lithium titanate (LTO). *RSC Adv.*, 3, 15618-15621. DOI: 10.1039/C3ra43237h.

Ohzuku T., Ueda A., Yamamoto N., 1995. Zero-strain insertion material of $Li[Li_{1/3}ti_{5/3}]O_4$ for rechargeable lithium cells. *J. Electrochem. Soc.*, 142, 1431-1435. DOI: 10.1149/1.2048592.

Olfe D.B., 1961. Mean beam length calculations for radiation from non-transparent gases. *J. Quant. Spectrosc. Ra.*, 1, 169-176. DOI: 10.1016/0022-4073(61)90022-X.

Padhi A.K., Nanjundaswamy K.S., Goodenough J.B. (1997). Phospho-olivines as positive-electrode materials for rechargeable lithium batteries. *J. Electrochem. Soc.,* 144, 1188-1194. DOI: 10.1149/1.1837571

Poullikkas A., 2013. A comparative overview of large-scale battery systems for electricity storage. *Renew. Sust. Energ. Rev.*, 27, 778-788. DOI: 10.1016/J.Rser.2013.07.017.

Pratsinis S.E., 1998. Flame aerosol synthesis of ceramic powders. *Prog. Energ. Combust.*, 24, 197-219. DOI: 10.1016/S0360-1285(97)00028-2.

Rudin T., Wegner K., Pratsinis S.E., 2011. Uniform nanoparticles by flame-assisted spray pyrolysis (FASP) of low cost precursors. *J. Nanopart. Res.*, 13, 2715-2725. DOI: 10.1007/s11051-010-0206-x.

Sotiriou G.A., Sannomiya T., Teleki A., Krumeich F., Voros J., Pratsinis S.E., 2010. Non-toxic dry-coated nanosilver for plasmonic biosensors. *Adv. Funct. Mater.*, 20, 4250-4257. DOI: 10.1002/Adfm.201000985.

Streltsov V.A., Belokoneva E.L., Tsirelson V.G., Hansen N. K., 1993. Multipole analysis of the electron-density in triphylite, $LiFePO_4$, using X-ray-diffraction data. *Acta Crystallogr. B*, 49, 147-153. DOI: 10.1107/S0108768192004701.

Strobel R., Pratsinis S.E., 2007. Flame aerosol synthesis of smart nanostructured materials. *J. Mater. Chem.*, 17, 4743-4756. DOI: 10.1039/b711652g.

Strobel R., Pratsinis S.E., 2009. Direct synthesis of maghemite, magnetite and wustite nanoparticles by flame spray pyrolysis. *Adv. Powder Technol.*, 20, 190-194. DOI: 10.1016/j.apt.2008.08.002.

Teleki A., Heine M.C., Krumeich F., Akhtar M.K., Pratsinis S.E., 2008. In situ coating of flame-made TiO_2 particles with nanothin SiO_2 films. *Langmuir*, 24, 12553-12558. DOI: 10.1021/La801630z.

Teleki A., Pratsinis S.E., Kalyanasundaram K., Gouma P.I., 2006. Sensing of organic vapors by flame-made TiO_2 nanoparticles. *Sens. Actuator B-Chem.*, 119, 683-690. DOI: 10.1016/j.snb.2006.01.027.

Teoh W.Y., Amal R., Madler L., 2010. Flame spray pyrolysis: An enabling technology for nanoparticles design and fabrication. *Nanoscale*, 2, 1324-1347. DOI: 10.1039/C0nr00017e.

Vlad A., Singh N., Rolland J., Melinte S., Ajayan P.M., Gohy J.F., 2014. Hybrid supercapacitor-battery materials for fast electrochemical charge storage. *Sci. Rep.*, 4, 1-7. DOI: 10.1038/Srep04315.

Wagemaker M., van Eck E.R.H., Kentgens A.P.M., Mulder F.M., 2009. Li-ion diffusion in the equilibrium nanomorphology of spinel $Li_{4+x}Ti_5O_{12}$. *J. Phys. Chem. B*, 113, 224-230. DOI: 10.1021/Jp8073706.

Waser O., Buchel R., Hintennach A., Novák P., Pratsinis S.E., 2011. Continuous flame aerosol synthesis of carbon-coated nano-$LiFePO_4$ for Li-ion batteries. *J. Aerosol Sci.*, 42, 657-667. DOI: 10.1016/J.Jaerosci.2011.06.003.

Waser O., Groehn A.J., Eggersdorfer M.L., Pratsinis S.E., 2014. Air entrainment during flame aerosol synthesis of nanoparticles. *Aerosol Sci. Technol.*, 48, 1195-1206. DOI: 10.1080/02786826.2014.969800.

Waser O., Hess M., Guntner A., Novák P., Pratsinis S.E., 2013. Size controlled CuO nanoparticles for Li-ion batteries. *J. Power Sources*, 241, 415-422. DOI: 10.1016/J.Jpowsour.2013.04.147.

Wegner K., Pratsinis S.E., 2003. Scale-up of nanoparticle synthesis in diffusion flame reactors. *Chem. Eng. Sci.*, 58, 4581-4589. DOI: 10.1016/J.Ces.2003.07.010.

Wegner K., Schimmoeller B., Thiebaut B., Fernandez C., Rao T.N., 2011. Pilot plants for industrial nanoparticle production by flame spray pyrolysis. *Kona Powder Part J.*, 251-265. DOI: 10.14356/kona.2011025.

Whitney E., 1994. *Ceramic cutting tools : materials, development, and performance*. Noyes Publications, Park Ridge, New Jersey, USA.

Zheng H.H., Li J., Song X.Y., Liu G., Battaglia V.S., 2012. A comprehensive understanding of electrode thickness effects on the electrochemical performances of Li-ion battery cathodes. *Electrochim Acta*, 71, 258-265. DOI: 10.1016/J.Electacta.2012.03.161.

Received 04 October 2016
Received in revised form 18 February 2017
Accepted 20 February 2017

APPENDICES

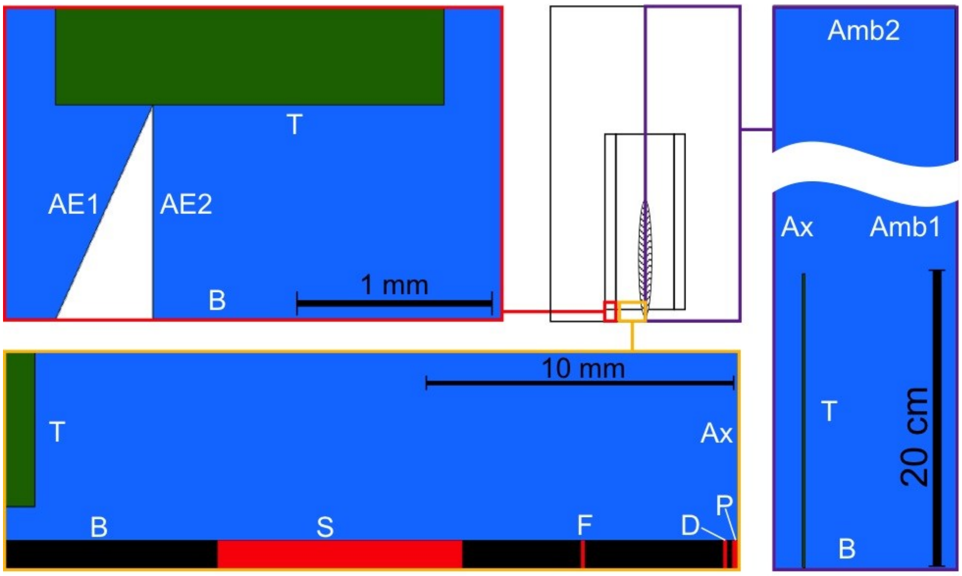

Fig. A1. Geometry of the simulation domain with fluid zone in blue and the 20 cm long tube (T) in green. The whole domain is depicted on the right (purple frame) and shows the tube on the lower left side. Total radius is 15 cm and total height is 100 cm. Top (Amb1) and right border (Amb2) have pressure boundary conditions assigned. The left edge corresponds to the symmetry axis (Ax) and the bottom end is given by the burner wall (B). The lower section (yellow frame) depicts the detailed burner geometry with red marked inlets from left to right for sheath gas (S), pilot flame (F), dispersion gas (D) and liquid precursor (P). The green square on the left side marks the tube (T) while the right-hand border of the figure is coincident with the symmetry axis (Ax). Detailed geometry of the air entrainment boundaries is depicted in the upper left corner (red frame). Boundary conditions for *AE* inlet (AE2) and outlet (AE1) are assigned to the edges of the white triangle

Table A1. Boundary conditions for the FSP simulations. All boundaries but the tube are at 300 K (labels in brackets refer to Fig. A1).

Boundary	Type	Material (mole %.)	Comment
Burner (B)	Wall	Aluminium (-)	No slip
Tube (T)	Wall	Quartz glass (-)	No slip; temperature set by heat transfer
Axis (Ax)	Axis	-	-
Inlet-Ambient (Amb1)	Pressure-inlet	N_2 (79); O_2 (21)	Ambient pressure
Outlet-Ambient (Amb2)	Pressure-outlet	N_2 (79); O_2 (21)	Gauge pressure: -10 Pa; draft of fume hood
Inlet-*AE* (AE2)	Mass-flow-inlet	N_2 (79); O_2 (21)	Negative radial flow direction;
Outlet-*AE* (AE1)	Pressure-outlet	N_2 (79); O_2 (21)	Flow normal to boundary
Sheath (*S*)	Mass-flow-inlet	O_2 (100)	Flow normal to boundary
Pilot flame (*F*)	Mass-flow-inlet	O_2 (66.7); CH_4 (33.3)	Flow normal to boundary
Dispersion gas (*D*)	Mass-flow-inlet	O_2 (100)	Ma ≈ 1
Precursor (*P*)	Wall	C_8H_{10} (32.1); $C_8H_{16}O_2$ (67.9)	

Chemical and Process Engineering 2017, 38 (1), 67-77
DOI: 10.1515/cpe-2017-0006

ADSORPTION AND CO-ADSORPTION OF POLYALDEHYDE DEXTRAN NANOPARTICLES AND NONIONIC SURFACTANT AT AN AIR–WATER INTERFACE: POTENTIAL IMPLICATIONS FOR PULMONARY DRUG DELIVERY

Katarzyna Jabłczyńska*, Tomasz R. Sosnowski

Warsaw University of Technology, Faculty of Chemical and Process Engineering, Waryńskiego 1, 00-645 Warsaw, Poland

Dedicated to Prof. Leon Gradoń on the occasion of his 70th birthday

Measurements of dynamic surface tension were carried out in aqueous systems (water or 0.1 mM Triton X-100) comprising nanoparticles formed from chemically modified polyaldehyde dextran (PAD). The nanostructures, considered as potential drug carriers in aerosol therapy, were obtained from biocompatible polysaccharides by successive oxidation and reactive coiling in an aqueous solution. The dynamic surface tension of the samples was determined by the maximum bubble pressure (MBP) method and by the axisymmetric drop shape analysis (ADSA). Experiments with harmonic area perturbations were also carried out in order to determine surface dilatational visco-elasticity. PAD showed a remarkable surface activity. Ward-Tordai equation was used to determine the equilibrium surface tension and diffusion coefficient of PAD nanoparticles ($D = 2.3 \times 10^{-6}$ m^2/s). In a mixture with Triton X-100, PAD particles showed co-adsorption and synergic effect in surface tension reduction at short times (below 10 s). Tested nanoparticles had impact on surface rheology in a mixed system with nonionic surfactant, suggesting their possible interactions with the lung surfactant system after inhalation. This preliminary investigation sets the methodological approach for further research related to the influence of inhaled PAD nanoparticles on the lung surfactant and mass transfer processes in the respiratory system.

Keywords: polysaccharide nanoparticles, lung surfactant, dynamic surface tension, surface visco-elasticity, hysteresis

1. INTRODUCTION

Lung surfactant (LS) present in the liquid phase which covers the inner surface of pulmonary alveoli is responsible for lowering the surface tension during breathing cycle and assures proper functioning of the respiratory system (Goerke, 2001). As proposed by Gradoń and co-workers (Gradoń et al., 1996; Gradoń and Podgórski, 1989; Podgórski and Gradoń 1993), the LS is responsible for Marangoni-type convection in the alveolar fluid, generating flows which influence mass transfer processes in the respiratory system. Several studies confirmed that dynamic surface tension gradients produced due to periodic variation of pulmonary air/liquid surface area during breathing, create the driving force for removal of inhaled particles from deep lungs ('pulmonary clearance') and possibly facilitate the respiratory gas exchange (Grotberg, 2001; Sosnowski et al., 1998). The characteristic feature found in the LS during periodically compressed and expanded air/liquid surface area, A, (i.e. in the situation characteristic for breathing) is the hysteresis of surface tension, γ. It is related to the correct

---

*Corresponding author, e-mail: k.jablczynska@ichip.pw.edu.pl

physiological functionality of LS but - from physical viewpoint - it can be considered as a measure of the amount of surface energy which is used to produce convective effects (Notter et al., 1982; Podgórski and Gradoń, 1989; Sosnowski, 2006). Therefore, reduction of this hysteresis is often used as an indication of a decrease of LS functions, particularly those related to the pulmonary mass transfer (Kondej and Sosnowski, 2013; Podgórski et al., 2001; Sosnowski et al., 2000). γ-A hysteresis can be analyzed in the framework of surface dilatational rheology, assuming that the observed time shift between surface tension and surface area reflects overall visco-elasticity of the interfacial region (Lyklema, 2000; Sosnowski, 2006).

Changes in the surface activity of the LS, which may occur due to interactions with particular drugs or drug carriers delivered by inhalation, can lead to abnormal physiological function of LS and, eventually, even to a respiratory failure (Kramek-Romanowska et al., 2015; Rosenberg et al., 2016; Zhang et al., 2012). On the other hand, the surface activity of administered drugs may have a supplemental effect if lung surfactant does not (e.g. due to its lack or damage) sufficiently lower the surface tension during the breathing cycle (Ellyett at al., 1996). Therefore, both the determination of surface activity of newly developed inhalable drug carriers and the evaluation of their interactions with LS are a very important step in safety assessment of aerosol therapy.

Recently, a new type of drug carrier for aerosol delivery was proposed in the form of modified polyaldehyde dextran (PAD) nanoparticles (NPS) (Jabłczyńska et al., 2015). It is known from the literature that some polymeric nanoparticles can adsorb at air/liquid interface and reduce the surface tension (Okubo, 1995). On the other hand, different types of polymeric and non-polymeric NPS have been demonstrated to inhibit the biophysical function of LS in vitro in a material- and concentration-dependent manner (Beck-Broichsitter et al., 2014; Kondej and Sosnowski, 2013). Until now, no data regarding surface activity of PAD nanoparticles are available, therefore the current paper is focused on this issue. In this first analysis, the interactions of PAD nanoparticles with a model nonionic surfactant (instead of LS) are also investigated in order to determine possible NPS-surfactant interactions in aqueous environment.

2. MATERIALS AND METHODS

The following reagents have been used in the synthesis of nanoparticles: dextran (MW = 75 kDa, Pharmacosmos, Denmark), dodecylamine hydrochloride, sodium periodate and alanine (Sigma Aldrich). Water used in all experiments was purified in a reverse osmosis system (Puricom, USA) and characterized by low conductivity of 3.8±1.0 µS. Nanoparticles were synthesized by successive oxidation and reactive coiling in an aqueous solution, according to a protocol described by Wasiak et al. (2016). Briefly, dextran was dissolved in water to gain the concentration of 5%, and sodium periodate was added in the molar ratio of 1:10 (IO_4^-/ glucose units). The solution was stirred for 1 h in the dark at the room temperature and subsequently dialyzed against water for 3 days (Carl-Roth membrane bag with MWCO 12-14 kDa). The obtained polyaldehyde dextran (PAD) was dried in a laboratory drying oven at the temperature of 40°C for 24 h. For the coiling step 10% w/v aqueous solution of PAD was prepared, and 5% dodecyloamine hydrochloride solution was added in the amount providing 33% degree of substitution of aldehyde groups. The rest of aldehyde groups were substituted by alanine which was added after 45 minutes of reaction. The reaction was carried out for 1.5 hours at 30°C and the pH of the mixture was gradually increased to 10. Finally the pH was adjusted to pH 7.4. pH adjustment was made by the addition of 1M NaOH or 2M HCl (Sigma Aldrich). The resultant suspension of nanoparticles was dialyzed for 30 min against water. Nanoparticles were spontaneously formed due to self-organization of polysaccharide chains in aqueous environment because of hydrophobicity of the attached coiling agent.

The nanosuspension of PAD was dried in a B-290 laboratory spray dryer (Büchi, Switzerland) directly after synthesis in order to obtain inhalable powder and increase the stability of the preparation. As demonstrated recently, the resultant micrometer-sized powder has very good properties for products typically used in aerosol therapy, moreover after rehydration it transforms to nanosuspension (Jabłczyńska et al., 2015). The precursor was pumped at the volumetric rate of 3 cm^3/min to the atomizing nozzle (diameter 0.7 mm) where it was mixed with compressed air (flow rate = 12 dm^3/min). Drying air was supplied with the rate of 20 m^3/h and inlet temperature of 200°C. Produced powder was separated in a high performance cyclone and collected in a product container.

For the evaluation of the surface activity, the powder was rehydrated to gain three values of concentration of reassembled nanoparticles: 1, 5 and 10 mg/cm^3. In addition to systems based on pure water, similar nanosuspensions were prepared with a model nonionic surfactant Triton X-100 (0.1 mM; Sigma Aldrich). The resultant dispersion was shown to reconstruct the size distribution of PAD nanoparticles from the precursor suspension as demonstrated by Jabłczyńska et al. (2015). The dynamic surface tension (DST) of each sample was determined by the maximum bubble pressure (MBP) method using a BP2 tensiometer (Krüss, Germany) and by the axisymmetric drop shape analysis (ADSA) with a profile analysis tensiometer (model PAT-1M, Sinterface, Germany). The accuracy of both tensiometers was 0.1 mN/m. BP2 tensiometer allows to measure DST in relatively short time-scales (0.01-50 s), while PAT-1M device gives an opportunity to study adsorption in longer times (1-10^3 s). The latter apparatus was also used in our work to perform experiments with harmonic perturbations of interfacial area carried out in order to determine rheological parameters of the interface (dilatational visco-elasticity). All surface tension measurements were performed at the temperature of 36.6 ± 0.2 °C. Both tensiometers were calibrated using pure water for which surface tension was taken to be 70.14 mN/m at the temperature of experiments. Experimental results were discussed on the basis of Ward-Tordai equation (Ward and Tordai, 1946), which allowed to evaluate the equilibrium surface tension and the diffusion coefficient of NPS. Details of this approach are given in the following section.

2.1. Adsorption theory

Since PAD nanoparticles were recognized as surface-active we decided to employ Ward-Tordai model of the diffusion-controlled mechanism for quantitative description of NPS adsorption at the air/liquid interface. NPS diffusion is considered to be a two-step process where particles diffuse from the bulk into the subsurface and then they are adsorbed at the interface. For diffusion-controlled mechanism, the time scale of adsorption is much faster than the diffusion step. The classic solution for this process is given by Eq. (1) (Ward and Tordai, 1946):

$$\Gamma(t) = 2c_0\sqrt{\frac{Dt}{\pi}} - 2\sqrt{\frac{D}{\pi}}\int_0^{\sqrt{t}} c_s \mathrm{d}\left(\sqrt{t-\tau}\right) \tag{1}$$

This equation cannot be solved analytically, but two asymptotic solutions: for very short or very long surface ages, can be applied in order to estimate diffusion coefficient of surface active agent.

For short time approximation ($t \to 0$), the limiting surface tension (γ) value is given by (Eastoe and Dalton, 2000):

$$\gamma_{t\to 0} = \gamma_0 - 2nRTc_0\sqrt{\frac{Dt}{\pi}} \tag{2}$$

where n =1 for non-ionic surfactants, and n = 2 for ionics. The long time approximation ($t \to \infty$) takes the form:

$$\gamma_{t\to\infty} = \gamma_{eq} + \frac{nRT\Gamma_{eq}^2}{c_0}\sqrt{\frac{\pi}{4Dt}} \tag{3}$$

For the purpose of calculations we treat nanoparticles as non-ionic surface-active macromolecules and we assume, according to Wasiak et al. (2016) that each nanoparticle consists of 10 dextran chains so it has molecular weight of around 750 kDa. It is also claimed that NPS content in the suspension is sufficiently low to assume that thermodynamic activity of particles is equal to their concentration, hence the diffusion coefficient of NPS is independent of their concentration in the examined range.

2.2. Surface visco-elasticity

To fully describe systems with dynamically changing interface such as the surface of alveolar fluid where the area changes harmonically during breathing cycle, the rheological approach can be useful (Sosnowski, 2006). The surface elasticity modulus E expresses the response of the surface tension, $\Delta\gamma$, to the change in the surface area (surface dilatation), ΔA. This parameter, also called surface dilatational (dilational) modulus, was defined by Gibbs (1961) as:

$$E = \frac{d\gamma}{d\ln A} \tag{4}$$

When some relaxation processes occur, for example reorientation of the molecules at the surface or diffusional exchange of the molecules/particles with the subsurface, the elasticity modulus becomes a complex number. The elasticity modulus consists then of a real part equal to the surface elasticity E' and an imaginary part E'', related to surface viscosity η_d (Miller, 2009):

$$E = E' + i\,E'' = E' + i\omega\eta_d \tag{5}$$

Where ω is the angular frequency of periodic changes of surface area.

3. RESULTS AND DISCUSSION

Data obtained by the axisymmetric drop shape analysis (ADSA) were plotted in the coordinates γ versus $t^{-½}$ (as a consequence of long time approximation - Eq. 3) and the linear portions of the dynamic tensiograms were extrapolated to the intersection with the ordinate axis as presented in Fig. 1. The estimated values of equilibrium surface tension γ_{eq} of PAD nanoparticles obtained for the $t^{-1/2} \to 0$ are shown in Table 1. Values of the derivative $(d\gamma / dt^{-1/2})_{t\to\infty}$ were used for the calculation of the equilibrium surface excess Γ_{eq} which is also listed in Table 1.

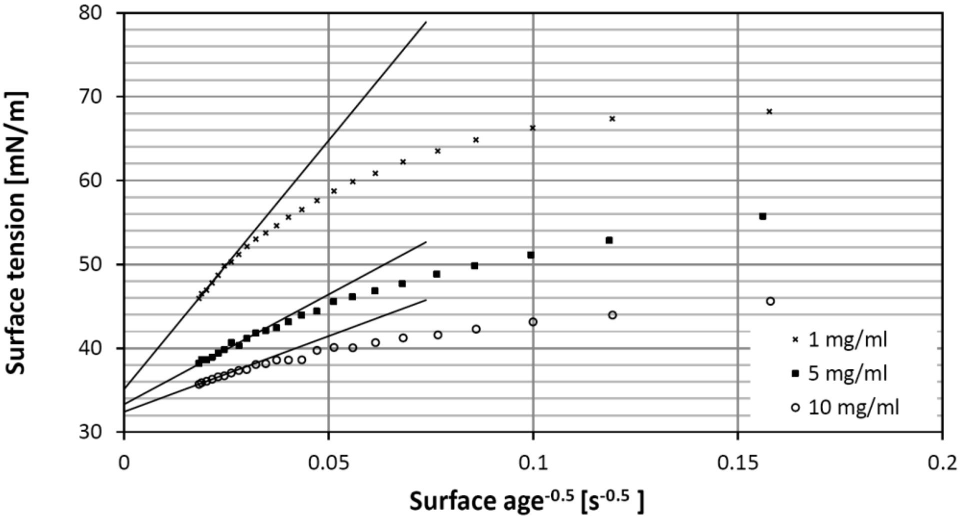

Fig. 1. Dynamic surface tension of PAD nanoparticle suspensions of different concentration as a function of $t^{-½}$. Straight lines are used for the determination of $d\gamma/dt^{-1/2}$ and γ_{eq} for $t\to\infty$.

The results of measurements of the surface tension as a function of surface age show a good agreement of both applied methods as presented in Fig. 2. Both methods are complementary since they are operative in different time-scales. The concentration of PAD nanoparticles strongly affects both the rate of surface tension reduction and the equilibrium value of the surface tension, γ_{eq}. For the highest tested concentration of 10 mg/ml and very long adsorption time (3000 s), NPS reduce surface tension down to 35.7 mN/m. Extrapolation according to the long time approximation ($t \rightarrow \infty$) of Ward-Tordai equation indicates an even lower value of γ_{eq} (32.4 mN/m). NPS at concentrations of 1 mg/ml and 5 mg/ml lowered surface tension to 46.1 mN/m and 38.3 mN/m, respectively, and extrapolated values of the equilibrium surface tensions were 35.1 and 33.3 mN/m, respectively. The obtained values indicate that the magnitude of adsorption (and surface tension reduction) was proportional to nanoparticle concentration in the bulk.

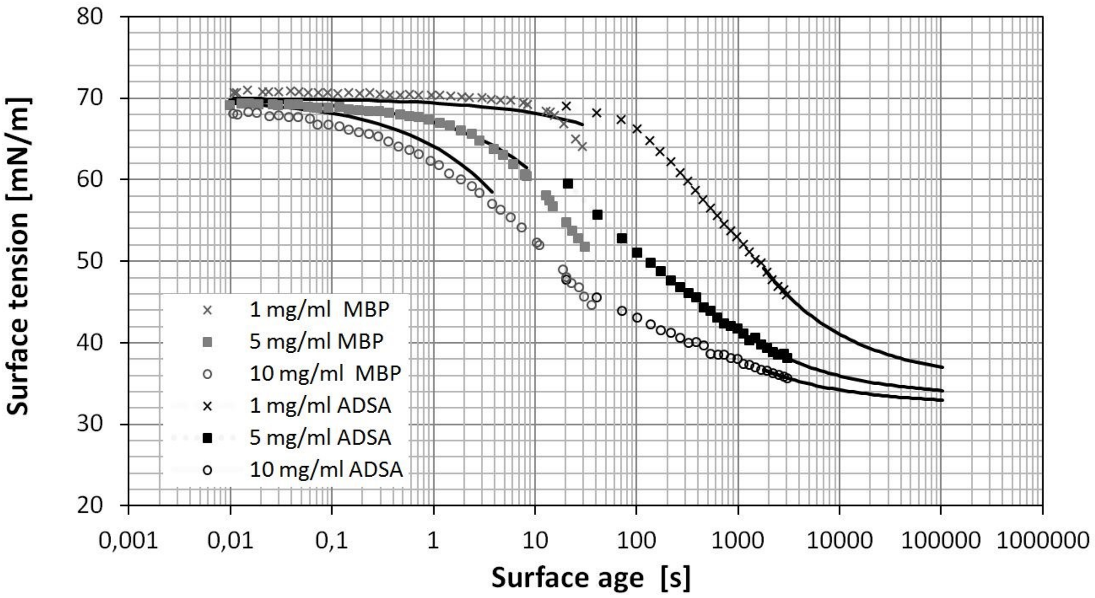

Fig. 2. Dynamic surface tension of PAD nanoparticles in aqueous suspensions at different concentration as a function of surface age - results obtained by MBP (grey markers) and ADSA (black markers). Lines represent theoretical prediction of surface tension changes.

Results obtained by the maximum bubble pressure method (for relatively short times of adsorption) were used to determine the diffusion coefficient. For each set of measurements, the diffusion coefficient providing the best fit to the experimental data was found according to Eq. (2). These values are collected in Table 1. Lines shown in Fig. 2 depict the theoretical surface tension calculated from Eqs. (2) and (3) for the averaged diffusion coefficient $D = 2.3\times10^{-10} \pm 0.6\times10^{-10}$ m^2/s. They allow to extrapolate the results for very long adsorption times which are not feasible experimentally.

Table 1. The most essential data derived from DST measurements for PAD nanoparticles in water

PAD NPS concentration [mg/ml]	γ_{eq} [mN/m]	$(d\gamma/dt^{-1/2})_{t\rightarrow\infty}$ [$mN\cdot s^{1/2}/m$]	$D\cdot10^{10}$ [m^2/s]	$\Gamma_{eq}\cdot10^5$ [mol/m^2]
1	35.1	593.4	2.1	7.3
5	33.3	262.2	1.9	10.8
10	32.4	180.7	3.0	12.7

* Estimated error value for calculated parameters is below 2%.

Dynamic surface tension results in an aqueous system with the non-ionic surfactant Triton X-100 (0.1 mM) and PAD nanoparticles (concentrations: 1, 5 and 10 mg/ml) are plotted in Fig. 3. Again, the series obtained by MBP and ADSA methods are complementary. As seen from Fig. 3, PAD nanoparticles affect the DST of Triton X-100. For short adsorption times, NPS immediately decrease the surface tension, and the range of this effect is greater than that of any single component which suggests synergic interactions between surfactant molecules and PAD nanoparticles. The reduction of surface tension is stronger when NPS concentration increases. However, for surface age longer than 100 seconds, nanoparticles seem to have negative impact on surface-activity of Triton X-100 (γ_{eq} of the solution of pure surfactant has the lowest value). Almost no effect of NPS is observed for time-scales relevant for dynamics of breathing (1-10 s), where the nonionic surfactant itself controls the DST value. It must be stressed though that presented results show only one type of specific interactions between NPS and surface-active compound. Since Triton X-100 cannot be considered as a realistic model of the LS, the actual impact of tested NPS on the lung surfactant can be different.

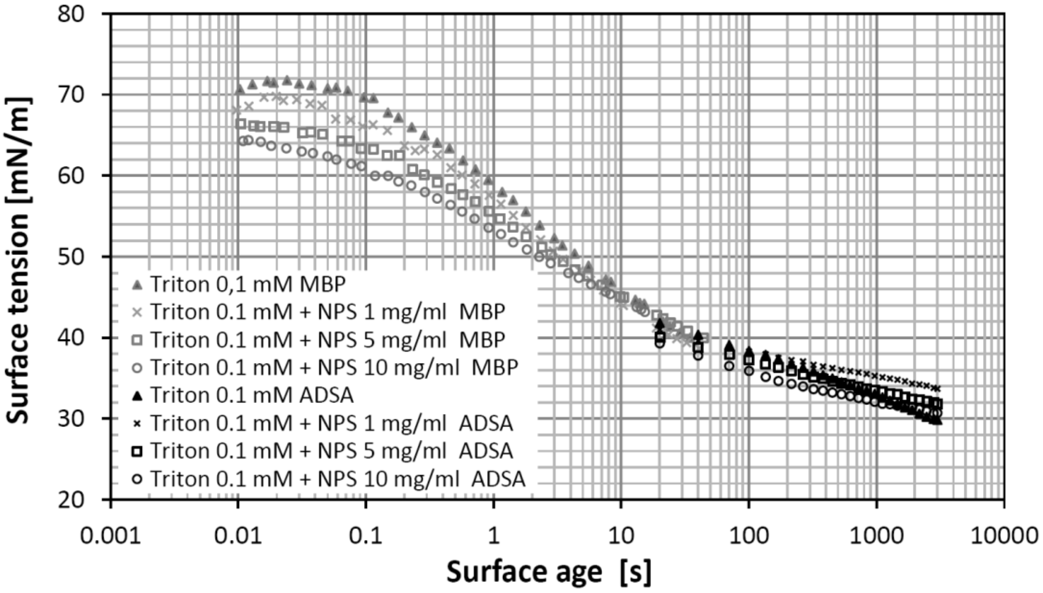

Fig. 3. Dynamic surface tension of mixture of Triton X-100 (0.1 mM aq.) and PAD nanoparticles (NPS) at different concentrations as a function of surface age – results obtained by MBP (grey markers) and ADSA (black markers) methods.

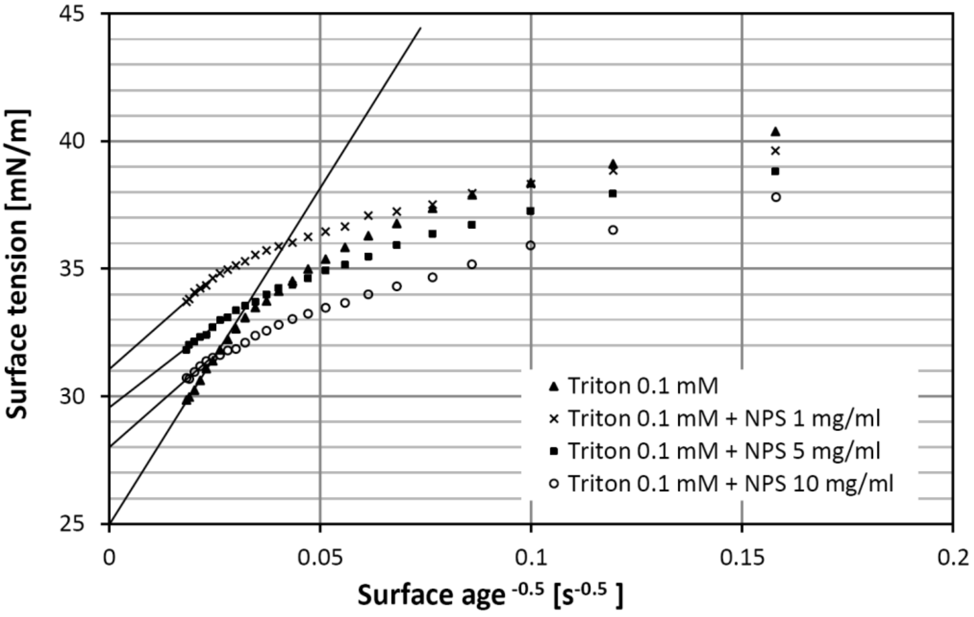

Fig. 4. Dynamic surface tension of mixtures of Triton X-100 (0.1 mM aq.) and PAD nanoparticles (NPS) as a function of $t^{-1/2}$. Straight lines given as an example for the determination of $d\gamma/dt^{-1/2}$ and γ_{eq} for $t \to \infty$.

Equilibrium surface tension values in mixed systems (surfactant + NPS) were calculated again from the long-time approximation of Ward-Tordai equation. It should be noted though, that in this case none of the physical parameters of this equation (bulk concentration, surface excess, diffusion coefficient) should be considered as real values since we deal with the co-operative or competitive adsorption of two surface-active components. Extrapolation done for $t \to \infty$ is shown in Fig. 4 and the obtained values of γ_{eq} and $(d\gamma/dt^{-1/2})_{t\to\infty}$ are listed in Table 2. It is seen that presence of NPS increases γ_{eq} which suggests that surface activity of PAD nanoparticles is really important only for processes with a short time scale. From the comparison of $(d\gamma/dt^{-1/2})_{t\to\infty}$ for 1 mg/ml PAD particles in Triton X-100 (second row in Table 2: 145.5 $\text{mN}\cdot\text{s}^{1/2}/\text{m}$) and for 1 mg/ml PAD particles in water (first row in Table 1: 593.4 $\text{mN}\cdot\text{s}^{1/2}/\text{m}$) it is seen that this co-adsorption lowers the rate of surface tension reduction close to the equilibrium value of the surface tension (31.1 and 35.1 mN/m, respectively).

Table 2. The most essential data for measurements derived from DST for mixtures of Triton X-100 / PAD nanoparticles.

PAD NPS concentration [mg/ml]	γ_{eq} [mN/m]	$(d\gamma/dt^{-1/2})_{t\to\infty}$ [$\text{mN}\cdot\text{s}^{1/2}/\text{m}$]
0	25.0	263.8
1	31.1	145.5
5	29.6	127.7
10	28.0	145.5

* Estimated error value for calculated parameters is below 2%.

The results of surface visco-elasticity measurements in PAD aqueous nanosuspensions during air/liquid surface oscillations are shown in Fig. 5. Applied oscillation periods were in the range of human lung function: 2 seconds for fast, 4 seconds for moderate, and 8 seconds for slow breathing.

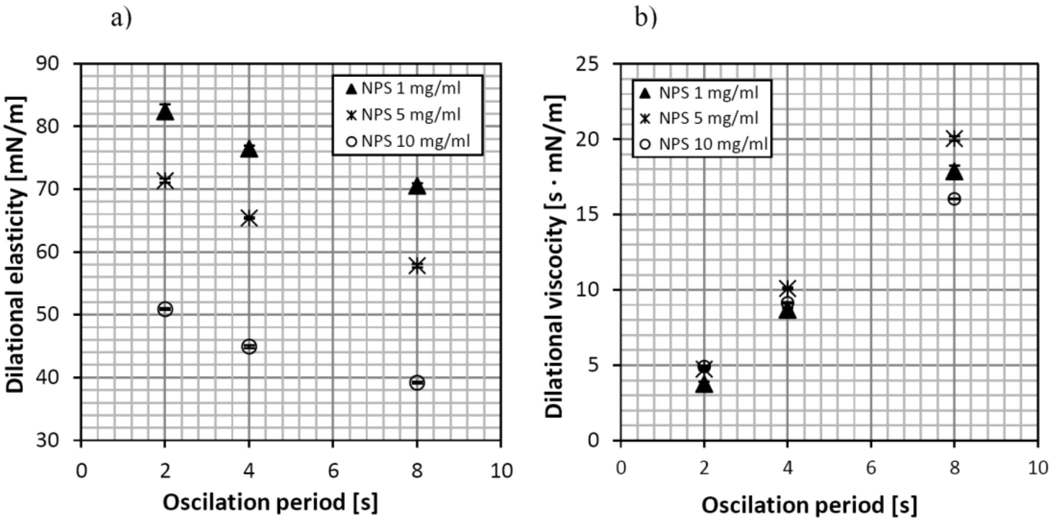

Fig. 5. Surface dilatational elasticity (a) and viscosity (b) of PAD nanosuspensions as a function of oscillation period

With increasing oscillation frequency, the dilatational elasticity, E' raises while dilatational viscosity, η_d - decreases. It is evident that surface elasticity of the air/liquid interface noticeably decreases with increasing concentration of nanoparticles, which suggests that the presence of NPS reduces the amplitude of surface tension variations during harmonic perturbations of air-liquid interface. This effect can be easily explained by fast exchange (mass transfer) of surface-active NPS between the surface and the adjacent liquid subphase during periodic variations of the interface. On the contrary, the concentration effect on the surface dilatational viscosity is very small, at least for most typical physiologically, i.e. relatively quick surface oscillations (period of 2 and 4 s). It means that time-lag between surface perturbation (contraction/expansion) and surface tension variation, which is reflected by γ-A hysteresis, remains similar independent of NPS concentration in the liquid phase.

The result obtained set the ground for a preliminary discussion on possible effects of inhaled PAD nanoparticles (used as drug carriers) in the lungs. The tested NPS are evidently surface-active under dynamic conditions which is in line with several other results regarding nanoparticle behavior in aqueous environment (Bizmark et al., 2014; Kondej and Sosnowski, 2016). Consequently, NPS can either compete or cooperate (synergic effect) with other surface-active components of the system, leading to increased dynamics of surface tension reduction at short time-scales, as shown in the experiments done for the mixtures of Triton X-100 and NPS. In a physiological situation, high surface-activity of these NPS may interfere with the balanced surface-tension variations caused by the activity of the natural components of the LS. Competitive adsorption of NPS may decrease the mass of phospholipids and proteins exchanged with the interface during surface variations (breathing). As a consequence, their physiological function and their role in effects dependent on the adequate surface-tension dynamics (e.g. mass transfer in the pulmonary region) may be altered. Such hypothesis is supported by literature data which confirm that inhalation of potent surface-active compounds can be detrimental for the LS and respiratory functions (Hall et al., 1985; Rao and Das, 1994). It must be noted though, that NPS concentrations tested in our experiments were intentionally very high, since they were used to highlight the potential physicochemical effects. In real inhalation it is not probable that the concentration of 1 mg/ml can be attained in the pulmonary liquid because it would require inhalation of more than 30 mg of fine (< 5 μm) powder particles at a time (Sosnowski et al., 2000). It is highly improbable since typical inhalation drugs contain less than 500 μg of active compounds (e.g. corticosteroids), while even for an inhaled systemic drug like insulin, the inhaled mass does not exceed 9 mg of powder per dose (Santos and Edelman, 2014).

Another important observation is related to surface tension hysteresis during harmonic surface perturbation, which is known to occur in the LS system. Our study shows that such hysteresis is also produced by PAD nanoparticles themselves, as demonstrated by the visco-elastic surface response. However, a more detailed analysis of these effects is needed to assess their possible physiological consequences for LS and the respiratory system dynamics.

4. CONCLUSIONS

Experimental results show high surface activity of the studied PAD nanoparticles in the aqueous environment. The equilibrium surface tension of systems which contain NPS decrease to the value of 30-odd mN/m in the concentration-dependent manner. The concentration affected the rate of surface reduction, as well as the time in which the equilibrium was reached. The Ward-Tordai equation was used to calculate the diffusion coefficient of NPS and predict the asymptotic, equilibrium surface tension value in studied systems. The average value of the diffusion coefficient of PAD nanoparticles in water was determined as $D = (2.3 \pm 0.6) \times 10^{-10}$ m^2/s.

DST in aqueous systems which contain a model nonionic surfactant is determined mainly by activity of this surfactant. However, the effect of additional surface tension reduction by NPS present in such systems is the most significant for a very short adsorption time and it depends on particle concentration. This suggest a co-adsorption mechanism in mixed NPS-surfactant system. However, for surface ages similar to the timescale of breathing cycle (several seconds) the impact of nanoparticles is not very high. Our measurements showed that PAD nanoparticles influence surface dilatational elasticity but do not cause significant changes in surface dilatational viscosity in the tested ranges of surface oscillation rates and NPS concentrations.

As stated earlier, at this stage it is possible only to speculate on the mechanisms of interactions of inhaled NPS in the lungs. Their co-adsorption on the air-liquid interface may influence the dynamic surface tension during breathing. The most important is concentration-dependent reduction of surface elasticity which is related to the shape of surface tension hysteresis recognized as a marker of lung surfactant activity (Sosnowski, 2006). However, to fully evaluate the safety of PAD nanoparticles as potential carriers of drugs delivered by inhalation it will be necessary to study their adsorption and effect on surface rheology of the realistic model of the lung surfactant, e.g. the one based on commercial medicines such as Survanta, Curosurf, Infasurf or other suitable multi-component systems under investigation (Sosnowski et al., 2016).

This work was supported by NCN project no. 2014/13/N/ST8/01667.

SYMBOLS

A	air/liquid surface area, m^2
c_0	bulk concentration, mol/m^3
c_s	concentration in the subsurface, mol/m^3
D	diffusion coefficient, m^2/s
E	surface dilatational modulus, N/m
E'	real part of complex surface dilatational modulus (surface elasticity), N/m
E''	imaginary part of complex surface dilatational modulus (loss modulus), Ns/m
n	constant (eq. 1)
R	gas constant, J/(mol K)
t	time (surface age), s
T	temperature, K

Greek symbols

γ	surface tension, N/m
γ_0	surface tension at $t = 0$, N/m
γ_{eq}	equilibrium surface tension, N/m
Γ	surface excess, mol/m^2
η_d	surface dilatational viscosity, Ns/m
τ	dummy variable of integration (eq. 1), s
ω	angular frequency of periodic changes of surface area, 1/s

Abbreviations

ADSA	axisymmetric drop shape analysis
DST	dynamic surface tension
LS	lung surfactant
MBP	maximum bubble pressure
MW	molecular weight
NPS	nanoparticles
PAD	polyaldehyde dextran

REFERENCES

Beck-Broichsitter M, Ruppert C, Schmehl T., Günther A., Seeger W., 2014. Biophysical inhibition of synthetic vs. naturally-derived pulmonary surfactant preparations by polymeric nanoparticles. *Biochim. Biophys. Acta - Biomembranes,* 1838, 474–481. DOI: 10.1016/j.bbamem.2013.10.016.

Bizmark N., Ioannidis M.A., Henneke D.E., 2014. Irreversible adsorption-driven assembly of nanoparticles at fluid interfaces revealed by a dynamic surface tension probe. *Langmuir,* 30, 710-717. DOI: 10.1021/la404357j

Eastoe J., Dalton J.S. 2000., Dynamic surface tension and adsorption mechanisms of surfactants at the air- water interface. *Adv. Coll. Interface Sci.,* 85, 103-144. DOI: 10.1016/S0001-8686(99)00017-2.

Ellyett K.M., Broadbent R.S., Fawcett E.R., Campbell A.J., 1996. Surfactant aerosol treatment of respiratory distress syndrome in the spontaneously breathing premature rabbit. *Pediatric Res.,* 39, 953-957. DOI: 10.1203/00006450-199606000-00005.

Gibbs J.W., 1961. On the equilibrium of heterogeneous substances. In: *The Scientific Papers of J. Willard Gibbs. Vol. I. Thermodynamics*. Dover Publications, New York.

Goerke J., 1992. Surfactant and lung mechanics. In: Robertson B., Van Golde L.M.G., Batenburg J.J. (Eds.). *Pulmonary Surfactant: From molecular biology to clinical practice.* Elsevier, Amsterdam, 165-192.

Gradoń L, Podgórski A., 1989. Hydrodynamical model of pulmonary clearance. *Chem. Eng. Sci.,* 44, 741-749. DOI: 10.1016/0009-2509(89)85048-1.

Gradoń L., Podgórski A., Sosnowski T.R., 1996. Experimental and theoretical investigations of transport properties of DPPC monolayer. *J. Aerosol Med.,* 9, 357-367. DOI:10.1089/ jam.1996.9.357.

Grotberg J.B., 2001. Respiratory fluid mechanics and transport processes. *Annu. Rev. Biomed. Eng.,* 3, 421-457. DOI: 10.1146/annurev.bioeng.3.1.421.

Hall S.B., Lu R.Z., Venkitaraman A.R., Hyde R.W., Notter R.H., 1985. Inhibition of pulmonary surfactant by oleic acid: mechanisms and characteristics. *J. Appl. Physiol.,* 72, 1708-1716.

Jabłczyńska K., Janczewska M., Kulikowska A., Sosnowski T.R., 2015. Preparation and characterization of biocompatible polymer particles as potential nanocarriers for inhalation therapy. *Int. J. Polym. Sci.,* 2015, Article ID 763020. DOI: 10.1155/2015/763020.

Kondej D., Sosnowski T.R., 2013. Alteration of biophysical activity of pulmonary surfactant by aluminosilicate nanoparticles. *Inhalation Toxicol.,* 25, 77-83. DOI: 10.3109/08958378. 2012.756087

Kondej D., Sosnowski T.R., 2016. Effect of clay nanoparticles on model lung surfactant: a potential marker of hazard from nanoaerosol inhalation. *Env. Sci. Pollut. Res.,* 23, 4660-4669. DOI: 10.1007/s11356-015-5610-4.

Kramek-Romanowska K., Odziomek M., Sosnowski T.R., 2015. Dynamic tensiometry studies on interactions of novel therapeutic inhalable powders with model pulmonary surfactant at the air-water interface. *Coll. Surfaces A: Physicochem. Eng. Aspects,* 480, 149-158. DOI: 10.1016/j.colsurfa.2015.02.017.

Lyklema J. 2000 Fundamentals of interface and colloid science. Academic Press, London-San Diego.

Miller R., Liggieri L., 2009. *Interfacial Rheology. Vol I. Progress in Colloid and Interface Science*, Brill, Leiden-Boston.

Notter R.H, Taubold R, Mavis R.D., 1982. Hysteresis in saturated phospholipid films and its potential relevance for lung surfactant function in vivo. *Exp. Lung Res.,* 3, 109-127.

Okubo T., 1995. Surface tension of structured colloidal suspensions of polystyrene and silica spheres at the air–water interface. *J. Coll. Interface Sci.,* 171, 55–62. DOI:10.1006/jcis.1995.1150.

Podgórski A,, Gradoń L., 1993. An improved mathematical model of hydrodynamical self-cleansing of pulmonary alveoli. *Ann. Occup. Hyg.,* 37, 347-365. DOI: 10.1093/annhyg/37.4.347

Podgórski A., Sosnowski T.R., Gradoń L., 2001. Deactivation of the pulmonary surfactant dynamics by toxic aerosols and gases. *J. Aerosol Med.,* 14, 455-466. DOI: 10.1089/08942680152744668.

Rao J., Das P.K., 1994. Pulmonary oedema due to inhalation of detergent aerosol. *Malaysian J. Pathol.,* 16, 165–166.

Rosenberg O.A., Lebedeva E.S., Loshakova L.V., Shulga A.E., Seiliev A.A., Volchkov V.A., 2016. Influence of long-term inhaled glucocorticoids on the lung surfactant phospholipid levels in rats. *Int. J. Biomed*., 6, 167-169. DOI: 10.21103/Article6(3)_OA1.

Santos C.T., Edelman S., 2014. Inhaled insulin: a breath of fresh air? A review of inhaled insulin. *Clin. Ther*., 36, 1275-1289. DOI: 10.1016/j.clinthera.2014.06.025.

Sosnowski T.R., 2006. *Dynamic effects in gas-liquid systems with an active interface* (in Polish: Efekty dynamiczne w układach ciecz-gaz z aktywną powierzchnią międzyfazową) OWPW, Warsaw.

Sosnowski T.R., Gradoń L., Skoczek M., Droździel H., 1998. Experimental evaluation of importance of the pulmonary surfactant for oxygen transfer rate in human lungs. *Int. J. Occup. Safety Ergon*., 4, 391-409. DOI: 10.1080/10803548.1998.11076401.

Sosnowski T.R., Gradoń L., Podgórski A., 2000. Influence of insoluble aerosol deposits on the surface activity of the pulmonary surfactant: a possible mechanism of alveolar clearance retardation? *Aerosol Sci. Technol.,* 32, 52-60. DOI: 10.1080/027868200303920.

Sosnowski T.R., Kubski P., Wojciechowski K. 2016. New experimental model of pulmonary surfactant for biophysical studies. *Coll. Surfaces A: Physicochem. Eng. Aspects,* DOI: 10.1016/j.colsurfa.2016.06.044.

Ward A.F.H., Tordai L., 1946. Time-dependence of boundary tensions of solutions I. The role of diffusion in time-effects. *J. Chem. Phys*., 14, 453–461.

Wasiak I., Kulikowska A., Janczewska M., Michalak M., Cymerman I.A., Nagalski A., Kallinger P., Szymanski W.W., Ciach T., 2016. Dextran nanoparticle synthesis and properties. *PLoS ONE* 11(1), e0146237. DOI: 10.1371/journal.pone.0146237

Zhang H., Wang Y.E., Neal C.R., Zuo Y.Y., 2012. Differential effects of cholesterol and budesonide on biophysical properties of clinical surfactant. *Pediatric Res.* 71, 316–323. DOI: 10.1038/pr.2011.78.

Received 5 December 2016
Received in revised form 10 February 2017
Accepted 22 February 2017

Chemical and Process Engineering 2017, 38 (1), 79-96
DOI: 10.1515/cpe-2017-0007

ENERGETIC EFFICIENCY OF MIXING AND MASS TRANSFER IN SINGLE PHASE AND TWO-PHASE SYSTEMS

Jerzy Bałdyga*, Magdalena Jasińska

Warsaw University of Technology, Faculty of Chemical and Process Engineering, ul. Waryńskiego 1, Warsaw, Poland

Dedicated to Prof. Leon Gradoń on the occasion of his 70th birthday

In this work a concept of energetic efficiency of mixing is presented and discussed; a classical definition of mixing efficiency is modified to include effects of the Schmidt number and the Reynolds number. Generalization to turbulent flows is presented as well. It is shown how the energetic efficiency of mixing as well as efficiencies of drop breakage and mass transfer in two-phase liquid-liquid systems can be identified using mathematical models and test chemical reactions. New expressions for analyzing efficiency problem are applied to identify the energetic efficiency of mixing in a stirred tank, a rotor stator mixer and a microreactor. Published experimental data and new results obtained using new systems of test reactions are applied. It has been shown that the efficiency of mixing is small in popular types of reactors and mixers and thus there is some space for improvement.

Keywords: chemical test reactions, energetic efficiency, mass transfer, mixing

1. INTRODUCTION

In this work the authors are concerned with the influence of mixing on the course of complex chemical reactions in single phase liquid systems and two-phase liquid-liquid systems. This problem is considered in the chemical reaction engineering literature (Bałdyga and Bourne, 1999; Bourne, 2003; Levenspiel, 1972) from two related points of view. First of all the design and performance of chemical reactors should enable to run chemical reactions with the highest possible selectivity. On the other hand, complex chemical reactions can be used as test reactions, to investigate the efficiency of mixing. Using test reactions one can characterize the level of mixedness (intensity of segregation, time constants for mixing) and use this information to improve the performance of processes carried out in the reactor. The time constant for turbulent mixing can be defined as the time scale of decay of the concentration variance of the passive scalar, *i*.

$$\tau_M = \frac{\overline{\left(c_i - \bar{c}_i\right)^2}}{\dfrac{d\overline{\left(c_i - \bar{c}_i\right)^2}}{dt}} \tag{1}$$

For effective laminar mixing by fluid elongation, one can define the characteristic mixing time (Bałdyga and Bourne,1986) by

$$\tau_M = \frac{1}{2\dot{\gamma}} \operatorname{arcsin} h\left(0.76\dot{\gamma}\delta_0^2 / D_i\right) \tag{2}$$

---

*Corresponding author, e-mail: J.Baldyga@ichip.pw.edu.pl where $\dot{\gamma}$ is the rate of elongation and δ_0 represents original thickness of the slab to be elongated. In the case of turbulent mixing the rate of elongation can be expressed as $(\varepsilon/\nu)^{1/2}$ and the slab thickness expressed using the Kolmogrov microscale, λ_K. Then the mixing time can be expressed by the Corrsin (1964) equation

$$\tau_M \cong \frac{1}{2}\left(\frac{\nu}{\varepsilon}\right)^{1/2} \ln(Sc) \qquad Sc >> 1 \tag{3}$$

When both the inertial-convective and viscous-convective subranges of the concentration spectrum exist then the time constant for mixing reads (Corrsin, 1964):

$$\tau_M \cong \frac{2\Lambda_c^{2/3}}{\varepsilon^{1/3}} + \frac{1}{2}\left(\frac{\nu}{\varepsilon}\right)^{1/2} \ln(Sc) \qquad Sc >> 1 \tag{4}$$

where the relaxed integral scale for turbulent fluctuations of concentration, Λ_c, is proportional to the scale of the large, energy containing eddies, L, $\Lambda_c \cong L/2$.

The process of mixing between elongated slabs in laminar flow or in the viscous-convective and viscous-diffusive subranges of turbulence can be represented by the rate of creation of the intermaterial area per unit volume, a_v [m^{-1}], as given by (Ottino, 1980):

$$\left|\frac{1}{a_v}\frac{da_v}{dt}\right| = eff(t)\left(\bar{D}:\bar{D}\right)^{1/2} \tag{5}$$

$$\bar{D} = \frac{1}{2}\left[grad(\vec{u}) + grad(\vec{u})^T\right] \tag{6}$$

that is defined using the velocity gradient, $grad(\vec{u})$.

Equation (5) depicts the fact that orientation of the intermaterial area with respect to the principle axes of deformation determines the effectiveness of mixing. It characterises the ratio of energy really applied to increase the intermaterial area to the whole energy dissipated during the flow. Using this concept one can define the efficiency of mixing using either a definition proposed by (Ottino, 1980) for 2D systems,

$$eff(t) = \frac{1}{a_v}\frac{da_v}{dt}\left(\frac{\varepsilon_T}{2\nu}\right)^{-1/2} = -\frac{1}{\lambda}\frac{d\lambda}{dt} \tag{7}$$

or a similar definition published by Rożeń (2008) for 3D deformation

$$eff(t) = \frac{1}{a_v}\frac{da_v}{dt}\left(\frac{\varepsilon_T}{3\nu}\right)^{-1/2} = -\frac{1}{\lambda}\frac{d\lambda}{dt} \tag{8}$$

where ε_T [m^{2}s^{-3}] represents the total rate of energy dissipation per unit mass and λ is the slab or striation thickness that is directly related to a_v, namely $\lambda = a_v^{-1}$. In this work the average values of efficiency during residence time t in the mixer will be considered.

2. THEORETICAL ASPECTS OF EFFICIENCY OF MICROMIXING

Equations (5) to (8) describe just fluid deformation but they do not consider mixing on the molecular scale. This means that intensity of segregation (a normalized variance of the passive scalar tracer) stays equal to unity during mixing. To illustrate an influence of the local flow structure on mixing, consider a spot of contaminant of finite molecular diffusivity, D_i, which is transported, deformed and rotated.

Following Tennekes and Lumley (1972) and Bałdyga and Bourne (1999), one can start from the conservation equation for the concentration, *c*

$$\frac{\partial c}{\partial t}+u_j\frac{\partial c}{\partial x_j}=D_i\frac{\partial^2 c}{\partial x_j^2} \tag{9}$$

and assume that the spot size is smaller than the Kolmogorov microscale λ_K. The spot position is determined by the position of the Lagrangian point $\vec{X}$ that can be interpreted as the centre of mass of the spot. One can write the differential mass balance in a local coordinate system (ξ_1, ξ_2 and ξ_3) attached to the Lagrangian point $\vec{X}$, where $\vec{\xi}=\vec{x}-\vec{X}$ is the position vector in the moving frame. The fluid element is assumed to be smaller than the Kolmogorov microscale, hence the relative motion $\vec{u}(\vec{\xi})=\vec{u}(\vec{x})-\vec{u}(\vec{X})-\vec{\omega}\,x\,\vec{\xi}$ is described by a linear relation, leading to

$$\frac{\partial c}{\partial t}+\xi_j\frac{\partial u_i}{\partial \xi_j}\frac{\partial c}{\partial \xi_i}=D\frac{\partial^2 c}{\partial \xi_i^2} \tag{10}$$

Treating now the concentration of the tracer substance as a three-dimensional probability density function one can characterize the shape of our spot by using the concentration moments (Tennekes and Lumley, 1972).

$$I_{kl}=\frac{\int\int\int_{-\infty}^{+\infty}\xi_k\xi_l c(\vec{\xi},t)\,d\xi_1 d\xi_2 d\xi_3}{\int\int\int_{-\infty}^{+\infty}c(\vec{\xi},t)\,d\xi_1 d\xi_2 d\xi_3} \tag{11}$$

This definition allows the diagonal moment I_{kk}, to be used as a quantity proportional to the square of the penetration distance of the contaminant in the "*k*" direction. The shape of the spot can be characterized by comparing the diagonal moments I_{11}, I_{22} and I_{33}

$$\delta_1^2:\delta_2^2:\delta_3^2=I_{11}:I_{22}:I_{33} \tag{12}$$

whereas the sum of diagonal components $I=I_{kk}=I_{11}+I_{22}+I_{33}$ is proportional to the square of the average spot radius. From Eqs. (10) and (11) one gets after transformation

$$\frac{dI_{kk}}{dt}-2(s_{km}+\Omega_{km})I_{km}=2D\delta_{kk} \tag{13}$$

where s_{km} and Ω_{km} represent the pure deformation and rotation tensors, respectively.

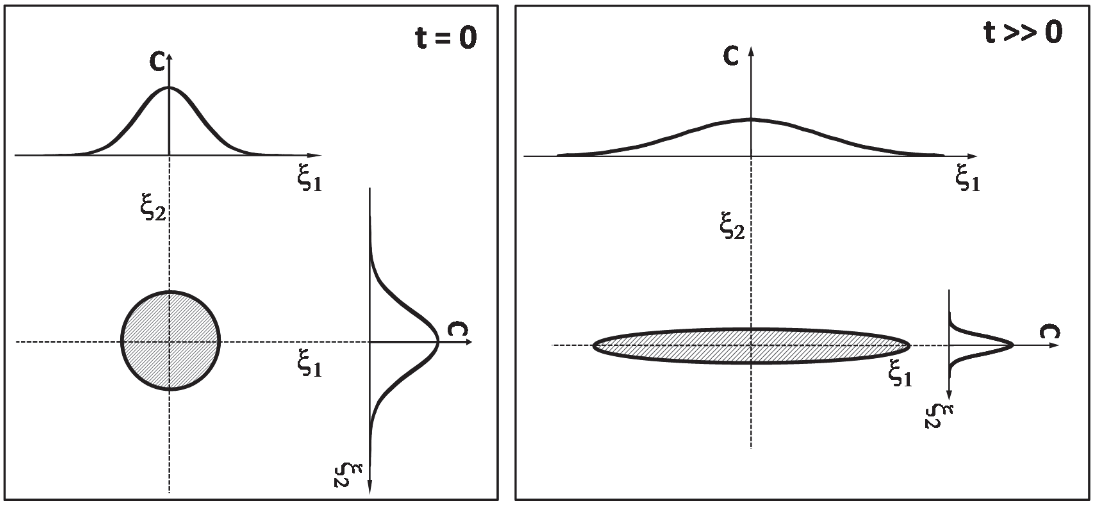

Fig. 1. Effect of stretching on spreading of the contaminant due to molecular diffusion

Equation (13) shows effects of deformation and rotation on spreading of the contaminant. To show relation between fluid deformation and mixing on molecular scale one can neglect effects of rotation, and follow spreading of the contaminant in the 2-dimensional flow, as shown in Fig. 1.

Equation (13) reduces then to

$$\frac{dI_{11}}{dt} - 2sI_{11} = 2D_i \tag{14}$$

$$\frac{dI_{11}}{dt} + 2sI_{11} = 2D_i \tag{15}$$

which can be solved with initial conditions $I_{11}(0) = \delta_0^2$ and $I_{22}(0) = \delta_0^2$, and $s = \text{const.}(\varepsilon/\nu)^{1/2}$, yielding

$$I_{SD} = I_{11} + I_{22} = 2\delta_0^2 \cosh(2st) + 2\frac{D_i}{s}\sinh(2st) \tag{16}$$

Notice that definitions (7) and (8) consider only the first term on the RHS of Eq.(16). When there is no deformation $(s = 0)$, Eq.(16) reduces to

$$I_D = I_{11} + I_{22} = 2\delta_0^2 + 4D_i t \tag{17}$$

To present effect of deformation on mixing one can plot the ratio I_{SD}/I_D versus dimensionless time, $s \cdot t$ for $\delta_0 = 0$, as shown in Fig. 2.

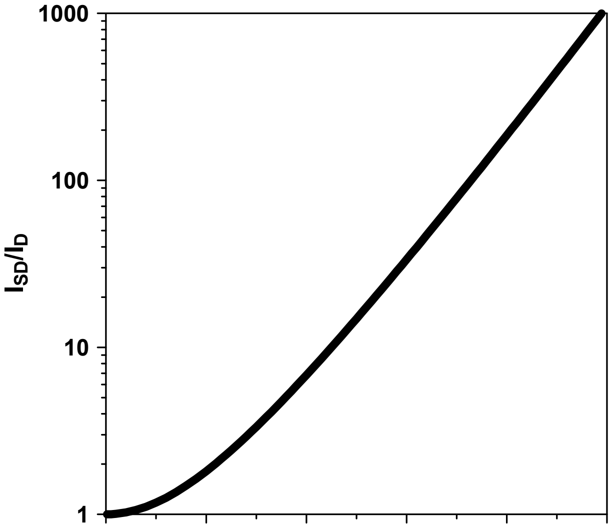

Fig. 2. Effect of fluid deformation on spreading of the contaminant

Figure 2 shows a dominating effect of stretching on spreading due to molecular diffusion. If, however, rotation effects are not neglected, and conditions presented in Fig. 1 are replaced by those given in Fig. 3, then the resulting solution will look different, as shown in Fig. 4. Figure 4 clearly shows that the growth of the spot of a contaminant is retarded by rotation; when rotation is small, the growth is still exponential, but with the resulting rate of stretching, e.g. $\dot{\gamma}_1'$, smaller than $s_{11} = s$. For intensive rotation the spot is turned to a new orientation before the gradients have opportunity to increase and accelerate molecular diffusion.

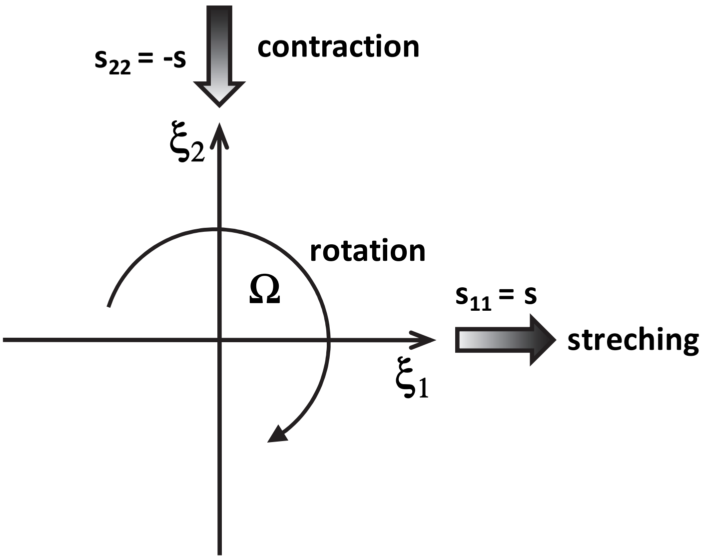

Fig. 3. The flow field including rotation

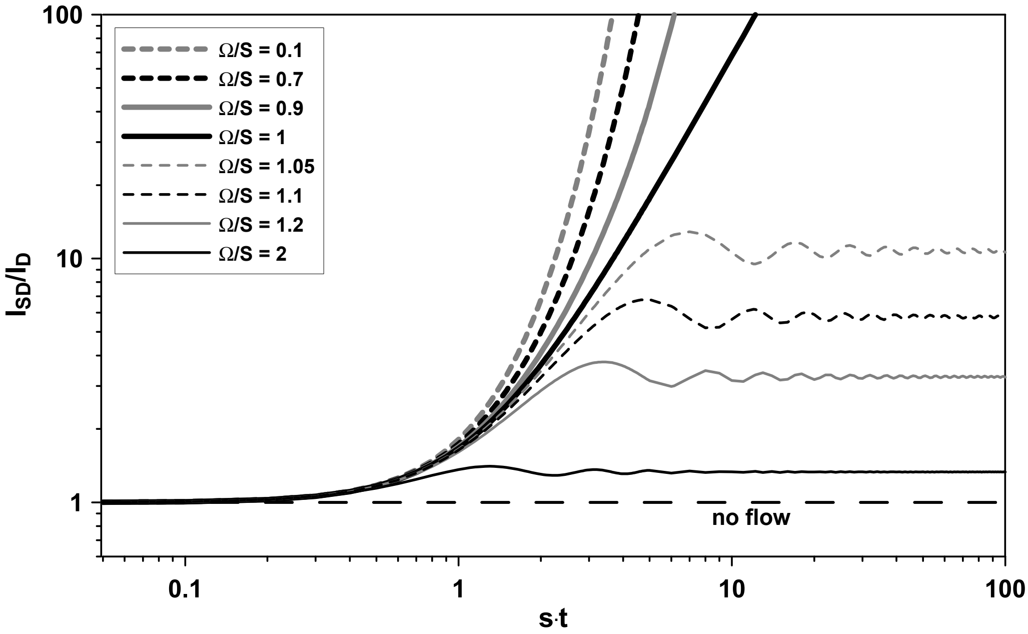

Fig. 4. Effects of stretching and rotation on spreading of the contaminant

Equation (13) for $\Omega/s < 1$can be presented in the local frame of reference (ξ_1', ξ_2') such that the off-diagonal moments vanish, and Eq. (13) is replaced by

$$\frac{1}{I_{ii}'}\frac{dI_{ii}'}{dt} = 2\left[\frac{D}{I_{ii}'} + \dot{\gamma}_i'(\vec{x},t)\right] \tag{18}$$

where $\dot{\gamma}_1' = \beta \cdot s = \beta \cdot \left(\frac{\varepsilon}{2\nu}\right)^{1/2}$ and $\dot{\gamma}_2' = -\beta \cdot s = \beta \cdot \left(\frac{\varepsilon}{2\nu}\right)^{1/2}$ with $0 \le \beta \le 0$. The coefficient β is equivalent to the efficiency *eff* defined by Eq. (7).

As mentioned earlier, Eqs. (5) to (8) are based on analysis of fluid deformation but they do not consider mixing on the molecular scale. In what follows let us consider turbulent mixing and include effects of molecular diffusion. This should lead to a more realistic definition of energetic efficiency. Considering that the slab or striation thickness is directly related to a_v, namely $\lambda = a_v^{-1}$, we get from Eqs. (5) and (8)

$$\frac{1}{\lambda}\frac{d\lambda}{dt} = -eff\left(t\right)\cdot\left(\frac{\varepsilon}{3\nu}\right)^{1/2} \tag{19}$$

When Eq. (19) is integrated from the Kolmogorov microscale $\lambda_K = \frac{\nu^{3/4}}{\varepsilon^{1/4}} = k_K^{-1}$ to the Batchelor microscale, $\lambda_B = \frac{\nu^{1/4}D^{1/2}}{\varepsilon^{1/4}} = k_B^{-1}$ the latter representing a cut-off of the spectrum due to molecular diffusion as shown in Fig. 5, then the time of decreasing λ from λ_K to λ_B corresponds to the mixing time, τ_M. This results in the new equation for efficiency of micromixing:

$$eff = \frac{\sqrt{3}}{2}\frac{\left(\frac{\nu}{\varepsilon}\right)^{1/2}\ln\left(\mathrm{Sc}\right)}{\tau_M} \tag{20}$$

Once the characteristic time scale for mixing is measured one can calculate the efficiency of mixing from Eq.(20). In this section we identify efficiency of mixing based on available in the mixing literature models of mixing on the molecular scale.

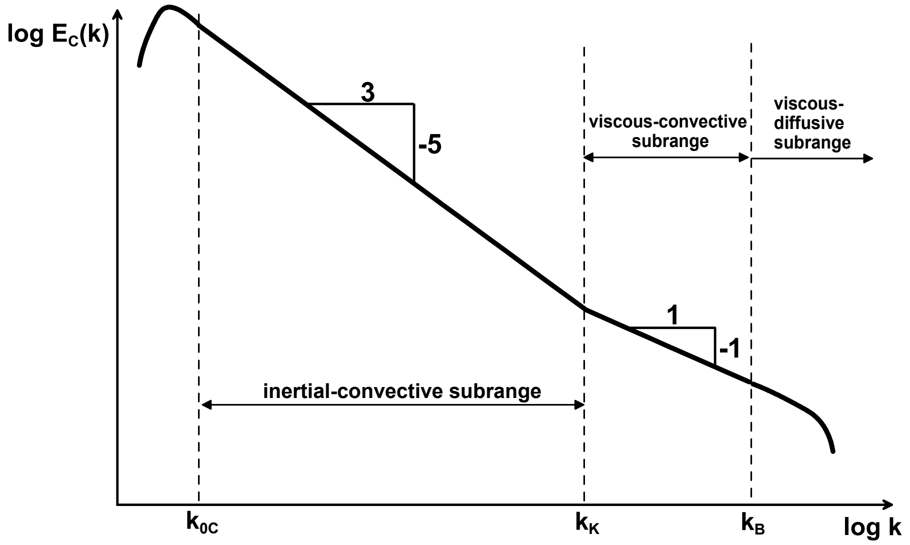

Fig. 5. Spectrum of concentration variance in liquids with very large Schmidt number at very high Reynolds number

Let us start from mixing in the viscous-convective and viscous-diffusive subranges of turbulence, Eq. (3). In Eq. (3) it was assumed that the rate of strain is equal to $\left(\varepsilon/\nu\right)^{1/2}$. We can replace now the prefactor for the rate of strain more precisely: based on Taylor's equation one gets $\left|du/dx\right| = \left(2\varepsilon/15\pi\nu\right)^{1/2}$, which leads to $\tau_M \cong 2.42\left(\nu/\varepsilon\right)^{1/2}\ln(\mathrm{Sc})$ instead of Eq. (3). A more exact expression including the effect of skewness factor was given by Batchelor (1980) for the characteristic rate of strain $\left|du/dx\right| = 7S\big/\left(6\sqrt{15}\right)\cdot\left(\varepsilon/\nu\right)^{1/2}$ where S is the skewness factor. After substituting for S the value 0.6 we get $\left|du/dx\right| = 0.151\left(\varepsilon/\nu\right)^{1/2}$ and

$$\tau_M \cong 3.3\left(\frac{\nu}{\varepsilon}\right)^{1/2}\ln(\mathrm{Sc}) \qquad \mathrm{Sc} >> 1 \tag{21}$$

which after substitution to Eq. (20) results in $eff = 0.26$. A slightly less exact estimate for isotropic turbulence based on Taylor's equation results in $eff = 0.36$.

The results show that due to reorientation of the rate of strain tensor at a small scale in turbulent flow the efficiency of mixing $eff = 1$ is not possible. $eff = 1$ would be possible for continuous elongation of threads of fluid in 3D space without reorientation, which does not take place in turbulent flows.

Introducing now Batchelor’s correction to Eq. (4) we get

$$\tau_M \cong \frac{2\Lambda_c^{2/3}}{\varepsilon^{1/3}} + 3.3\left(\frac{\nu}{\varepsilon}\right)^{1/2} \ln(\mathrm{Sc}) \qquad \mathrm{Sc} >> 1 \tag{22}$$

and substituting for the integral scale of concentration fluctuations the relaxed value, $\Lambda_c \cong L/2$,

$$eff = \frac{\frac{\sqrt{3}}{2}\left(\frac{\nu}{\varepsilon}\right)^{1/2} \ln(\mathrm{Sc})}{\frac{\Lambda_c^{2/3}}{\varepsilon^{1/3}} + 3.3\left(\frac{\nu}{\varepsilon}\right)^{1/2} \ln(\mathrm{Sc})} = \frac{\frac{\sqrt{3}}{2}\left(\frac{\nu}{\varepsilon}\right)^{1/2} \ln(\mathrm{Sc})}{1.26\frac{L^{2/3}}{\varepsilon^{1/3}} + 3.3\left(\frac{\nu}{\varepsilon}\right)^{1/2} \ln(\mathrm{Sc})} = \frac{0.69\ln(\mathrm{Sc})}{\mathrm{Re}_L^{1/2} + 2.6\ln(\mathrm{Sc})} \tag{23}$$

where $\mathrm{Re}_L = u'L/\nu$ is the Reynolds number based on the root-mean-square velocity fluctuation u' and the scale of the large, energy containing eddies, L. Equation (23) is based on the definition of efficiency given by Eq. (20). A special definition for turbulent mixing can be proposed when instead of $\left(\frac{\varepsilon}{3\nu}\right)^{1/2}$ valid for laminar flow we will use after Batchelor (1980) the maximum possible rate of deformation for turbulent flow $|du/dx| = 7S/\left(6\sqrt{15}\right)\cdot(\varepsilon/\nu)^{1/2}$. Then efficiency for turbulent mixing, eff_2, defined as

$$eff_2 = \frac{3.3\left(\frac{\nu}{\varepsilon}\right)^{1/2} \ln(\mathrm{Sc})}{\frac{\Lambda_c^{2/3}}{\varepsilon^{1/3}} + 3.3\left(\frac{\nu}{\varepsilon}\right)^{1/2} \ln(\mathrm{Sc})} = \frac{3.3\left(\frac{\nu}{\varepsilon}\right)^{1/2} \ln(\mathrm{Sc})}{1.26\frac{L^{2/3}}{\varepsilon^{1/3}} + 3.3\left(\frac{\nu}{\varepsilon}\right)^{1/2} \ln(\mathrm{Sc})} = \frac{2.6\ln(\mathrm{Sc})}{\mathrm{Re}_L^{1/2} + 2.6\ln(\mathrm{Sc})} \tag{24}$$

will take values between 0 and 1.

Figure 6 shows effects of the Reynolds number and the Schmidt number on mixing efficiency.

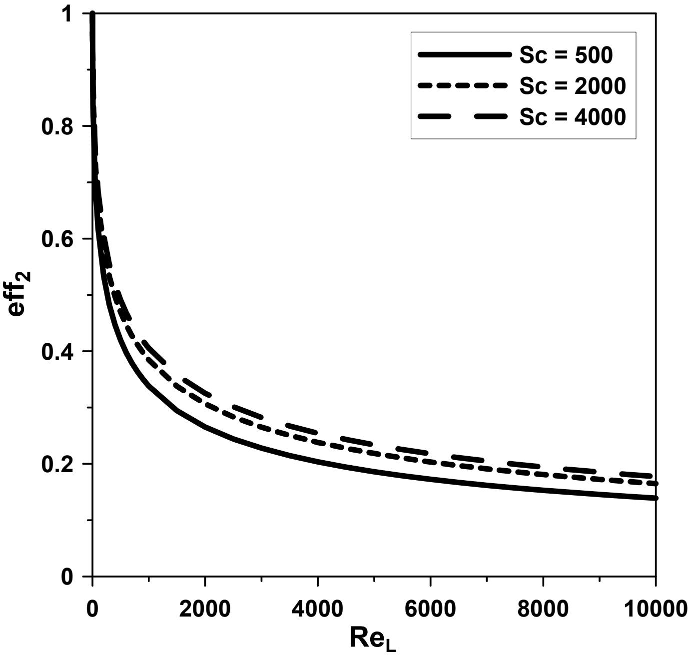

Fig. 6. Effects of the Reynolds and Schmidt numbers on efficiency of mixing

The efficiency of mixing decreases significantly with increasing the Reynolds number due to the increasing role of the inertial-convective mixing and increases slightly with increasing the Schmidt number. To run the process at high efficiency it is important to decrease the integral scale, Λ_c, in Eq. (22). When reagents are fed to the tank very slowly through the feeding nozzle of small diameter then one has $\Lambda_c << L$ and its effect in Eq. (22) is negligible (see Bałdyga and Bourne (1999)). In such a case multiple feeding pipes are recommended to have a faster overall feeding rate.

For description of micromixing under such asymptotic conditions the Engulfment model is recommended. The model describes viscous-convective processes of building lamellar structures by engulfment and deformation.

When micromixing is controlled by a viscous-convective engulfment process, then the c_i concentration history can be calculated from the engulfment equations:

$$\frac{dc_i}{dt} = E\left(\langle c_i\rangle - c_i\right) + r_i \tag{25}$$

$$\frac{d\left(\delta V_i\right)}{dt} = E \cdot \delta V_i \tag{26}$$

with engulfment parameter $E = 0.058\left(\frac{\varepsilon}{\nu}\right)^{1/2}$, that depends on flow conditions and fluid viscosity. $\langle c_i\rangle$ represents here the concentration of reactant *i* in the environment. For this model the efficiency as defined by Eq. (8) is equal to $eff = 0.1$. Because the E-model is easy to use and validated experimentally, we will treat the value predicted by this model as the reference one and define relative efficiency based on it. Of course it is always possible to express the absolute efficiency defined by Eqs. (7) or (8) by multiplying the efficiency identified using E-model by 0.1. In such a case the E-model, or any other model of this type, takes the role of an agent of efficiency identification. Notice that a somewhat similar approach was applied by Falk and Commenge (2010), where as a reference model the model for laminar mixing (Bałdyga and Bourne, 1986) was used in combination with the IEM model (Villermaux, 1986).

3. EXPERIMENTAL IDENTIFICATION OF MICROMIXING EFFICIENCY

The procedure to characterize efficiency of mixing includes modelling of effects of mixing on the course of the test chemical reactions using the E-model of micromixing (Bałdyga and Bourne, 1999). In the E-model the engulfment parameter, $E = 0.058\left(\varepsilon/\nu\right)^{1/2}$ depends on the rate of energy dissipation, ε. One can construct then the calibration curve representing the theoretical dependence of the product distribution on the rate of energy dissipation. Having measured the value of product distribution one identifies then the rate of energy dissipation, ε as the theoretical reference value. Comparing the theoretical rate of energy dissipation, ε necessary to obtain the same product distribution, X_S, as the one observed in experiment under consideration, characterized by the rate of energy dissipation equal to ε_T, one can express the average efficiency of mixing, $\overline{eff}$, by

$$\overline{eff} = \left(\frac{\varepsilon}{\varepsilon_T}\right)^{1/2} \tag{27}$$

Let us consider the set of competing or parallel reactions as given by Eq. (28):

$$\mathrm{A} + \mathrm{B} \xrightarrow{k_1} \mathrm{R}, \quad \mathrm{C} + \mathrm{B} \xrightarrow{k_2} \mathrm{S} \tag{28}$$

A good example of such a reacting system is competitive neutralization of hydrochloric acid and alkaline hydrolysis of monochloroacetate methyl or ethyl esters of monochloroacetic acid (Bałdyga and Bourne, 1999). In what follows in this section we use as a reference system the one given by Eq. (28) with A = HCl, B = NaOH, C = $CH_2ClCOOC_2H_5$, R = H_2O or NaCl, S = C_2H_5OH or $CH_2ClCOONa$ and a new one, with C replaced by $CHCl_2COOC_2H_5$ and thus S represented this time by $CHCl_2COONa$. To illustrate application of the test reactions, both experiments and simulations have been performed. Experiments were carried out using a semibatch stirred tank reactor of diameter T = 145 mm, equipped with the Rushton type impeller of diameter D_{imp}=50 mm and 4 baffles of a width equal to 15 mm.

The product distribution was represented by the ratio of number of reacted moles of the ester to the number of moles of the base (B) for $N_A = N_B = N_C$.

$$X_S = \frac{\Delta N_C}{N_A} \tag{29}$$

The feeding of B solution to premixture A and C was so slow that there was no effect of feeding rate observed on the product distribution. In this situation the inertial-convective mixing is not active and one can expect $\overline{eff} = \left(\frac{\varepsilon}{\varepsilon_T}\right)^{1/2} \cong 1$

Figure 7 shows that results of simulation with the E-model agree very well with experimental data, hence $\varepsilon = \varepsilon_T$. Notice that the relative efficiency based on comparison with the E-model is equal to 1, but the efficiency characterising E-model itself is 10%.

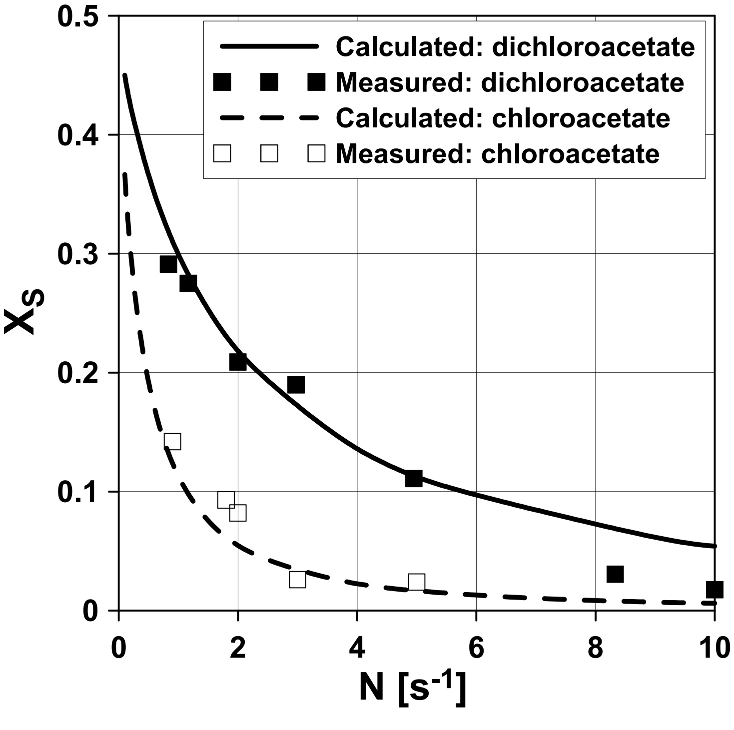

Fig. 7. Effect of agitation rate on selectivity X_S for ethyl chloroacetate and ethyl dichloroacetate; c_B=1M, c_{A0}=c_{C0}=0.02M, α=50, feeding position A close to the impeller

When as a system of the test reactions a simultaneous diazo-coupling between 1- and 2-naphtols and diazotized sulphanilic acid is applied (Bourne et al., 1992), two measures of product distribution can be used, one concentrating on the yield of secondary product S (a bisazo dye) and the other on the yield of the competitive product Q (a single monoazo dye). X_Q means then a fraction of the diazotized sulphanilic acid converted into Q and similarly X_S presents a fraction of the diazotized sulphanilic acid converted into S.

$$A_1 + B \xrightarrow{k_{1p}} p - R \tag{30}$$

$$A_1 + B \xrightarrow{k_{1o}} o - R \tag{31}$$

$$p - R + B \xrightarrow{k_{2o}} S \tag{32}$$

$$o - R + B \xrightarrow{k_{2p}} S \tag{33}$$

$$A_2 + B \xrightarrow{k_3} Q \tag{34}$$

$$X_S = 2c_S \big/ \left(c_{oR} + c_{pR} + c_Q + 2c_S \right) \tag{35}$$

$$X_Q = c_Q \big/ \left(c_{oR} + c_{pR} + c_Q + 2c_S \right) \tag{36}$$

where A_1 denotes 1-naphthol, A_2 is 2-naphthol, B represents diazotized sulphanilic acid, o-R and p-R are two mono-substituted dyes (ortho and para), S represents a bisazo dye and Q is a single monoazo dye.

Effects of energy dissipation ε and the volume ratio of reactants α on X_S and X_Q as predicted by the E-model are presented in Fig. 8. To this end Eqs. (25) and (26) are applied together with the kinetics describing rates of reactions represented by Eqs. (30) to (36) (Bałdyga and Bourne, 1999; Bourne et al., 1992). Notice that Fig. 8 has been constructed in a similar way as Fig. 7, just for different kinetics and without replacing the rate of energy dissipation by equivalent frequency of impeller. One can see that for high values of the rate of energy dissipation one should apply rather X_Q than X_S to interpret effects of mixing due to higher sensitivity to the rate of energy dissipation.

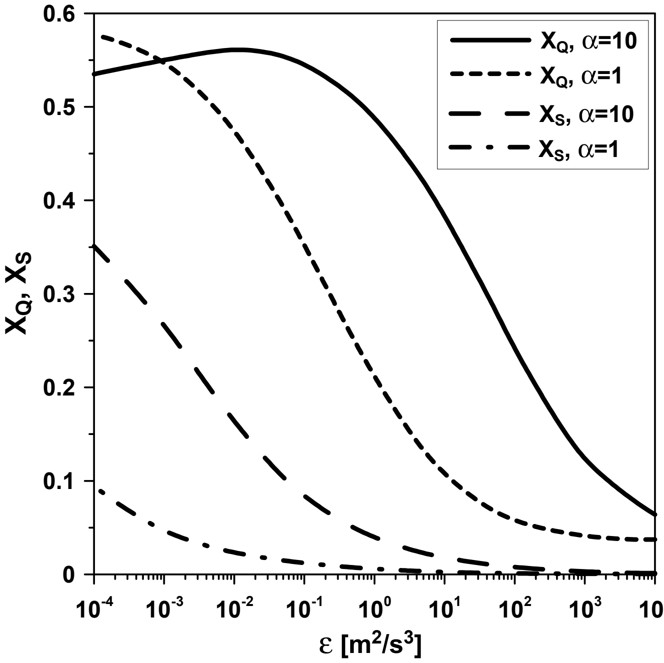

Fig. 8. Predicted effect of the energy dissipation rate, ε, on product distributions X_Q and X_S:
for $\alpha = Q_A/Q_B = 1$, $c_{A1,0} = 1.2$ mol/m^3, $c_{A2,0} = 2.4$ mol/m^3, $c_{B0} = 1$ mol/m^3,
for $\alpha = Q_A/Q_B = 10$, $c_{A1,0} = 1.2$ mol/m^3, $c_{A2,0} = 2.4$ mol/m^3, $c_{B0} = 10$ mol/m^3

As shown in Fig. 9, Fig. 8 can be used in what follows as a calibration curve, which based on experimentally determined X_Q values gives the smallest, “theoretical” values of the rate of energy dissipation necessary to obtain experimental X_Q, that can be later compared with the energy really used in the experiment.

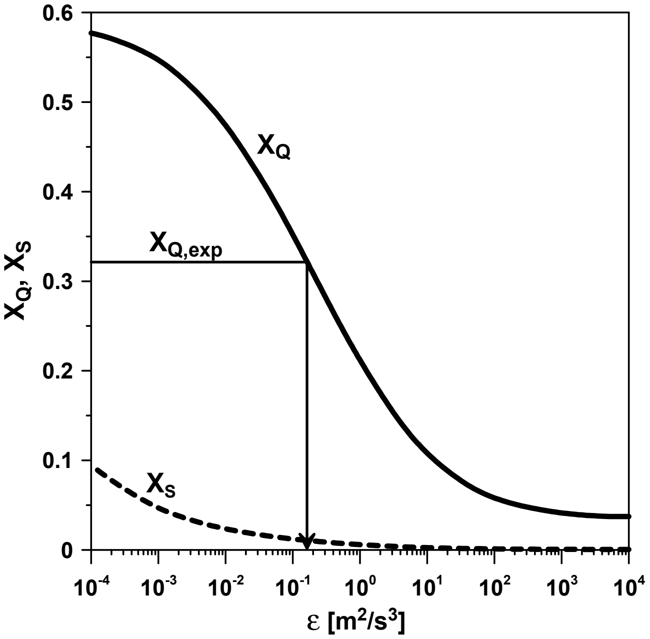

Fig. 9. Application of calibration curve

Applying this procedure to experimental data presented by (Jasińska et al., 2013a) for homogeneous mixing in a Silverson 150/250 MS rotor-stator mixer one obtains results shown in Fig. 10. The efficiency is calculated from Eq. (27) with the energy dissipation ε_T resulting from both, agitation and flow $\varepsilon_T = \varepsilon_{N,Q}$. In this paper the rate of energy dissipation $\varepsilon_{N,Q}$ is calculated from the power number correlation (Jasińska et al., 2013a) and the rotor swept volume V_H.

$$\mathrm{N_P}=6.0\cdot \mathrm{N_Q}+0.24 \tag{37}$$

where

$$\mathrm{N_Q} = Q/\left(ND^3\right) \tag{38}$$

represents dimensionless flow rate.

The average rate of energy dissipation is thus given by Eq. (39)

$$\varepsilon_{N,Q} = \mathrm{N_P}\, N^3 D^5 / V_H \tag{39}$$

One can see in Fig. 10 that as expected with increasing rotor speed the product distribution X_Q decreases, so mixing becomes faster. However, it becomes less efficient with increasing Re as well, in agreement with the theory, Eq. (24) and Fig. 6.

The same procedure has been applied to other systems, including microreactors (Malecha et al., 2009). It is interesting to compare results obtained for the rotor-stator device presented in Fig. 10 with similar results obtained in the serpentine microreactor are shown in Fig. 11.

The theoretical rate of energy dissipation was identified using the procedure presented in Figure 9 and the overall rate of energy dissipation was recalculated from measured pressure drop and flow rate, $\varepsilon_{\Delta P} = Q\Delta P/\left(\rho V_R\right)$. One can see from Figure 11 that in this case efficiency of mixing increases with increasing the Reynolds number. This happens because of destabilization of the laminar flow; at small Re number molecular diffusion controls mixing and energy is just used to move the fluid parallel to reactor walls. In a simple linear stable laminar shear flow the shearing motion will stretch and rotate fluid elements, with consequences explained earlier. At higher Re numbers the flow is destabilised and faster mixing is induced by flow instability. Lamellar structures are first formed by unstable flow, then fluid deformation accelerates molecular diffusion and this effect increases with increasing Re. Figures 10 and 11 show that measured effects of the Reynolds number on mixing efficiency can help to identify mechanism of mixing.

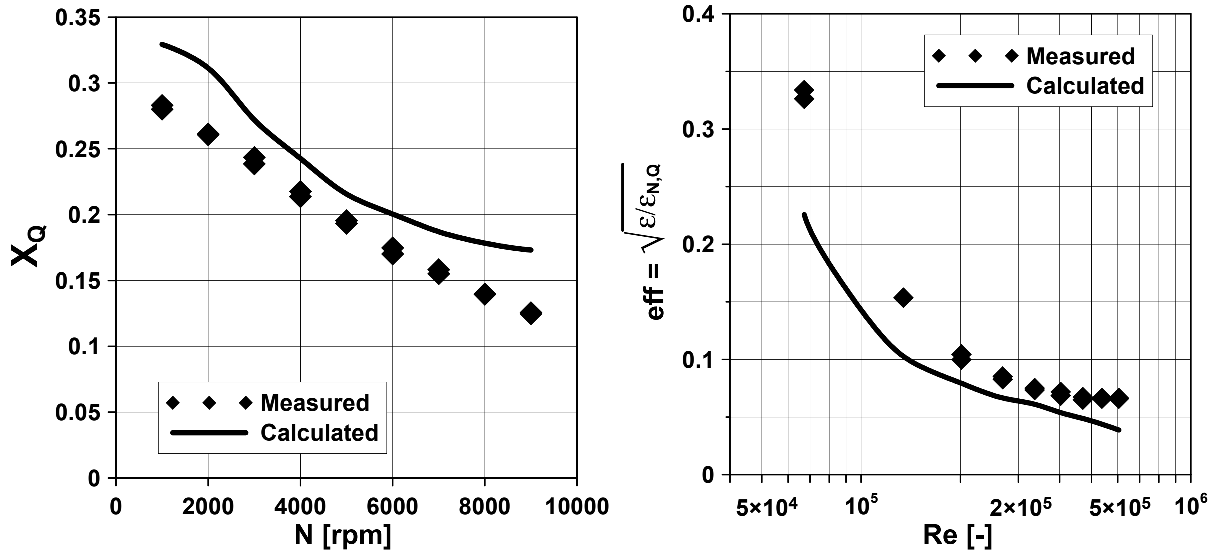

Fig. 10. Dependences of the product distribution X_Q on the rotor speed and efficiency of mixing ***eff*** on the Reynolds number, Re

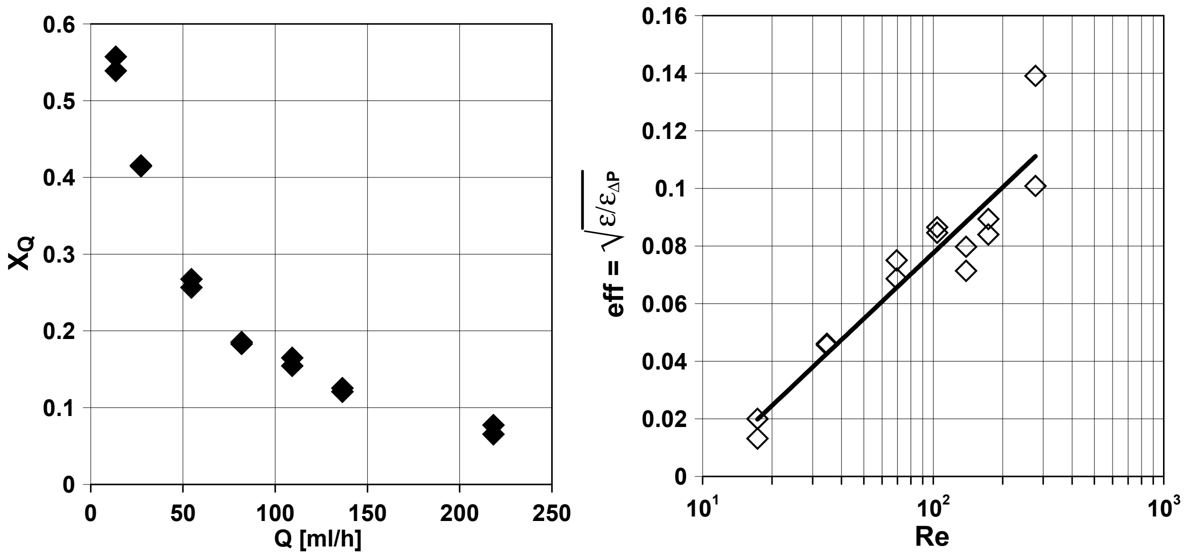

Fig. 11. Dependences of the measured product distribution X_Q on the flow rate and efficiency of mixing **eff** on the Reynolds number, *Re* (based on Malecha et al., 2009)

4. MASS TRANSFER EFFICIENCY IN LIQUID-LIQUID SYSTEMS

Equations (20), (23) and (24) can be interpreted as the ratio of two time constants with the minimum possible time constant in the numerator and the real one in the denominator. Theoretical interpretation of efficiency of the mass transfer in liquid-liquid systems can be constructed in a similar way. The time constant for mass transfer can be defined as

$$\tau_D = \frac{1}{K_L a} \tag{40}$$

where $K_L a$ represents the volumetric mass transfer coefficient, and

$$K_L = \left(\frac{1}{k_{Ld} \cdot P} + \frac{1}{k_{Lc}} \right)^{-1} \tag{41}$$

with k_{Ld} and k_{Lc} being mass transfer coefficients in the dispersed and continuous phase respectively and P is the equilibrium distribution coefficient between phases.

Then the energetic efficiency can be defined by

$$eff = \frac{\tau_{D,min}}{\tau_D} \tag{42}$$

For low solubility of the solute in the continuous phase one has $P >> 1$ and then $K_L \cong k_{Lc}$. This happens when an organic solute is dissolved in the organic dispersed phase and the aqueous solution represents the continuous phase as considered by Jasińska et al., (2013b).

Two aspects of the efficiency can be considered based on definition, Eq. (42): the first one is related to efficiency of drop breakage, the second one to efficiency of mass transfer.

Similarly as the E-model was chosen as a reference model for mixing in homogeneous systems, one can choose a reliable reference model for mass transfer. In this paper the value of $k_{Lc}a$ will be calculated using the model of Favelukis and Levrenteva (2013), $k_{Lc} = k_{FL}$, which includes effects of drop deformation to the shape of prolate ellipsoid

$$k_{FL} a_{drop} = 4\pi R_{eq} D_i \sqrt{\frac{3}{2\pi(1+K))}} \left[1 - \frac{4(4+31K)Y}{315(1+K)} \mathrm{N}_{\mathrm{Ca}} \right] \mathrm{Pe}^{1/2} \tag{43}$$

where $Y = (19K+16)/(16K+16)$. The capillary number and the Péclet number are defined using the equivalent radius, i.e. the radius of a sphere of equal volume to that of the deformed drop $R = R_{eq} = d_{eq}/2$. Using $k_{FL} a_{drop}$ and the population balance to calculate the interfacial area per unit volume a, $a = 6\varphi a_{drop} / \left(\pi d_{eq}^3 \right)$, one can determine $k_{Lc} a = k_{FL} a$ and related time constant τ_D.

Efficiency of drop breakage can be expressed by effect of drop size on the time constants for mass transfer, τ_D. The time constant $\tau_{D,min}$ in Eq. (42) can be interpreted as the shortest mass transfer time calculated from the model of Favelukis and Levrenteva (2003) using the maximum stable drop size d_d, $R_{eq} = d_d/2$. The maximum stable drop size d_d can be estimated including intermittency effects using an equation given by Bałdyga and Podgórska (1998).

$$d_d = C_x^{1.54} L \left(\frac{\sigma}{\rho_c \varepsilon^{2/3} L^{5/3}} \right)^{0.93} \tag{44}$$

where L is the integral scale of turbulence, $C_x = 0.23$, and the rate of energy dissipation ε applied in Equations (43) and (44) represent the values really used in experiments. This gives

$$\tau_{D,min} = \frac{\pi d_d^3}{6\varphi \left(k_{FL} a_{drop} \right)_{R_{eq}=d_d/2}} \tag{45}$$

where φ represents the mean value of the volume fraction of the organic, dispersed phase. Similar calculations but performed for $R_{eq} = d_{32}/2$ give the time constant τ_D.

$$\tau_D = \frac{\pi d_{32}^3}{6\varphi\left(k_{FL} a_{drop}\right)_{R_{eq}=d_{32}/2}} \tag{46}$$

Then efficiency of development of the interfacial area reads

$$eff_a = \left(\frac{d_d}{d_{32}}\right)^3 \cdot \frac{\left(k_{FL} a_{drop}\right)_{R_{eq}=d_{32}/2}}{\left(k_{FL} a_{drop}\right)_{R_{eq}=d_d/2}} = \frac{\tau_{D,\min}}{\tau_D} \tag{47}$$

The efficiency as given by Eq.(47) has been defined using the reference model represented by Eq. (44), similarly as the E-model has been used to determine efficiency of micromixing. As mentioned before, the E-model has been used as an agent necessary to identify the absolute efficiency as defined by Eqs. (7) and (8). One can define such absolute efficiency also in the case of development of the interfacial area, a.

The work dw done to expand the interfacial area dA can be presented as $dw = \sigma dA$. This leads directly to

$$\frac{da}{dt} = \frac{\rho\varepsilon'}{\sigma} \tag{48}$$

where ε' represents this part of mechanical energy that is used to increase an interfacial area.

For a continuous flow system with the mean residence time $\overline{t}$ one has then

$$\Delta a = \frac{\rho\varepsilon'\overline{t}}{\sigma} \tag{49}$$

where Δa is an increase of the interfacial area between an inlet and an outlet of the system. Based on measured Δa one can calculate ε' and express efficiency of development of interfacial area as

$$eff'_a = \frac{\varepsilon'}{\overline{\varepsilon}} \tag{50}$$

where $\overline{\varepsilon}$ is the average rate of energy dissipation in the system. However, the values of efficiency resulting from Eq.(50) are extremely low, which means that the application of Eq. (50) can be cumbersome.

Consider now efficiency of mass transfer for given drop size distribution. On can use directly Eq.(43) as the reference one and calculate efficiency of mass transfer either based on experimental data or applying any model of mass transfer, specific for given process conditions.

$$eff_{k_L} = \frac{k_L}{k_{FL}\left(a_{drop}/a_{eq}\right)} \tag{51}$$

where a_{eq} is the surface of a sphere with identical volume as the considered droplet.

As an example let us consider mass transfer of benzoic acid from toluene drops to aqueous solution in dense emulsion of volume fraction $\varphi = 0.75$ processed in a rotor-stator mixer as described by Bałdyga et al. (2016).

2D numerical CFD simulations of the process in the in-line rotor-stator device for drops whose diameter falls within the inertial subrange of turbulence were carried out using the standard k-ε model of Fluent-Ansys and the multiple reference frame method (MRFR) linked to the population balance equation. Simulations were performed to predict the hydrodynamic properties of the flow, the size distribution of droplets forming emulsion, its viscosity and volumetric mass transfer coefficient. An unstructured mesh consisting of 178 845 cells and 180 309 nodes was applied. Gambit was used including application of its smoothing procedures to redistribute nodes, and the resulting drop sizes were mesh independent. Simulations were performed using a computer cluster consisting of 17 single-processor PCs and 7 double-processor nodes connected by a local network.

Figure 12 shows distribution of the time scale τ_D as calculated from Eqs. (43) and (46). Based on Eq. (47) one can calculate the eff_a efficiency: $eff_a \approx 0.15$ at $N = 1000$ rpm and $eff_a = 0.058$ at $N = 11\ 000$ rpm.

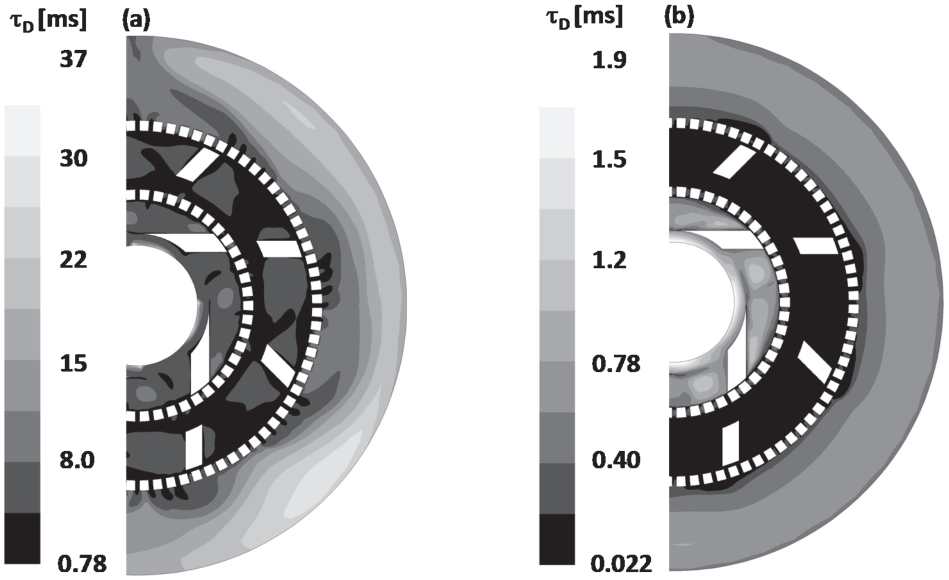

Fig. 12. The time constant for mass transfer of benzoic acid from toluene drops to aqueous solution emulsion for $\varphi = 0.75$ $\eta_c = 0.91$ mPas , $\eta_d = 0.587$ mPas, Q_m=600 kg/h (a) N=1000 rpm, (b) N=11000 rpm

To illustrate how one can find eff_{k_L} let us consider effects of presence of surface-active contaminants in the system. Such impurities can eliminate internal circulation, thereby significantly reducing mass transfer rate. Assuming that droplets behave as hard spheres because of no internal circulation, one can use the model of Batchelor (1980) for k_L.

$$\mathrm{Sh}=\frac{k_L R}{D_i}=0.55\mathrm{Pe}^{1/3}=0.55\left(\frac{R^2\varepsilon^{1/2}}{D_i\nu^{1/2}}\right)^{1/3} \tag{52}$$

with $R = R_{32} = d_{32}/2$ and the Sauter mean diameter taken in the considered example from CFD results. Based on Eq.(48) we get for the mass transfer efficiency $eff_{k_L} \approx 0.24$ at $N = 1000$ rpm and $eff_{k_L} = 0.19$ at $N = 11\ 000$ rpm.

The general efficiency including both aspects of the process i.e. drop breakage and mass transfer, takes the values $eff = eff_a \cdot eff_{k_L} = 0.036$ at N=1000 rpm and $eff = eff_a \cdot eff_{k_L} = 0.011$ at $N = 10\ 000$ rpm.

To check if turbulence is intensive enough to use the models developed for turbulent flow, the Reynolds number $\mathrm{Re}_L = \dfrac{u'L}{\nu}$ based on the scale of large, energy containing eddies is plotted in Fig. 13.

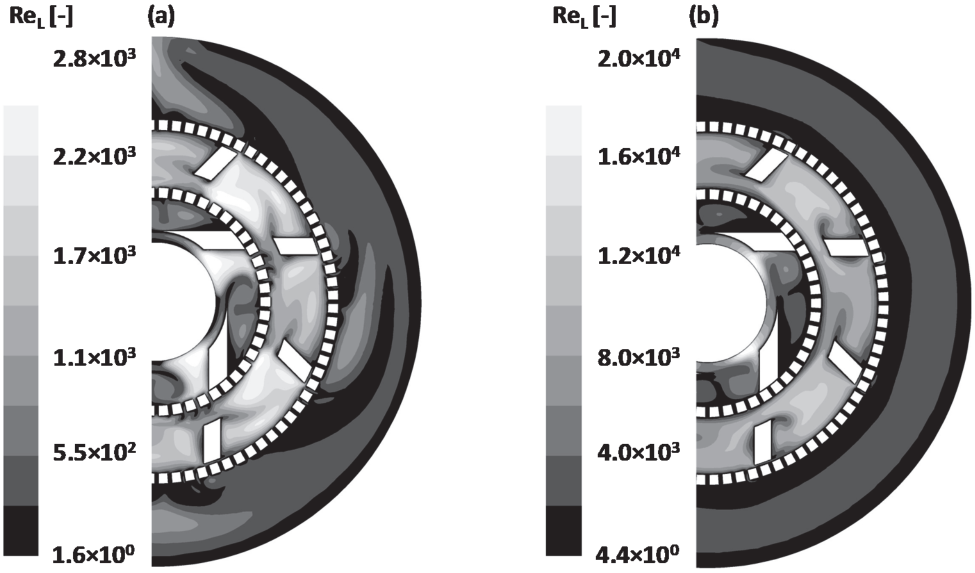

Fig. 13. The Reynolds number for emulsion flow for $\varphi = 0.75$, $\eta_c = 0.91$ mPas, $\eta_d = 0.587$ mPas, $Q_m = 600$ kg/h at $N = 1000$ rpm, (b) at $N = 11000$ rpm

Figure 13 shows that turbulence is well developed in most of the rotor-stator inside, especially in the rotor swept region, so the assumption on turbulent flow in the mixer is justified.

5. CONCLUSIONS

A new definition of efficiency of mixing in homogeneous systems is proposed, discussed and applied to interpret experimental data. The new definition represents modification and generalization to turbulent flows of a definition proposed originally by Ottino (1980). It has been shown that similar methods can be applied to investigate efficiency of drop breakage and mass transfer in two-phase liquid-liquid systems. Results show that the value of efficiency of mixing is not high in popular types of reactors and mixers, but can be used to compare different methods of contacting reactants and identify the mechanism of mixing.

The authors acknowledge the financial support from Polish National Science Centre (Grant agreement number: DEC-2013/11/B/ST8/00258).

SYMBOLS

a	interfacial area per unit volume of emulsion, m^{-1}
a_{drop}	drop area, m^2
a_v	intermaterial area, m^{-1}
c	concentration, mol m^{-3}
c_i	concentration of component "i", mol m^{-3}
D	rotor diameter, m
$\overline{D}$	deformation tensor, s^{-1}
D_i	molecular diffusivity of component "i", m^2 s^{-1}
d	drop diameter, m
d_d	maximum stable drop size, m
d_{32}	Sauter diameter, m

E	engulfment parameter, s^{-1}
eff	efficiency
I_{ij}	concentration moments, m^2
I_D	concentration moment for pure diffusion, m^2
I_{SD}	concentration moment for diffusion and deformation, m^2
K	viscosity ratio, $K=\eta_d/\eta_c$
K_L	overall mass transfer coefficient, m s
k_2	rate constant of the 2nd order chemical reaction, $m^3mol^{-1}s^{-1}$
k_L	mass transfer coefficient, m s^{-1}
k_{Lc}	mass transfer coefficient in continuous phase, m s^{-1}
k_{Ld}	mass transfer coefficient in dispersed phase, m s^{-1}
L	integral scale of turbulence, m
N	rotor speed, rps
N_{Ca}	capillary number, $\eta_c\dot{\gamma}d/\sigma$; for Eq.(43) $\eta_c\dot{\gamma}R_{eq}/\sigma$
N_P	power number, $P/(\rho N^3D^5)$
N_Q	dimensionless pumping capacity, $Q/(ND^3)$
P	power, W
P	equilibrium distribution coefficient
Pe	Péclet number, $R^2\dot{\gamma}D_i^{-1}$
Re	Reynolds number
Q	volumetric flow rate, m^3s^{-1}
Q_m	mass flow rate, kgs^{-1}
R_{eq}	equivalent radius, m
Sc	Schmidt number, νD_i^{-1}
Sh	Sherwood number, $k_LRD_i^{-1}$
S	skewness factor
s_{ij}	deformation tensor, s^{-1}
t	time, s
$\vec{u}$	velocity vector, ms^{-1}
u_i	component of velocity vector, ms^{-1}
u'	root-mean-square velocity component , ms^{-1}
V_H	rotor swept volume, m^3
X_S, X_Q	product distributions of complex reactions
Y	deformation parameter in Eq. (43), $Y=(19K+16)/(16K+16)$

Greek symbols

α	volume ratio
β	coefficient in definition of effective shear rate
ε	rate of energy dissipation, m^2 s^{-3}
δ_0	initial slab thickness, m
$\dot{\gamma}$	rate of shear, rate of elongation, s^{-1}
$\dot{\gamma}'$	rate of shear, s^{-1}
η_d	viscosity of dispersed phase, Pa s
η_c	viscosity of continues phase, Pa s
Λ_c	integral scale for turbulent fluctuations of concentration, m
λ	striation thickness, m
λ_B	Batchelor microscale, m
λ_K	Kolmogorov microscale, m
ν	kinematic viscosity, m^2 s^{-1}

$\vec{\xi}$	position vector in a moving frame, m
ρ_d	density of dispersed phase, kg m^{-3}
ρ_c	density of continuous phase, kg m^{-3}
σ	[N m^{-1}] interfacial tension
τ_D	time constant for mass transfer, N m^{-1}
τ_M	time constant for mixing, s
φ	volume fraction of dispersed phase
Ω_{ij}	rotation tensor, s^{-1}
$\vec{\omega}$	vorticity vector, s^{-1}

REFERENCES

Bałdyga J., Bourne J.R., 1986. Principles of micromixing, Chapter 6 In: Cheremisinoff N.P. (Ed.), *Encyclopedia of Fluid Mechanics*, Gulf Publishing Company, Houston, Texas, 1986.

Bałdyga, J., Jasińska M., Kowalski A.J., 2016. Effect of rheology of dense emulsions on the flow structure in agitated systems. *Chem. Eng. Res. Des.*, 108, 3-12. DOI:10.1016/j.cherd.2015.11.026.

Bałdyga J., Podgórska W., 1998. Drop break-up in intermittent turbulence: Maximum stable and transient sizes of drops. *The Canadian J. Chem. Eng.*, 76, 456-470. DOI: 10.1002/cjce.5450760316.

Bałdyga J., Bourne J.R., 1999. *Turbulent Mixing and Chemical Reactions.* Wiley, Chichester.

Batchelor G.K., 1980. Mass transfer from small particles suspended in turbulent flow. *J. Fluid. Mech.*, 98, 609-623. DOI: 10.1017/S0022112080000304.

Bourne J.R., Kut O.M., Lenzner J., 1992. An Improved reaction system to investigate micromixing in high-intensity mixers. *Ind. Eng. Chem. Res.*, 31, 949-958. DOI: 10.1021/ie00003a042.

Bourne J.R., 2003. Mixing and the selectivity of chemical reactions. *Org. Proc. Res. Dev.*, 7, 471-508. DOI: 10.1021/op020074q.

Corrsin S., 1964. Further generalizations of Onsager's cascade model for turbulent spectra. *Phys. Fluids*, 7, 1156-1159. DOI: 10.1063/1.1711355.

Falk L., Commenge J.-M., 2010. Performance comparison of micromixers. *Chem. Eng. Sci.*, 65, 405 -411. DOI: 10.1016/j.ces.2009.05.045.

Favelukis M., Lavrenteva O. M., 2013. Mass transfer around prolate spheroidal drops in an extensional flow. *Can. J. Chem. Eng.*, 91, 1190-1199. DOI: 10.1002/cjce.21727.

Jasińska M., Bałdyga J., Cooke M., Kowalski A.J., 2013a. Application of test reactions to study micromixing in the rotor-stator mixer (test reactions for rotor-stator mixer). *Appl. Therm. Eng.*, 57, 172-179. DOI: 10.1016/j.applthermaleng.2012.06.036.

Jasińska M., Bałdyga J., Cooke M., Kowalski A.J., 2013b. Investigations of mass transfer with chemical reactions in two-phase liquid-liquid systems. *Chem. Eng. Res. Des.*, 91, 2169-2178. DOI: 10.1016/j.cherd.2013.05.010.

Levenspiel O., *Chemical Reaction Engineering*. Wiley, New York 1972.

Malecha K., Golonka L.J., Bałdyga J., Jasińska M., Sobieszuk P., 2009. Serpentine microfluidic mixer made in LTCC. *Sens. Actuators B: Chem.*, 143, 400-413. DOI: 10.1016/j.snb2009.08.010.

Ottino J.M., 1980. An efficiency for batch mixing of viscous fluids. *Chem. Eng. Sci.*, 35, 1454 -1457. DOI: 10.1016/0009-2509(80)85142-6.

Rożeń A., 2008. *Micromixing of fluids differing in viscosity in laminar flow systems*. Oficyna Wydawnicza Politechniki Warszawskiej, Warsaw.

Tennekes H., Lumley J.L., 1972. *A first course in turbulence.* MIT Press, Cambridge, MA, USA.

Villermaux, J., 1986. Micromixing phenomena in stirred reactors. Chapter 27 In: *Encyclopedia of Fluid Mech.* Gulf Publishing Company, Houston, TX.

Received 3 December 2016
Received in revised form 27 August 2017
Accepted 28 August 2017

DE GRUYTER OPEN
Chemical and Process Engineering 2017, 38 (1), 97-110
DOI: 10.1515/cpe-2017-0008

LIQUID-LIQUID EXTRACTION IN SYSTEMS CONTAINING BUTANOL AND IONIC LIQUIDS – A REVIEW

Artur Kubiczek*[1], Władysław Kamiński[2]

[1]Lodz University of Technology, Faculty of Process and Environmental Engineering, Department of Molecular Engineering, 90-924 Łódź, Wólczańska 213, Poland

[2] Lodz University of Technology, Faculty of Process and Environmental Engineering, Department of Process Thermodynamics, 90-924 Łódź, Wólczańska 213, Poland

Room-temperature ionic liquids (RTILs) are a moderately new class of liquid substances that are characterized by a great variety of possible anion-cation combinations giving each of them different properties. For this reason, they have been termed as designer solvents and, as such, they are particularly promising for liquid-liquid extraction, which has been quite intensely studied over the last decade. This paper concentrates on the recent liquid-liquid extraction studies involving ionic liquids, yet focusing strictly on the separation of *n*-butanol from model aqueous solutions. Such research is undertaken mainly with the intention of facilitating biological butanol production, which is usually carried out through the ABE fermentation process. So far, various sorts of RTILs have been tested for this purpose while mostly ternary liquid-liquid systems have been investigated. The industrial design of liquid-liquid extraction requires prior knowledge of the state of thermodynamic equilibrium and its relation to the process parameters. Such knowledge can be obtained by performing a series of extraction experiments and employing a certain mathematical model to approximate the equilibrium. There are at least a few models available but this paper concentrates primarily on the NRTL equation, which has proven to be one of the most accurate tools for correlating experimental equilibrium data. Thus, all the presented studies have been selected based on the accepted modeling method. The reader is also shown how the NRTL equation can be used to model liquid-liquid systems containing more than three components as it has been the authors' recent area of expertise.

Keywords: extraction, ionic liquids, butanol, liquid-liquid equilibrium, NRTL equation

1. INTRODUCTION

Ionic liquids (ILs) are liquid organic salts with melting points below 373 K (Brennecke and Maginn, 2001). However, a separate group termed as room-temperature ionic liquids (RTILs), liquid at room temperature, can also be distinguished. Although the first RTIL – ethylammonium nitrate – was synthesized already in 1914 (Earle and Seddon, 2000), the intensive investigation of ionic liquids started only in the 1990s. An important breakthrough came with the discovery of chloroaluminate ionic liquids based on the ethylmethylimidazolium cation (Wilkes and Zaworotko, 1992).

One of the possible and interesting applications of ILs is the liquid-liquid extraction of *n*-butanol from aqueous media. *n*-Butanol, nowadays produced chiefly by the petrochemical industry, can also be synthesized biologically in the process of Acetone-Butanol-Ethanol (ABE) fermentation (Ezeji et al., 2007; García et al., 2011; Qureshi and Blaschek, 2006). This traditional method was exploited at the

---

*Corresponding author, e-mail: artur.kubiczek@p.lodz.pl

beginning of the 20th century by the military industry, but almost completely abandoned in the 1950s and early 1960s (Dürre, 2007; Jones and Woods, 1986; Lütke-Eversloh and Bahl, 2011).

n-Butanol has numerous commercial uses; moreover, it can be successfully blended with both gasoline and diesel fuel. Because of convenient combustion characteristics it was even suggested that butanol be used directly in the existing engines (García et al., 2011; Kumar and Gayen, 2011; Lee et al., 2008; Ramey, 2007; Siwale et al., 2013). In light of the Stanford Research Institute statistical data, in 2010 the global consumption of petrochemical *n*-butanol amounted to ca. 3 million tons along with a production capacity exceeding 3.5 million tons. The world's two largest *n*-butanol manufacturers are now BASF and Dow Chemical Company. The top ten manufacturers, including companies, such as Oxea Group, Formosa Plastics Group and Eastman Chemical Company, provide about 78% of the world's production capacity. The three most developed regions in terms of production ability are Asia, North America and Western Europe (38, 31 and 18%, respectively). At the same time, Asia is the biggest consumer of butanol being responsible for 53% of the world's total consumption. North America and Western Europe use up to 22 and 19% of *n*-butanol respectively. In view of the SRI predictions, further growth of *n*-butanol demand and production is expected up to the year 2020 (Liu and Xue, 2012).

Currently, China is an undisputed leader in commercial ABE fermentation. Between 2000 and 2006, China imported over 50% of butanol required to satisfy growing domestic needs. Thus, there was a niche to be filled by an alternative technology. Up to the end of 2008, over a dozen Chinese fermentation plants had been built or retrofitted for the purpose of restarting the ABE production, offering a total capacity exceeding 300,000 tons per year, but with further plans to enhance the solvent production to about 1,000,000 tons per year within the next few years (Ni and Sun, 2009). Similar initiatives are also being undertaken in other countries such as Brazil and the United States (Huang et al., 2014; Natalense and Zouain, 2013).

At this point, ABE fermentation is less economical than petrochemical synthesis. The achievable total concentration of solvents in conventional batch reactors fluctuates around 20 g/dm^3 (depending on the bacterial strain and substrate type), of which butanol is barely about 13 g/dm^3. For this reason, recovery of ABE has to be particularly efficient. Theoretically, a few unit operations are capable of separating fermentation products from the broth. However, they are not equally encouraging in terms of energy demand and costs. As reported by several authors, liquid-liquid extraction is considered to be one of the most promising methods (Abdahagh et al., 2014; Ha et al., 2010; Huang et al., 2014; Kraemer et al., 2011; Stoffers et al., 2013; Vane, 2008).

2. SOLVENTS INVESTIGATED FOR THE RECOVERY OF BUTANOL

Initially, the majority of studies devoted to the recovery of *n*-butanol via liquid-liquid extraction dealt with batch fermentation (*in situ* extraction), thus the appropriate extracting agents were selected based on their non-toxicity towards the fermentation bacteria. Consequently, two main groups of extracting agents were distinguished, i.e. alkanes and alcohols. As it transpired, alcohols usually provided high distribution ratios of butanol ($D > 5$) and moderate selectivities. On the other hand, alkanes, although highly selective, displayed rather low affinity for butanol ($D < 0.5$) (Kraemer et al., 2011; Matsumura et al., 1988).

The benchmark solvent for butanol is oleyl alcohol, whose density (0.845–0.855 g/cm^3) is favorable for further separation of the extract from the raffinate. Promising results of extracting butanol with oleyl alcohol were presented already in 1985 (Davison and Thompson, 1993; Ishii et al., 1985; Roffler et al., 1988) and the reported distribution ratios fell in the range between 3.0 and 4.1. However, the main fault of oleyl alcohol is its low separation ability with regard to acetone and ethanol (0.45 and 0.22 according to Ishii et al., 1985), which, in the case of extractive ABE fermentation, may lead to high solvent demand in order to prevent from excessive accumulation of acetone in the broth (Kraemer et al., 2011).

The other solvents that have been tested with the intention of recovering biobutanol include substances such as glyceryl tributyrate, methylated crude palm oil and other modified plant oils, biodiesel, gasoline, decyl alcohol, mesitylene, surfactants and ionic liquids (Adhami et al., 2009; Evans and Wang, 1988; Huang et al., 2014; Ishizaki et al., 1999; Kraemer et al., 2011). Decanol and mesitylene provide satisfying separation performance but they are toxic and thus capable of being used only in *ex situ* extraction. Kraemer et al. (2011) simulated integrated extraction-distillation of butanol assuming either mesitylene or oleyl alcohol as the extracting agent. The estimated energy demand was 5.7 MJ/kg$_{\text{BuOH}}$ in the case of mesitylene and 15 MJ/kg$_{\text{BuOH}}$ in the case of oleyl alcohol. When traditional distillation was simulated instead, the energy demand increased to 19 MJ/kg$_{\text{BuOH}}$.

3. EXTRACTION OF N-BUTANOL WITH IONIC LIQUIDS

Over the last decade, liquid-liquid extraction employing room-temperature ionic liquids has become a very popular topic. Among the advantages of RTILs the following are most often mentioned: negligible vapor pressure (Earle and Seddon, 2000; Ji et al., 2012; Sowmiah et al., 2009), thermal stability (Kosmulski et al., 2004), wide liquidus regions (Brennecke and Maginn, 2001; Johnson, 2007), ability to dissolve both organic and inorganic compounds (Simoni et al., 2010) as well as hydrophobicity or hydrophilicity (Klähn et al., 2010).

The potential ability of ionic liquids to extract *n*-butanol from aqueous solutions has also been intensely studied. The properties of ionic liquids determining their separation performance towards butanol vary considerably from one to another. Depending on the anion and the cation structures, the achievable distribution ratios range from a few to several hundred while selectivities vary from a few tens to over a thousand (Domańska and Królikowski, 2012; Garcia-Chavez et al., 2012; Ha et al., 2010; Huang et al., 2014; Marciniak et al., 2016; Rabari and Banerjee, 2013; Simoni et al., 2010; Stoffers and Górak, 2013).

Currently, high prices of ionic liquids are the main obstacle to their application in the extraction process. One should also keep in mind that additional energy is required to regenerate the used-up solvent and, in the case of ABE fermentation, separate the mixture of the extracted substances, which is most easily done through distillation. Butanol is a dominant product of fermentation and, depending on the type of fermenting bacteria, its amount in the broth constitutes between 60 and 80% of the total ABE product (Ezeji et al., 2004; Green, 2011; Qureshi and Blaschek, 2001). Acetone is the second most important component of the broth while the fraction of ethanol in total ABE usually does not exceed 10%.

4. SELECTED ASPECTS OF LIQUID-LIQUID EQUILIBRIUM IN SYSTEMS CONTAINING N-BUTANOL, WATER AND IONIC LIQUID

In order to design a commercial extraction process, it is necessary to know the dependence of thermodynamic equilibrium in the mixture of the feed solution and the extracting agent on its initial composition and physical parameters such as temperature and pressure. This knowledge allows further simulation of multi-stage extraction and, consequently, integrated extraction-distillation. To approximate the equilibrium, one of the available mathematical models can be employed. Due to proven accuracy in approximating liquid-liquid equilibria, the most popular equations are NRTL and UNIQUAC (based on the 'local composition' concept), which enable estimation of activity coefficients of the respective components in both liquid phases. Often, the NRTL equation provides more precise results as well as enables modeling liquid-liquid systems containing both water and uncommon organic substances such as ionic liquids (Cheruku and Banerjee, 2012; Domańska and Lukoshko, 2015; Haghnazarloo et al., 2013; Haghtalab and Paraj, 2012; Królikowski, 2016; Liu et al., 2016; Mohsen-Nia et al., 2008; Rabari and Banerjee, 2013; Zhang et al., 2010). The crucial question in applying the NRTL equation is the determination of its binary parameters related to the interactions between the respective constituents of the system. Thus, experimental data, describing the equilibrium in a model system, are required for further considerations.

Domańska and Królikowski (2012) studied the extraction of *n*-butanol from aqueous solutions at 308.15K using three tetracyanoborate-based ionic liquids, i.e. 1-hexyl-3-methylimidazolium tetracyanoborate [hmim][TCB], 1-decyl-3-methylimidazolium tetracyanoborate [dmim][TCB], and trihexyltetradecylphosphonium tetracyanoborate [$P_{14,6,6,6}$][TCB], and obtained very encouraging results. The authors measured the compositions of both liquid phases using gas chromatography. They used mole fractions to calculate distribution ratios of butanol and selectivities, and correlated the experimental LLE data by means of the NRTL equation. In order to estimate the unknown binary parameters, they used an objective function minimizing the squared differences between the experimental and calculated concentrations. The approximation proved very accurate. The root-mean-square deviation (*RMSD*) values calculated for each of the ternary systems were equal to 0.0024, 0.0022 and 0.0034, respectively.

All three ionic liquids displayed low solubility in water, [$P_{14,6,6,6}$][TCB] being the least soluble due to its long alkyl chain, while [dmim][TCB] and [$P_{14,6,6,6}$][TCB] provided the best separation performance. Density of [$P_{14,6,6,6}$][TCB], equal to 0.885 g/cm^3 at 308.15 K, is the most favorable for the extraction from aqueous solutions. Densities of [hmim][TCB] and [dmim][TCB] at the same temperature are 0.983 and 0.956 g/cm^3. Table 1 presents the minimum and maximum values of the experimental distribution ratios and selectivities together with the lowest and the highest measured solubilities of water in the organic phase and ionic liquid in the aqueous phase.

Table 1. Minimum and maximum experimental values of the distribution ratios (*D*) and selectivities (*S*) towards butanol in the systems [hmim][TCB] or [dmim][TCB] or [$P_{14,6,6,6}$][TCB] + *n*-butanol + water at 308.15 K and mutual solubility of the ionic liquids and water (Domańska and Królikowski, 2012)

Ionic liquid		Distribution ratio D_{BuOH}	Selectivity S_{BuOH}	Mole fraction	
				H_2O in the organic phase	IL in the aqueous phase
[hmim][TCB]	min	25.6	45.9	0.502	0.000
	max	33.5	66.5	0.560	0.002
[dmim][TCB]	min	24.0	51.1	0.23	0.00
	max	48.0	137.9	0.46	0.00
[$P_{14,6,6,6}$][TCB]	min	35.6	96.3	0.134	0.000
	max	127.0	903.0	0.364	0.003

Rabari and Banerjee (2013) extracted *n*-butanol from water using trihexyl(tetradecyl)phosphonium bis(2,4,4-trimethylpentyl)phosphinate [TDTHP][Phosph]. In the article, they present the experimental data that were used to estimate the NRTL and UNIQUAC parameters. To determine the compositions of both the organic and the aqueous phases, they employed nuclear magnetic resonance spectroscopy (NMR). According to the authors, the investigated ionic liquid practically does not dissolve in water although certain solubility of water in the ionic liquid can be observed. Density of [TDTHP][Phosph], lower than the density of water, is convenient for the separation of butanol from aqueous feeds. The calculated values of the distribution ratio and selectivity as well as mutual solubility of the ionic liquid and water are given in Table 2.

Table 2. Minimum and maximum experimental values of the distribution ratio (*D*) and selectivity (*S*) towards butanol in the system [TDTHP][Phosph] + *n*-butanol + water at. 298.15 K and mutual solubility of the ionic liquid and water (Rabari and Banerjee, 2013)

Ionic liquid		Distribution ratio D_{BuOH}	Selectivity S_{BuOH}	Mole fraction	
				H_2O in the organic phase	IL in the aqueous phase
[TDTHP][Phosph]	min	18.89	80.18	0.1559	0
	max	377.75	2138.16	0.2279	0

The mean *RMSD* values comparing the experimental and predicted concentrations of butanol were equal to 0.002809 and 0.005552 for the NRTL and UNIQUAC equations, respectively. Therefore, better results were obtained with the NRTL equation.

Marciniak et al. (2016) studied phase equilibria in three ternary systems containing *n*-butanol, water and one of the following ionic liquids: 1-butyl-1-methylpiperidinium bis(trifluoromethylsulfonyl)imide [bmPIP][NTf_2], 1-(2-methoxyethyl)-1-methylpiperidinium bis(trifluoromethylsulfonyl)imide [COC_2mPIP][NTf_2] or 1-(2-methoxyethyl)-1-methylpyrrolidinium bis(trifluoromethylsulfonyl)imide [COC_2mPYR][NTf_2] at 298.15K. They measured equilibrium compositions using gas chromatography.

All the ionic liquids tested by the authors displayed low solubility in water; although they provided lower distribution ratios and selectivities than the ionic liquids investigated by Domańska and Królikowski (2012). The calculated root-mean-square errors of approximation (*RMSD*) with the NRTL equation were 0.002, 0.008 and 0.007 for the systems containing [bmPIP][NTf_2], [COC_2mPIP][NTf_2] and [COC_2mPYR][NTf_2], respectively. The minimum and maximum recorded distribution ratios and selectivities as well as mutual solubilities of the ionic liquids and water are gathered in Table 3.

Table 3. Minimum and maximum experimental values of the distribution ratios (*D*) and selectivities (*S*) towards butanol in the systems [bmPIP][NTf_2] or [COC_2PIP][NTf_2] or [COC_2PYR][NTf_2] + *n*-butanol + water at 298.15 K and mutual solubility of the ionic liquids and water (Marciniak et al., 2016)

Ionic liquid		Distribution ratio D_{BuOH}	Selectivity S_{BuOH}	Mole fraction	
				H_2O in the organic phase	IL in the aqueous phase
[bmPIP][NTf_2]	min	14.7	48.2	0.265	0.000
	max	25.7	61.2	0.523	0.001
[COC_2PIP][NTf_2]	min	14.9	37.0	0.352	0.000
	max	26.5	49.8	0.586	0.002
[COC_2PYR][NTf_2]	min	11.6	28.6	0.360	0.000
	max	22.2	55.4	0.597	0.002

As demonstrated by Ha et al. (2010), mutual solubility of the imidazolium-based ionic liquids and water, being a very important factor in the extraction process, increases with temperature. Altogether, the authors studied eleven ionic liquids containing 1-alkyl-3-methylimidazolium cations and four types of anions such as trifluoromethanesulfonate [OTf], hexafluorophosphate [PF_6], bis(trifluoromethylsulfonyl)imide [NTf$_2$] and tetrafluoroborate [BF$_4$]. Table 4 shows mutual solubilities of the ionic liquids and water in binary systems at 298.15K and 323.15K expressed in mass fractions and recalculated to mole fractions for convenient comparison. The significant differences between the mass fraction and the mole fraction are typical for the systems containing ionic liquids, whose molecular masses are usually relatively high. Likewise, distribution ratios and selectivities calculated using mole fractions are commonly about one order of magnitude higher.

Table 4. Mutual solubility of selected 1-alkyl-3-methylimidazolium ionic liquids and water at 298.15K and 323.15K (Ha et al., 2010)

Ionic liquid	*T* [K]	Mass fraction		Mole fraction	
		H_2O in IL	IL in H_2O	H_2O in IL	IL in H_2O
[hmim][PF$_6$]	298.15	0.0269	0.0170	0.3036	0.0011
	323.15	0.0338	0.0221	0.3555	0.0014
[bmim][NTf$_2$]	298.15	0.0175	0.0051	0.2930	0.0002
	323.15	0.0202	0.0114	0.3242	0.0005
[hmim][NTf$_2$]	298.15	0.0147	0.0023	0.2703	0.0001
	323.15	0.0152	0.0047	0.2771	0.0002
[omim][OTf]	298.15	0.2603	0.0109	0.8706	0.0006
	323.15	0.2699	0.0126	0.8760	0.0007
[hmim][BF$_4$]	298.15	0.1793	0.0664	0.7549	0.0050
	323.15	0.1987	0.0687	0.7776	0.0052

According to Kubiczek and Kamiński (2013), who studied the extraction equilibrium in quinary systems comprising water, acetone, butanol, ethanol and ionic liquid, mutual solubility of ionic liquids and water increases also in the presence of acetone, butanol and ethanol. A similar correlation can be observed in the above-mentioned studies concerning ternary systems containing butanol. The minimum recorded solubilities of water in the organic phase given in Tables 1–3 essentially occur in ionic liquid + water binary systems when butanol is not present. Increasing the concentration of butanol in the mixture raises the equilibrium concentration of water in the organic IL-rich phase, which reduces the extractant's selectivity. This phenomenon is illustrated in Figs. 1–3 using the data taken from Marciniak et al. (2016) and Domańska and Królikowski (2012).

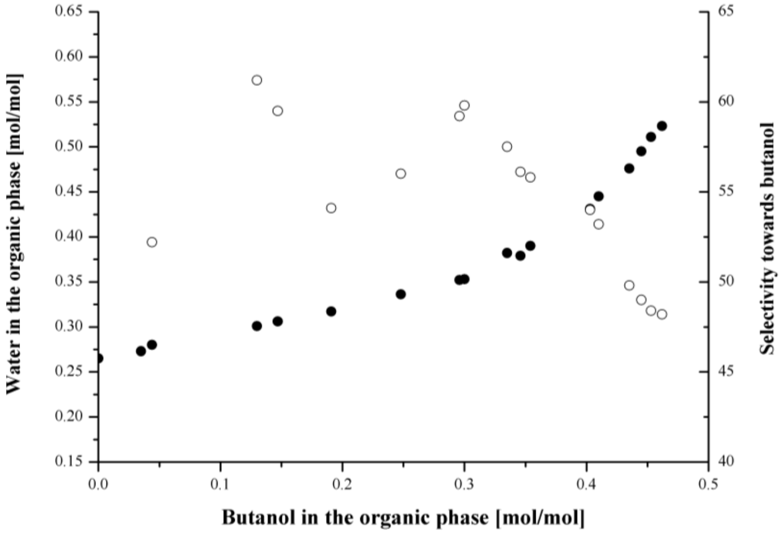

Fig. 1. Solubility of water in the organic phase (●) and selectivity of the IL towards butanol (○) in the system [bmPIP][NTf$_2$] + *n*-butanol + water (based on the data taken from Marciniak et al., 2016)

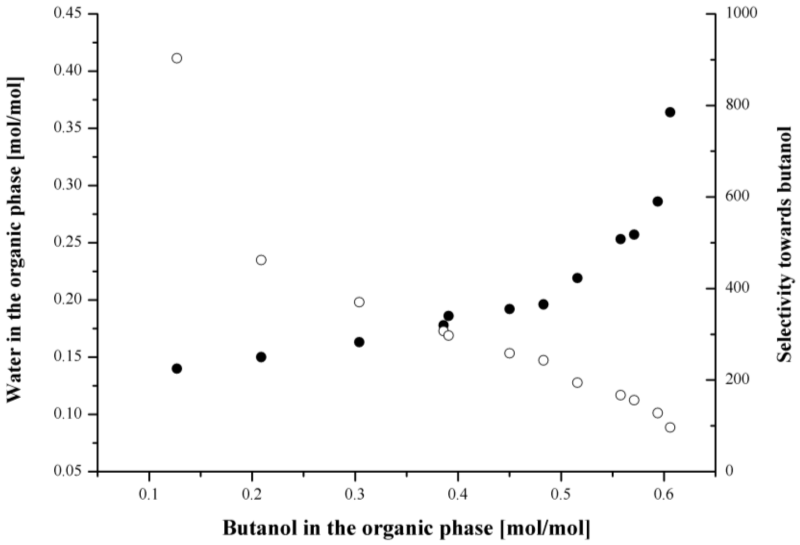

Fig. 2. Solubility of water in the organic phase (●) and selectivity of the IL towards butanol (○) in the system $[P_{14,6,6,6}]$[TCB] + *n*-butanol + water (based on the data taken from Domańska and Królikowski, 2012)

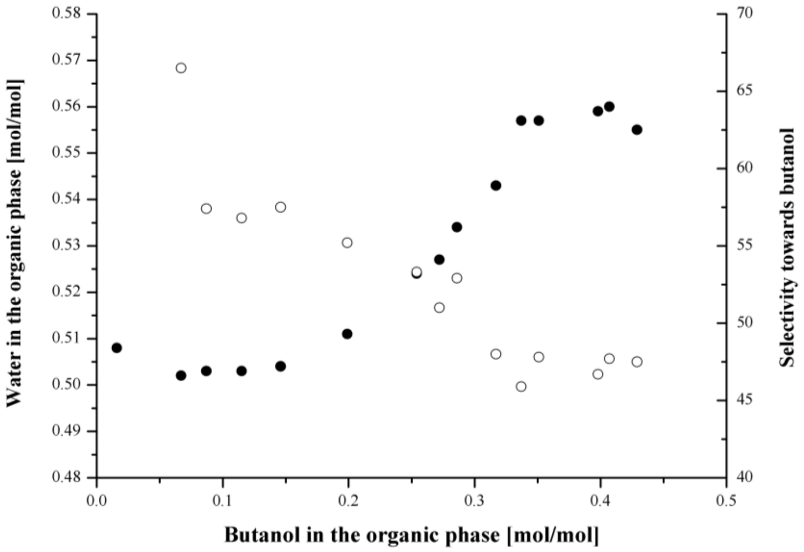

Fig. 3. Solubility of water in the organic phase (●) and selectivity of the IL towards butanol (○) in the system [hmim][TCB] + *n*-butanol + water (based on the data taken from Domańska and Królikowski, 2012)

Kubiczek and Kamiński (2013), using non-linear regression, determined correlations describing mutual solubility of the investigated ionic liquids and water as a function of temperature and concentrations of acetone, butanol and ethanol in the respective phase, which corroborated the observations made by Ha et al. (2010). Figs. 4 & 5 present exemplary relations concerning quinary systems containing 1-butyl-3-methylimidazolium bis(trifluoromethylsulfonyl)imide [bmim][NTf_2] as the extracting agent. At each point on the *x* axis, the concentrations of acetone, butanol and ethanol are assumed as equal and range from 0 to 3 wt%.

An increase in temperature, enhancing mutual solubility of the extractant and water, causes the extractant's selectivity towards the separated components to drop. However, as reported by Kubiczek (2015), this effect is to a certain degree compensated by growing distribution ratios, because higher temperatures favor dissolving acetone, butanol and ethanol in the organic phase.

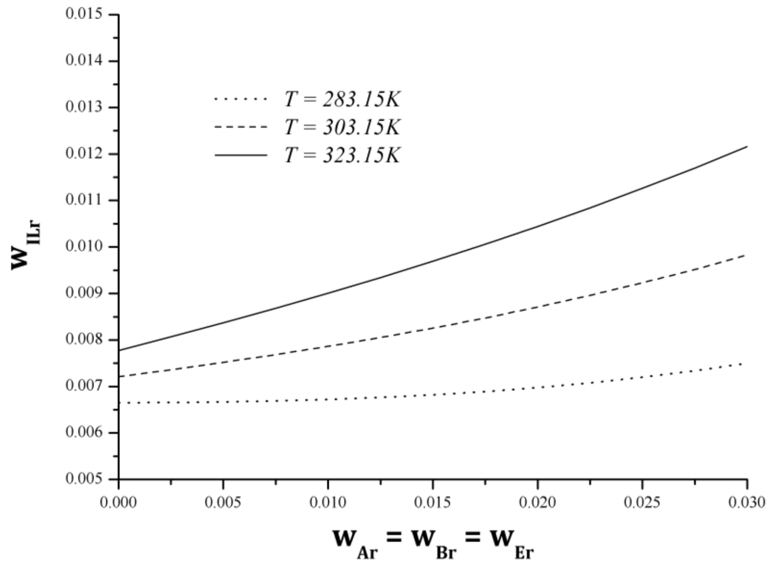

Fig. 4. Mass fraction of the ionic liquid in the raffinate (aqueous phase) vs. mass fractions of ABE in the raffinate in the system [bmim][NTf$_2$] + acetone + *n*-butanol + ethanol + water (Kubiczek, 2015)

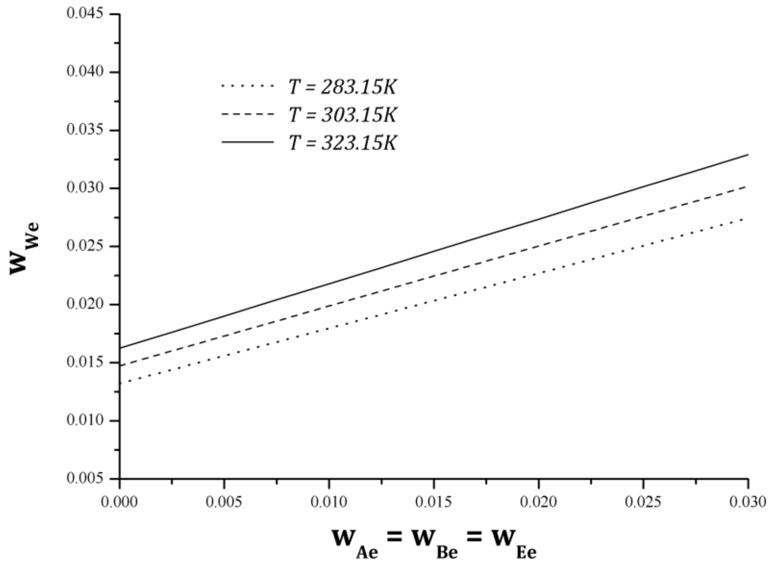

Fig. 5. Mass fraction of water in the extract (organic phase) vs. mass fractions of ABE in the extract in the system [bmim][NTf$_2$] + acetone + *n*-butanol + ethanol + water (Kubiczek, 2015)

Still, the increased amount of an extractant in the raffinate negatively affects the extraction economics, especially when the price of the ionic liquid is high. It leads to the conclusion that heating the feed before the extraction step in order to improve the separation efficiency serves no useful purpose.

5. APPLICATION OF THE NRTL EQUATION IN DESIGN OF THE EXTRACTION PROCESS

The majority of studies on the extraction equilibrium, not only those dealing with butanol and ionic liquids, focus on ternary systems comprising a feed solution, an extracting agent and a separated solute. These studies can help to determine the extractant's ability to recover a specific substance from a given feed solution although, in reality the systems subject to liquid-liquid extraction are more complex. In the case of extractive separation of the ABE fermentation broth, the feed contains not only butanol, but also acetone, ethanol and other organic products, which can be transferred into the extract to different extents. This phenomenon can be either favorable or unfavorable for the quality of the process. For example, acetone present in the broth can be considered a valuable intermediate improving the economics of fermentation. Some of the other products can be considered as impurities, which should be disposed of after extraction. Taking the above into account, it is helpful if the accepted mathematical model takes these products into consideration. In the system containing water, acetone, butanol, ethanol and an extractant, binary parameters of the NRTL equation are available with regard to the common constituents, i.e. water, acetone, butanol and ethanol. The unknown parameters between these components and the extracting solvent (e.g. ionic liquid) must be determined with the aid of optimization algorithms using experimental data.

Stoffers and Górak (2013) employed the experimental data of Domańska and Królikowski (2012) concerning the [hmim][TCB] + *n*-butanol + water system in order to calculate the missing NRTL parameters and simulate a liquid-liquid extraction process. To validate the model, the authors performed experiments in a three-stage counter-current mixer-settler unit and then simulated the unit using the Aspen Plus software. Consequently, they obtained good agreement between the experimental and simulated results. As reported by the authors, equilibrium was reached in each extraction stage. When using a solvent-to-feed ratio of 0.91 g/g, about 99% of butanol was recovered from the feed solution.

Some of the experiments in the mixer-settler unit were performed using a feed containing butanol, acetone, ethanol, acetic acid and butyric acid, normally present in the fermentation broth. During the first experiment, the feed solution contained 6 wt% butanol and 0.87 g/g of fresh [hmim][TCB] was used. During the second experiment, regenerated [hmim][TCB] was employed in an amount of 0.27 g/g and the concentration of butanol in the feed was reduced to 2 wt%. The recorded efficiencies of recovery were equal to 99 and 85% respectively. The simulated concentrations of butanol in the raffinate and the extract in the respective extraction stages were in close agreement with the experimental results.

The authors of this paper investigated three quinary systems containing water, acetone, butanol, ethanol and one of the following ionic liquids: 1-butyl-3-methylimidazolium bis(trifluoromethylsulfonyl)imide [bmim][NTf$_2$], 1-hexyl-3-methylimidazolium hexafluorophosphate [hmim][PF$_6$] or 1-butyl-1-methylpyrrolidinium bis(trifluoromethylsulfonyl)imide [bmp][NTf$_2$]. The experiments were conducted at 283.15 K, 303.15 K and 323.15 K with concentrations of acetone, butanol and ethanol in the feed varied from 0.5 to 5.5 wt%. The minimum and maximum distribution ratios of acetone, butanol and ethanol and selectivities of the investigated ionic liquids, calculated using mole fractions, are summarized in Table 5.

Table 5. Minimum and maximum experimental values of the distribution ratios (D) and selectivities (S) towards acetone, butanol and ethanol in the systems [bmim][NTf$_2$] or [hmim][PF$_6$] or [bmp][NTf$_2$] + acetone + *n*-butanol + ethanol + water at 283.15 K - 323.15 K (Kubiczek, 2015)

Ionic liquid		Distribution ratio			Selectivity		
		D_A	D_B	D_E	S_A	S_B	S_E
[bmim][NTf$_2$]	min	10.54	14.77	1.87	34.83	54.60	6.81
	max	19.02	24.05	3.32	65.67	80.41	10.98
[hmim][PF$_6$]	min	6.92	7.53	0.71	28.29	30.05	2.91
	max	15.08	17.38	2.58	53.61	56.81	8.26
[bmp][NTf$_2$]	min	9.80	11.85	1.34	31.96	49.61	4.69
	max	16.18	23.30	3.15	60.35	78.91	11.35

The equilibrium data were further used to estimate the unknown NRTL parameters related to the interactions between the ionic liquids and the remaining components of the mixture. It was achieved with two different tools, i.e. Matlab and Aspen Plus software. As a result, two different sets of parameters were obtained for each binary system but, subsequently, they provided comparable results when predicting the equilibrium state. The exact description of the experimental and calculation methods can be found in the works of Kamiński et al. (2014), Kubiczek (2015) and Kubiczek et al. (2016).

The root-mean-square errors of prediction calculated for acetone, butanol and ethanol are given in Table 6. They are close to the errors concerning ternary systems, presented by the other authors.

Table 6. Root-mean-square errors of equilibrium prediction in the systems [bmim][NTf$_2$] or [hmim][PF$_6$] or [bmp][NTf$_2$] + acetone + *n*-butanol + ethanol + water expressed in mole fractions and calculated using the NRTL parameters estimated with Matlab and Aspen Plus

Ionic liquid	Calculation method	*RMSD*		
		A	B	E
[bmim][NTf$_2$]	Matlab	0.00136	0.00157	0.00143
	Aspen Plus	0.00130	0.00054	0.00124
[hmim][PF$_6$]	Matlab	0.00252	0.00161	0.00232
	Aspen Plus	0.00162	0.00122	0.00138
[bmp][NTf$_2$]	Matlab	0.00225	0.00239	0.00231
	Aspen Plus	0.00147	0.00105	0.00158

The main advantage of applying the NRTL equation to quinary systems comes from the possibility to simulate simultaneous extraction of acetone, butanol and ethanol from aqueous solutions. Simulations of this kind were performed by the authors of this paper using Aspen Plus and enabled a comparison of ABE purification systems based on both traditional distillation and integrated extraction-distillation. In each case, the following feed parameters were assumed:

- a temperature of 308.15K (typical fermentation conditions),
- a feed flow rate of 100kg/s,
- concentrations of acetone, butanol and ethanol in the feed solution equal to 0.005, 0.010 and 0.001 g/g, respectively.

The aim of the process was to obtain butanol purer than 99.9%, acetone purer than 99% and ethanol 92-94% pure. The system based on direct distillation of the feed comprised 5 distillation columns and its ABE production rates were estimated at 3600 kg/h butanol, 1815 kg/h acetone and 380 kg/h ethanol. Considering the heat supplied to the columns, the estimated energy demand amounted to 37.46 MJ/kg$_{\mathrm{BuOH}}$ or 23.28 MJ/kg in relation to the total ABE product.

The simulated integrated extraction-distillation system comprised a counter-current extraction column containing 12 theoretical stages. The solvent-to-feed ratio was so adjusted that 90% of butanol was removed from the feed (0.618 g/g). Moreover, the purification system included an ionic liquid regeneration step and 5 distillation columns. Considering the heat necessary for distillation and regeneration (performed via flash evaporation) the energy demand was reduced to 10.82 MJ/kg$_{\mathrm{BuOH}}$ or 7.76 MJ/kg$_{\mathrm{ABE}}$. The resulting production rates were equal to 3218 kg/h butanol, 1228 kg/h acetone and 41.5 kg/h ethanol.

In the case of integrated extraction-distillation, the additional cost related to the recycling and partial losses of the extracting solvent through the raffinate stream can be reduced by applying an ionic liquid providing a higher distribution ratio and higher hydrophobicity or directing part of the raffinate back to the fermentation process. The latter solution is possible if the ionic liquid is non-toxic to the fermentation bacteria. Additional waste heat recovery can significantly decrease the overall energy consumption in the purification process. At the same time, the price of ionic liquid remains a crucial factor shaping the cost level.

6. SUMMARY AND CONCLUSIONS

Ionic liquids are a new class of solvents with a great potential for liquid-liquid extraction because of their negligible vapor pressure and adjustable properties being a function of their chemical structure. For instance, ionic liquids can be employed to recover biobutanol produced via ABE fermentation.

The paper provides an overview of the latest research concerning the application of different ionic liquids in liquid-liquid extraction of butanol from aqueous media and additionally presents and interprets the authors' own data concerning quinary systems containing acetone, butanol and ethanol.

In the referenced studies, their authors approximate phase equilibrium with the help of the NRTL equation and optionally the UNIQUAC equation. The analysis of statistical indicators, however, proves that the former gives closer agreement between the experimental and predicted compositions of both liquid phases at equilibrium.

In addition, the paper discusses mutual solubility of ionic liquids and water, which is not only a function of temperature but also concentrations of acetone, butanol and ethanol in the liquid mixture. It is an important issue in terms of potential losses and regeneration of the extracting agent. Finally, the paper points at the possibility of prediciting multi-stage extraction results thanks to the application of proper calculation methods.

SYMBOLS

D	distribution ratio
RMSD	root-mean-square deviation
S	selectivity
T	absolute temperature, K
w	mass fraction

Subscripts

A	acetone
B	butanol
e	extract (organic phase)
E	ethanol
IL	ionic liquid
r	raffinate (aqueous phase)
W	water

REFERENCES

Abdehagh N., Tezel F.H., Thibault J., 2014. Separation techniques in butanol production. Challenges and developments. *Biomass Bioenerg*., 60, 222-246. DOI: 10.1016/j.biombioe.2013.10.003.

Adhami L., Griggs B., Himebrook P., Taconi K., 2009. Liquid-liquid extraction of butanol from dilute aqueous solutions using soybean-derived biodiesel. *J. Am. Oil Chem. Soc*., 86 (11), 1123-1128. DOI: 10.1007/s11746-009-1447-7.

Brennecke J.F., Maginn E.J., 2001. Ionic liquids. innovative fluids for chemical processing. *AIChE Journal*, 47, 2384-2389. DOI: 10.1002/aic.690471102.

Cheruku S.K., Banerjee T., 2012. Liquid-liquid equilibrium data for 1-ethyl-3-methylimidazolium acetate-thiophene-diesel compound. experiments and correlations. *J. Solution Chem*., 41, 898-913. DOI: 10.1007/s10953-012-9840-5.

Davison B.H., Thompson J.E., 1993. Continuous direct solvent extraction of butanol in a fermenting fluidized-bed bioreactor with immobilized *Clostridium acetobutylicum*. *Appl. Biochem. Biotechnol*., 39-40, 415-426. DOI: 10.1007/BF02919007.

Domańska U., Królikowski M., 2012. Extraction of butan-1-ol from water with ionic liquids at T = 308.15K. *J. Chem. Thermodyn*., 53, 108-113. DOI: 10.1016/j.jct.2012.04.017.

Domańska U., Lukoshko E.V., 2015. Separation of pyridine from heptane with tricyanomethanide-based ionic liquids. *Fluid Phase Equilib*., 395, 9-14. DOI: 10.1016/j.fluid.2015.03.027.

Dürre P., 2007. Biobutanol. An attractive biofuel. *Biotechnol. J*., 2, 1525-1534. DOI: 10.1002/biot.200700168.

Earle M.J., Seddon K.R., 2000. Ionic liquids. Green solvents for the future. *Pure Appl. Chem*., 72, 1391-1398. DOI: 10.1351/pac200072071391.

Evans P.J., Wang H.Y., 1988. Enhancement of butanol formation by clostridium acetobutylicum in the presence of decanol-oleyl alcohol mixed extractants. *Appl. Environ. Microbiol*., 54 (7), 1662-1667.

Ezeji T.C., Qureshi N., Blaschek H.P., 2004. Butanol fermentation research. Upstream and downstream manipulations. *Chem. Rec*., 4, 305-314. DOI: 10.1002/tcr.20023.

Ezeji T.C., Qureshi N., Blaschek H.P., 2007. Bioproduction of butanol from biomass. from genes to bioreactors. *Curr. Opin. Biotech*., 18, 220-227. DOI: 10.1016/j.copbio.2007.04.002.

García V., Päkkilä J., Ojamo H., Muurinen E., Keiski R.L., 2011. Challenges in biobutanol production. How to improve the efficiency? *Renew. Sust. Energ. Rev*., 15, 964-980. DOI: 10.1016/j.rser.2010.11.008.

Garcia-Chavez L.Y., Garsia C.M., Schuur B., de Haan A.B., 2012. Biobutanol recovery using nonfluorinated task-specific ionic liquids. *Ind. Eng. Chem. Res*., 51, 8293-8301. DOI: 10.1021/ie201855h.

Green E.M., 2011. Fermentative production of butanol – the industrial perspective. *Curr. Opin. Biotech*., 22, 337-343. DOI: 10.1016/j.copbio.2011.02.004.

Ha S.H., Mai N.L., Koo Y.M., 2010. Butanol recovery from aqueous solution into ionic liquids by liquid-liquid extraction. *Process Biochem*., 45, 1899-1903. DOI: 10.1016/j.procbio.2010.03.030.

Haghnazarloo H., Lotfollahi M.N., Mahmoudi J., Asl A.H., 2013. Liquid-liquid equilibria for ternary systems of (ethylene glycol + toluene + heptane) at temperatures (303.15, 308.15, and 313.15) K and atmospheric pressure. Experimental results and correlation with UNIQUAC and NRTL models. *J. Chem. Thermodyn*., 60, 126-131. DOI: 10.1016/j.jct.2012.12.027.

Haghtalab A., Paraj A., 2012. Computation of liquid-liquid equilibrium of organic-ionic liquid systems using NRTL, UNIQUAC and NRTL-NRF models. *J. Mol. Liq*., 171, 43-49. DOI: 10.1016/j.molliq.2012.04.008.

Huang HJ, Ramaswamy S, Liu Y., 2014. Separation and purification of biobutanol during bioconversion of biomass. *Sep. Purif. Technol*., 132, 513-540. DOI: 10.1016/j.seppur.2014.06.013.

Ishii S., Taya M., Kobayashi T., 1985. Production of butanol by Clostridium acetobutylicum in extractive fermentation system. *J. Chem. Eng. Jpn*., 18, 125-130. DOI: 10.1252/jcej.18.125.

Ishizaki A., Michiwaki S., Crabbe E., Kobayashi G., Sonomoto K., Yoshino S., 1999. Extractive acetone-butanol-ethanol fermentation using methylated crude palm oil as extractant in batch culture of *Clostridium saccharoperbutylacetonicum* N1-4 (ATCC 13564). *J. Biosci. Bioeng*., 87, 352-356. DOI: 10.1016/S1389-1723(99)80044-9.

Ji X, Held C, Sadowski G., 2012. Modeling imidazolium-based ionic liquids with ePC-SAFT. *Fluid Phase Equilib*., 335, 64-73. DOI: 10.1016/j.fluid.2012.05.029.

Johnson K.E., 2007. What's an ionic liquid? The Electrochemical Society *Interface*.

Jones D.T., Woods D.R., 1986. Acetone-butanol fermentation revisited. *Microbiol. Rev*., 50 (4), 484-524. PMCID. PMC373084.

Kamiński W., Górak A., Kubiczek A., 2014. Modeling of liquid-liquid equilibrium in the quinary system of water, acetone, n-butanol, ethanol, and ionic liquid. *Fluid Phase Equilib*., 384, 114-121. DOI: 10.1016/j.fluid.2014.10.017.

Klähn M., Stüber C., Seduraman A., Wu P., 2010. What determines the miscibility of ionic liquids with water? Identification of the underlying factors to enable a straightforward prediction. *J. Phys. Chem. B*., 114 (8), 2856-2868. DOI: 10.1021/jp1000557.

Kosmulski M., Gustafsson J., Rosenholm J.B., 2004. Thermal stability of low temperature ionic liquids revisted. *Thermochim. Acta*, 412, 47-53. DOI: 10.1016/j.tca.2003.08.022.

Kraemer K., Harwardt A., Bronneberg R., Marquardt W., 2011. Separation of butanol from acetone-butanol-ethanol fermentation by a hybrid extraction-distillation process. *Comput. Chem. Eng.*, 35 (5), 949-963. DOI: 10.1016/j.compchemeng.2011.01.028.

Królikowski M., 2016. Liquid−liquid extraction of p-xylene from their mixtures with alkanes using 1-butyl-1-methylmorpholinium tricyanomethanide and 1-butyl-3-methylimidazolium tricyanomethanide ionic liquids. *Fluid Phase Equilib*., 412, 107-114. DOI: 10.1016/j.fluid.2015.12.032.

Kubiczek A., 2015. *Investigation of the extraction equilibrium in the quinary system of water, acetone, butanol, ethanol and ionic liquid*. PhD thesis, Lodz University of Technology, Poland.

Kubiczek A., Kamiński W., 2013. Mutual solubility of selected ionic liquids and water in five-component systems containing acetone, butanol and ethanol. *Chemical Engineering and Equipment*, 52 (4), 351-352 (in Polish).

Kubiczek A., Kamiński W., Górak A., 2016. Modeling of single- and multi-stage extraction in the system of water, acetone, butanol, ethanol and ionic liquid. *Fluid Phase Equilib*., 425, 365-373. DOI: 10.1016/j.fluid.2016.05.023.

Kumar M., Gayen K., 2011. Developments in biobutanol production. New insights. *Appl. Energy*, 88, 1999-2012. DOI: 10.1016/j.apenergy.2010.12.055.

Lee S.Y., Park J.H., Jang S.H., Nielsen L.K., Kim J., Jung K.S., 2008. Fermentative butanol production by *Clostridia*. *Biotechnol. Bioeng*., 101, 209-228. DOI: 10.1002/bit.22003.

Liu W., Zhang Z., Ri Y., Xu X., Wang Y., 2016. Liquid−liquid equilibria for ternary mixtures of water + 2-propanol + 1-alkyl-3-methylimidazolium bis(trifluoromethylsulfonyl)imide ionic liquids at 298.15K. *Fluid Phase Equilib*., 412, 205-210. DOI: 10.1016/j.fluid.2015.12.051.

Liu Y., Xue H., 2012. OXO Market supply and demand forecast & investment economic analysis. *Finance Research*, 1 (2), 4-10.

Lütke-Eversloh T., Bahl H., 2011. Metabolic engineering of Clostridium acetobutylicum. recent advances to improve butanol production. *Curr. Opin. Biotech*., 22, 1-14. DOI: 10.1016/ j.copbio.2011.01.011.

Marciniak A., Wlazło M., Gawkowska J., 2016. Ternary (liquid + liquid) equilibria of {bis(trifluoromethylsulfonyl)-amide based ionic liquids + butan-1-ol + water}. *J. Chem. Thermodyn*., 94, 96-100. DOI: 10.1016/j.jct.2015.11.002.

Matsumura M., Kataoka H., Sueki M., Araki K., 1988. Energy saving effect of pervaporation using oleyl alcohol liquid membrane in butanol purification. *Bioprocess Engineering*, 3, 93-100.

Mohsen-Nia M., Nekoei E., Mohammad Doulabi F.S., 2008. Ternary (liquid + liquid) equilibria for mixtures of (methanol + aniline + n-octane or n-dodecane) at T=298.15 K. *J. Chem. Thermodyn*., 40, 330-333. DOI: 10.1016/j.jct.2007.05.018.

Natalense J., Zouain D., 2013. Technology roadmapping for renewable fuels. case of biobutanol in Brazil. *J. Technol. Manag. Innov*., 8 (4), 143-152. DOI: 10.4067/S0718-27242013000500013.

Ni Y., Sun Z., 2009. Recent progress on industrial fermentative production of acetone-butanolethanol by *Clostridium* acetobutylicum in China. *Appl. Microbiol. Biotechnol*., 83, 415-423. DOI: 10.1007/s00253-009-2003-y.

Qureshi N., Blaschek H.P., 2001. ABE production from corn. a recent economic evaluation. *J. Ind. Microbiol. Biotechnol*., 27, 292-297. DOI: 10.1038/sj.jim.7000123.

Qureshi N., Blaschek H.P., 2006. Butanol production from agricultural biomass. In K. Shetty, G. Paliyath, A. Pometto, R.E. Levin (Eds.), *Food biotechnology*. 2nd ed. (pp. 525-549). New York. CRC Press, Taylor & Francis.

Rabari D., Banerjee T., 2013. Butanol and n-propanol recovery using a low density phosphonium based ionic liquid at T = 298.15K and p = 1atm. *Fluid Phase Equilib*., 355, 26-33. DOI: 10.1016/j.fluid.2013.06.047.

Ramey D.E., 2007. Butanol. The other alternative fuel. In Eaglesham A. and Hardy R.W.F. (Eds.), *Agricultural Biofuels. Technology, Sustainability and Profitability*. NABC Report 19 (pp. 137-147). Ithaca, NY. National Agricultural Biotechnology Council 2007.

Roffler S.R., Blanch H.W., Wilke C.R., 1988. In situ extractive fermentation of acetone and butanol. *Biotechnol. Bioeng*., 31 (2), 135-143. DOI: 10.1002/bit.260310207.

Simoni L.D., Chapeaux A., Brennecke J.F., Stadtherr M.A., 2010. Extraction of biofuels and biofeedstocks from aqueous solutions using ionic liquids. *Comput. Chem. Eng*., 34, 1406-1412. DOI: 10.1016/j.compchemeng.2010.02.020.

Siwale L., Kristóf L., Torok A., Bereczky A., Mbarawa M., Penninger A., Kolesnikov A., 2013. Performance characteristics of n-butanol-diesel fuel blend fired in a turbo-charged compression ignition engine. *J. Power Energy Eng.*, 1, 77-83. DOI: 10.4236/jpee.2013.15013.

Sowmiah S., Srinivasadesikan V., Tseng M.C., Chu Y.H., 2009. On the chemical stabilities of ionic liquids. *Molecules*, 14, 3780-3813. DOI: 10.3390/molecules14093780.

Stoffers M., Górak A., 2013. Continuous multi-stage extraction of n-butanol from aqueous solutions with 1-hexyl-3-methylimidazolium tetracyanoborate. *Sep. Purif. Technol.*, 120, 415-422. DOI: 10.1016/j.seppur.2013.10.016.

Stoffers M, Heitmann S, Lutze P, Górak A., 2013. Integrated processing for the separation of biobutanol. Part A. experimental investigation and process modelling. *Green Process. Synth.*, 101-120. DOI: 10.1515/gps-2013-0009.

Vane LM. ,2008. Separation technologies for the recovery and dehydration of alcohols from fermentation broths. *Biofuels, Bioprod. Biorefin.*, 2, 553-588. DOI: 10.1002/bbb.108.

Wilkes J.S., Zaworotko M.J., 1992. Air and water stable 1-Ethyl-3-methylimidazolium based ionic liquids. *J. Chem. Soc., Chem. Commun.*, 965-967. DOI: 10.1039/C39920000965.

Zhang W., Hou K., Mi G., Chen N., 2010. Liquid-liquid equilibria of the ternary system thiophene + octane + dimethyl sulfoxide at several temperatures. *Appl. Biochem. Biotechnol.*, 160, 516-522. DOI: 10.1007/s12010-008-8382-1.

Received 26 October 2016
Received in revised form 14 December 2016
Accepted 20 December 2016

DE GRUYTER OPEN
Chemical and Process Engineering 2017, 38 (1), 111-120
DOI: 10.1515/cpe-2017-0009

THE PARAMETERS OF CLEANING A CIP SYSTEM AFFECTED ENERGY CONSUMPTION AND CLEANING EFFICIENCY OF THE PLATE HEAT EXCHANGER

Joanna Piepiórka-Stepuk*, Jarosław Diakun, Marek Jakubowski

Koszalin University of Technology, Faculty of Mechanical Engineering, Department of Food Industry Processes and Facilities, Racławicka 15–17, 75-620 Koszalin, Poland

This paper presents a study on the effect of cleaning factors on the energy consumption of the cleaning process in a CIP system, and the correlation between single components of electricity necessary to perform this process and the cleanliness degree obtained. Studies were carried out in a laboratory cleaning station, wherein a plate heat exchanger contaminated with hot milk was included. The research program was developed according to a 5-level statistical plan. Based on the results, obtained with Experiment Planner 1.0, a regression function of energy requirement considering variables such as: cleaning time, temperature and flow rate of the cleaning liquid via the cleaned exchanger has been developed. Describing this relationship, linear and quadratic functions with double interactions were used. Significance level for the analysis was established at $\alpha = 0.05$. Correlation analysis between components of the electricity necessary to perform the cleaning process (pump drive and heating of the cleaning agent) and the resulting degree of cleaning of heat exchanger plates was performed.

Keywords: cleaning, CIP system, energy consumption, cleaning parameters, cleanliness, cleaning efficiency

1. INTRODUCTION

The food industry is a major consumer of water and energy. Furthermore water and energy are interrelated with wastewater production (Krzemińska et al. 2013). The demand for agro food processing facilities for water and energy is dependent on many factors (Kowalczyk and Karp, 2005; Steinhoff-Wrześniewska et al., 2013; Williams and Anderson, 2006; Wojdalski et al., 2013). The basic ones include technology of food processing, technical equipment, degree of automation and mechanization of production operations, thermophysical properties of materials, requirements for products, magnitude and structure of production and its organization (Bunse et al., 2011; Marchini et al., 2014; 2015; Wojdalski and Dróżdż, 2012) and related with those the operations of cleaning and disinfection of machines and production equipment. Some reports indicate that the cleaning processes in food industry are energy-intensive processes and that in the food industry they require even about 13.5 - 14% of the total process energy consumption (Neryng et al., 1990; Pawełas, 2010; Rad and Lewis, 2014). This consumption primarily results from the operation conditions of the CIP cleaning station, type and size of the objects subjected to cleaning and the choice of cleaning agents (Piepiórka-Stepuk et al., 2016; Ramirez et al., 2006; Wojdalski et al., 2013). Studies conducted by many authors on cleaning of milk installations suggest that energy requirement of cleaning process in flow mainly results from the necessity of heating a large volume of cleaning agents in storage tanks (even up to

---

*Corresponding author, e-mail: joanna.piepiorka@tu.koszalin.pl

95 °C) and maintaining their appropriate temperature throughout the cleaning time (Berlin et al., 2007; Diakun et al., 2012; Eide et al., 2003). Electricity consumption for this aspect of the cleaning process exceeds twelve times that necessary to force the flow of cleaning agents. Other studies regarding the selection of optimum cleaning conditions in the CIP system demonstrate that it is possible to increase the degree of cleanliness of washed installation with a simultaneous reduction of energy consumed (Jude and Lemaire, 2014; Piepiórka-Stepuk et al., 2016). For the process optimization is necessary to develop a function which is a mathematical description of this process containing the variable factors. In the available literature, there are no reports on the theoretical and analytical modeling describing the effect of cleaning agents in flow (time, temperature and flow rate) on energy intensity of this process. Moreover, there are no experimental results, based on which we could infer the character of interactions between these factors and energy consumption of the process. The objective of the study was to develop a regression function describing the relationship between the amount of energy necessary to perform the process of cleaning of a plate heat exchanger and different factors, such as time, temperature and flow rate.

2. MATERIALS AND METHODS

2.1. Construction of research station and research program

Experiments were conducted using a two-tank cleaning station in the CIP system (1, 2) (Fig. 1), wherein S4 IT PN 10 (1) (Sondex) plate heat exchanger was included (Table 1). One of the tank installations (2) had a built-in heater of 3 kW power and thermal insulation, which enabled the preparation of cleaning solutions of a specified temperature and restricted heat loss into the environment. Heater power supply accomplished through a thermostatic control system which allowed heating and stabilization of liquid temperature in the tank. Water of different temperatures was prepared in this tank.

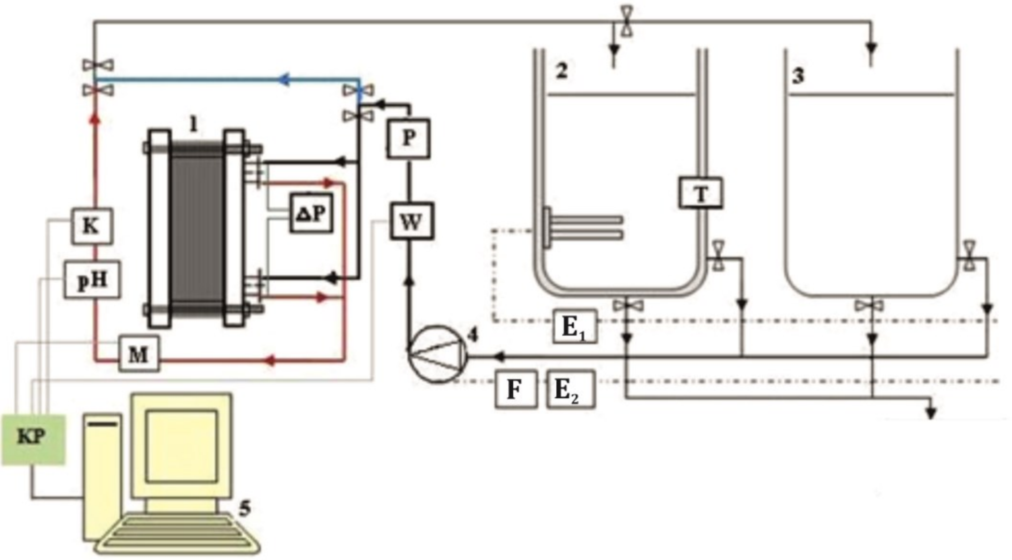

Fig. 1. Scheme of a laboratory CIP station. Legend: *K* – conductivity meter; *pH* – pH-meter; *M* – turbidity meter; *KP* – computer card; *P* – pressure gauge; Δ*P* – pressure drop between inlet and outlet of the heat exchanger; *W* – flow rate meter; *F* – inverter; E_1 – consumed energy meter used to power the pump; E_2 – consumed energy meter used to heat the cleaning liquid; *T* – thermometer; 1 – object to be cleaned (plate heat exchanger); 2 – insulated tank with a heater; 3 – non-insulated tank; 4 – pump; 5 – computer

Table 1. Main geometrical characteristics of the plate heat exchanger used in the study

Geometrical characteristics	Symbol	Unit	Value
Effective length of the plate	L_w	m	0.381
Effective width of the plate	L_s	m	0.111
Area of a single plate	$A = L_w \cdot L_s$	m^2	0.042
Area of heat transfer	A_c	m^2	0.378
The largest distance between plates	b	m	0.008
Mean distance between the plates	$c = (b/2)$	m	0.004
Surface area of the flow cross-section	$P_{str} = cL_s$	m^2	0.0005
Wetted perimeter	$Ob_c = 2c + 2L_s$	m	0.23
Total number of plates in the heat exchanger	N_p	items	11
Number of channels in the plate heat exchanger	$N_c = (N_p - 1)/2$	items	5
Hydraulic diameter of the channel	d_{ch}	m	0.009
Corrugation angle	β	°	60
Type of plates	*Straight - flow*		

Table 2. Cleaning programs used in the research

Level of the research plan	Variables			Reynolds number
	T (min)	T (°C)	u_c (m·s^{-1})	Re (-)
1	32	24	0.45	4420
2	98	24	0.45	4420
3	32	66	0.45	9251
4	98	66	0.45	9251
5	32	24	0.65	6384
6	98	24	0.65	6384
7	32	66	0.65	13362
8	98	66	0.65	13362
9	120	45	0.55	8187
10	10	45	0.55	8187
11	65	80	0.55	13494
12	65	10	0.55	3786
13	65	45	0.75	11164
14	65	45	0.35	5210
15	65	45	0.55	8187
16	65	45	0.55	8187
17	65	45	0.55	8187
18	65	45	0.55	8187
19	65	45	0.55	8187
20	65	45	0.55	8187

The cleaning system was equipped with an impeller pump (4) and meters for measuring the quantities characterizing the flow, i.e. flow rate in the pipeline (W), pressure (P) and the pressure drop between the inlet and the outlet of the heat exchanger (ΔP). Furthermore, the system had sensors which registered changes in the properties of the washing liquid, i.e. temperature (T), turbidity (M), conductivity (K), pH (pH), electricity required to heat the washing liquid (E_1-PM 390 meter, Elektro-Trading company) and and to power the pump (E_2-C-52 three-phase electricity meter, Inventor company). All the process data were recorded (5). The cleaning process was carried out only with pure water. The plan of the study covered the cleaning process including the factors for which variability was within the range:

- cleaning time – $t = 10 \div 120$ min;
- mean flow rate between plates of the heat exchanger calculated based on the flow rate measured in the pipeline – $u_c = 0.35 \div 0.75$ m·s^{-1};
- temperature of the washing liquid – $T = 10 \div 80$ °C.

The research program was developed according to a 5-level statistical plan $2^3+2\times3+6$, based on which we could obtain an experiment matrix presented in Table 2.

2.2. Evaluation of energy consumption of the process and cleaning efficiency

For test purposes, a single measuring cycle covered milk contamination of plates, installation of the heat exchanger and cleaning in flow with simultaneous measurement of energy requirement of pump drive (E_{Pi}) and heating the cleaning agent (E_{Gi}). Total energy consumption of the cleaning process was calculated according to Eq. (1) (Wojdalski et al., 2012).

$$E_C = E_{Pi} + E_{Gi} \text{ (kWh)} \tag{1}$$

After completion of the cleaning process, the exchanger was disassembled and using the *Clean-Trace^{TM} Surface Protein Plus* swab tests based on Cu^{2+}-induced color reaction and protein complexes, information on the amount of residual protein contaminants was obtained (Piepiórka-Stepuk, 2012). The degree of purity was determined on a 0–10 point scale, in which 0 denoted an initial contamination of plates with milk, and 10 points - desired purity of plates (lack of any contaminants). All plates in the exchanger were evaluated, in five identical areas on the plate of 5.0 cm × 5.0 cm in diameter. Based on test results, the overall average cleanliness of the heat exchanger plates (J_M) was determined from Eq. (2).

$$J_M = \frac{\sum (J_{MOi})}{m} \tag{2}$$

Studies were carried out in triplicate for each set of factor values. After collecting the experimental study results, the Pearson correlation coefficient which defines a linear relationship between the energy consumption (E_{Pi}; E_{Gi}) and the total consumption (E_C) in the cleaning process and the purity of plate exchanger (J_M), was calculated. Furthermore, for each cleaning program, cleaning efficiency (C_E) could be calculated according to Eq. (3). It was defined as the increase of cleaning degree in 1 kWh of energy.

$$C_E = \frac{J_M}{E_C} \left(\frac{1}{\text{kWh}}\right) \tag{3}$$

2.3. Methodology for the development of regression function of energy consumption in the cleaning process

The obtained results constituted a basis to develop a regression function describing the energy consumption of the cleaning process in the CIP system of the plate heat exchanger in a function of time, temperature and average flow rate in the gap between E_C plates (t, T, u_c). To describe the proposed relationship, linear and quadratic functions with double interactions (4) were proposed. Linear components determine the trend of linear character of interactions of single factors on the energy intensity of the process, while the square components can be used to determine the optima of interactions for each factor, deviations from non-linearity and extremes.

$$\breve{\bar{Y}} = \breve{\bar{E}}_C = k_0 + k_1 t + k_2 T + k_3 u_c + k_{12} tT + k_{13} tu_c + k_{23} Tu_c + k_{11} t^2 + k_{22} T^2 + k_{33} {u_c}^2 \qquad (4)$$

Calculations were done in the Experiment Planner 1.0 software, according to the method described by Kukiełka (2002) and Diakun et al. (2012) for a significance level of $\alpha = 0.05$. Based on the obtained results, ten unknown coefficients of the model equation were determined; k_0; k_1; k_2; k_3; k_{12}; k_{13}; k_{23}; k_{11}; k_{22}; k_{33}. Results of the experimental study were subjected to statistical analysis according to the following algorithm:

- elimination of results affected by a gross error;
- calculation of inter-row variability and standard deviation;
- evaluation of variance homogeneity in the sample;
- calculation of the coefficients in the regression function;
- statistical analysis of the regression function;
- evaluation of significance of multidimensional correlation coefficient;
- assessment of the adequacy of mathematical model;
- regression function decoding;
- determination of the confidence intervals.

The resulting equation describes the function of the energy consumption of plate heat exchanger cleaning. The obtained function was presented in a graphical form as a configuration of different factors.

3. RESULTS AND DISCUSSION

3.1. Analysis of regression model describing energy consumption in the cleaning process

Based on study results obtained and statistical analysis, we developed a regression function describing the total energy consumption in the cleaning process. Multidimensional correlation coefficient for the adopted class of mathematical model was $R = 0.993$. After taking into account non-significant factors which were highlighted in the equation by a continuous line, the regression function as a second degree polynomial with double interactions, takes the following form encoded as Eq. (5):

$$\begin{gathered}\breve{\bar{Y}} = \breve{\bar{E}}_c = 4.966 + 1.198\breve{\bar{x}}_1 + 3.221\breve{\bar{x}}_2 + 0.1\breve{\bar{x}}_3 + 0.567\breve{\bar{x}}_1\breve{\bar{x}}_2 + \\ - 0.125\breve{\bar{x}}_1\breve{\bar{x}}_3 - 0.502\breve{\bar{x}}_2\breve{\bar{x}}_3 + 0.142{\breve{\bar{x}}_1}^2 + 0.476{\breve{\bar{x}}_2}^2 - 0.005{\breve{\bar{x}}_3}^2\end{gathered} \qquad (5)$$

The *F-Snedecor* test showed that there were no grounds to reject the hypothesis about the significance of the multidimensional correlation coefficient and there were no grounds to reject the hypothesis on the truth of the regression coefficients. The critical value of the *F-Snedecor* test for the analysis was estimated at $F_{kr} = 3.02$, resulting in the inequality $F_E = 86.68 > F_{kr} = 3.02$. After decoding, the function describing the energy consumption of cleaning the plate heat exchanger is described in the following form:

$$\begin{gathered}\breve{\bar{E}}_c = -6.62 + 0.002\bar{t} + 0.133\bar{T} + 12.8\bar{u}_c + 0.0008(\bar{t}\bar{T}) + \\ - 0.038(\bar{t}\bar{u}_c) - 0.239(\bar{T}\bar{u}_c) + 0.0001(\bar{t}^2) + 0.0011(\bar{T}^2)\end{gathered} \qquad (6)$$

Considering confidence interval for the obtained function (7), the function is described as (8):

$$\Delta\breve{\breve{E}}_c = \pm 0.0484\sqrt{\begin{aligned}&0.123\left[\left(\frac{t-65}{27.5}\right)^4+\left(\frac{T-45}{17.5}\right)^4+\left(\frac{u_c-0.55}{0.1}\right)^4\right]+\\&0.246\left[\left(\frac{t-65}{27.5}\right)^2\left(\frac{T-45}{17.5}\right)^2+\left(\frac{t-65}{27.5}\right)^2\left(\frac{u_c-0.55}{0.1}\right)+\left(\frac{T-45}{17.5}\right)^2\left(\frac{u_c-0.55}{0.1}\right)^2\right]+\\&0.036\left[\left(\frac{t-65}{27.5}\right)^2\left(\frac{T-45}{17.5}\right)^2+\left(\frac{u_c-0.55}{0.1}\right)^2\right]+0.217\end{aligned}} \tag{7}$$

$$\breve{\breve{E}}_C = \breve{\breve{E}}_C \pm \Delta\breve{\breve{E}}_C \tag{8}$$

The obtained function describes the energy consumption of the cleaning process of the plate heat exchanger in flow, under certain conditions and research scope adopted. Minus introduced in the beginning denotes a certain inconsistency, because when substituting zero values with t, T, u_c factors, a negative value of energy is obtained. It results from the fact that the lowest temperature of the cleaning agent, for which the studies were carried out, was 10 °C and therefore the developed equation is true only within the tested range. Cleaning below this temperature value is consistent. A similar situation occurs in terms of square of the temperature and the time. Energy consumption during the process should be linear, which means that electricity consumption should be proportional to the duration of a given operation or process. From the resulting function it can be concluded however, that time in the quadratic function is also important in cleaning processes. It results from a constant need to heat the cleaning solutions during the process in order to maintain the cleaning temperature at the assumed level. The longer the process of cleaning, the more frequent the heater was run to compensate for heat losses into the environment and maintain thermal conditions. In consequence, it leads to deviation of the function from non-linearity. As a result of statistical analysis, it can be concluded that within the tested range, the square of the flow rate (u_c^2) on energy requirement (E_C) is non-significant. The impact of cleaning parameters on energy consumption of the process was graphically presented in Figure 2, as a configuration of two variables. Factors which are not present on the plots have fixed, central values of the research program: $t = 65$ min; $T = 45$ °C; $u_c = 0.55$ m·s^{-1}.

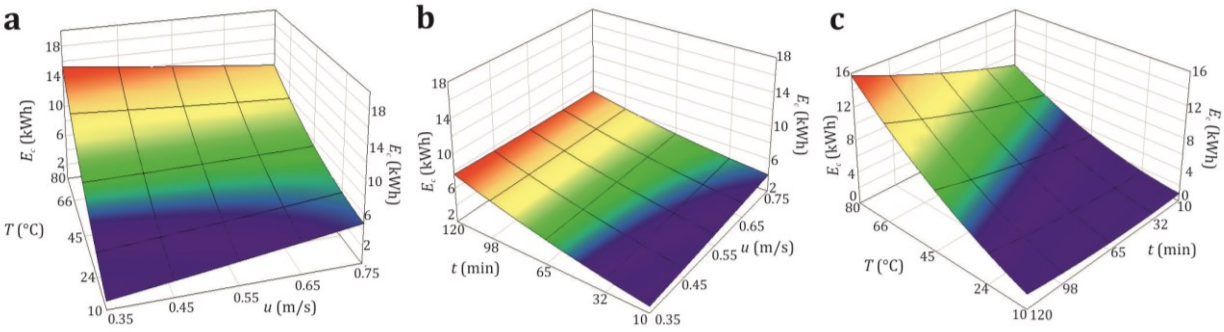

Fig. 2. Total energy consumption E_c as a function of temperature (T), flow rate (u_c) and time (t): a – relationship between energy consumption as a function of temperature and flow rate; b – relationship between energy consumption as a function of time and flow rate; c – relationship between energy consumption as a function of temperature and time

The graphical form of the function confirms that energy consumption of the process increases with temperature of the cleaning factor, which is consistent with previous reports (Diakun et al., 2012). This relationship for the cleaning time equal to $t = 65$ minutes is linear with maximum for $T = 80$ °C (Fig. 2a). Increase in a flow rate of the cleaning agent affects energy consumption of the process to a small extent (Fig. 2b). However, a different effect is exerted by cleaning time which is related to temperature up to which cleaning agents are heated. At low temperatures, extension of the cleaning time does not affect the overall energy increase, while for high temperatures, it leads to its increase by almost 100% (Fig. 2c).

It mainly results from cooling of the cleaning agent with time, resulting from temperature difference between the tank and the heated liquid, as well as cooling by the cleaned objects, which occurs immediately after starting the installation. As a consequence of cooling, the cleaning agent was continuously heated in order to maintain the temperature at an assumed level, which affected the form of equation.

3.2. Analysis of the efficiency of cleaning in relation to total energy requirement

In Fig. 3, we summarize the obtained values of the energy requirement *(E_{Pi}; E_{Gi})* and total energy consumption *(E_C)* in cleaning process for each trials of the research program according to Table 2.

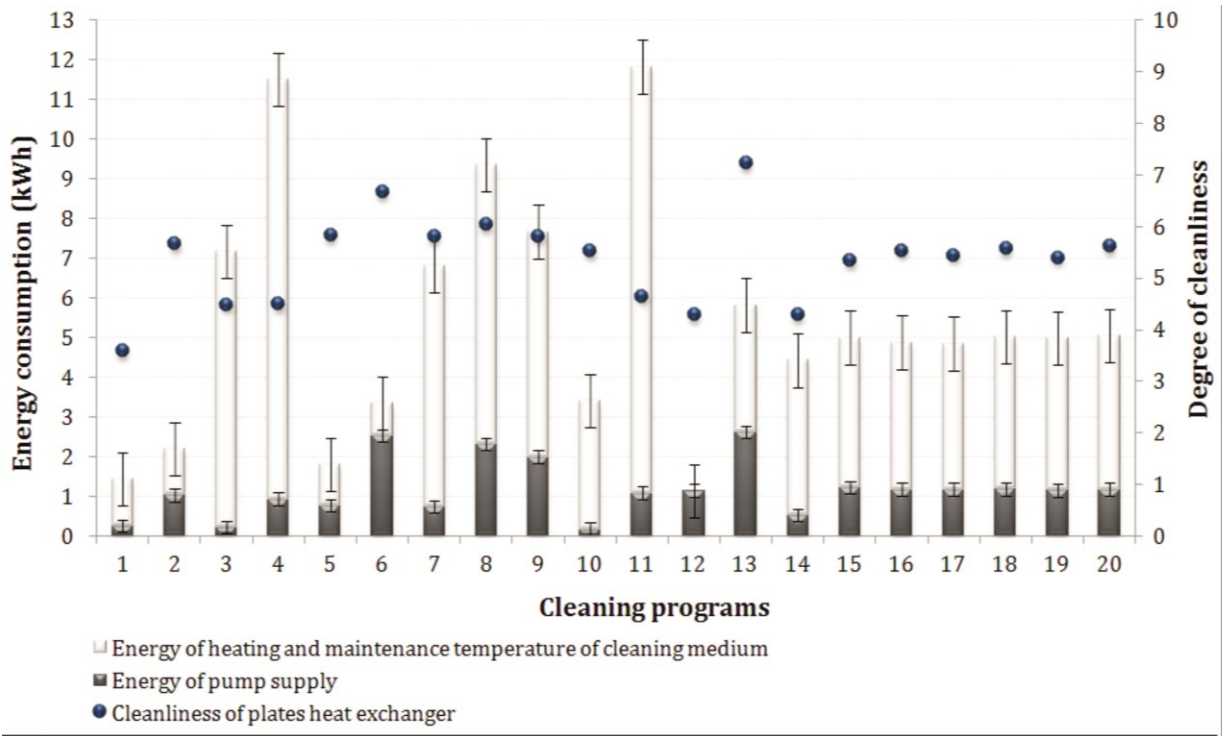

Cleaning program	1	2	3	**4**	5	6	7	8	9	10	**11**	**12**	13	14	15	16	17	18	19	20
Cleaning efficiency (C_E)	2.57	2.58	0.62	**0.39**	3.24	1.96	0.85	0.64	0.76	1.63	**0.39**	**3.91**	1.25	0.98	1.07	1.13	1.14	1.12	1.08	1.12

Fig. 3. The degree of cleaning of plate heat exchanger for single components (E_{Pi} and E_{Gi}) and the total *(E_C)* energy requirement in particular trials of the research program: a – electricity necessary to heat and maintain temperature of the cleaning liquid; b-electricity necessary to drive the pump; c-overall average purity of plates of the heat exchanger.

The conducted studies demonstrated that within the programs, in which the highest total electricity consumption (program 4 and 11-about 12 kWh) was reported, no satisfactory results of cleaning were obtained. The maximum cleanliness of the surface of heat exchanger plates for these cleaning programs, reached the value of less than 5 points. For those programs the least cleaning efficiency a about 0.39 was achieved. A similar effect of cleaning (between 4÷5 points) was obtained for the program 12, for which we reported the lowest total energy consumption (1 kWh) related solely to the operation of the impeller pump during cleaning. In this program, the highest coefficient of cleaning efficiency was achieved (3.91). The value of the Pearson correlation coefficient for the total energy consumption (E_C) and obtained purity of exchanger plates (J_M) was $r = 0.01$, what indicates a lack of relationship between the variables which were analyzed. The obtained results also demonstrated that the main reason for high energy consumption in the process of cleaning of the dairy installations, is high temperature of cleaning agents in the range of 65 − 85 °C (Rad and Lewis, 2014; Ramirez et al., 2006), although according to presented results, this factor does not improve the efficiency of removal of milk residues from the exchanger plates (programs 3, 4, 11). Similar results were obtained by Diakun et al. (2012) and Wojdalski et al. (2013). The Pearson correlation coefficient for these variables (E_{Gi}; J_M) was $r = -0.17$, indicated a negative correlation between the analyzed variables. When interpreting this result, we can conclude that with increase in the amount of electricity consumed for heating rinsing water, the efficiency of removal of milk residues from the installation decreases. Properties of milk residues may be an explanation for that phenomenon as they are not dissolved in high temperature of the cleaning liquid (Almecija et al., 2009; Changani et al., 1997; Fryer et al., 2006). Analysis of the study results also showed that with an increase in the electricity necessary for the operation of the impeller pump, effectiveness of the heat exchanger cleaning is increasing. The Pearson correlation coefficient for these variables (E_{Pi}; J_M) was positive and accounted for $r = 0.74$. This was confirmed by the study results obtained in the cleaning programs 6 and 13, in which electricity consumption to force the flow of cleaning liquid was the highest (about 2.5 kWh) with the highest cleaning efficiency of the heat exchanger (about 7 points). The cleaning efficiency coefficients for these programs were in range of 1.25 – 1.96. Thus, increase in the flow rate during the cleaning process not only improves the cleaning efficiency, as observed by other authors (Goode et al., 2010; Fryer et al., 2006), but also affects the reduction of costs associated with performance of the process with simultaneous decreasing of the temperature of cleaning agents.

4. CONCLUSIONS

- Energy consumption in the cleaning process is mainly related to heating the cleaning media and maintaining them at a certain level.
- The obtained results indicate that in case of milk residues which are formed during high-temperature treatment of milk on plates in heat exchangers, high temperature of rinsing water does not always provide a better end result of the cleaning.
- Negative correlation was reported between the requirement for the electricity associated with heating of the cleaning liquid and the efficiency of removal of milk residues from the plates of the heat exchanger.
- Requirement for energy related to forcing the flow is much lower in comparison to the requirement for heating the washing liquid.
- Flow rate is a cleaning factor which leads to the improvement of the cleaning quality with its increase.
- There is a high correlation ($r = 0.74$) between the energy necessary to drive the pump and the efficiency of washing plates of the heat exchanger contaminated with milk.
- In the ecological and safety aspects of food production, it is advised to use possibly high flow rates of the cleaning media ($u_c = 0.75$; $Re \approx 11\,000$) at the cost of very high temperature (T = 80 °C) and very long cleaning time ($t = 120$ min).

SYMBOLS

m	sample size (the product of the number of areas on a single plate and the number of plates subjected for evaluation): $m = 25$
t	cleaning time, min
u_c	mean flow velocity per channel, $\mathrm{m \cdot s^{-1}}$
C_E	cleaning efficiency, $\mathrm{kWh^{-1}}$
E_{Gi}	energy of heating and temperature maintenance of cleaning agents, kWh
E_{Pi}	pump power supply, kWh
E_C	total energy consumption in the cleaning process, kWh
J_M	effectiveness of cleaning of the heat exchanger plates
J_{MOi}	cleanliness of a single area on subsequent plates of the heat exchanger
T	temperature of the cleaning liquid, °C
Re	Reynolds number

REFERENCES

Almecija M.C., Martinez-Ferez A., Guadix A., Paez M.P., Guadix E.M., 2009. Influence of the cleaning temperature on the permeability of ceramic membranes. *Desalination,* 245, 708–713. DOI: 10.1016/j.desal.2009.02.041.

Berlin J., Sonesson U., Tillman A.M., 2007. A life cycle based method to minimize environmental impact of dairy production through product sequencing. *J. Cleaner Prod.*, 15, 347–356. DOI: 10.1016/j.jclepro.2005.07.019.

Bunse K., Vodicka M., Schönsleben P., Brülhart M., Ernst F.O., 2011. Integrating energy efficiency performance in production management – gap analysis between industrial needs and scientific literature. *J. Cleaner Prod.*, 19, 667–679. DOI: 10.1016/j.jclepro.2010.11.011.

Changani S.D., Belmar-Beiny M.T., Fryer P.J. 1997. Engineering and chemical factors associated with fouling and cleaning in milk processing. *Exp. Therm Fluid Sci.*, 14, 392–406. DOI: 10.1016/S0894-1777(96)00141-0.

Diakun J., Mierzejewska S., Kukiełka K., 2012. The regression equation of energy requirement in the process of cleaning the pipeline by CIP method. *Polish Journal of Food Engineering,* 1/4(1), 5–8.

Eide, M.H., Homleid, J.P., Mattsson, B., 2003. Life cycle assessment (LCA) of cleaningin-place processes in dairies. *LWT Food Sci. Technol.,* 36, 303-314. DOI: 10.1016/S0023-6438(02)00211-6.

Fryer P.J, Christian G.K., Liu W., 2006. How hygiene happens: physics and chemistry of cleaning. *Int. J. Dairy Technol.,* 59, 76–84. DOI: 10.1111/j.1471-0307.2006.00249.x.

Goode K.R., Asteriadou K., Fryer P.J., Picksley M., Robbins P.T., 2010. Characterizing the cleaning mechanisms of yeast and the implications for Cleaning In Place (CIP). *Food Bioprod. Process.,* 88, 365–374. DOI: 10.1016/j.fbp.2010.08.005.

Jude B., Lemaire E. 2014. Optimising clean-in-place processes in food and beverage operations: Part 1. *Process Control Systems*. Available at: http://www.processonline.com.au/articles/69571.

Kowalczyk R., Karp K., 2005. Energy consumption at sewage treatment in selected plant of dairy industry. *Problemy Inżynierii Rolniczej*, 4, 79–88.

Krzemińska D., Neczaj E., Parkitna K., 2013. Zastosowanie reakcji Fentona do wspomagania biologicznego oczyszczania ścieków z przemysłu mleczarskiego. *Annual Set The Environment Protection,* 15, 2381–2397.

Kukiełka, L., 2002. *Basics of engineering research*. PWN, Warszawa, 174–208.

Marchini D., Rinaldi M., Montanari R., Bottani E., Solari F., 2014. Performance analysis of the water supply system of a dairy company by means of an advanced simulation tool. *Int. J. Food Eng.*, 10, 557–571. DOI: 10.1515/ijfe-2013-0067.

Marchini D., Rinaldi M., Montanari R., Bottani E., Solari F., 2015. Temperature analysis of the water supply system of a dairy company by means of a simulation model. *Int. J. Food Eng.*, 11, 731–745. DOI: 10.1515/ijfe-2015-0065.

Neryng A., Wojdalski J., Budny J., Krasowski E., 1990. *Energy and water in agro-food industry*. WNT, Warsaw, 103–106, 189–194.

Pawełas A., 2010. Energy effectiveness on the example of the brewery. *Agro Industry*, 3-4, 44-47.

Piepiórka J., 2012. Comparison of evaluation methods degree of cleaning surface production in the CIP system. *Polish Journal of Food Engineering,* 2/4(2), 23–26. Available at: http://ips.wm.tu.koszalin.pl/doc/2012/2.2012/5_art_piepiórka-stepuk.pdf.

Piepiórka-Stepuk J., Diakun J., Mierzejewska S., 2016. Poly-optimization of cleaning conditions for pipe systems J. and plate heat exchangers contaminated with hot milk using the Cleaning In Place method. *J. Cleaner Prod.,* 112, 946-952. DOI: 10.1016/j.jclepro.2015.09.018.

Rad S.J., Lewis M.J., 2014. Water utilisation, energy utilisation and waste water management in the dairy industry: A review. *Int. J. Dairy Technol.*, 67, 1-20. DOI: 10.1111/1471-0307.12096.

Ramirez C.A., Patel M., Blok K. 2006. From fluid milk to milk powder: Energy use and energy efficiency in the European dairy industry. *Energy*, 31, 1984-2004. DOI: 10.1016/j.energy.2005.10.014.

Steinhoff-Wrześniewska A., Rajmund A., Godzwon J., 2013. Water consumption in selected branches of food industry. *Inżynieria Ekologiczna*, 32, 164–171.

Williams P.J., Anderson P.A., 2006. Operational cost savings in dairy plant water usage. *Int. J. Dairy Technol.*, 59, 147–154. DOI: 10.1111/j.1471-0307.2006.00256.x.

Wojdalski J., Dróżdż B., 2012. Energy efficiency of food processing plants key issues and definitions. *Polish Journal of Food Engineering,* 3/4(3), 37–49.

Wojdalski J., Dróżdż B., Piechocki J., Gaworski M., Zander Z., Marjanowski J., 2013. Determinants of water consumption in the dairy industry. *Pol. J. Chem. Technol.,* 15, 61-72. DOI: 10.2478/pjct-2013-0025.

Wojdalski J., Kaleta A., Dróżdż B., Chojnacka A., 2012. Factors influencing the energy efficiency in dairy processing plants. *TEKA Commission of Motorization and Energetic in Agriculture,* 12(1), 307–313.

Received 08 April 2016
Received in revised form 26 December 2016
Accepted 04 January 2017

DE GRUYTER OPEN
Chemical and Process Engineering 2017, 38 (1), 121-133
DOI: 10.1515/cpe-2017-0010

A SIMPLE ANALYTICAL METHOD FOR DETERMINING BASIC HYDRODYNAMIC CHARACTERISTICS OF HYBRID FLUIDIZED-BED AIR-LIFT APPARATAE

Bolesław Tabiś*, Dominika Boroń

Cracow University of Technology, Department of Chemical and Process Engineering,
ul. Warszawska 24, 30-155 Kraków, Poland

A simple analytical method for determination of basic hydrodynamic characteristics of hybrid fluidized-bed air-lift devices was presented. These devices consist of two parts: a two-phase air-lift part and a two-phase liquid-solid fluidized-bed part. Forced circulation of fluid in the air-lift part is used for fluidization of solid particles in the fluidized-bed part. According to the opinion given in the literature, if such apparatus is used for aerobic microbiological processes, its advantage is lower shear forces acting on the biofilm immobilized on fine-grained material compared with shear forces in three-phase fluidized-bed bioreactors. Another advantage is higher biomass concentration due to its immobilization on fine particles, compared with two-phase airlift bioreactors. A method of calculating gas hold-up in the air-lift part, and gas and liquid velocities in all zones of the analyzed apparatus is presented.

Keywords: fluidized-bed, hydrodynamics, air-lift, hybrid apparatus, bioreactor

1. INTRODUCTION

In aerobic microbiological processes, widespread in biotechnology, several types of bioreactors are used. Tank and column bubble bioreactors are the simplest types of reactor construction. Air-lift devices, both with an external and internal circulating tube, are also classified as bubble bioreactors.

Fluidized-bed two- and three-phase bioreactors have been proposed in the last decades to increase mean biomass concentration inside the apparatus. Utilization of fine particles in fluidized-bed bioreactors facilitates a greater mass transfer surface between the liquid phase and the biofilm. In addition, fluidization prevents bed clogging, which can occur in fixed-bed bioreactors, for example in biofilters.

Immobilization of microorganisms in the fluidized bed has other advantages as well (Mowla and Ahmadi, 2007; Tang and Fan, 1987), such as: i) an increase in the overall microbiological process rate because of high total biomass concentration, ii) a possibility of continuous exchange of bioparticles and supervision of the thickness and age of biofilm, iii) a smaller device, compared with other reactors of the same efficiency.

The advantages of fluidized-bed bioreactors have caused significant spread of this type of devices (Tabiś and Stryjewski, 2013). Fluidized-bed bioreactors usually are three-phase vessels. They can be divided into bioreactors without liquid recirculation (Fig. 1a) and bioreactors with internal circulation used as fluidized-bed air-lift reactors (Fig. 1b-d). Aeration intensity has an essential influence on the

---

*Corresponding author, e-mail: btabis@usk.pk.edu.pl hydrodynamic characteristics of such bioreactors. A sufficiently high gas flow rate may cause internal circulation of all three phases, i.e. liquid, gas and solid phase (Fig. 1d).

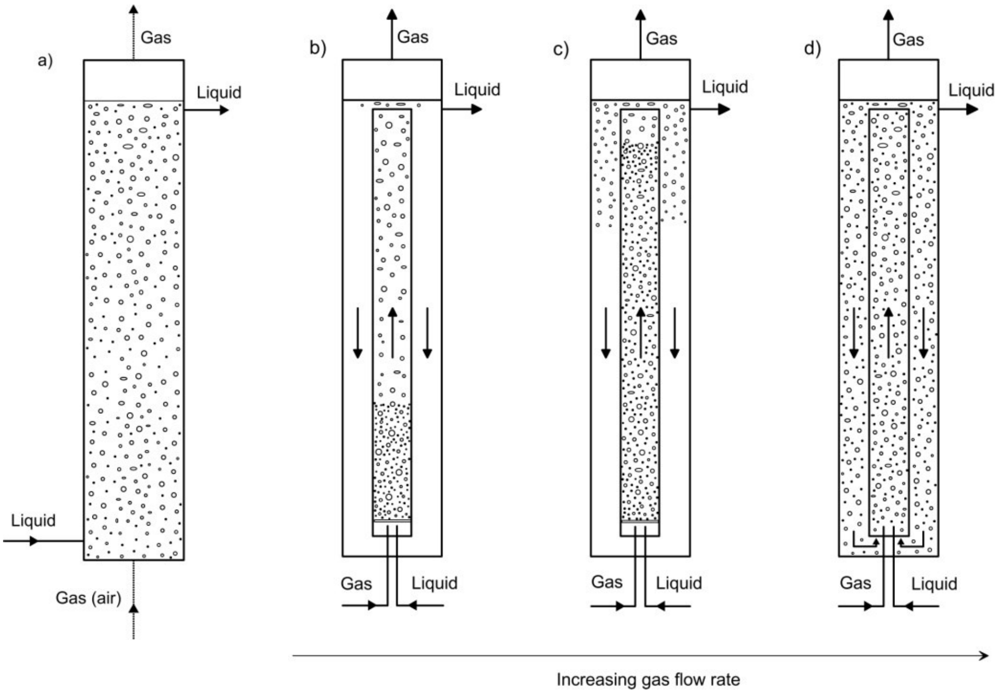

Fig. 1. Two configurations of three-phase bioreactors a) bubble column three-phase bioreactor; b) – d) possible hydrodynamic conditions in a three-phase air-lift bioreactor

Three-phase bioreactors have been the subject of numerous studies in various scientific centers throughout the world. These investigations concerned hydrodynamics (Heijnen et al., 1997; Kawalec-Pietrenko, 2004; Lu, Hwang and Chang, 1995; Merchuk and Siegel, 1988; Merchuk, 2003; Miyahara and Kawate, 1993; Nore et al., 1992; Vuniak-Novakovic et al., 1992), as well as microbiological processes carried out in such devices (Dunn et al, 2003; Huang et al., 1997; Livingstone, 1991; Onysko et al., 2002; Sarra et al., 1997; Tabiś and Georgiou, 2003; Wisecarver and Fan, 1989).

In spite of many advantages mentioned above, three-phase bioreactors have an essential disadvantage. It consists in the existence of shear forces appearing near the gas sparger and in the surrounding of gas bubbles. These forces destroy the biofilm formed on fine particles of inert support. This phenomenon results in a detachment of the biofilm and its drifting with the liquid phase. Guo et al. (1997) and Olivieri et al. (2010) consider this phenomenon as the main disadvantage of three-phase fluidized-bed bioreactors. Therefore a number of scientists analyzed two-phase devices (Dziubiński and Sowiński, 1999; Dziubiński and Sowiński, 2002; Grzywacz, 2013; Kawalec-Pietrenko and Holowacz, 1998). Another question is to separate bioparticles from aeration zone (Dunn et al., 1983; Kawalec-Pietrenko, 2004). There is also a number of publications concerning inverse fluidized-bed airlift reactors. They deal with such issues as hydrodynamics, mass transfer conditions and process parameters (Garnier et al., 1990; Kawalec-Pietrenko and Łazarczyk, 2004; Kawalec-Pietrenko and Matczak, 2006; Kawalec-Pietrenko, 2000). These devices use low density particles. However, particle heavier than liquid phase are also frequently used in microbiological processes.

2. HYBRID FLUIDIZED-BED AIR-LIFT APPARATUS

A concept of hybrid fluidized-bed bioreactors with a two phase fluidized bed was proposed and published in the late 1990s (Guo et al., 1997) and then at the beginning of the present century (Olivieri et al., 2010). The two fundamental ideas of these hybrid bioreactors are the increase of biomass concentration in comparison with air-lift bioreactors and the separation of the gas phase from the fluidized bed. There are two characteristic components which determine the work mode of the hybrid devices. One part of the apparatus works as a two-phase gas-liquid air-lift device. The other part is a two-phase liquid-solid fluidized-bed vessel. The forced circulation of liquid in the air-lift part maintains fluidization of solid particles in the fluidized-bed part. The hybrid apparatus can operate with external (Fig. 2a), as well as with internal circulation of liquid (Fig. 2b). Figure 2b shows characteristic dimensions used for a quantitative description of the hydrodynamics of the device considered bellow.

The authors have analyzed the hydrodynamic characteristics of the apparatus presented in Fig. 2b. The gas phase, i.e. air, is supplied at a certain height of the internal circulation tube. The movement of the liquid is caused by density difference between the riser „2" and the downcomer „3". The liquid flows through an annular cross section to the lower part of the apparatus (zone number „1") beneath the perforated bottom. If the velocity of liquid circulation is high enough, solid particles start to fluidize. An additional net beneath the gas sparger retains solid particles in the upper section „2".

Although hybrid fluidized-bed devices are rather novel and not well-known yet such constructions of the reactors have been used in biotechnology. Up to date, both steady-state and dynamic properties of such bioreactors are unknown. During numerical simulation of such devices working as bioreactors, one has to solve model equations many times, which is a time consuming operation. Thus it will be useful for engineers to have a rather simple analytical model describing the hydrodynamics of such devices. Wherefore, the aim of the work was to propose a simple method for fast estimation of basic hydrodynamic parameters needed for the simulation of hybrid fluidized-bed microbiological reactors. On the basis of the proposed model some hydrodynamic limitations imposed on the operation of such devices may also be determined. The presented results of numerical experiments make the choice of the operating parameters easier. It is important not only for numerical simulations, but also for the engineers who will deal with hybrid fluidized-bed bioreactors in the future.

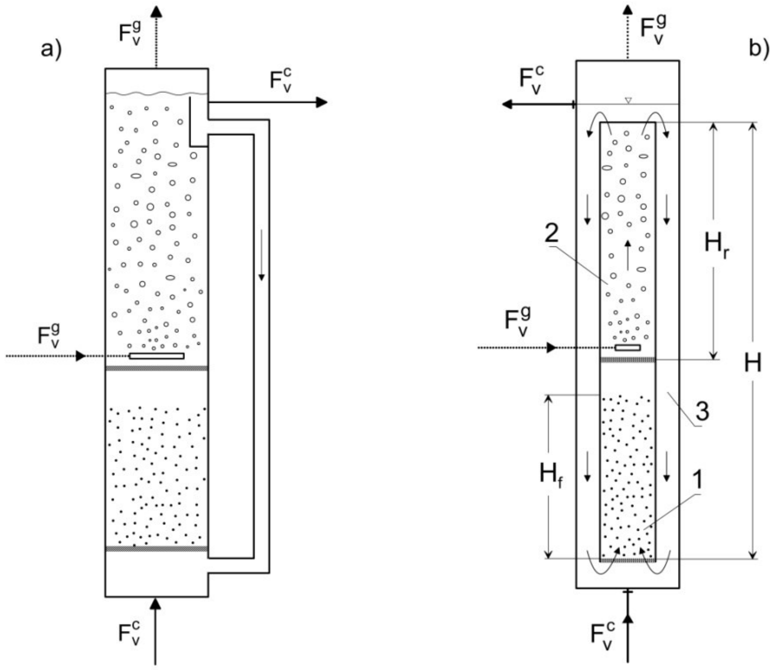

Fig. 2. Two types of hybrid fluidized-bed devices; a) apparatus with external recirculation of the liquid phase; b) apparatus with an internal draft tube

3. HYDRODYNAMIC MODEL OF A CONTINUOUS HYBRID FLUIDIZED-BED AIR-LIFT APPARATUS

In order to model and design a hybrid apparatus (shown in Fig. 2b), the following hydrodynamic quantities are needed: i) superficial liquid velocity in the zone „1", u_{0c1}, ii) gas hold-up, ε_2, and velocity of gas, u_{g2}, in the riser „2", iii) superficial velocity of liquid in the riser zone, u_{0c2}, iv) superficial velocity of liquid in the downcomer zone, u_{0c3}, v) dynamic height of the fluidized bed, H_f.

The superficial velocity of liquid in the fluidized-bed zone should satisfy the conditions:

$$u_{mf} < u_{0c1} < u_t \tag{1}$$

It is well known that fluidized-bed expansion depends on the velocity of a fluidizing medium. Therefore, we should impose another condition on the superficial liquid velocity in zone „1", that is:

$$u_{0c1} : H_f < H - H_r \tag{2}$$

The superficial liquid velocity in zone „3" should be lower than slip velocity, that was defined by Heijnen et al. (1997). This velocity may be calculated as follows

$$\upsilon = 1.53 \cdot \left(\frac{g\sigma(\rho_c - \rho_g)}{\rho_c^2} \right)^{0.25} \tag{3}$$

The liquid velocity in the downcomer „3" should satisfy the following condition:

$$u_{c3} = u_{0c3} < \upsilon \tag{4}$$

The last inequality indicates that gas bubbles do not enter the downcomer. This, in turn, prevents the gas phase from penetrating the fluidized-bed zone.

The density difference between the two-phase medium in the zone „2" and the degassed liquid in the zone „3" is a driving force needed for liquid circulation between the air-lift zone and the fluidized-bed zone. The pressure difference between both zones can be written as

$$\Delta p = H_r \varepsilon_2 \rho_c g \tag{5}$$

The driving force of the liquid phase movement at steady state is balanced by the following pressure drops:

i) pressure drops in the internal tube (zone „1" and „2") and the downcomer zone „3"

$$\Delta p_1 = 0.5\lambda_1 \frac{H - H_r}{d_1} u_{c1}^2 \rho_c \tag{6}$$

$$\Delta p_2 = 0.5\lambda_2 \frac{H_r}{d_2} u_{c2}^2 \rho_c \tag{7}$$

$$\Delta p_3 = 0.5\lambda_3 \frac{H}{d_h} u_{0c3}^2 \rho_c, \quad d_h = d_3 - d_2 \tag{8}$$

ii) pressure drop in the fluidized bed

$$\Delta p_f = H_{mf}(\rho_s - \rho_c)(1 - \varepsilon_{mf})g \tag{9}$$

iii) pressure drop in the surroundings of the lower edge of the draft tube

$$\Delta p_b = 0.5 \zeta_b u_{0c3}^2 \rho_c \tag{10}$$

iv) pressure drop at both nets

$$\Delta p_s = \zeta_s u_{c1}^2 \rho_c \tag{11}$$

The following formula results from the comparison of the impellent and total pressure drop

$$\Delta p = \Delta p_1 + \Delta p_2 + \Delta p_3 + \Delta p_f + \Delta p_b + \Delta p_s \tag{12}$$

A slightly different approach to calculating the pressure balance was proposed by Olivieri et al. (2010). However, it is possible to show that their method gives the same outcomes like the one presented in this work.

In order to calculate the above-mentioned hydrodynamic parameters, i.e. superficial liquid velocity and gas velocity and gas hold-up in zone number „2", one has to complete Eq. (12) with the gas and liquid mass balances:

$$S_2 \varepsilon_2 (u_{c2} + \upsilon) = S_2 u_{0g} \tag{13}$$

$$S_2 (1 - \varepsilon_2) \cdot u_{c2} = S_3 u_{0c3} + F_V^c = S_3 u_{0c3} + S_2 u_{0c} \tag{14}$$

At steady-state conditions, liquid velocities in zones „1" and „2" are tied up by the following continuity equation:

$$S_1 u_{0c1} = S_2 u_{c2} (1 - \varepsilon_2) \tag{15}$$

Based on Eqs. (14) and (15), it is possible to calculate the superficial liquid velocities in zones „1" and „3", which occur in Eqs. (6), (8), (10) and (11):

$$u_{0c1} = \frac{S_2}{S_1} u_{c2} (1 - \varepsilon_2) \tag{16}$$

$$u_{0c3} = \frac{S_2}{S_3} \left[(1 - \varepsilon_2) \cdot u_{c2} - u_{0c} \right] \tag{17}$$

In this way, the gas hold-up in zone „2", ε_2 , and the liquid velocity in this zone, u_{c2}, are the only unknown variables. To calculate these quantities, we can use two equations:

$$\varepsilon_2 u_{g2} - u_{0g} = f_1(\varepsilon_2, u_{c2}) = 0 \tag{18a}$$

$$\Delta p - \Delta p_1 - \Delta p_2 - \Delta p_3 - \Delta p_f - \Delta p_b - \Delta p_s = f_2(\varepsilon_2, u_{c2}) = 0 \tag{18b}$$

These are two nonlinear algebraic equations with respect to ε_2 and u_{c2}. They can be solved by Newton method, for instance. In this paper, hydrodynamic properties of a hybrid fluidized-bed bioreactor are described by a set of six functions: $u_{0c1}(u_{0g})$, $\varepsilon_2(u_{0g})$, $u_{g2}(u_{0g})$, $u_{0c2}(u_{0g})$, $u_{0c3}(u_{0g})$, $H_f(u_{0g})$. These functions were evaluated in a certain range of values $u_{0g} \geq u_{0g,\min}$. This range satisfies the conditions (1), (2) and (4), where:

$$u_{0g,\min} : u_{0c1} = u_{mf} \tag{19}$$

Condition (2) was verified by calculating the dynamic bed height, H_f, for each value of u_{0g}, according to empirical relationships

$$H_f = H_{mf} \frac{(1 - \varepsilon_{mf})}{(1 - \varepsilon_f)} \tag{20}$$

or

$$\frac{H_f}{H_{mf}} = f\left(\frac{u_{0c1}}{u_{mf}}\right) \tag{21}$$

When modeling the hydrodynamics of the hybrid fluidized-bed apparatus, it is important to choose an accurate formula, that allows to calculate the dynamic height of the fluidized bed in the entire range of fluidization ratio, especially for l_f close to l_{ft}. It is so because inequality (2) has to be fulfilled. In order to verify the existing correlations, experimental measurements of expansion of two-phase liquid-solid beds were performed. The results of these measurements are presented in Fig. 3. Various densities of solid particles were considered. The properties of solids are presented in Table 1. The Morphologi G3, a high-accuracy analyzer of the size and shape of particles was used to obtain geometrical characteristics of solid particles. This microscope with dedicated software determines the diameter and shape factor for every single particle. The result is the distribution of geometrical parameters of a test sample. Furthermore, it is possible to calculate the mean parameters of fine-grained materials. The fluidization agent was tap water. Homogeneous fluidization was observed over the whole range of the fluidization ratio.

Table 1. Properties of analyzed fine-grained materials

	Density, kg/m^3	Range of diameters, m	Height of the fluidized bed at minimum fluidization conditions, m
coal	1412	$4.25\cdot10^{-4}$ - $8.0\cdot10^{-4}$	0.02; 0.04; 0.06
brick	2384	$4.25\cdot10^{-4}$ - 10^{-3}	0.02; 0.04; 0.06
sand	2620	$4.25\cdot10^{-4}$ - 10^{-3}	0.02; 0.04; 0.06

The results of the experiments presented in Fig. 3 show that association of the dynamic bed height solely with the fluidization ratio is rather scanty. For the high fluidization ratio, the experimental data are scattered. This indicates the existence of an additional dependence of the bed height on other parameters.

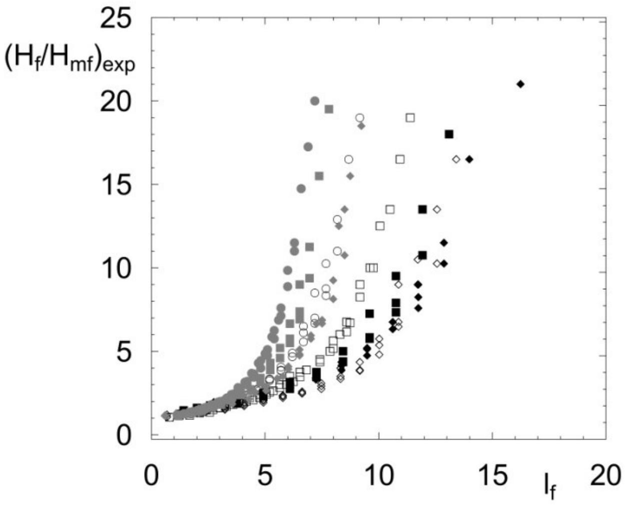

Fig. 3. Experimental data of liquid-solid fluidized-bed expansion (◇ – sand $d_s = 0.53$ mm, ◆ – coal $d_s = 0.53$ mm; ◆ – brick $d_s = 0.53$ mm; □ – sand $d_s = 0.72$ mm, ■ – coal $d_s = 0.72$ mm; ■ – brick $d_s = 0.72$ mm; ○ – sand $d_s = 0.90$ mm, ● – brick $d_s = 0.90$ mm)

In the literature there exist a lot of empirical correlations that tie porosity or height of a fluidized bed with fluidizing medium velocity and with physicochemical properties of both phases. They are quoted in many papers concerning fluidized-bed hydrodynamics, among others, the works of Di Felice (1995), Kmieć (1980), Razumov (1975) and Tripathy et al., (2013).

To calculate a dynamic bed height, one can use the empirical Eq. (21) or more complicated equations, which account for physiochemical properties of the heterogeneous environment

$$f\left(\frac{H_f}{H_{mf}}\right) = \varphi(\mathrm{Re}, \mathrm{Ar}, l_f, \Phi) \tag{22a}$$

Reynolds number Re and Archimedes number Ar in Equation (22a) can be calculated according to formulas (22b) and (22c)

$$\mathrm{Re} = \frac{u_{0c} d_1 \rho_c}{\eta_c} \tag{22b}$$

$$\mathrm{Ar} = \frac{g d_s^3 (\rho_s - \rho_c) \rho_c}{\eta_c^2} \tag{22c}$$

A simple, two-parameter correlation to calculate ε_f was proposed by Razumow (1975)

$$\varepsilon_f = 1 - \frac{1 - \varepsilon_{mf}}{a + b l_f} \tag{23}$$

In this formula parameters a and b are experimental values.

Another correlation, published recently by Tripathy (2013), is

$$\frac{H_f}{H_{mf}} = 1 + 6 \cdot 10^{-7} \cdot l_f^{1.4046} \cdot \left(\frac{\rho_c}{\rho_s}\right)^{1.4843} \left(\frac{d_r}{d_s}\right)^{1.962} \tag{24}$$

whereas Kmieć (1980) proposed the following empirical formula to calculate ε_f

$$\varepsilon_f = 1.733 \cdot \mathrm{Re}_s^{0.2926} \cdot \mathrm{Ar}^{-0.209} \tag{25a}$$

Reynolds number Re_s in Equation (25a) is defined as

$$\mathrm{Re}_s = \frac{u_{0c} d_s \rho_c}{\eta_c} \tag{25b}$$

The expansion of the fluidized bed may also be calculated from semi-empirical equations. For example, in order to apply Leva`s equation (1959), one has to assume that a fluidized bed is considered to be a fixed bed with changing porosity. Furthermore, while using this equation, one has to assume a constant pressure drop during fluidization with changing velocity of liquid, which is a property of a fluidized bed. Thus, Leva`s equation takes the following from

$$\lambda \cdot \frac{u_f^2}{2 d_s} \cdot \rho_c \left(\frac{(1 - \varepsilon_f)^{2-n}}{\varepsilon_f^{\,3}} \cdot \Phi^{3-n}\right) - (\rho_s - \rho_c) \cdot g = 0 \tag{26}$$

In Eq. (26), empirical dependency $\lambda(\mathrm{Re}_s, \varepsilon_f)$ proposed by Ergun (1952) may be applied. In this way, we obtain Eq. (27)

$$\frac{150 \cdot (1 - \varepsilon_f)}{\varepsilon_f^{\,3} \cdot \Phi_s^{\,2}} \cdot \mathrm{Re}_s^{\,2} + \frac{1.75}{\varepsilon_f^{\,3} \cdot \Phi_s} \cdot \mathrm{Re}_s^{\,2} - \mathrm{Ar} = 0 \tag{27}$$

On the other hand, the streamlined model, presented by Dziubiński and Prywer (2009), results from the balance of forces for a single solid particle. The force of gravity is compared with the sum of buoyancy and viscous drag forces. On this basis the following dependency (Dziubiński and Prywer, 2009) was proposed

$$\varepsilon_f^{4.7} = \frac{(C_x)_u \cdot A_s \cdot \rho_c \cdot u_f^2}{2 \cdot V_s \cdot g \cdot (\rho_s - \rho_c)} \tag{28}$$

Figure 4 shows the results obtained using several empirical and semi-empirical equations considering two-phase liquid-solid fluidized-bed expansion. Our own experimental data are also given.

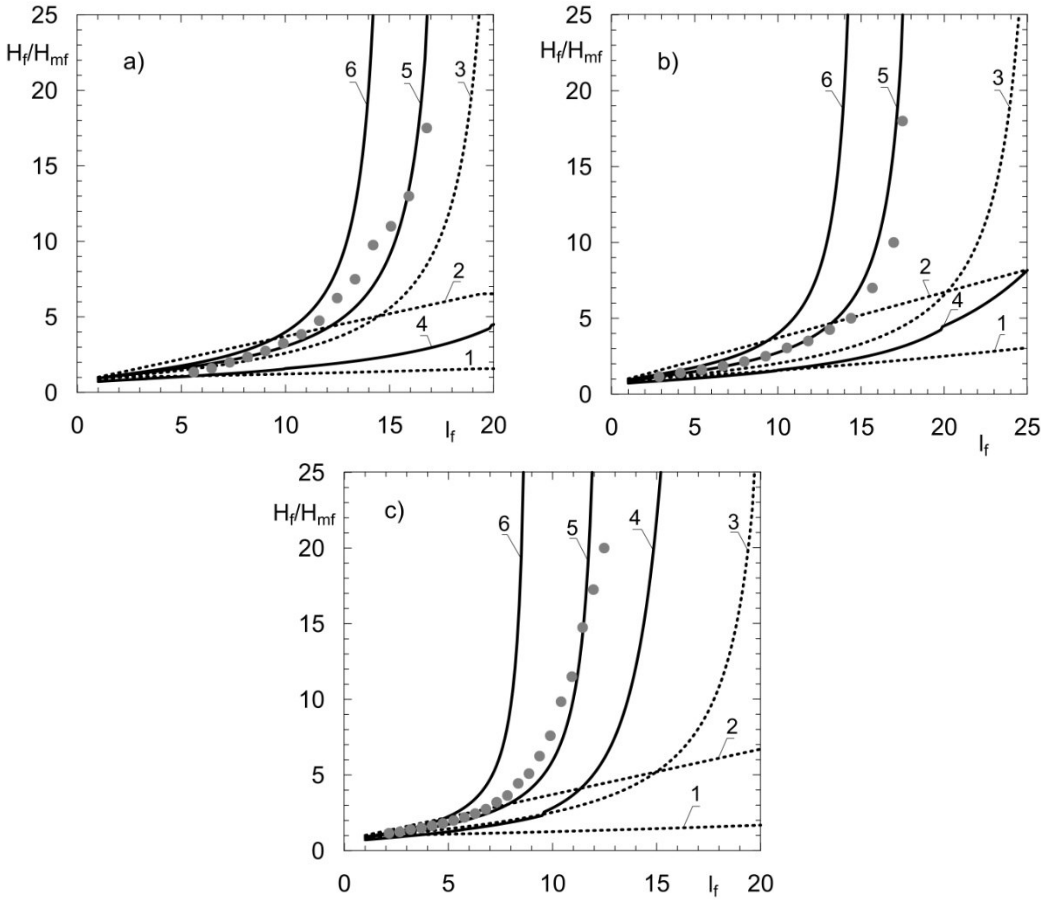

Fig. 4. Comparison of experimental and calculated bed expansion for two-phase liquid-solid fluidization (a- sand, $d_s = 0.90$ mm, $\rho_s = 2620$ kg/m^3; b- coal, $d_s = 0.90$ mm, $\rho_s = 1412$ kg/m^3; c- brick , $d_s = 0.90$ mm, $\rho_s = 2384$ kg/m^3) 1- Thripaty (2013); 2- Razumow (1975) (a= 0.715; b = 0.30); 3- Kmieć (1980); 4- Leva (1959); 5- Dziubiński (2009); 6- Ergun (1952); ● – experimental data

The graphs presented in Figs. 4a and 4b indicate that for $l_f < 10$ the experimental data H_f/H_{mf} lie between the values calculated according to Razumow and Tripathy correlations. In Fig. 4c this condition is fulfilled for $l_f < 5$. As the fluidization ratio increases, the calculated values of fluidized-bed expansion based on selected empirical correlations diverges more and more from the experimental data. The correlation proposed by Kmieć (1980) reflects the tendency of nonlinear rise in the fluidized-bed expansion along with an increasing fluidization ratio. However, this tendency is smaller than that obtained from the experimental data. None of the tested empirical relations predict exactly the increase in the fluidization-bed height for a high fluidization ratio, i.e. when superficial liquid velocity, u_{0c}, approaches the terminal velocity of solid particles, u_t. On the other hand, all semi-empirical correlations reflect a nonlinear rise in the fluidized-bed height. The formula proposed by Dziubiński et al. (2009) seems to have the smallest errors for high values of l_f, therefore it was decided to use it in subsequent calculations.

The results of calculations of hydrodynamic characteristics of the analyzed hybrid apparatus, according to the proposed model shown above, are presented in Fig. 5 and Fig. 6. These graphs were plotted for selected operating parameters, which are reported in Table 2.

Table 2. Values of parameters used for calculations of hydrodynamics characteristics

Parameter	a)	b)	c)	Dimension
d_1	0.2	0.2	0.2	m
d_2	0.2	0.2	0.2	m
d_3	0.25	0.23	0.25	m
H	3	3	2	m
H_r	1.5	1.5	1.5	m

For all analyzed cases values of the other parameters were the same, i.e.: $d_s = 7\cdot10^{-4}$ m; $\rho_s = 1800$ kg·m^{-3}; $H_{mf} = 0.1$ m; $\varepsilon_{mf} = 0.5$; $\rho_c = 1000$ kg·m^{-3}; $\eta_c = 0.001$ kg·m^{-1}·s^{-1}; $\sigma_c = 7.27\cdot10^{-2}$ kg·s^{-2}.

Figure 5 shows the relationship between superficial liquid velocity in the zone number „1", u_{0c1}, and superficial gas velocity u_{0g}. The superficial velocity of liquid in this zone has two limits according to inequalities (1). These limits are marked in Fig. 5 by dotted lines. Figure 5a shows that for given dimensions of the bioreactor and according to Razumow's correlation (1975), it is possible to achieve two limit values u_{0g}, for which $u_{0c1} = u_{mf}$ or $u_{0c1} = u_t$. When applying Dziubiński`s formula (2009), which is considered to be the most reliable, in the device of the same dimensions it is not possible to fulfill the equality $u_{0c1} = u_t$, because already at a lower superficial velocity, u_{0c1}, the other limiting value, corresponding to the bed height is satisfied (condition (2)).

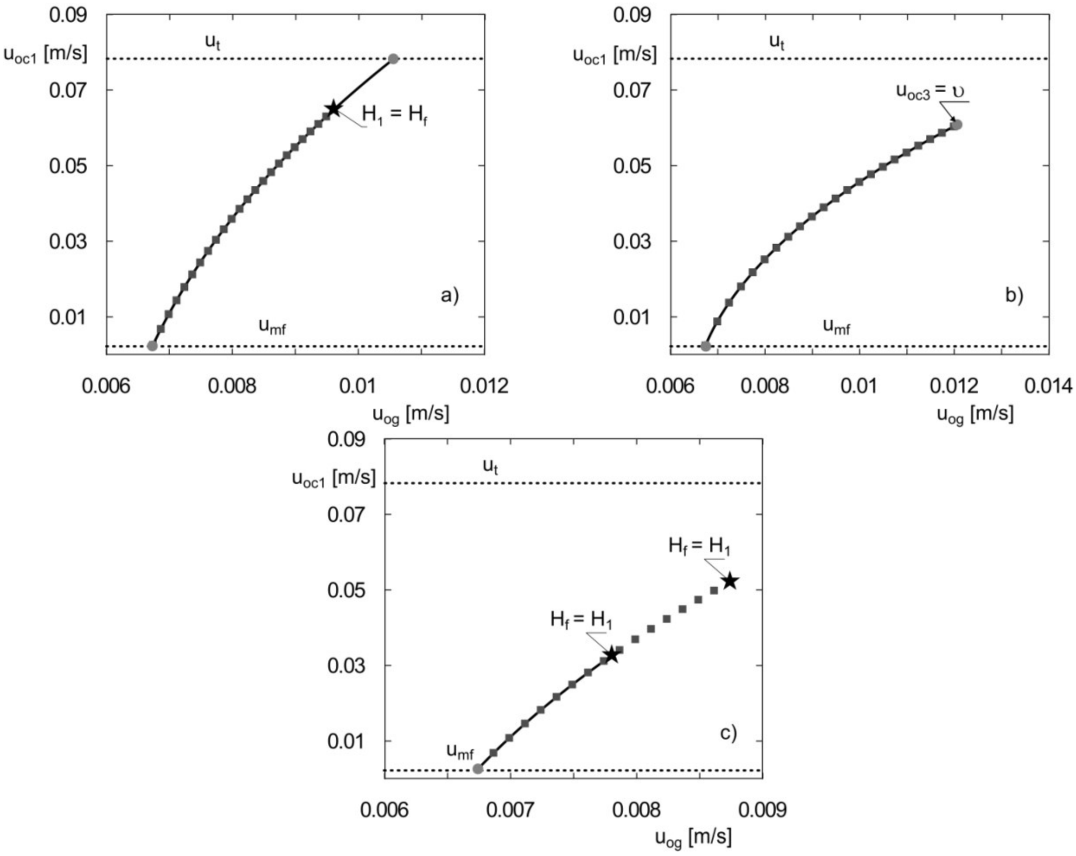

Fig. 5. Limit values of superficial gas velocity u_{0g} for various sizes of bioreactors
(— Razumow (1975); ■ - Dziubiński (2009))

If the column diameter, d_3, decreases, superficial liquid velocity in zone „3", u_{03}, can be higher than the slip velocity of gas bubbles. In this work it is assumed that there are no gas bubbles in zone „3". Therefore, the condition $u_{0c3} = \upsilon$ determines the maximum value of superficial gas velocity, u_{0g}. That limitation is shown in Fig. 5b. The application of Razumow`s (1975) and Dziubiński`s (2009) formulas gives similar results. Because of sufficient height of the device, despite bigger bed expansion calculated according to Dziubiński`s formula (2009), the fluidized bed does not achieve the height of zone "1".

The graph presented in Fig. 5c corresponds to the situation when the upper limit value of superficial gas velocity, u_{0g}, is determined by the height of zone number „1". An increase in superficial gas velocity, u_{0g}, causes an increase in liquid circulation velocity in the device as well as expansion of the fluidized bed in zone „1". Thus for given dimensions of the reactor it is possible to determine the limit value of superficial gas velocity, for which $H_f = H_1$, where $H_1 = H - H_r$. According to Dziubiński`s formula (2009) the limit bed height, $H_f = H_1$, was achieved for lower values of superficial liquid velocity, $u_{0c1}$, than those calculated from Razumow`s formula quoted before. The dynamic bed height calculated from Razumow`s correlation is higher compared with experimental data for low fluidization ratios (Fig. 4). The analysis preformed here leads to the conclusion that the device works in the range of low values of fluidization ratio, $l_f$, for lower heights of zone "1". Therefore, the application of Dziubiński`s formula (2009) is recommended because designing such devices seems to be much safer. This correlation was experimentally verified in a wide range of fluidization ratios by the authors.

Maximum and minimum superficial gas velocities, u_{0g}, which ensure effective utilization of the fluidized-bed part of the apparatus, depend on physical properties of liquid, gas and solids. In Fig. 6 the mentioned limit values of superficial gas velocity, as two functions of Archimedes number for a device with given dimensions i.e. H, H_r and d_3 are shown. The upper curve corresponds to the values of u_{0g}, for which the superficial liquid velocity, u_{0c1}, in the fluidization zone is equal to the terminal velocity of solids, i.e. $u_{0c1} = u_t$. The lower curve corresponds to the values of u_{0g}, for which $u_{0c1} = u_{mf}$. The limit curves presented in Fig. 6 may be considered as a basis for designing such hybrid devices. The lower limit of superficial velocity is appropriate for an apparatus with any height of fluidization zone, H_1. On the other hand, the upper limit should be taken into consideration for a high enough fluidization zone which satisfies condition (2). For this reason it may be used for evaluation of the maximum height of this zone while designing such devices.

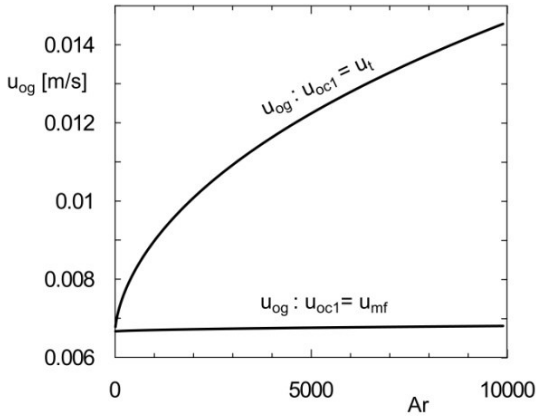

Fig. 6. Lower and upper limits of superficial gas velocity versus Archimedes number ($H = 3$ m, $H_r = 1.5$ m, $d_1 = 0.2$ m, $d_2 = 0.2$ m, $d_3 = 0.25$ m)

4. CONCLUSIONS

Hydrodynamic characteristics of a hybrid apparatus consisting of an air-lift and two-phase fluidized-bed parts is presented. The application of this type of hybrid devices working as bioreactors brings about higher biomass concentration and eliminates main problems arising from the use of three-phase fluidization. However, splitting the apparatus into two parts makes it possible to work only within a specific range of operating and geometrical parameters. It is caused by hydrodynamic limitations tied up with proper work of such devices.

For the purpose of simulating and designing hybrid fluidized-bed bioreactors it is necessary to create simple and sufficiently accurate equations for momentum and mass balances of flowing media. This paper presents equations that allow to assess the operating parameters influencing hydrodynamics of such devices. The presented hydrodynamic model facilitates the proper selection of basic reactor geometry, i.e. diameters and heights of particular zones. When the analysis of a reactor existing in a real installation is performed, we can determine the ranges of operating parameters, wherein the apparatus may work correctly, i.e. as a hybrid device.

In this work, selected and representative correlations for calculation of fluidized-bed expansion are compared. Our work contains only a few correlations arisen in 1952- 2013. Correct determination of the dynamic height of fluidized bed is an essential element during the process design, numerical simulations, and technological practice. Incorrect matching of the fluidized bed height makes it impossible for the apparatus to work. If the height of this zone is insufficient, fine-grained solid will accumulate under the upper net. This will result in the presence of a fixed bed instead of a fluidized bed. On the other hand, an excessive increase of the height of this zone brings about the increase of pressure drop tied up with medium flow and it could make liquid circulation impossible.

Hydrodynamic analysis of hybrid fluidized-bed bioreactors is important because of the possibility of utilizing these reactors in many aerobic bioprocesses. The appropriate selection of hydrodynamic and geometrical parameters is the basis for modeling and designing microbiological processes in such bioreactors.

SYMBOLS

Ar	Archimedes number
A	surface area, m^2
$(C_x)_u$	drag coefficient
d	diameter, m
F_V^g, F_V^c	volumetric flow rate of gas and liquid, respectively, m^3/s
g	gravity acceleration, m/s^2
H	total height of the bioreactor, m
H_f	dynamic height of the fluidized bed, m
H_r	height of the riser, m
l_f	fluidization ratio, $l_f = u_{0c}/u_{mf}$
l_{fmin}, l_{ft}	fluidization ratio corresponding u_{mf} and u_t, respectively
n	index parameter , $n=f(\mathrm{Re}_s)$
Δp	pressure drop, Pa
S	cross sectional area, m^2
u_c, u_g	velocity of liquid and gas, m/s
u_{mf}	minimum fluidization velocity, m/s
u_t	terminal velocity of solid particles, m/s
V	volume, m^3

Greek symbols

ε_f	dynamic porosity of fluidized bed
ζ	local friction factor

η	viscosity, kg/(m·s)
λ	friction factor
ρ	density, kg/m^3
σ	surface tension, kg/s^2
υ	slip velocity of gas bubbles, m/s
Φ	shape coefficient

Subscripts

1, 2, 3	refers to a particular zone (see Fig.2b)
0	values referring to the cross sectional area of a particular zone
b	surroundings of the lower edge of the riser
c	liquid
f	refers to fluidized bed
k	column
mf	refers to minimum fluidization conditions
r	riser
s	solid
t	refers to terminal velocity of solid particles

REFERENCES

Dunn I.J., Tanaka H., Uzman S., Denac M., 1983. Biofilm fluidized-bed reactors and their application to waste water nitrification. *Ann. NY Acad. Sci.*, 413, 168-183. DOI: 10.1111/j.1749-6632.1983.tb47887.x.

Dunn I.J., Heinzle E., Ingham J., Prenosil J.E., 2003. *Biological reaction engineering. Dynamic modelling fundamentals with simulation examples*. Wiley-VCH Verlag, Weinhem.

Di Felice R., 1995. Hydrodynamics of liquid fluidisation. *Chem. Eng. Sci*., 50, 1213-1245. DOI: 10.1016/0009-2509(95)98838-6.

Dziubiński M., Prywer J., 2009. *Two-phase fluid mechanics* (*Mechanika płynów dwufazowych*). WNT, Warszawa, Poland.

Dziubiński M., Sowiński J., 1999. The specific interfacial area in an air-lift column (*in Polish*). *Chem. Proc. Eng.*, 20(3), 409-421.

Dziubiński M., Sowiński J., 2002. Liquid circulation velocity in pilot-plant scale air-lift columns (*in Polish*). *Chem. Proc. Eng*., 23, 141-150.

Ergun S., 1952. Fluid flow through packed columns. *Chem. Eng. Prog*., 48, 89-94.

Garnier A., Chavarie C., Andre G., Klvana D., 1990. The inverse fluidization airlift bioreactor, Part I: hydrodynamic studies. Chem. Eng. Comm., 98 , 31–45. DOI: 10.1080/00986449008911559.

Grzywacz R., 2013. *Airlift Bioreactor*. Wydawnictwo Politechniki Krakowskiej, Kraków, Poland.

Guo Y.X., Rathor M.N., Ti H.C., 1997. Hydrodynamic and mass transfer studies in a novel external-loop airlift reactor. *Chem. Eng. J.*, 67, 205-214. DOI: 10.1016/S1385-8947(97)00043-0.

Heijnen J.J., Hols J., Van der Lans R.G.J.M., Van Leeuwen H.L.J.M., Mulder A., Welte-vrede R., 1997. A simple hydrodynamic model for the liquid circulation velocity in a full scale two- and three-phase internal airlift reactor operating in the gas recirculation regime. *Chem. Eng. Sci*., 52, 2527-2540. DOI: 10.1016/S0009-2509(97)00070-5.

Huang Y.L., Shu C.H., Yang S.T., 1997. Kinetics and modeling of GM-CSF production by recombinant yeast in 3-phase fluidized-bed bioreactor. *Biotechnol. Bioeng*., 53, 470-477. DOI: 10.1002/(SICI)1097-0290(19970305)53:5<470:AID-BIT4>3.0.CO;2-E.

Kawalec- Pietrenko B., 2000. Liquid circulation velocity in the inverse fluidized bed airlift reactor. *Bioproc. Eng.*, 23, 397-402. DOI: 10.1007/s004499900182.

Kawalec- Pietrenko B., 2004. Three-phase airlift reactors (*in Polish*). *Chem. Proc. Eng*., 25, 1925-1935.

Kawalec- Pietrenko B., Holowacz I., 1998. Region-dependent oxygen transfer rate in the rectangular airlift reactor. *Bioproc. Eng.*, 18, 163-170. DOI: 10.1007/s004490050426.

Kawalec- Pietrenko B., Łazarczyk M., 2004. Application of an air-lift reactor with the inverse fluidized-bed in biodegradation of dimethyl ketone *(in Polish). Inż. Ap. Chem*., 2, 3-5.

Kawalec- Pietrenko B., Matczak B., 2006. Comparison of the oxygen transfer rate in the inverse fluidized-bed airlift reactor and related bubble column reactors (*in Polish*). *Chem. Proc. Eng*., 27, 125-139.

Kmieć A., 1980. *Bed expansion and heat and mass transfer in fluidized beds* (*in Polish*). Scientific papers of the Institute of Chemical Engineering and Heating Equipment, Wrocław, Poland.

Leva M., 1959. *Fluidization*, Mc Graw-Hill, New York.

Livingston A.G., 1991. Biodegradation of 3,4-dichloroaniline in a fluidized bed reactor and a steady state biofilm kinetic model. *Biotechnol. Bioeng*., 38, 260-272. DOI: 10.1002/bit.260380308.

Lu W.J., Hwang S.J., Chang C.M., 1995. Liquid velocity and gas holdup in three-phase internal loop airlift reactors with low-density particles. *Chem. Eng. Sci*., 50, 1301-1310. DOI: 10.1016/0009-2509(95)98842-3.

Merchuk J.C., 2003. Airlift bioreactors: review of recent advances. *Can. J. Chem. Eng.*, 81, 324-337. DOI: 10.1002/cjce.5450810301.

Merchuk J.C., Siegel M.H., 1988. Airlift reactors in chemical and biological technology. *J. Chem. Tech. Biotechnol.*, 41, 105-120. DOI: 10.1002/jctb.280410204.

Miyahara T., Kawate O., 1993. Hydrodynamics of a solid-suspensed bubble column with a draught tube containing low density particles. *Chem. Eng. Sci*., 48, 127-133. DOI: 10.1016/0009-2509(93)80289-3.

Mowla D., Ahmadi M., 2007. Theoretical and experimental investigation of biodegradation of hydrocarbon polluted water in a three phase fluidized-bed bioreactor with PVC biofilm support. *Biochem. Eng. J.* 36, 147-156. DOI: 10.1016/j.bej.2007.02.031.

Nore O., Briens C., Margaritis A., Wild G., 1992. Hydrodynamics, gas-liquid mass transfer and particles-liquid heat and mass transfer in a three-phase fluidized bed for biochemical process applications. *Chem. Eng. Sci*., 47, 3573-3580. DOI: 10.1016/0009-2509(92)85072-J.

Olivieri G., Marzocchella A., Salatino P., 2010. A novel three-phase airlift reactor without circulation of solids. *Can. J. Chem. Eng*., 88, 574-578. DOI: 10.1002/cjce.20314.

Onysko K.A., Robinson C.W., Budman H.M., 2002. Improved modelling of the unsteady-state behavior of an immobilized-cell, fluidized-bed bioreactor for phenol biodegradation. *Can. J. Chem. Eng*., 80, 239-252. DOI: 10.1002/cjce.5450800209.

Razumow I.M., 1975. *Fluidization and pneumatic transport of fine materials (in Polish).* WNT, Warszawa.

Sarra M., Casas C., Godia F., 1997. Continuous production of a hybrid antibiotic by Streptomyces-lividans Tk21 pellets in a 3-phase fluidized-bed bioreactor. *Biotechnol. Bioeng*., 53, 601-610. DOI: 10.1002/(SICI)1097-0290.

Tabiś B., Georgiou A., 2003. Method for the determination of the steady states of a three-phase fluidized-bed bioreactor. *Chem. Proc. Eng*., 24, 551-566.

Tabiś B., Kupiec K., 2003. Hydrodynamics of a three-phase airlift bioreactor containing low-density particles (*in Polish*). *Chem. Proc. Eng*., 24, 217-233.

Tabiś B., Stryjewski W., 2013. Conditions for application of fluidized-bed bioreactors in aerobic processes (*in Polish*). *Inż. Ap. Chem.* 52, 487-489.

Tang W.-T., Fan L.-S., 1987. Steady state phenol degradation in a draft-tube, gas-liquid-solid fluidized-bed bioreactor. *AICHE J.* 33, 239-249. DOI: 10.1002/aic.690330210.

Tang W.T., Wisecarver K., Fan L.S., 1987. Dynamics of a draft tube gas-liquid-solid fluidized bed bioreactor for phenol degradation. *Chem. Eng. Sci*., 42, 2123-2134. DOI: 10.1016/0009-2509(87)85033-9.

Tripathy A., Sahu A.K., Biswal S.K., Mishra B.K., 2013. A model for expansion ratio in liquid-solid fluidized beds. *Particuology*. 11, 789-792. DOI: 10.1016/j.partic.2012.11.006.

Vunjak-Novakovic G., Jovanovic G., Kundakovic L., Obradovic B., 1992. Flow regimes and liquid mixing in a draft tube gas-liquid-solid fluidized bed. *Chem. Eng. Sci*., 47, 3451-3458. DOI: 10.1016/0009-2509(92)85057-I.

Wisecarver K.D., Fan L.S., 1989. Biological phenol degradation in a gas-liquid-solid fluidized bed reactor. *Biotechnol. Bioeng*., 33, 1028-1038. DOI: 10.1002/bit.260330812.

Received 10 July 2015
Received in revised form 27 October 2016
Accepted 12 January 2017

Chemical and Process Engineering 2017, 38 (1), 135-145
DOI: 10.1515/cpe-2017-0011

COAL CHAR KINETICS OF OXIDATION AND GASIFICATION REACTIONS

Robert Lewtak*, Jarosław Hercog

Institute of Power Engineering, Thermal Processes Department, Augustówka 36, 02-981 Warsaw, Poland

Experimental investigations and numerical simulations have been conducted in this study to derive and test the values of kinetic parameters describing oxidation and gasification reactions between char carbon and O_2 and CO_2 occurring at standard air and oxy-fuel combustion conditions. Experiments were carried out in an electrically heated drop-tube at heating rates comparable to full-scale pulverized fuel combustion chambers. Values of the kinetic parameters, obtained by minimization of the difference between the experimental and modeled values of char burnout, have been derived and CFD simulations reproducing the experimental conditions of the drop tube furnace confirmed proper agreement between numerical and experimental char burnout.

Keywords: kinetic parameters, char particle oxidation and gasification, oxy-fuel combustion

1. INTRODUCTION

From the three main groups of the CCS technologies, oxy–fuel combustion seems to be the most promising one due to the lowest energy penalty associated with the investment and operational costs (Jenni et al., 2013). The main feature of this technology is the combustion of fuel in the mixture of recycled flue gases and O_2. However, diluents present in a combustion system, such as CO_2 and H_2O, have different physical and chemical properties than N_2 present in air (Chen et al., 2012), which changes the particle temperature, heat transfer, emissions and char burnout (Toftegaard, 2010).

Rathnam et al. (2009) conducted oxy-fuel combustion tests in a DTF and reactivity analysis in TGA of four Australian coals. They found that the influence of CO_2 on coal burnout is coal dependent but in general the burnout was higher or similar in oxy-fuel conditions compared to air-combustion, which was attributed to higher char reactivity in the oxy-fuel atmosphere due to char–CO_2 reaction. Chars formed during pyrolysis experiments in pure CO_2 exhibited higher specific surface area in comparison to chars produced in N_2, which can also catalyse the surface reactions (Al-Makhadmeh, 2009; Rathnam et al., 2009). On the other hand, Brix et al. (2010) observed no significant differences in volatile yield or specific surface between chars produced in CO_2 and N_2 explaining this effect with shorter particle residence times than in previous study, which prevented char gasification reaction from occuring. Additionally, as the char combustion is concerned, Brix et al. (2010) observed no apparent difference between combustion in CO_2/O_2 and N_2/O_2 atmospheres. This result was also confirmed in a study of Maffei et al. (2013), where experiments of the single particle combustion of two, different rank coals have been conducted in a DTF in quiescent gas conditions in which longer particle burnout times and lower surface temperatures in CO_2/O_2 mixtures were observed. One should note though that the oxygen concentrations varied between 21 and 100% in the bulk gas, and the oxygen diffusivity in CO_2 lower

---

*Corresponding author, e-mail: robert.lewtak@ien.com.pl than that in N_2 mixtures may have played a significant role. On the other hand, Gonzalo–Tirado et al. (2012) found that, at low oxygen concentrations, the contribution of gasification with CO_2 to the overall rate can compensate for the change of the atmosphere and oxy-fuel combustion results in a slightly enhanced consumption rate with respect to char oxidation in air.

Thus, there is still a requirement for comprehensive studies of coal char combustion in air and oxy-fuel combustion conditions at scales comparable to pulverized fuel boilers. Moreover, it is necessary to address the changed combustion mechanism in oxy–fuel modeling since both oxidation and gasification reactions take place in parallel. It is also important to note that there is no fully convincing experimental evidence about the real reaction path, especially when models of different complexity are available that are often contradictory to each other (Hurt, et al., 2001).

In this study, experimental data, achieved in a number of tests carried out in a DTF, were used to derive a set of most adequate kinetic parameters of oxidation and gasification reactions applicable to numerical simulations of the oxy–fuel combustion process in pulverized fuel boilers.

2. EXPERIMENTAL SETUP

Experiments of pulverized coal char combustion have been carried out in a 6–meter drop tube, presented in Fig. 1, with 38.5 mm of inner diameter, in operating conditions similar to full scale combustion furnaces, i.e. the gas reactor temperature ranging from 900 to 1300 °C, oxygen mole fractions from 3 to 9% in CO_2 or N_2 diluents and residence time up to 1.2 s. All gas flows were adjusted using mass flow controllers in order to maintain the required atmosphere composition and particle residence times. Reactor wall temperatures were controlled by S-type thermocouples measuring the outer surface of the tube, while the reactor gas temperature was measured by the suction pyrometer inserted through one of the horizontal ports. Wall temperatures were adjusted accordingly to maintain the desired gas temperatures inside the reactor.

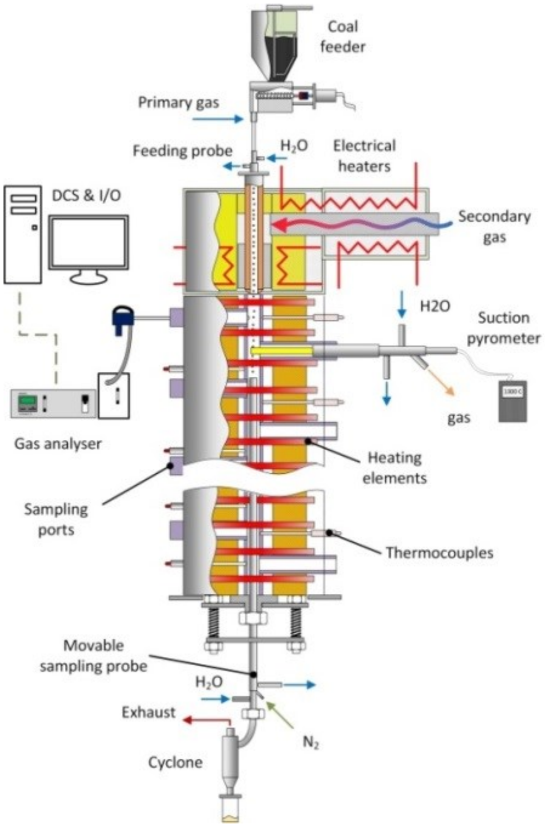

Fig. 1. Schematic of char combustion facility

Char particles were pneumatically fed into the reactor using a precise screw feeder and a water-cooled probe through one of the twelve, sloped ports installed along the reactor height. The particle mass flow was adjusted before starting of the test to hinder the concentration changes of the reaction gases (CO_2 and O_2) of more than 10%. That ensured virtually constant bulk gas compositions during the experiments. Changing the position of the feeding probe while the collection point remained stationary varied the particle residence time. Char burnout, X_C, was determined using the ash tracer method and calculated with the following formula:

$$X_C = \frac{f_a - f_{a,0}}{f_a\left(1 - f_{a,0}\right)}. \tag{1}$$

Char, from bituminous coal, screened between 63 and 90 µm, was produced at high heating rate of $10^4 - 10^5$ K/s and reactor temperature of 1300 °C, either in pure CO_2 or N_2 for oxy-fuel or air combustion, respectively, although coal devolatilization usually proceeds with small O_2 amount in industrial coal-burning installations. The residence time of devolatilization was set up to 250 ms ensuring complete devolatilization and preventing extensive gasification in case of oxy–fuel devolatilization (some gasification level could be nevertheless observed). The properties of the parent fuel and resulting chars are collected in Table 1. It is worth noting there is a difference of carbon content in char devolatilized in CO_2 and N_2 that indeed influences the burning time but has no effect on the combustion rate. Fig. 2 shows particle volume distributions measured with a Kamika 2DiSA instrument.

Table 1. Parent fuel and char properties

properties	raw coal	CO_2 char	N_2 char
moisture, %wt. ab	8.80	1.30	1.22
ash, %wt. db	11.62	28.23	21.89
volatiles, %wt. db	38.60	0.91	1.11
C, %wt. db	70.50	69.10	75.52
H, %wt. db	4.88	0.34	0.32
N, %wt. db	1.36	1.48	1.53
S, %wt. db	0.49	0.49	0.43
O, %wt. db, diff	11.14	0.36	0.32

ab-analytical basis, db-dry basis, diff-calculated by difference

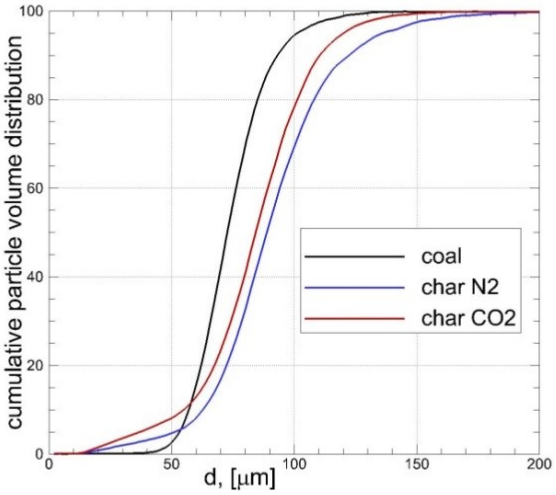

Fig. 2. Cumulative particle volume distribution of coal and chars

3. DESCRIPTION OF THE CHAR COMBUSTION MODEL

When pulverized char particles are burnt in oxy-fuel conditions, besides oxidation, the combustion mechanism additionally takes into account the gasification by CO_2. Here, the single film-model (Caram et al., 1977), widely used to describe char oxidation, is also used here to describe gasification. Similar to O_2, it is assumed that CO_2 diffuses to the char particle surface where it reacts to form CO which then diffuses outward the particle surface without oxidation (Caram et al., 1977; Fendell, 1969; Mitchell, 1987). For the oxidation reaction, the production of CO_2 can be assumed to be negligible at high temperatures so that CO is the primary product of char carbon oxidation (Shaddix et al., 2013). Moreover, the homogeneous reaction of CO oxidation is not considered in the model while its thermal effect can further affect the combustion process. Thus, the combustion mechanism of char carbon is composed of two surface reactions as follows:

$$\mathrm{C} + \tfrac{1}{2}\mathrm{O_2} \rightarrow \mathrm{CO}\,, \tag{2}$$

$$\mathrm{C} + \mathrm{CO_2} \rightarrow 2\mathrm{CO}\,. \tag{3}$$

The total rate of char carbon consumption, r_C, is defined as follows:

$$r_C = \sum_{i=1}^{i=2} r_{C,i} \tag{4}$$

where i denotes the i-th surface reaction, and

$$r_{C,1} = A_p f(X_C) M_C \psi_1 \frac{k_{c,1} k_d}{k_d + k_{c,1} f(X_C)} C_{O_2,\infty} \tag{5}$$

since both diffusion and kinetics can affect the oxidation rate, and

$$r_{C,2} = A_p f(X_C) M_C \psi_2 k_{c,2} C_{CO_2,\infty} \tag{6}$$

since the rate of the gasification reaction is limited only by the char chemical reactivity, and $\psi_1 = 2$ mol-C/mol-O_2, $\psi_2 = 1$ mol-C/mol-CO_2, $C_{O2,\infty}$ is the g-th species concentration in the bulk flow, $M_C = 12$ kg/kmol. The individual reaction rates, $r_{C,i}$ are expressed in terms of the external particle surface $A_p = \pi d_p^2$ so that the current model of char combustion belongs to a family of global char combustion models (Smith, 1982; Smith et al., 1994; Wall, 1986) unlike to intrinsic modeling approach considering development of the internal structure inside the fuel particle. The rate coefficient of the i-th surface reaction is expressed in the form of the Arrhenius equation

$$k_{c,i} = A_i e^{-E_i/(RT_s)} \tag{7}$$

in which A_i and E_i are the kinetic parameters. The mass transfer coefficient is defined as

$$k_d = \frac{Sh\, D}{d_p} \tag{8}$$

in which Sh is the Sherwood number, and the effective diffusion coefficient is expressed as

$$D(T,p) = D_0 \left(\frac{T_f + T_p}{2T_0} \right)^{1.75} \frac{p_0}{p} \tag{9}$$

where $D_0 = D_{O2\text{-}N2} = 0.181$ cm^2/s at $T_0 = 273$ K and $p_0 = 1$ bar (Maloney, 2008) was used in O_2/N_2 combustion, while $D_0 = 0.154$ cm^2/s was used in O_2/CO_2 combustion, and

$$f(X_C) = (1 - X_C(t))^{\,q} \tag{10}$$

is the correction function which takes into account the development of the specific surface area and the effect of the non–reactive ash surface during the particle combustion (Haas et al., 1997; Baum et al., 1971).

Finally, the governing equations of the char combustion model can be presented. Gas phase is treated in the Eulerian approach and coal particles are treated as Lagrange discrete particles whose mass and temperature evolution is described by equations given below. It was assumed that the particle volume, $V_p = \frac{\pi}{6} d_p^3$, is constant during combustion so that the mass conservation law of the char particle is expressed in the following form:

$$V_p \frac{d\rho_p}{dt} = -r_C(t), \quad \rho_p(0) = \rho_{p,0} \tag{11}$$

and the char particle mass is then defined as

$$m_p(t) = m_a + m_C(t) \tag{12}$$

in which

$$m_a = f_{a,0}\, \rho_{p,0}\, V_p \tag{13}$$

is constant mass of ash contained in the char particle.

The char particle temperature, T_p, is defined by the conservation law of particle energy as follows (Lewtak et al., 2013):

$$m_p(t) c_p \frac{dT_p(t)}{dt} = h^* A_p \left(T_{f,\infty} - T_p(t)\right) + A_p \varepsilon_p \sigma \left(T_{f,\infty}^4 - T_p^4(t)\right) + \sum_{i-1}^{i=2} r_{C,i}(t) \Delta H_i \tag{14}$$

with the initial condition

$$T_p(t=0) = T_{p,0}, \tag{15}$$

where the heat transfer coefficient, h^*, corrected by the Ackermann correction, is defined as

$$h^* = \frac{k_{f,\infty}}{d_p} Nu \frac{\Phi}{e^{\Phi} - 1} \tag{16}$$

in which

$$\Phi = \frac{r_C}{2\pi\, d_p\, \rho_f\, D} \tag{17a}$$

is the non-dimensional heat transfer rate coefficient, and

$$Nu = 2 + 0.6 Re_p^{1/2} Pr^{1/3} \tag{17b}$$

is the Nusselt number.

Furthermore, in the current study, the partial oxidation of CO in the char particle boundary layer is taken into consideration by the modification of the heat released during coal char oxidation as follows

$$\Delta H_1 = (1-\chi) H_{CO} + \chi H_{CO_2} \tag{18}$$

where $\chi \in \langle 0,1 \rangle$ and H_{CO} = 9.21 MJ/kg-C, H_{CO2} = 32.8 MJ/kg-C while ΔH_2=- 4.3 MJ/kg-C for the gasification reaction. Moreover, it should be also noted that CO oxidation influences the char combustion rate by the additional heat release and by O_2 consumption reducing its availability (reducing its flow to the particle surface). In addition, CO oxidation is negligible even at a surface temperature as high as 2500 K when water and hydrogen are absent (Goel et al., 1996).

4. RESULTS AND DISCUSSION

The mathematical model describing combustion of a char particle is comprised of a set of two ordinary differential Eqs. (11) and (14) in which the optimal values of the model parameters, i.e. the kinetic parameters, A_i and E_i, and the q exponent, exist and satisfy

$$\min_{A_i,\, E_i,\, q} \sum_j \left| X_C^{num}(t_j) - X_C^{\exp}(t_j) \right| \tag{19}$$

where j are numbers of all experimental points. The optimal values of A_i, E_i and q shown in Table 2 have been determined by the generalized reduced gradient method (Lasdon et al., 1975) for which the fourth-order Runge-Kutta method was used to solve the system (11) and (14) to determine the values of X_C^{num}.

Table 2. Optimal values of the kinetic parameters and q

model	q	A_1 (m/s)	E_1 (kJ/mol)	A_2 (m/s)	E_2 (kJ/mol)
χ =0	1.65	6700	77.5	2.55×10^6	214
χ =0.2	1.65	5390	75.8	3.58×10^6	221
χ =0.4	1.65	3370	71.8	4.21×10^6	222

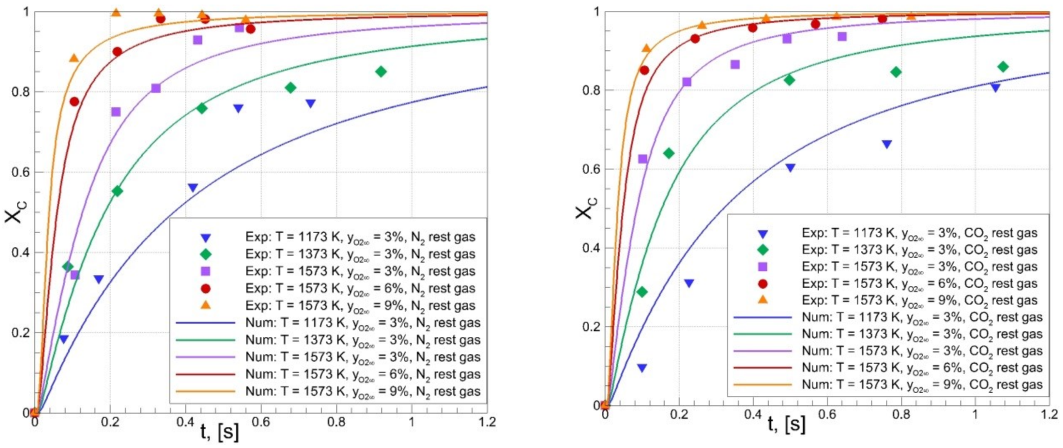

a) char burnout, X_C, for O_2/N_2 b) char burnout, X_C, for O_2/CO_2

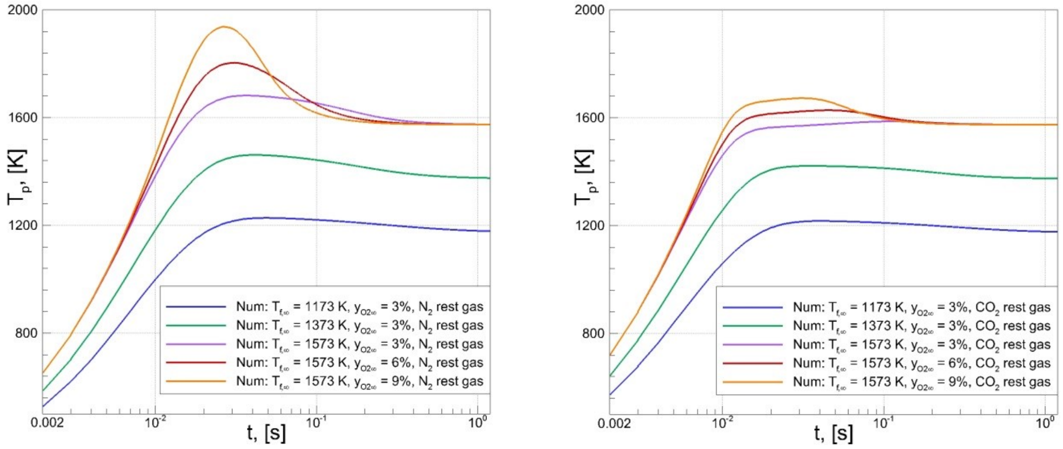

c) char temperature, T_p, for O_2/N_2 d) char temperature, T_p, for O_2/CO_2

Fig. 3. Char burnout and temperature. Solid lines represent a numerical solution of Eq. (11) and Eq. (14) without CO oxidation (χ =0) derived for the optimal values of the model parameters. Points represent X_C derived from experiments

As shown in Fig. 3, the numerical char burnout correctly reproduces the experimental results for both standard and oxy–fuel conditions. Moreover, the particle temperature predicted by the model shows different behavior for O_2/N_2 that in O_2/CO_2. For standard combustion in O_2/N_2 mixtures, the particle temperature curves show steep slopes with the in–between temperature peak, especially visible for high gas temperature and concentrations of O_2. For the oxy-fuel conditions, the particle temperature curves are flat with no temperature peaks due to the active endothermic gasification reaction. One can also note that the ratio between burnouts in oxy-fuel and air conditions changes with the temperature and oxygen concentration. At lower temperatures (900 °C) and low oxygen mole fraction (3 %), the burnouts in oxy-fuel and air are similar due to the low effect of the gasification reaction. At higher temperatures (1100 and 1300 °C) and low oxygen mole fraction (3 %), the burnouts in oxy-fuel are higher than in air since the gasification rate increases and contributes significantly to the overall burnout. At high temperature (1300 °C) and moderate oxygen mole fraction (6 %), the burnouts in oxy-fuel and air are again comparable because the oxidation rate increases and the effect of oxygen diffusion to the particle surface starts to play a role. Finally, at high temperature (1300 °C) and higher oxygen mole fraction (9 %), the burnout in oxy-fuel is lower than in air due to the significant effect of the oxygen diffusion. Thus, it is important to take into account the influence of the gasification reaction and oxygen diffusion in mathematical modeling of oxy-fuel combustion in practical combustion systems.

The mathematical model of char particle combustion described above has been implemented in ANSYS Fluent to simulate the experimental drop-tube furnace conditions and test the values of the kinetic parameters already derived.

Figure 4 shows the evolution of char burnout and particle temperature for char burnt in standard and oxy-fuel conditions. Experimental char burnout shown as points has been compared with the numerical solution of Eq. (11) and Eq. (14) carried out for the optimal values of the model parameters presented in Table 2 without CO oxidation in the particle boundary layer ($\chi = 0$). Additionally, Table 2 presents the optimal model parameters when partial oxidation of CO in the particle boundary layer is taken into consideration, i.e. selected for $\chi = 0.2$ and $\chi = 0.4$. It can be observed that the effect of CO partial oxidation on the kinetic parameters mainly affects values of the pre-exponential factors while values of the activation energies remain nearly constant. Numerical optimization has been carried out for average char particle diameters equal to 69 μm for char produced in N_2, and 62 μm for char produced in CO_2. Additionally, particle emissivity and specific heat were assumed to be equal to 0.9 and 1680 J/(kg·K), respectively.

Fig. 4 shows selected contours of gas velocity and temperature, CO mole fraction and particle trajectories from the CFD modeling of coal char combustion in the drop-tube furnace. All CFD simulations have been carried out for pulverized coal char particles in a diameter range conformed with the experimental particle size distributions. Char particles which are immediately transported close to the hot wall of the drop-tube furnace heat up quicker than char particles flowing through the centre, where the gas temperature is lower, due to cold primary air introducing char particles.

Figure 5 shows the evolution of coal char burnout for oxy-fuel conditions derived from experimental and CFD investigations. The CFD lines plotted for all particle sizes considered in the CFD modeling create a family of lines limited by a top and bottom envelope. The experimental points are located near the top envelope of all CFD lines since the kinetic parameters have been derived assuming the ideal process conditions of constant gas temperature and constant gas concentrations during combustion of char particles. Meanwhile, the conditions of gas temperature and concentrations acting on the char particles were variable in CFD and experimental investigations have given a wide band of CFD char burnout. Moreover, the top envelope exactly represents the char burnout line achieved for the ideal conditions considered during optimization of the model parameters.

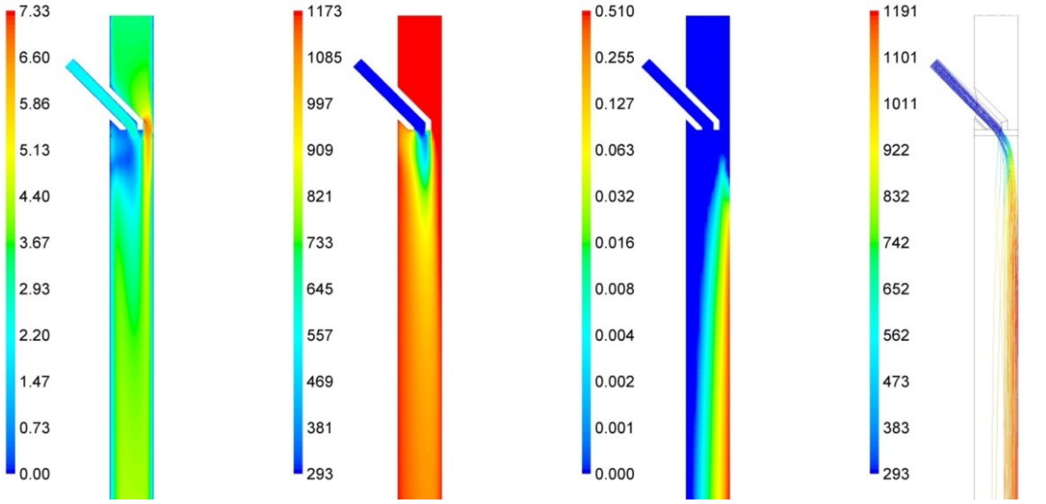

a) velocity, [m/s] b) temperature, [K] c) CO mole fraction[%] d) particle trajectories

Fig. 4. Selected CFD modeling of pulverized char combustion in the drop tube furnace at oxy-fuel conditions of $T_{f,\infty} = 1173$ K, $y_{O2,\infty} = 3\%$. Particle trajectories, (d), coloured by particle temperature in K

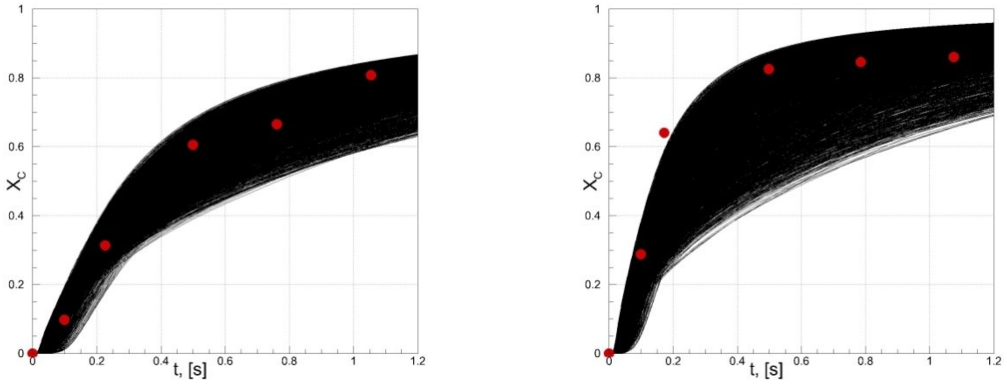

a) $T_{f,\infty} = 1173$ K, $y_{O2,\infty} = 3\%$ b) $T_{f,\infty} = 1373$ K, $y_{O2,\infty} = 3\%$

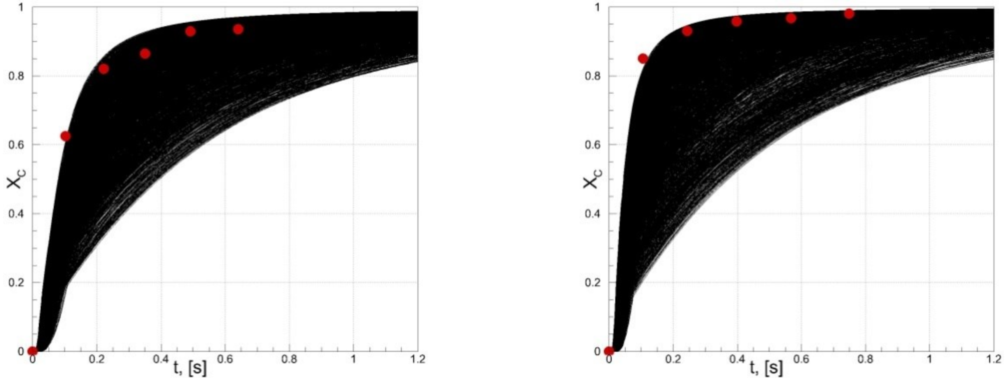

c) $T_{f,\infty} = 1573$ K, $y_{O2,\infty} = 3\%$ d) $T_{f,\infty} = 1573$ K, $y_{O2,\infty} = 6\%$

Fig. 5. Evolution of char burnout for oxy-fuel conditions (CO_2 as the rest gas),
— CFD solution, ● experimental points

5. CONCLUDING REMARKS

The experimental investigations carried out in the current study revealed the influence of the combustion atmosphere on char burnout. It has been observed that when char particles are burnt in oxy-fuel conditions, i.e. at a high amount of CO_2 with low O_2 concentrations that is usually encountered in oxy-fuel combustion chambers, gasification enhances char burnout so that its influence has to be taken into consideration although the oxidation process always plays the dominant role in combustion.

Next, to determine the values of kinetic parameters that describe the combustion process, both the experimental investigations and CFD simulations have been combined which turned out to be an attractive and well-posed approach to apply.

Numerical results, predicted by the mathematical model proposed here and describing char combustion in oxy-fuel conditions, are in proper agreement with experimental data. Thus, the approach presented here to derive kinetic parameters has been verified and the model can be applied to CFD simulations of pulverized fuel flames in oxy-fuel conditions.

This scientific work was carried out within the confines of the RELCOM project founded by the European Community's Seventh Framework Programme (FP7/2007-2013) under grant agreement no. 268191.

SYMBOLS

A	pre-exponential factor , m/s, or surface area, m^2
c	specific heat, J/(kg K)
C	mole concentration, kmol/m^3
d	diameter, m
D	effective diffusion coefficient, cm^2/s
E	activation energy, kJ/mol
f	mass fraction
ΔH	heat of reaction, MJ/kg-C
m	mass, kg
M	molecular weight, kg/kmol
k_c	rate coefficient of a surface reaction, m/s
k_d	mass transfer coefficient, m/s
p	pressure, Pa
R	gas constant
r	rate of gas-solid reaction, kg/s
t	time, s
T	temperature, K
V	volume, m^3
X	burnout, non-dimensional

Greek symbols

ε	emissivity
ρ	density, kg/m^3
ψ	conversion factor, mol-C/mol-*g*
σ	Stefan–Boltzmann constant, W/(m^2 K^4)

Subscripts

0	initial or reference condition
a	ash
C	carbon
i	reaction index
g	gas

p	particle
∞	bulk flow condition

REFERENCES

Al-Makhadmeh L., 2009. *Coal pyrolysis and char combustion under oxy-fuel conditions*, PhD thesis, Stuttgart, Universität Stuttgart.

Baum M.M., Street P.J., 1971. Predicting the combustion behaviour of coal particles. *Combust. Sci. Technol.*, 3 (5), 231-243. DOI: 10.1080/00102207108952290.

Brix J., Jensen P.A., Jensen A.D., 2010. Coal devolatilization and char conversion under suspension fired conditions in O_2/N_2 and O_2/CO_2 atmospheres. *Fuel,* 89, 3373–3380. DOI: 10.1016/j.fuel.2010.03.019.

Caram H.S., Amundson N.R., 1977. Diffusion and reaction in a stagnant boundary layer about a carbon particle. *Industrial & Engineering Chemistry Fundamentals*, 16 (2), 171–181. DOI: 10.1021/i160062a001.

Chen L., Yong S.Z., Ghoniem A.F., 2012. Oxy-fuel combustion of pulverized coal: Characterization, fundamentals, stabilization and CFD modeling. *Progress in Energy and Combustion Science*, 38, 156-214. DOI: 10.1016/j.pecs.2011.09.003.

Fendell F.E., 1969. The burning of spheres gasified by chemical attack. *Combust. Sci. Technol.*, 1, 13–24. DOI: 10.1080/00102206908952188.

Goel S., Lee C.H., Longwell J.P., Sarofim A.F., 1996, Modelling of ignition and CO oxidation in the boundary layer of a single char particle, *Energy Fuels*, 10, 1091-1098. DOI: 10.1021/ef9502416.

Gonzalo–Tirado C., Jiménez S., Ballester J., 2012. Gasification of a pulverized subbituminous coal in CO_2 at atmospheric pressure in an entrained reactor. *Combust. Flame*, 159, 385 – 395. DOI: 10.1016/j.combustflame.2011.07.001.

Haas J.H.P., Maalman T., Gallagher G., van de Kamp W., 1997. Pulverized fuel combustion. Characterization of coal blends. *IFRF* Doc No F 37/y/38.

Hurt R., Calo J., 2001. Semi–global intrinsic kinetics for char combustion modelling. *Combust. Flame,* 125, 1138-1149. DOI: 10.1016/S0010-2180(01)00234-6.

Jenni K.E., Baker E.D., Nemet G.F., 2013. Expert elicitations of energy penalties for carbon capture technologies. *Int. J. Greenhouse Gas Control*, 12, 136–145. DOI: 10.1016/j.ijggc.2012.11.022.

Lasdon L.S., Waren A.D., Jain A., Ratner M., 1975. *Design and testing of a generalized reduced gradient code for nonlinear optimization.* USA, NTIS.

Lewtak R., Milewska A., 2013. Application of different diffusion approaches in oxy-fuel combustion of single coal char particles. *Fuel*, 113, 844-853. DOI: 10.1016/j.fuel.2013.01.053.

Maloney J.O., *Perry's chemical engineers' handbook*, McGraw-Hill; 2008.

Maffei T., Khatami R., Pierucci S., Faravelli T., Ranzi E., Levendis Y.A., 2013. Experimental and modeling study of single coal particle combustion in O_2/N_2 and Oxy-fuel (O_2/CO_2) atmospheres. *Combust. Flame*, 160, 2559-2572. DOI: 10.1016/j.combustflame.2013.06.002.

Mitchell R.E., 1987. Experimentally determined overall burning rates of coal chars. *Combust. Sci. Technol.*, 53, 165–186. DOI: 10.1080/00102208708947025.

Rathnam RK, Elliott LK, Wall TF, Liu Y, Moghtaderi B., 2009. Differences in reactivity of pulverised coal in air (O_2/N_2) and oxy-fuel (O_2/CO_2) conditions. *Fuel Process Technol.*, 90, 797–802. DOI: 10.1016/j.fuproc.2009.02.009.

Shaddix C.R., Holzleithner F., Geier M., Haynes B.S., 2013. Numerical assessment of Tognotti determination of CO_2/CO production ratio during char oxidation. *Combust. Flame*, 160, 1827 – 1834. DOI: 10.1016/j.combustflame.2013.03.019.

Smith I.W., 1982. The combustion rates of coal chars: a review. *19th Int. Symposium on Combustion*, Technion-Israel Institute of Technology, Haifa, Israel, 8-13 August 1982, 1045-1065. DOI: 10.1016/S0082-0784(82)80281-6.

Smith K.L Smoot L.D., Fletcher T.H., Pugmire R.J., 1994. *The structure and reaction processes of coal*. The Plenum Chemical Engineering Series.

Toftegaard M.B., Brix J., Jensen P.A., Glarborg P., Jensen A.D., 2010. Oxy–fuel combustion of solid fuels. *Prog. Energy Combust. Sci.*, 36, 581–625. DOI: 10.1016/j.pecs.2010.02.001.

Wall T.F., Gururajan V.S., 1986. Combustion kinetics and the heterogeneous ignition of pulverized coal. *Combust. Flame*, 66, 151-157. DOI: 10.1016/0010-2180(86)90087-8.

Received 16 June 2016
Received in revised form 31 January 2017
Accepted 05 February 2017

www.czasopisma.pan.pl www.journals.pan.pl
Chemical and Process Engineering 2017, 38 (1), 147-162
DOI: 10.1515/cpe-2017-0012

METHANOL AS A HIGH PURITY HYDROGEN SOURCE FOR FUEL CELLS: A BRIEF REVIEW OF CATALYSTS AND RATE EXPRESSIONS

Maria Madej-Lachowska*[1, 2], Maria Kulawska[1], Jerzy Słoczyński[3]

[1]Institute of Chemical Engineering, Polish Academy of Sciences, Bałtycka 5, 44-100 Gliwice, Poland

[2]Faculty of Production Engineering and Logistics, Opole University of Technology, Luboszycka 5, 45-036 Opole, Poland

[3]Jerzy Haber Institute of Catalysis and Surface Chemistry Polish Academy of Sciences, Niezapominajek 5, 30-239 Cracow, Poland

Hydrogen is the fuel of the future, therefore many hydrogen production methods are developed. At present, fuel cells are of great interest due to their energy efficiency and environmental benefits. A brief review of effective formation methods of hydrogen was conducted. It seems that hydrogen from steam reforming of methanol process is the best fuel source to be applied in fuel cells. In this process Cu-based complex catalysts proved to be the best. In presented work kinetic equations from available literature and catalysts are reported. However, hydrogen produced even in the presence of the most selective catalysts in this process is not pure enough for fuel cells and should be purified from CO. Currently, catalysts for hydrogen production are not sufficiently active in oxidation of carbon monoxide. A simple and effective method to lower CO level and obtain clean H_2 is the preferential oxidation of monoxide carbon (CO–PROX). Over new CO–PROX catalysts the level of carbon monoxide can be lowered to a sufficient level of 10 ppm.

Keywords: copper catalysts, noble metal catalysts, fuel cell, hydrogen production, CO-PROX

1. INTRODUCTION

The rising demand for energy in all developed countries causes the rising production of energy and a parallel increase of environmental pollution. Therefore, new energy sources should be effective and friendly for environment. New processes are being intensively developed. World Renewable Energy Network (WREN) formed in 1992 is one of the most effective organizations to support and enhance the utilization and implementation of renewable energy sources like solar-, wind-, hydro-, bio-, ocean and hydrogen energy and others. Some aspects of catalytic processes in search for alternative fuels are described in several works (Mastalir et al., 2007; Momirlan and Veziroglu, 2005; Spivey, 2005; Yong et al., 2013). Yong et al. (2013) described reaction mechanisms in their review and concluded that no consensus on the surface reaction mechanisms had been established. Hydrogen seems to be a commercially important element. Using hydrogen in polymer electrolyte proton-exchange membrane fuel cells (PEMFC) can be a promising technology of safe energy. These are galvanic cells fed by hydrogen. At present, they are the most interesting objective of research in many automobile research centers. Vehicles that use hydrogen as their onboard fuel for motive power have much better efficiency factors in fuel cells and a lower toxic content of exhaust gases compared with classical engines. Fuel cells are also used in stationary applications. They can be compacted in batteries with power values

---

*Corresponding author, e-mail: m.lach@iich.gliwice.pl from a few kW to hundreds of megawatts (Squadrito et al., 2014). Buildings can also be heated by fuel cells (Dodds et al., 2014). Hydrogen is mainly produced from natural gas or in the reaction of electrolysis of water; these are expensive and dangerous processes. To avoid transport it is strongly recommended to produce hydrogen in the destination place. There are very strict restrictions concerning purity of hydrogen used in fuel cells, particularly the maximum content of carbon monoxide should be 10-20 ppm in low-temperature fuel cells; and below 2 vol.% in high-temperature fuel cells (Snytnikov et al., 2012). Special catalysts should be applied to reduce CO content.

The aim of our work was to present effective catalysts developed in new processes and available kinetic indications useful in reactor modeling.

2. PROCESSES OF HYDROGEN PRODUCTION FROM METHANOL

Important processes (Yong et al., 2013; Mastalir et al., 2007) are as follows:

- thermal decomposition of methanol (DM)
- partial oxidation of methanol (POM)
- steam reforming of methanol (SRM)
- oxidative steam reforming of methanol (OSRM)

2.1. DM – Decomposition of methanol

The reverse reaction to synthesis of methanol from carbon monoxide and hydrogen:

$$\mathrm{CH_3OH} \rightarrow 2\mathrm{H_2} + \mathrm{CO} \qquad \Delta H^0 = +91\, kJ/mol \tag{1}$$

gives a product mixture containing up to 67 mol% of hydrogen. However, the reduction of such a high level of CO 33 mol% to about 10 ppm is technologically very difficult and therefore not profitable from the economic point of view. The decomposition of methanol is an endothermic catalytic reaction. DM catalysts are classified into two groups: Cu-based (in particular Cu/ZnO, Cu/Cr_2O_3, etc.) and those based on elements of 8th group (Ni, Ni-Pt, Pt, Pd, Rh) supported on SiO_2, $Al_2 O_3$, ZrO_2 (Kapran et al., 2015). Depending on the catalyst used, the process temperature varied from 473 to about 1200 K (Laosiripojana at al., 2006).

2.2. POM - Partial oxidation of methanol

Also in this reaction:

$$\mathrm{CH_3OH} + 0.5\cdot\mathrm{O_2} \rightarrow 2\mathrm{H_2} + \mathrm{CO_2} \quad \Delta H^0 = -192\, kJ/mol \tag{2}$$

a mixture containing up to 67 mol% of hydrogen is formed, if pure (and expensive) oxygen is used. Practically, air is used, so hydrogen is produced with 41% yield. It is a very exothermic reaction, so heating is not supplied, but controlling such a process causes many operating problems. Though CO does not exist as a reaction product in Eq. (2), it has been detected in this reaction over Cu- and Pd-containing catalysts on oxide carriers (Alejo et al., 1997; Agrell et al., 2001, 2003; Cubeiro et al., 1998; Navarro et al., 2002) because of undesired reactions: DM, SRM, full oxidation of methanol towards carbon dioxide and water, water gas shift reaction (WGS) and reverse water gas shift reaction (RWGS). Undesired reactions result in lowering the yield of hydrogen and increase in the yield of CO, which goes up to dozen mol% or even more. The lowest selectivity with respect to CO (1.5 mol%) has been obtained over Au/TiO_2-MO_x (M= Fe, Co, Zn) catalysts (Chang et al., 2006).

2.3. *SRM - Steam reforming of methanol*

The reaction formula is as follows:

$$\mathrm{CH_3OH + H_2O \rightarrow 3H_2 + CO_2} \quad \Delta H^0 = +50\, kJ/mol \tag{3}$$

The yield of hydrogen reaches (Mastalir et al., 2007; Yong et al., 2013) up to 75 mol%. The disadvantages are that this reaction is endothermic and that simultaneously the reversible reaction WGS/RWGS (5) occurs. Proper catalysts allow a decrease in CO level and decrease in the temperature of the process.

2.4. *OSRM – Oxidative Steam Reforming of Methanol*

In recent years, OSRM process has attracted a lot of attention.

$$\mathrm{CH_3OH} + (1-2n)\mathrm{H_2O} + n\mathrm{O_2} \rightarrow (3-2n)\mathrm{H_2} + \mathrm{CO_2} \tag{4}$$

The process represented by Eq. (4), is a combined reaction of POM and SRM with quick start-up, (Park and Kwon, 2015), conducted in the presence of a small amount of oxygen, n mols. Lower amounts of CO are observed in the exit gas, compared with SRM process, but there are additional products from oxidation of methanol: formaldehyde and dimethyl ether. Lopez et al. (2012) in investigation on Cu and Ni impregnated on ZrO_2 catalysts in oxidative steam reforming of methanol, obtained high methanol conversion and the biggest hydrogen yields for temperatures about 350 °C. Unfortunately, for the most active catalyst, these results correspond to hydrogen selectivity of about 70% and CO selectivity of 30%. For less active catalysts hydrogen yields were by about 25% lower, hydrogen selectivity equalled to about 90 - 95 % and that of CO from 5 to 10%.

Pojanavaraphan et al. (2012, 2014) when investigating Au/CeO_2 and Au/$Ce_{1-x}Zr_xO_2$ catalysts obtained the highest methanol conversion of 92% at 400°C, with H_2 and CO concentration of 15% and 2500 ppm, and a very good stability for Au deposits on CeO_2-ZrO_2 oxide catalyst with Zr/(Ce+Zr) ratio – 0.25, calcination temperature – 400 °C and Au loading 3 mass%.

The best results have been obtained for Cu/Zn/Al_2O_3 catalyst originating from hydrotalcite precursor (Liu et al., 2003). It was up to 500 ppm, but the value was still too high.

It seems that at present, hydrogen from steam reforming of methanol process is the best fuel source to be applied in fuel cells, because of the highest yield of hydrogen at a low amount of CO.

3. STEAM REFORMING OF METHANOL

The interest in steam reforming of methanol process arose in the 1980s. Up to 2005 an assumption was made, that decomposition of methanol (1) is connected with water gas shift (WGS) reaction (5) (Amphlett et al., 1985; Barton et al., 1980 ; Santacesaria et al. 1978):

$$\mathrm{CO + H_2O \rightarrow H_2 + CO_2} \tag{5}$$

After detailed investigations such an assumption was later rejected. Now it is supposed that formation of methyl formate as an intermediate is most probable (Idem and Bakhshi, 1996; Jiang et al., 1993; Jiang et al., 1993; Papavasiliou et al., 2009; Takahashi et al., 1982; Takezawa and Iwasa, 1997; Yong et al., 2013).

According to Papavasiliou et al. (2009) the production of hydrogen and carbon dioxide by SRM over Cu-containing catalysts could proceed through the following paths:

- methanol decomposition and WGS

$$CH_3OH \rightarrow 2H_2 + CO \tag{1}$$

$$CO + H_2O \rightarrow H_2 + CO_2 \tag{5}$$

- via methyl formate intermediate
  - methanol dehydrogenation to formaldehyde and H_2

$$CH_3OH \rightarrow HCHO + H_2 \tag{6}$$

$$CH_3OH + HCHO \rightarrow HCOOCH_3 + H_2 \tag{7}$$

  - or direct dehydrogenation of methanol to methyl formate and H_2

$$CH_3OH + HCHO \rightarrow HCOOCH_3 + H_2 \tag{8}$$

  - hydrolysis of methyl formate

$$HCOOCH_3 + H_2O \leftrightarrow CH_3OH + HCOOH \tag{9}$$

  - formic acid decomposition

$$HCOOH \rightarrow H_2 + CO_2 \tag{10}$$

- via formaldehyde intermediate
  - methanol dehydrogenation to formaldehyde

$$CH_3OH \rightarrow HCHO + H_2 \tag{6}$$

  - formaldehyde hydrolysis

$$CH_3OH \rightarrow HCHO + H_2 \tag{11}$$

  - formic acid decomposition

$$HCOOH \rightarrow H_2 + CO_2 \tag{10}$$

SRM process is carried out at atmospheric pressure, usually at a temperature of about 520 K, the substrate mole ratio of CH_3OH/H_2O of about 1, in a stream of inert gas (N_2 or Ar) of GHSV = 3 300 – 8 000 h^{-1}. Before the process begins, catalysts are reduced in hydrogen diluted in nitrogen.

Since the 1980s there have been many attempts to work out more active, selective and stable catalysts (Ilinich, 2013; Rameshan et al., 2012; Urasaki et al., 2005; Yong et al., 2013). For every catalytic system the mechanism of the process could be different, so kinetic investigations are needed.

3.1. Catalysts for SRM process

Copper- based catalysts and catalysts based on group VIII-X metals are used for methanol steam reforming (Sá et al., 2010). According to many literature reports the catalysts composed of metals of VIII-X group present higher long-term stability compared to copper-based catalysts but much lower reaction activities (Takezawa and Iwasa, 1997). Their costs are a serious problem. Copper- based catalysts favor the production of H_2 with high selectivity towards CO_2 (therefore low selectivity towards CO) and for that reason many researchers have been focusing on Cu-based catalysts for the application of hydrogen in fuel cell system.

Table 1. Cu/ZnO-based catalysts for SRM

Cat. No	Cu/ZnO additives	*t* [°C]	Methanol conversion [%]	Molar ratio S/M**	CO selectivity* [%]	References
1		240	78.8	1.3	0.221	Wang et al., (2007)
2		200	27	1.2	1.2	Shishido et al., (2011)
2		300	100	1.2	4.6	Shishido et al., (2011)
3		220	16.4	1	0.2	Liu et al., (2003)
3		260	66.8	1	0.9	Liu et al., (2003)
4	Al_2O_3	200	47.4	1.2	0	Shishido et al., (2011)
4	Al_2O_3	300	100	1.2	7.3	Shishido et al., (2011)
5	Al_2O_3	250	74	1.1	0.47	Huang et al., (2009)
5	Al_2O_3	270	89.2	1.1	0.92	Huang et al., (2009)
6	Al_2O_3	250	90	1	1	Purnama et al., (2004)
7	Al_2O_3	220	14.7	1	0.2	Liu et al., (2003)
7	Al_2O_3	260	58.4	1	0.8	Liu et al., (2003)
8	Al_2O_3	220	40	1.4	0.6	Patel and Pant (2006)
8	Al_2O_3	260	90	1.4	1.9	Patel and Pant (2006)
9	Al_2O_3	300	100	1.3	1.2	Lindström et al., (2002)
10	Al_2O_3/ CeO_2	250	60.2	1.1	0.31	Huang et al., (2009)
10	Al_2O_3/CeO_2	270	79.3	1.1	0.66	Huang et al., (2009)
11	Al_2O_3/ Y_2O_3/In_2O_3	400	100	1.3	1.3	Matsumura (2014)
11	Al_2O_3/ Y_2O_3/In_2O_3	500	75	1.9	1.9	Matsumura (2013)

*Definition of CO selectivity $S_{CO} = \dfrac{F_{CO}^{out}}{(F_{H_2}^{out} + F_{CO_2}^{out} + F_{CO_2}^{out})} \cdot 100\%$

**S/M – steam to methanol molar ratio

Table 2. Cu/ZnO/ZrO_2-based catalysts for SRM

Cat. No	Cu/ZnO/ZrO_2 additives	*t* [°C]	Methanol conversion [%]	Molar ratio *S/M*	CO selectivity [%]	
12		500	100	2.5	2.5	References
13		200	45	1.0	0	Lachowska (2004)
13		160	8	1.0	0	Lachowska (2004)
14	Al_2O_3	260	97	1.4	0.6	Patel and Pant (2006)
14	Al_2O_3	220	50	1.4	0.1	Patel and Pant (2006)
15	Al_2O_3	300	77	1.1	0.7	Chang et al. (2012)
16	Al_2O_3	250	76.7	1.1	0.44	Huang et al. (2009)
16	Al_2O_3	270	92.7	1.1	0.97	Huang et al. (2009)
17	Al_2O_3/CeO_2	250	77.6	1.1	0.32	Huang et al. (2009)
17	Al_2O_3/CeO_2	270	89.4	1.1	0.85	Huang et al. (2009)
18	CeO_2	200	100	1.0	1.6	Madej-Lachowska (2012)
18	CeO_2	160	73	1.0	0.79	Madej-Lachowska (2012)
19	CeO_2/Cr_2O_3	200	100	1.0	1.88	Madej-Lachowska (2012)
19	CeO_2/Cr_2O_3	160	53	1.0	0	Madej-Lachowska (2012)
20	Ga_2O_3	220	100	1.0	0.9	Lachowska (2006)
20	Ga_2O_3	160	16	1.0	0	Lachowska (2006)
21	La	200	100	1.0	0	Madej-Lachowska (2012)
21	La	160	50	1.0	0	Madej-Lachowska (2012)

The majority of these catalytic systems contain metallic copper dispersed on the surface of ZnO and ZrO_2 with Al_2O_3 or Cr_2O_3 and sometimes SiO_2 or CeO_2 addition. Similar catalysts were applied long time ago in methanol synthesis from CO + H_2 and CO_2 + H_2 mixtures. In these reactions metallic Cu is the active component acting in synergy with ZnO while Al_2O_3 and SiO_2 are the agents lowering the sintering of active components (Skrzypek et al., 1994; Hansen, 1997). High dispersion of copper and good cooperation of Cu with ZnO is the main objective in SRM catalyst production. Extension of specific surface of catalyst is also very beneficial. Various methods of its preparation have been used: co-precipitation (CP), hydrothermal synthesis (HT), wet impregnation (WT), gel co-precipitation (CGP), precursors of citrate decomposition (CDP) and polymer template sol-gel method (PTSG). CP and CGP are relatively simple methods. However, from our earlier experiments (Kulawska, 2008), they do not assure full repeatability of crystalline structure in all series of preparation. By using CDP or PTSG methods highly active and thermally stable nanostructure catalysts are prepared (Sá et al., 2010).

The characteristics of selected catalysts are listed in Table 1 (CuZnO - based catalysts), Table 2 ($CuZnOZrO_2$ - based catalysts), Table 3 and in Figs. 1 - 2. A detailed catalyst composition has not been given in many cases. The mole ratio of water to methanol varied in the range of 1.0 - 1.3**.** Differences in methanol conversion and CO selectivity for the same catalyst composition can result from various methods of preparation and various reaction parameters. The majority of researchers did not give data for CO selectivity. There is a great discrepancy in the formula of CO selectivity. Due to lack of full experimental data it is hard to reach proper view of results found in literature. So, we could make only a rough comparison of results obtained in many different laboratories.

The $Cu/ZnO/ZrO_2$ catalyst is the "primary" one, and small amounts of various metal oxides with a suitable promoter improve catalytic activity and carbon monoxide selectivity at relatively low temperature. As in the methanol synthesis, Cu/ZnO synergy is crucial for the performance of a catalyst used in fuel cells. The disadvantages of copper catalysts are weak thermal stability and susceptibility to impurities like sulfur, chlorine and phosphorus. Also, carbon monoxide is formed in large amounts. It is connected with temperature, see investigations of Madej-Lachowska et al. (2012).

Table 3. Other Cu-based catalysts for SRM

Cat. No	Cu additives	t [°C]	Methanol conversion [%]	Molar ratio *S/ M*	CO selectivity* [%]	References
22	Cr_2O_3/Al_2O_3	300	63	1,3	1.1	Lindström et al, (2002)
23	Mn spinel	240	80	0	0.7	Liu et al, (2008)
23	Mn spinel	260	93	0	0.7	Liu et al, (2008)
24	$Y_2O_3/Pr_2O_3/ Al_2O_3$	240	80[a]	0		Yang and Chan (2011)
24	$Y_2O_3/Pr_2O_3/ Al_2O_3$	280	99[a]	0.09		Yang and Chan (2011)
25	ZrO_2		100	1,3	0.51	Yao et al, (2006)
26	ZrO_2	250	92	1	0,22	Purnama et al, (2004)
27	ZrO_2/Al_2O_3	300	44	1,3	0,75	Lindström et al, (2002)

[a] H_2 yield [%]

While considering thermodynamic relations of a system of chemical reactions (3 and 5), the constraint in this process is temperature. The relationship between equilibrium conversion and temperature is almost linear in reaction (3) but almost exponential in reaction (5) rising faster for substrate ratios ≤1. Although any increase in temperature above 480 K is beneficial for methanol conversion, it causes rapid increase in CO selectivity. So, investigation of Lindström et al. (2002) should be carefully considered because conducted at such a high reaction temperature and at surprisingly high gas hourly space velocity equal to 25 000 h^{-1}. Additionally, the obtained CO selectivity was relatively high and methanol conversion high only for classic Cu/Zn/Al catalyst supported on Zr. From a practical point of view, lower reaction temperatures in the reformer are desirable because of the lower temperature difference between the reactor and the fuel cell (Liu et al., 2008).

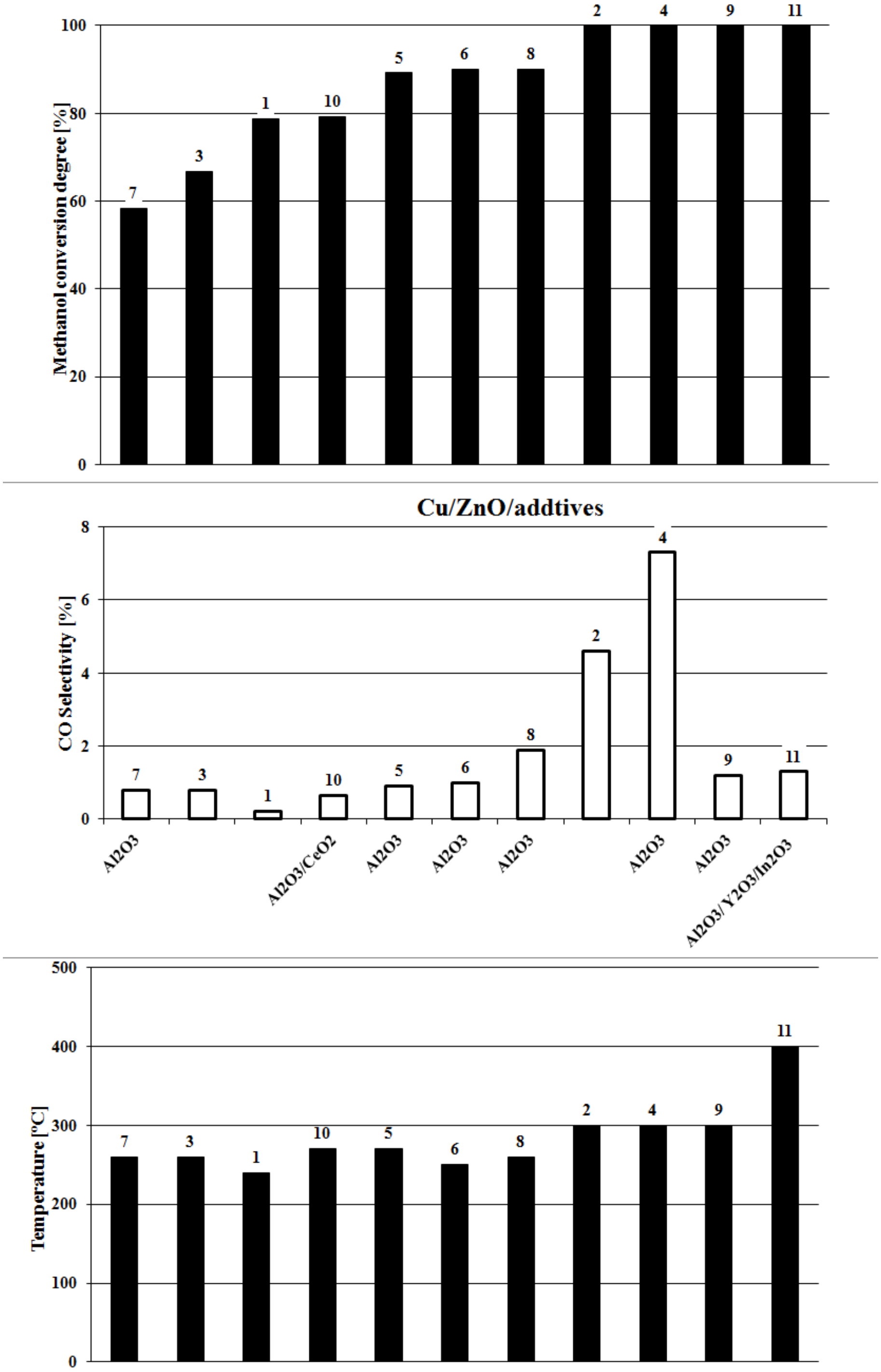

Fig. 1. Methanol conversion and CO selectivity for optimal temperature of Cu/ZnO/additive catalyts, where the numbers above the bars refer to the numbers in the first column of Table 1

It can be seen that many catalysts have high activity (near 100 % conversion of methanol), but the lowest level of CO is still at about 1000 ppm. Total elimination of CO is not possible because of the course of RWGS reaction.

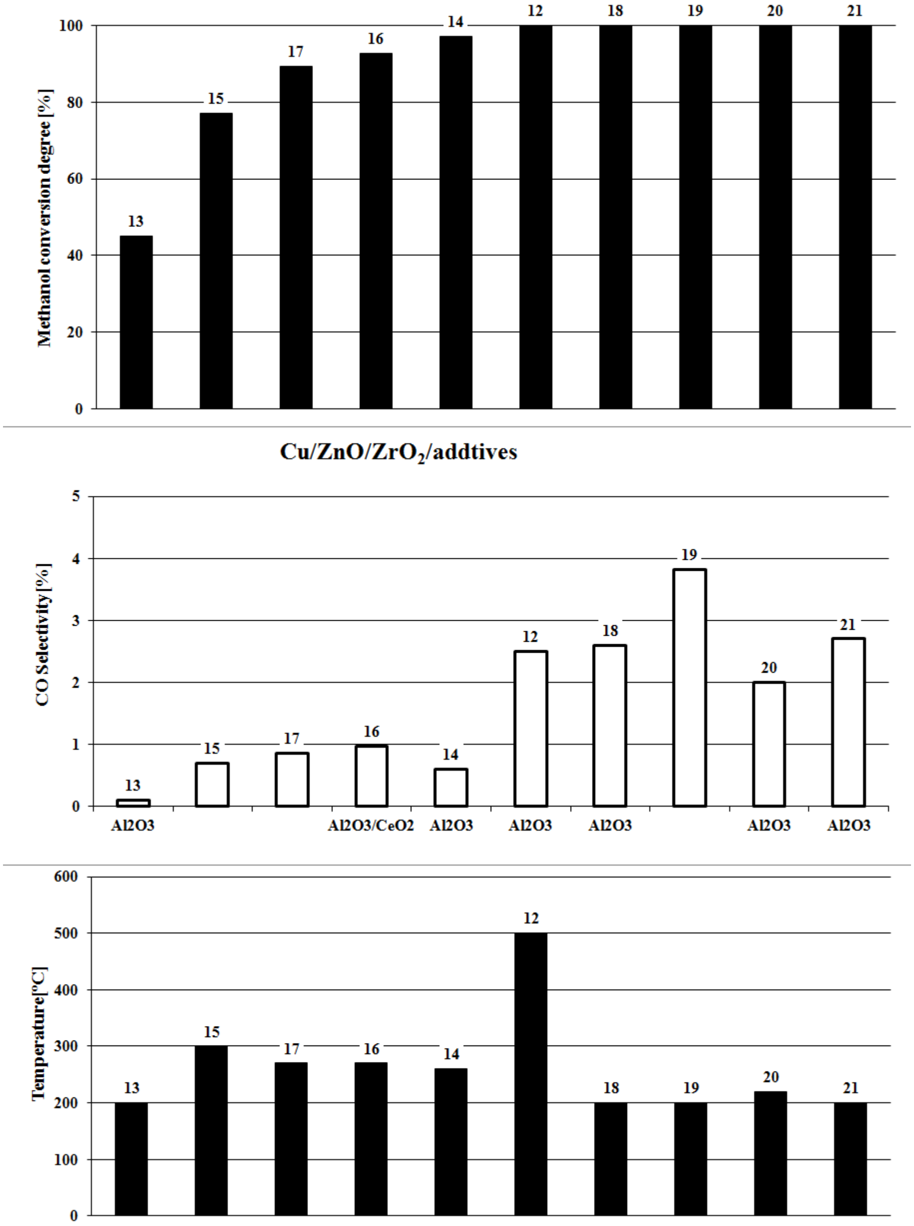

Fig. 2. Methanol conversion and CO selectivity for optimal temperature of Cu/ZnO/ZrO$_2$/additive catalyts where the numbers above the bars refer to the numbers in the first column of the Table 1

3.2. Kinetics of SRM process

SRM kinetic equations for the process conducted on copper catalysts are collected in Table 4. Some of them are Langmuir-Hinshelwood type, others, purely empirical, are in a power law form. There is no agreement regarding the effect of particular reagents on the reaction rate, do they have positive or inhibiting effect. Moreover, not all effects are considered; the effect of CO_2 and H_2O is often ignored. There are important differences in describing the effect of methanol concentration on the reaction rate; an exponent in power law equations differs from 0.04 (Idem and Bakhshi, 1996) to 0.7 (Papavasiliou et al., 2007). The effect of hydrogen concentration on the reaction rate is very often neglected or an inhibiting effect is described, with an exponent varying between 0 and -1.3 (Barton and Pour, 1980). Some of the listed kinetic equations have very complicated formulae, see Peppley et al. (1999) which contain concentrations of various types of active sites, equilibrium constants of intermediates and other constants. Their application is very narrow.

Table 4. Kinetic equations of steam reforming of methanol

<table>
<tr><th>Catalyst</th><th colspan="4">Kinetic equation</th><th>E
kJ
mol^{-1}</th><th>References</th></tr>
<tr><td>Cu/ZrO$_2$/CeO$_2$
Cu content
4.4–31mass%</td><td colspan="4">$-r_M = kp_M^{0.6} p_W^{0.4} - k^{-1} p_C p_H^3$</td><td>109–61</td><td>Mastalir et al. (2005)</td></tr>
<tr><td>Cu/ZnO/Al$_2$O$_3$
(BASF K3-110)</td><td colspan="4">$-r_M = kp_M^{0.63} p_W^{0.39} p_H^{-0.23} p_C^{-0.07}$</td><td>74</td><td>Samms et al. (2002)</td></tr>
<tr><td>Cu/ZnO/Al$_2$O$_3$</td><td colspan="4">$-r_M = kp_M^{0.564}(11.6 + p_H)^{-0.647}$</td><td>103</td><td>Lee et al. (2004)</td></tr>
<tr><td>Cu/ZnO/Al$_2$O$_3$</td><td colspan="4">$-r_M = kK_1 p_M p_H^{-0.5}((1 + kK_1 p_M p_H^{-0.5})(1 + (K_2 p_H)^{0.5})^{-1}$</td><td>111</td><td>Lee et al. (2004)</td></tr>
<tr><td>Cu/MnO/Al$_2$O$_3$</td><td colspan="4">$-r_M = kP_M^{0.04}$ at temperatures <190° C</td><td>80</td><td>Idem and Bakhshi (1996)</td></tr>
<tr><td>Cu/MnO/Al$_2$O$_3$</td><td colspan="4">$-r_M = k(p_M - p_C p_H^3 (K_p p_W)^{-1})(1 + Kp_M)^{-1}$</td><td>77</td><td>Idem and Bakhshi (1996)</td></tr>
<tr><td>Cu/MnO/Al$_2$O$_3$</td><td colspan="4">$-r_M = kp_M^{0.28} p_C^{0.99}$</td><td>78</td><td>Idem and Bakhshi (1996)</td></tr>
<tr><td>Cu/MnO/Al$_2$O$_3$</td><td colspan="4">$-r_M = k(p_M p_W p_H^{-1} - p_C p_H^2 K_p^{-1})/(1 + Kp_M)^{-4}$</td><td>117</td><td>Idem and Bakhshi (1996)</td></tr>
<tr><td>Cu$_{0.30}$Mn$_{0.70}$</td><td colspan="4">$-r_M = kp_M^{0.7} p_W^{0.5}$</td><td>71</td><td>Papavasiliou et al. (2007)</td></tr>
<tr><td>Cu/ZnO/Al$_2$O$_3$
(BASF S3-85)</td><td colspan="4">$-r_M = k(K_1 p_M (K_3 \cdot p_H)^{-0.5}(1 + K_1 p_M (K_3 p_H)^{0.5} +$
$(K_3 p_H)^{-0.5})^{-2})$</td><td>110</td><td>Jiang et al. (1993b)</td></tr>
<tr><td>Cu/ZnO/Al$_2$O$_3$
(BASF S3-85)</td><td colspan="4">$-r_M = kp_M^{0.26} p_W^{0.03} p_H^{-0.2}$</td><td>105</td><td>Jiang et al. (1993a)</td></tr>
<tr><td>Cu/ZnO
Girdler G66B)</td><td colspan="4">$-r_M = (kK_M p_M - k' p_{CO} p_M^2)/(1 + Kp_{CO})$</td><td>96</td><td>Amphlett et al. (1985)</td></tr>
<tr><td>Cu/ZnO/Cr$_2$O$_3$/
Al$_2$O$_3$</td><td colspan="4">$-r_M = k(p_M p_W)^{0.5} p_H^{-1.3}$</td><td>116</td><td>Barton and Pour (1980)</td></tr>
<tr><td>Cu/ZnO/Al$_2$O$_3$
(BASF K3-110)</td><td colspan="4">$-r_M = kK_{CH_3O(1)} p_M p_H^{-0.5}(1 - p_H^3 p_C (kp_M p_W)^{-1} C_{S1}^T C_{S1a}^T / DEN^*$</td><td>103</td><td>Peppley et al. (1999)</td></tr>
<tr><td>Cu/ZnO/Al$_2$O$_3$
(BASF)</td><td colspan="4">$-r_M = (kK_M p_M)/(1 + K_M p_M + K_W p_W)$</td><td>103</td><td>Santacesaria and Carrà, (1983)</td></tr>
<tr><td>Cu/ZnO/Al$_2$O$_3$</td><td colspan="4">$-r_M = kp_M^{0.4}(1 - p_C P_H^3 / K_E p_M p_W)$</td><td>83</td><td>Geissler et al. (2001)</td></tr>
<tr><td>Cu/ZnO/Al$_2$O$_3$
(Süd-Chemie)</td><td colspan="4">$-r_M = kP_M^{0.6} P_W^{0.4}$</td><td>76</td><td>Purnama et al. (2004)</td></tr>
<tr><td>Cu/ZnO/ZrO$_2$/
Ga$_2$O$_3$</td><td colspan="4">$r = kp_M^{0,29} p_W^{-0.193}(0.5 + p_H)^{-1}$</td><td>57</td><td>Madej-Lachowska (2012)</td></tr>
<tr><td>Cu-Zn-Al</td><td colspan="4">$r = \dfrac{\eta \cdot k_M \cdot b_M \cdot p_M}{1 + b_M \cdot p_M + b_W \cdot p_W}$ inhibiting effect of water is included</td><td>119</td><td>Tesser (2009)</td></tr>
<tr><td>Cu-Zn-Al</td><td colspan="4">$-r_M = (\eta \cdot k_M \cdot b_M \cdot p_M)/(1 + b_M \cdot p_M + b_W \cdot p_W + b_H \cdot p_H)$
inhibiting effect of water and hydrogen is included</td><td>102</td><td>Tesser (2009)</td></tr>
<tr><td>Cu-Zn-Al</td><td colspan="4">$-r_M = k \cdot p_M^a \cdot p_W^b \cdot p_C^c \cdot p_H^d$</td><td></td><td rowspan="7">Tesser (2009)</td></tr>
<tr><td rowspan="6"></td><td>a</td><td>b</td><td>c</td><td>d</td><td></td></tr>
<tr><td>0.351</td><td>0</td><td>0.134</td><td>0</td><td>91</td></tr>
<tr><td>0.310</td><td>-0.151</td><td>0</td><td>0</td><td>101</td></tr>
<tr><td>0.389</td><td>0</td><td>0</td><td>0.195</td><td>85</td></tr>
<tr><td>0.235</td><td>0.216</td><td>0</td><td>0.436</td><td>80</td></tr>
<tr><td>0.402</td><td>-0.468</td><td>0.578</td><td>-0.793</td><td>117</td></tr>
</table>

C - carbon dioxide, H - hydrogen, M - methanol, W - water; C_S^T - concentration of active sites

Tesser et al. (2009) conducted very detailed investigations on industrial $CuO/ZnO/Al_2O_3$ catalyst – BASF K-3-10. They found water to be an inhibiting agent at a constant partial pressure of methanol and to be responsible for low methanol conversion, the reaction rate is a linear function of the initial mole substrate ratio of CH_3OH /H_2O. They proposed 3 types of kinetic equations based on their experiments and literature data. Two of them are of Langmuir-Hinshelwood type; in the first the inhibiting effect of water is included, while in the second – the inhibiting effect of water and hydrogen. In both equations an effectiveness factor is introduced concerning the effect of internal diffusion in catalyst tablets.

The third kinetic equation is an expression in a power law form with various values of exponents for different mechanisms. In authors' opinion, all these equations satisfactorily describe kinetic data. However, applicability ranges for these equations are not precisely stated. Therefore, they can only be considered an estimation. The most reliable are papers by Jiang et al. (1993a) and Samms et al. (2002). Jiang et al. (1993a) proposed power law equations of SRM process in the presence of an industrial $CuO/ZnO/Al_2O_3$ catalyst, BASF S3-85. They conducted kinetic experiments in the temperature range of 445-535 K at methanol conversion below 20%. The reaction rate has been determined as a function of concentrations of products and initial concentrations of substrates. The effect of partial pressure of methanol on the reaction rate (exponent equal to 0.26) and the inhibiting effect of partial pressure of H_2 (exponent equal to -0.2), neither the effect of partial pressure of H_2O (exponent equal to 0.03), nor the effect of partial pressure of CO_2 on the reaction rate was found.

Samms et al. (2002) carried out their kinetic investigations over a $CuO/ZnO/Al_2O_3/MgO$ catalyst [Synetix 33-5] in the temperature range of 435-535 K, for values of the initial mole substrate ratio of CH_3OH /H_2O equal to 1, 2/3, and 1/2. Similarly to Jiang et al. (1993a) they found an effect of partial pressure of methanol and partial pressure of H_2, and no effects of partial pressures of H_2O and CO_2.

Kinetic propositions of Idem and Bakhshi (1996) should be treated very cautiously. The authors presented four various kinetic equations, the two of them in a power law form, based on the same experiments, over the same catalyst. The values of activation energy were very close for the three equations, but the practically constant value of the reaction rate (the exponent of partial pressure of methanol close to zero) makes these estimations somewhat uncertain. In the last equation, in a more complicated form, the exponent of fourth power in the denominator could excessively change the results.

Such attempts at estimation of the reaction rate of SRM reveal complexity of the process. It is also concerned with a very complex structure of catalysts used; an effect of any metal acting is not apparent in coupling with other components. The authors of these kinetic investigations cannot describe one experimental set with one kinetic equation. So, it is impossible for the reader to select proper relationships for their own experiments.

4. CATALYSTS FOR PREFERENTIAL OXIDATION OF CARBON MONOXIDE (CO-PROX)

Regardless of the method used, the hydrogen feed gas for energy production produced by converting a conventional fuel such as a natural gas, gasoline or methanol usually consist of: 45-74 vol. % H_2, 15-25 vol. % CO_2, 0.5-2 vol. % CO and a few vol. % H_2O and N_2 (Di Benedetto et al., 2013). This concentration of CO is too high for polymer electrolyte membrane fuel cells and the gas mixture requires reduction of CO concentration. Hydrogen produced even over the best selective catalysts should be purified from CO. Catalysts for hydrogen production are not sufficiently active in oxidizing of carbon monoxide. An additive process, in which carbon monoxide will be very selectively oxidized to carbon dioxide in the presence of significant excess of hydrogen is then needed. Catalytic preferential oxidation of carbon monoxide (CO-PROX) is a method to avoid poisoning of Pt-based anode in a proton exchange membrane fuel cell (PEMFC). CO–PROX catalysts should be very active in the oxidation of carbon monoxide to decrease its concentration to 10 ppm, following the reaction formula:

$$CO + 0.5O_2 \rightarrow CO_2 \tag{12}$$

Additionally, these catalysts cannot be active in the reaction of oxidation of hydrogen, it is in excess in the gas mixture, so in the presence of less selective catalysts the prevailing reaction could be as follows:

$$H_2 + 0.5O_2 \rightarrow H_2O \tag{13}$$

For assessment of the effectiveness of CO-PROX catalysts the selectivity towards CO is defined as a part of oxygen that oxidizes CO while the rest of oxygen oxidizes hydrogen:

$$S_{CO} = \frac{[CO]_1 - [CO]_2}{2([O_2]_1 - [O_2]_2)} \tag{14}$$

where: [CO], $[O_2]$ – concentration of CO and O_2; Subscripts: 1,2 – initial, output

PROX Process is conducted at atmospheric pressure in the temperature range of 80-150^{0}C with oxygen excess, compared to the stoichiometric value. Active CO–PROX catalysts are mainly noble metals supported on oxide carriers promoted by base metal oxides. The most active are:

- catalysts containing copper: Cu/CeO_2 (Di Benedetto et al., 2013; Gu et al. 2014; Liu et al., 2004; Monte et al. 2014; Tang et al. 2014),
- catalysts containing dispersed gold: Au/SiO_2, Au/TiO_2, Au/Al_2O_3, Au/ Fe_2O_3 (Kung et al., 2003); Au/MgO promoted with Mn and Fe (Margitfalvi et al., 2004); $Au/CeO_2–CoO_4$ (Wang et al., 2008; Au/α-Fe_2O_3 (Avgouropoulos et al., 2002); Au(Pt-Au)/CeO_2 (Liu et al., 2013),
- catalysts containing platinum, rhodium or ruthenium: Pt/ γ-Al_2O_3 (Avgouropoulos et al., 2002); Pt(Pt-Au)/CeO_2 (Liu et al., 2013); K promoted Rh on zeolit USY (SiO_2/ Al_2O_3 (Tanaka et al., 2003); base metal promoted 5% Pt on monolithic cordierite impregnated with γ-Al_2O_3 Korotkikh and Farrauto, 2000) monolithic Pt/Fe on mordenit (Maeda et al., 2008); Pt (Ru, Rh)/ γ-Al_2O_3 (Kim et al., 2009).

Only in the presence of the catalysts containing platinum, rhodium or ruthenium, the level of carbon monoxide can be lowered to 10 ppm.

For this type of catalysts further investigations to optimize process parameters and composition of the catalysts are continued. The inhibition of oxidation of carbon monoxide by steam and carbon dioxide and the rate of deactivation of catalysts used are still the important problems to be investigated.

Dudfield et al. (2001) reported the construction of a CO-PROX reactor integrated with reforming of a methanol reactor. The set has been designed for automotive transport, 2.5 mass% Pt/Ru supported on hopcalite CO-PROX catalyst enables a decrease in CO concentration to 10 ppm thus enabling its application in 20 kW power fuel cells. The work has been granted as Mercatox Project coordinated by Wellman CJB Ltd. UK.

5. CONCLUSIONS

The production of hydrogen from methanol can be performed in 4 different ways: thermal decomposition of methanol (MD), partial oxidation of methanol (POM), steam reforming of methanol (SRM), oxidative steam reforming of methanol (OSRM). OSRM system integrates the advantages of POM and SRM, but also shares their disadvantages.

The development of Cu-based catalysts has been focused on steam reforming of methanol. An effort has been put in to improve the low surface area of the catalyst. Recently, Cu-based spinel-latticed catalysts have been extensively studied due to their high thermal stability, thus avoiding Cu sintering. Different mechanisms have been proposed concerning reactions occurring on copper surface and reactions at the boundary between Cu and metal oxide. Full explanation of these phenomena will allow to design an optimal catalyst and thus optimum process. Despite many attempts, the required purity of hydrogen production in SRM process over a Cu based catalyst was not obtained. Ensuring high purity of hydrogen is a priority, so preferential oxidation of carbon monoxide (CO-PROX) over the best catalysts should be applied. Agrell et al. (2002) proposed the addition of steam to the substrate mixture, decrease temperature and contact time to increase hydrogen purity, at the cost of conversion of methanol.

While that area of research is of great importance, it is also quite difficult, both in experimental and theoretical parts. The available body of literature concerning these topics is too small to describe it in certain terms. The most important tendencies in the production of high purity hydrogen for fuel cells have been described in the presented paper.

SYMBOLS

DEN	$= (1 + K_{\mathrm{CH_3O(1)}} p_M \, p_{\mathrm{H}}^{-0.5} + K_{\mathrm{OH(2)}} p_W \, p_{\mathrm{H}}^{-0.5})(1 + K_{\mathrm{H}(2a)}^{0.5} \, p_{\mathrm{H}}^{0.5})$
E	energy of activation, kJ·mol^{-1}
$GHSV$	gas hourly space velocity, h^{-1}
k	rate constant for methanol stem reforming reaction; units are specific to the form of the rate expression
k^{-1}	rate constant for reverse methanol stem reforming reaction; units are specific to the form of the rate expression
K_i	equilibrium constant of reaction i or adsorption coefficient for surface species i
p	partial pressure of component, MPa
r	reaction rate, mol·s^{-1}·g$_{cat}^{-1}$
t	temperature, °C
T	temperature, K

Greek symbols

η	effectiveness factor taking into account internal diffusion

Superscripts

a, b, c, e	exponents in power law equation

Subscripts

C	carbon dioxide
H	hydrogen
M	methanol
W	water

REFERENCES

Agrell J., Germani G., Järås S. G., Boutonnet M., 2003. Production of hydrogen by partial oxidation of methanol over ZnO-supported palladium catalysts prepared by microemulsion technique. *Appl. Catal. A-Gen.*, 242, 233-245. DOI: 10.1016/S0926-860X(02)00517-3.

Agrell J., Birgersson H., Boutonnet M., 2002. Steam reforming of methanol over a Cu/ZnO/Al_2O_3 catalyst: A kinetic analysis and strategies for suppression of CO formation *J. Power Sources*, 106, 249-257. DOI: 10.1016/S0378-7753(01)01027-8.

Agrell J., Hasselbo K., Jansson K., Järås S.G., Boutonnet M., 2001. Production of hydrogen by partial oxidation of methanol over Cu/ZnO catalysts prepared by microemulsion technique. *Appl. Catal. A-Gen*., 211, 239-250. DOI: 10.1016/S0926-860X(00)00876-0.

Alejo L, Lago R, Peňa M. A., Fierro J.L.G., 1997. Partial oxidation of methanol to produce hydrogen over Cu-Zn-based catalysts. *Appl. Catal. A-Gen*.,162, 281-297. DOI: 10.1016/S0926-860X(97)00112-9.

Amphlett J.C., Evans M.J., Mann R. F., Weir R.D., 1985. Hydrogen production by the catalytic steam reforming of methanol. Part 2: Kinetics of methanol decomposition using girdler G66B catalyst. *Can. J. Chem. Eng.*, 63, 605-611. DOI: 10.1002/cjce.5450630412.

Avgouropoulos G., Ioannides T., Papadopoulou C., Batista J., Hocevar S., Matralis H., 2002. A comparative study of Pt/γ-Al_2O_3, Au/α-Fe_2O_3 and CuO-CeO_2 catalysts for the selective oxidation of carbon monoxide in excess hydrogen. *Catal. Today*, 75,157-167. DOI: 10.1016/S0920-5861(02)00058-5.

Barton J., Pour V., 1980. Kinetics of catalytic conversion of methanol at higher pressures. *Collect. Czech. Chem. Commun*., 45, 3402-3407.

Chang F.W., Yu H.Y., Roselin L.S. , Yang H.Ch., Ou T.Ch., 2006. Hydrogen production by partial oxidation of methanol over gold catalysts supported on TiO_2-MO_x (M = Fe, Co, Zn) composite oxides. *Appl. Catal. A-Gen*., 302, 157-167. DOI: 10.1016/j.apeata.2005.12.028.

Cheng-Chun C., Jhih-Wei W., Ching-Tu C., Biing-Jye L., Yin-Zu C., 2012. Effect of ZrO_2 on steam reforming of methanol over CuO/ZnO/ZrO_2/Al_2O_3 catalysts. *Chem. Eng. J.*, 192, 350-356. DOI: 10.1016/j.cej.2012.03.063.

Cubeiro M.L., Fierro J.L. G., 1998. Selective production of hydrogen by partial oxidation of methanol over ZnO-Supported palladium catalysts. *J. Catal.*, 179, 150-162. DOI: 10.1006/jcat.1998.2184.

Di Benedetto A., Landi G., Lisi L., Russo G., 2013. Role of CO_2 on CO preferential oxidation over CuO/CeO_2 catalyst. *Appl. Catal. B-Environ*., 142-143, 169-177. DOI: 10.1016/j.apcatb.2013.05.001

Dodds P.E., Staffell I., Hawkes A.D., Li F., Grünewald P., McDowall W., Ekins P., 2015. Hydrogen and fuel cell technologies for heating: A review. *Int. J. Hydrogen Energy*, 40, 2065-2083. DOI: 10.1016/j.ijhydene.2014.11.059.

Dudfield C.D., Chen R., Adcock P.L., 2001. A carbon monoxide PROX reactor for PEM fuel cell automotive application. *Int. J. Hydrogen Energ.*, 26, 763-775. DOI: 10.1016/S0360-3199(00)00131-2.

Geissler K., Newson E., Vogel F., Truong T.B., 2001. Hottinger P, Wokaun A. Autothermal methanol reforming for hydrogen production in fuel cell applications. *Phys. Chem. Chem. Phys*., 3, 289-293. DOI: 10.1039/b004881j.

Gu D., Jia C. J., Bongard H., Spliethoff B., Weidenthaler C., Schmidt W., Schüth F., 2014. Ordered mosorporous Cu-Ce-O catalysts for CO preferential oxidation in H_2-rich gasees: Influance of copper content and pretreatment conditions. *Appl. Catal. B- Envinron.*, 152-153, 11-18. DOI: 10.1016/j.apcatb.2014.01.011.

Hansen J.B., 1997. Handbook of Heterogeneous Catalysis, Ertl G., Knözinger H., Weitkamp J. (Eds.), VCH, Weinheim, Vol. 4, 1856.

Huang G., Liaw B.J., Jhang C.J., Chen Y.Z., 2009. Steam reforming of methanol over CuO/ZnO/CeO_2/ZrO_2/Al_2O_3 catalysts. *Appl. Catal. A-Gen*., 358, 7-12. DOI: 10.1016/j.apcata.2009.01.031.

Hung-Ming Y. Min-Ke C., 2011. Steam reforming of methanol over copper-yttria catalyst supported on praseodymium-aluminum mixed oxides. *Catal. Commun.* 12, 1389-1395. DOI: 10.1016/j.catcom.2011.05.022.

Idem R.O., Bakhshi N.N., 1996. Characterization studies of calcined, promoted and non-promoted methanol-steam reforming catalysts. *Can. J. Chem. Eng*., 74, 288-300. DOI: 10.1002/cjce.5450740214.

Ilinich O.M., Liu Y., Waterman E.M., Farrauto R.J., 2013. Kinetics of methanol steam reforming with a Pd-Zn-Y/CeO_2 catalyst under realistic operating conditions of a portable reformer in fuel cell applications. *Ind. Eng. Chem. Res*., 52, 638-644. DOI: 10.1021/ie301606w.

Jiang C.J., Trimm D.L., Wainwright M.S., Cant N.W., 1993. Kinetic mechanism for the reaction between methanol and water over a Cu-ZnO-Al_2O_3 catalyst. *Appl. Catal. A-Gen*., 97, 145-158. DOI: 10.1016/0926-860X(93)80081-Z.

Jiang C.J., Trimm D.L., Wainwright M.S., Cant N.W., 1993. Kinetic study of steam reforming of methanol over copper-based catalysts. *Appl. Catal. A-Gen.*, 93, 245-255. DOI: 10.1016/0926-860X(93)85197-W.

Kim Y.H., Park E.D., Lee H.Ch., Lee D., Lee D.K., 2009. Preferential CO oxidation over supported noble metal catalysts. *Catal. Today*, 146, 253259. DOI: 10.1016/j.cattod.2009.01.045.

Korotkikh O., Farrauto R., 2000. Selective catalytic oxidation of CO in H-2: Fuel cell applications. *Catal. Today*, 62, 249-254. DOI: 10.1016/S0920-5861(00)00426-0.

Kulawska M., 2008. Termodynamika, zagadnienia katalityczne i kinetyka w procesie syntezy wyższych alkoholi alifatycznych. Prace Naukowe IICh PAN.

Kung H.H., Kung M.C., Costello C.K., 2003. Supported Au catalysts for low temperature CO oxidation. *J. Catal.*, 216, 425-432. DOI: 10.1016/S0021-9517(02)00111-2.

Lachowska M., 2010. Steam reforming of methanol over Cu/Zn/Zr/Ga catalyst - effect of the reduction conditions on the catalytic performance. *Reac. Kinet. Mech. Cat.,* 101, 85-91. DOI: 10.1007/s11144-010-0213-z.

Lachowska M., 2004. Reforming metanolu parą wodną na katalizatorze miedziowo-cynkowo-cyrkonowym modyfikowanym Ga, Mn oraz Mg. *Inż. Chem. Proc.*, 25, 1243-1247.

Lee J.K., Ko J.B., Kim D.H., 2004. Methanol steam reforming $Cu/ZnO/Al_2O_3$ catalyst: kinetics and effectiveness factor. *Appl. Catal. A-Gen.*, 278, 25-35. DOI: 10.1016/j.apcata.2004.09.022.

Lindström B., Pettersson L.J., Govind M.P., 2002. Activity and characterization of Cu/Zn, Cu/Cr and Cu/Zr on γ-alumina for methanol reforming for fuel cell vehicles. *Appl. Catal. A-Gen.*, 234, 111-125. DOI: 10.1016/S0926-860X(02)00202-8.

Liu Q., Wang L.C., Chen M., Liu Y.M., Cao Y., He H.Y., Fan K.N., 2008. Waste-free soft reactive grinding synthesis of high-surface-area copper–manganese spinel oxide catalysts highly effective for methanol steam reforming. *Catal. Lett.*, 121, 144-150. DOI: 10.1007/s10562-007-9311-6.

Liu Y., Fu Q., Stephanopoulos M. F., 2004. Preferential oxidation of CO in H_2 over CuO-CeO_2 catalysts. *Catal. Today,* 93-95, 241-246. DOI: 10.1016/j.cattod.2004.06.049.

Liu Y., Hayakawa T., Tsunoda T., Suzuki K., Hamakawa S., Murata K., Shiozaki R., Ishii Kumagai T.M., 2003. Steam reforming of methanol over Cu/CeO_2 catalysts studied in comparison with Cu/ZnO and Cu/Zn(Al)O catalysts. *Top. Catal.*, 22, 205-213. DOI: 10.1023/A:1023519802373.

Liu Y., Hayakawa T., Tsunoda T., Suzuki K., Hamakawa S., Murata K., Shiozaki R., Ishii T., Kumagai M., 2003. Steam reforming of methanol over Cu/CeO_2 catalysts studied in comparison with Cu/ZnO and Cu/Zn(Al)O catalysts. *Top. Catal.*, 22, 205-213. DOI: 10.1023/A:1023519802373.

Liu Y., Liu B., Liu Y., Wang Q., Hu W., Jing P., Liu L., Yu S., Zhang J. , 2013. Improvement of catalytic performance of preferential oxidation of CO in H_2-richgases on three-dimensionally ordered macro-and meso-porous Pt-Au/CeO_2 catalysts. *Appl. Catal.- B Environ.*, 142-143, 615-625. DOI: 10.1016/j.apcatb.2013.06.002.

Lopez P., Mondragon-Galicia G., Espinosa-Pesqueita M.E., 2012. Hydrogen production from oxidative steam reforming of methanol: Effect of the Cu and Ni impregnation on ZrO_2 and their molecular simulation studies. *Int. J. Hydrogen Energ.*, 37, 9018-9027. DOI: 10.1016/j.ijhydene.2012.02.105.

Madej-Lachowska M., 2012. *Reforming metanolu parą wodną - Termodynamika, kataliza i kinetyka procesu*. Agencja Wydawnicza ARGI s.c., Wrocław.

Maeda N., Matsushima T., Uchida H., Yamashita H., Watanabe M., 2008. Performance of Pt-Fe/mordenite monolithic catalysts for preferential oxidation of carbon monoxide in a refor-mate gas for PEFCs. *Appl. Catal. A-Gen.*, 341, 93-97. DOI: 10.1016/j.apcata.2008.02.022.

Margitfalvi J.L., Hegedús M., Szegedi A., Sajó I., 2004. Modification of Au/MgO catalysts used in low temperature CO oxidation with Mn and Fe. *Appl. Catal. A-Gen.*, 272, 87-97. DOI: 10.1016/j.apcata.2004.05.035.

Mastalir A., Frank B., Szizybalski A., Soerijanto H., Deshpande A., Niederbrger M., Schomäcker R., Schlögl R., Resseler T., 2005. Steam reforming of methanol over $Cu/ZrO_2/CeO_2$ catalysts: a kinetic study. *Appl. Catal. A-Gen.*, 230, 464-475. DOI: 10.1016/j.jcat.2004.12.020.

Mastalir Á., Patzkó Á., Frank B., Schomäcker R., Ressler T., Schlögl R., 2007. Steam reforming of methanol over $Cu/ZnO/Al_2O_3$ modified with hydrotalcites. *Catal. Commun.*, 8, 1684-1690. DOI: 10.1016/j.catcom.2007.01.031.

Matsumura Y., 2013. Development of durable copper catalyst for hydrogen production by high temeperature methanol steam refo.rming. *Int. J. Hydrogen Energ.*, 38, 13950-13960. DOI: 10.1016/j.ijhydene.2013.08.066

Matsumura Y., 2014. Durable Cu composite catalyst for hydrogen production by high temperature methanol steam reforming. *J. Power Sources*, 272, 961-969. DOI: 10.1016/j.jpowsour.2014.09.047.

Matsumura Y., 2013. Stabilization of $Cu/ZnO/ZrO_2$ catalyst for methanol steam reforming to hydrogen by coprecipitation on zirconia support. *J. Power Sources*, 238, 109-116. DOI: 10.1016/j.jpowsour.2013.03.074

Momirlan M., Veziroglu, T.N, 2005. The properties of hydrogen as fuel tomorrow in sustainable energy system for a cleaner planet. *Int. J. Hydrogen Energ.*, 30, 795-802. DOI: 10.1016/j.ijhydene.2004.10.011.

Monte M., Gamarra D., López Cámara A., Rasmussen S. B., Gyorffy N., Schay Z., Martínez-Arias A., Conesa J. C., 2014. Preferential oxidation of CO in excess H_2 over CuO/CeO_2 catalysts: Performance as a function of copper coverage and exposed face present in the CeO_2 support. *Catal. Today*, 229, 104-113. DOI: 10.1016/j.cattod.2013.10.078.

Navarro R.M., Peňa M.A., Fierro J.G., 2002. Production of hydrogen by partial oxidation of methanol over a $Cu/ZnO/Al_2O_3$ catalyst: Influence of the initial state of the catalyst on the start-up behaviour of the reformer. *J. Catal.*, 212, 112-118. DOI: 10.1006/jcat.2002.3764.

Papavasiliou J., Avgouropoulos G., Ioannides T., 2007. Combined steam reforming of methanol over Cu-Mn spinel oxide catalysts. *J. Catal.*, 251, 7-20. DOI: 10.1016/j.jcat.2007.07.025.

Papavasiliou J., Avgouropoulos G., Ioannides T., 2009. Steady-state isotopic transient kinetic analysis of steam reforming of methanol over Cu-based catalysts. *Appl. Catal. B-Environ.*, 88, 490-496. DOI: 10.1016/j.apcatb.2008.10.018.

Park B., Kwon S., 2015. Compact design of oxidative steam reforming of methanol assisted by blending hydrogen peroxide. *Int. J. Hydrogen Energ.*, 40, 12697-12704. DOI: 10.1016/j.ijhydene.2015.07.084

Patel S., Pant K.K., 2006. Influence of preparation method on performance of Cu(Zn)(Zr)-alumina catalysts for the hydrogen production via steam reforming of methanol. *J. Porous Mat.*, 13, 373-378. DOI: 10.1007/s10934-006-8033-2.

Peppley B.A. Amphlett J.C., Kearns L.M., Mann R.F., 1999. Methanol-steam reforming on $Cu/ZnO/Al_2O_3$ catalysts. Part 2: A comprehensive kinetic model. *Appl. Catal. A-Gen.*, 179, 31-49. DOI: 10.1016/S0926-860X(98)00299-3.

Pojanavaraphan Ch., Luengnaruemitchai A., Gulari E., 2012. Hydrogen production by oxidative reforming of methanol over Au/CeO_2 catalysts. *Chem. Eng. J.*, 192, 105-103. DOI: 10.1016/j.cej.2012.03.083.

Pojanavaraphan Ch., Nakaranuwattana W., Luengnaruemitchai A., Gulari E., 2014. Effect of support composition and metal loading on $Au/Ce_{1-x}Zr_xO_2$ catalysts for the oxidative steam reforming of methanol. *Chem. Eng. J.*, 240, 99-108. DOI: 10.1016/j.cej.2013.11.062.

Purnama H., Girgsdies F., Ressler T., Schattka J. H., Caruso R. A., Schomäcker R., Schlögl R., 2004. Activity and selectivity of a nanostructured CuO/ZrO_2 catalyst in the steam reforming of methanol. *Catal. Lett.*, 94, 61-68. DOI: 10.1023/ B:CATL.0000019332.80287.6b.

Purnama H., Ressler T., Jentoft R.E., Soerijanto H., Schlogl R., Schomacker R., 2004. CO formation/ selectivity for steam reforming of methanol with a commercial $CuO/ZnO/Al_2O_3$ catalyst. *Appl. Catal. A-Gen.*, 259, 83-94. DOI: 10.1016/j.apcata.2003.09.013.

Rameshan Ch., Lorenz H., Mayr L., Penner S., Zemlyanow D., Arrigo R., Haevecker M., Blume R., Knop-Gericke A., Schlögl R., 2012. CO_2-selective methanol steam reforming on In-doped Pd studied by in situ X-ray photoelectron spectroscopy. *J. Catal.,* 295, 185-194. DOI: 10.1016/j.jcat.2012.08.008.

Sá S., Silva H., Brandão L., Sousa J.M., Mendes A., 2010. Catalysts for methanol steam reforming - A review. *Appl .Catal. B- Environ.*, 99, 43-57. DOI: 10.1016/ j.apcatb.2010.06.015.

Samms S.R., Savinell R.F., 2002. Kinetics of methanol-steam reformation in an internal reforming fuel cell. *J. Power Sources*, 112, 13-29. DOI: 10.1016/S0378-7753(02)00089-7.

Santacesaria E., Carrà E., 1978. Cinetica dello steam reforming del metanolo. *La Rivista dei Combustibili*, XXXII: 227-232.

Santacesaria E., Carrà S., 1983 Kinetics of catalytic steam reforming of methanol in a CSTR reactor. *Appl. Catal.*, 5, 345-358. DOI: 10.1016/0166-9834(83)80162-6.

Shishido T., Yamamoto Y., Morioka H., Takaki K., Takehira K., 2004. Active Cu/ZnO and $Cu/ZnO/Al_2O_3$ catalysts prepared by homogeneous precipitation method in steam reforming of methanol. *Appl. Catal. A: Gen.*, 263, 249-253. DOI: 10.1016/j.apcata.2003.12.018.

Skrzypek J., Słoczyński J., Ledakowicz S., 1994. Methanol synthesis. PWN, Warszawa.

Snytnikov P.V., Badmaev S.D., Volkova G.G., Potemkin D.I., Zyryanova M.M., Belyaev V.D., Sobyanin V.A., 2012. Catalysts for hydrogen production in a multifuel processor by methanol, dimethyl ether and bioetanol steam reforming for fuel cell applications. *Int. J. Hydrogen Energ.*, 37, 16388 - 16369. DOI: 10.1016/j.ijhydene.2012.02.116.

Spivey J.J., 2005. Catalysis in the development of clean energy technologies. *Catal. Today*, 100, 171-180. DOI: 10.1016/j.cattod.2004.12.011.

Squadrito G., Andaloro L., Rerraro M. Antonucci V., 2014. In: Basil A., Julianelli A. (Eds.), *Hydrogen fuel cell technology*. Elsevier, New York, 451-496. DOI: 10.1533/9780857097736.3.451.

Takahashi K., Takezawa N., Kobayashi H., 1982. The mechanism of steam reforming of methanol over a copper-silica catalyst. *Appl. Catal.*, 2, 363-366. DOI: 10.1016/0166-9834(82)80154-1.

Takezawa N., Iwasa N., 1997. Steam reforming and dehydrogenation of methanol: Difference in the catalytic function of copper and group VIII metals. *Catal. Today*, 36, 45-56. DOI: 10.1016/S0920-5861(96)00195-2.

Tanaka H., Ito S., Kameoka S., Tomishige K., Kunimori K., 2003. Catalytic performance of K-promoted Rh/USY catalysts in preferential oxidation of CO in rich hydrogen. *Appl. Catal. A: Gen*., 250, 255-263. DOI: 10.1016/S0926-860X(03)00320-X.

Tang C., Sun J., Yao X., Cao Y., Liu L., Ge C., Gao F., Dong L., 2014. Efficient fabrication of active CuO-CeO_2/SBA-15 catalysts for preferential oxidation of CO by solid state impregnation. *Appl. Catal. B- Environ*., 146, 201-212. DOI: 10.1016/j.apcatb.2013.05.060.

Tesser R., Di Serio M., Santacesaria E., 2009. Methanol steam reforming: A comparison of different kinetics in the simulation of a packed bed reactor. *Chem. Eng. J.*, 154, 69-75. DOI: 10.1016/j.cej.2009.06.007.

Urasaki K., Tanimoto N., Hayashi T., Sekine Y., Kikuchi E., Matsukata M., 2005. Hydrogen production via steam-iron reaction using iron oxide modified with very small amounts of palladium and zirconia. *Appl. Catal. A- Gen*., 288, 143-148. DOI: 10.1016/j.apcata.2005.04.023.

Wang H., Zhu H., Qin Z., Wang G., Liang F., Wang J., 2008. Preferential oxidation of CO in H_2 rich stream over Au/CeO_2–Co_3O_4 catalysts. *Catal. Commun*., 9, 1487-1492. DOI: 10.1016/j.catcom.2007.12.017.

Wang L.C., Liu Y.M., Chen M., Cao Y., He H.Y., Wu G.S., Dai L.W., Fan K. N., 2007. Production of hydrogen by steam reforming of methanol over Cu/ZnO catalysts prepared via a practical soft reactive grinding route based on dry oxalate-precursor synthesis. *J. Catal*., 246, 193-204. DOI: 10.1016/j.jcat.2006.12.006.

Wu G.-S., Mao D.-S., Lu G.-Z., Cao Y., Fan K.-N., 2009. The role of the promoters in Cu based catalysts for methanol steam reforming. *Catal. Lett*., 130, 177–184. DOI: 10.1007/s10562-009-9847-8.

Yao C. Z., Wang L. C., Liu Y. M., Wu G. S., Cao Y., Dai W. L., He H.Y., Fan K.N., 2006. Effect of preparation method on the hydrogen production from methanol steam reforming over binary Cu/ZrO_2 catalysts. *Appl. Catal. A-Gen*., 297, 151-158. DOI: 10.1016/j.apcata.2005.09.002.

Yong S. T., Ooi C.W., Chai S.P., Wu X.S.,2013. Review of methanol steam reforming – Cu – based catalysts, surface reaction mechanisms, and reaction schemes. *Int. J. Hydrogen Energ.*, 38, 9541-9552. DOI: 10.1016/j.ijhydene.2013.03.023.

Received 27 July 2016
Received in revised form 05 September 2016
Accepted 10 February 2017

DE GRUYTER OPEN
Chemical and Process Engineering 2017, 38 (1), 163-175
DOI: 10.1515/cpe-2017-0013

SIMULATION OF N-PROPANOL DEHYDRATION PROCESS VIA HETEROGENEOUS AZEOTROPIC DISTILLATION USING THE NRTL EQUATION

Andrzej Wyczesany*

Institute of Organic Chemistry and Technology, University of Technology, 31-155 Kraków, Poland

Numerical values of the NRTL equation parameters for calculation of the vapour – liquid – liquid equilibria (VLLE) at atmospheric pressures have been presented for 5 ternary mixtures. These values were fitted to the experimental VLLE and vapour – liquid equilibrium (VLE) data to describe simultaneously, as accurately as possible, the VLE and the liquid – liquid equilibria (LLE). The coefficients of this model called further NRTL-VLL were used for simulations of n-propanol dehydration via heterogeneous azeotropic distillation. The calculations performed by a ChemCAD simulator were done for 4 mixtures using hydrocarbons, ether and ester as an entrainer. In majority simulations the top streams of the azeotropic column had composition and temperature similar to the corresponding experimental values of ternary azeotropes. The agreement between the concentrations of both liquid phases formed in a decanter and the experimental values of the LLE was good for all four simulations. The energy requirements were the most advantageous for the simulation with di-n-propyl ether (DNPE) and isooctane. Simulations were performed also for one mixture using the NRTL equation coefficients taken from the ChemCAD database. In that case the compositions of the liquid organic phases leaving the decanter differed significantly from the experimental LLE data.

Keywords: dehydration of n-propanol, heterogeneous azeotropic distillation

1. INTRODUCTION

There is increasing interest in the use of dehydrated alcohols (ethanol, *n*-propanol, isopropanol and *n*-butanol) as a transport fuel. Biological fermentation delivers low concentration aqueous solutions of these alcohols. They may be relatively easily concentrated by a simple distillation. However, those alcohols form with water low boiling point azeotropes, which requires the use of other techniques to obtain anhydrous alcohols. One of them is a heterogeneous azeotropic distillation with the addition of a third component, which can form with water – an alcohol mixture, a ternary heteroazeotrope. A classic example is the dehydration of ethanol using benzene (Young, 1902). It has very good properties as an entrainer but carcinogenic nature. Therefore, it is proposed in the literature to use diisopropyl ether (DIPE) (Pienaar et al., 2013; Pla-Franco et al., 2014a) or other hydrocarbons: cyclohexane (Gomis et al., 2005), *n*-hexane (Gomis et al., 2007a), isooctane (Font et al., 2003) and *n*-heptane (Gomis et al., 2006). In the case of n-propanol dehydration process the following substances have been proposed to be used as an entrainer: cyclohexane (Lee and Shen, 2005), isooctane (Pla-Franco et al., 2014a), DNPE (Lladosa et al., 2008) and *n*-propyl acetate (Pla-Franco et al., 2014b).

The flowsheet of heterogeneous azeotropic distillation can be examined by professional simulators. Font et al. (2003) obtained the Uniquac equation parameters for the water – ethanol – isooctane system by correlation of the VLE and VLLE data and used them in the simulation of ethanol dehydration. The

---

*Corresponding author, e-mail: awyczes@chemia.pk.edu.pl same system was investigated by Cairns and Furzer (1990). Pla-Franco et al. (2014b) proposed a flowsheet consisting of three columns for separation of the mixture water - *n*-propanol using *n*-propyl acetate. The same authors (Pla-Franco et al., 2014a) compared the simulations of ethanol dehydration process using benzene or DIPE. Arifin and Chien (2007), Chang et al. (2012) and Wu and Chien (2009) performed the simulations of isopropanol dehydration process using cyclohexane. Wyczesany (2011) applied the NRTL equation for the simulations of ethanol dehydration process using hydrocarbons such as cyclohexane, *n*-hexane, *n*-heptane, and isooctane. The parameters of this equation were fitted to the experimental VLLE data but the minimized objective function calculated separately the VLE and the LLE for these data. NRTL-VLL parameters obtained in the presented papers were fitted to the experimental data when the minimized objective function described the full VLLE. Gomis et al. (2015) compared the results of the experimental work of a semi-pilot plant scale distillation column with the calculated results obtained from the simulations for the process of ethanol dehydration using: n-hexane, cyclohexane, isooctane and toluene.

The calculation results of simulation are strongly dependent on a properly chosen thermodynamic model, which in heterogeneous azeotropic distillation should describe both the VLE and the LLE as accurately as possible. Equations such as the NRTL and the Uniquac can correlate the VLE and separately LLE with high precision. Unfortunately, the correlated parameters describing exactly the VLE predict the LLE very inaccurately and vice versa. The ChemCad data bank contains the coefficients of the NRTL and the Uniquac equations for the water - n-propanol mixture fitted with the VLE data. Both equations describe the VLE of this mixture with high precision but predict also the miscibility gap. (In reality water and n-propanol are miscible completely). The same phenomenon can be observed for the majority of the coefficients of both equations presented in literature for the water - n-propanol mixture.

The problem of parameter correlation for the VLLE was described in a previous work by the author (Wyczesany 2014), using the NRTL equation. Its parameters were fitted simultaneously to the experimental VLLE and VLE data. For 27 ternary systems measured at atmospheric pressure calculation results showed that the NRTL equation can describe quite accurately the VLLE and the VLE of ternary mixtures and their binary subsystems if the parameters of this equation were fitted simultaneously to three-phase and two-phase equilibrium data. The NRTL-VLL model parameters calculated in this paper were used to simulate the n-propanol dehydration process using a ChemCAD simulator (ChemCAD, 2010). The following entrainers were used: cyclohexane, isooctane, DNPE and *n*-propyl acetate. Therefore, in this work the NRTL-VLL parameters were fitted for ternary mixtures containing water, n-propanol and entrainer. The DIPE was tested also as the entrainer but it turned out that this ether did not form a heteroazeotrope with water and n-propanol and it was not used in the simulations. The correlated model parameters were used to: the VLLE calculations of the considered ternary mixtures, the VLE calculations of their binary subsystems (water - n-propanol and n-propanol - entrainer) and prediction of the temperature and concentrations of ternary and binary azeotropes. Calculation results showed that the NRTL-VLL parameters describe all these various properties with a good (but not perfect) accuracy. Therefore, the NRTL-VLL parameters were additionally tested in the simulations of n-propanol dehydration. It is known from literature that models describing the VLLE have the greatest difficulty with a precise description of LLE. Therefore, particular emphasis was placed on checking whether the concentrations of the liquid phases leaving the decanter are close to the experimental LLE data. Simulations presented in the literature do not contain such comparisons.

The results of simulations show also which variant of the *n*-propanol dehydration process is the most preferred from the standpoint of energy requirements. For comparison, calculations were also carried out for one mixture using the NRTL equation coefficients taken from the ChemCAD database.

2. CALCULATION OF VLLE

The article uses the classical version of the NRTL equation (Eq. 1) which has three adjustable parameters (A_{ij} , A_{ji} and α_{ij}), fitted to experimental equilibrium data.

$$\ln\gamma_i = \frac{\sum\limits_j \tau_{ji}G_{ji}x_j}{\sum\limits_l G_{li}x_l} + \sum_j \frac{x_j G_{ij}}{\sum\limits_l G_{lj}x_l}\left(\tau_{ij} - \frac{\sum\limits_k \tau_{kj}G_{kj}x_k}{\sum\limits_l G_{lj}x_l}\right), \qquad \tau_{ji} = \frac{A_{ji}}{T}, \qquad G_{ji} = \exp\left(-\alpha_{ji}\tau_{ji}\right) \tag{1}$$

In my previous paper (Wyczesany, 2014) two approaches were used for the VLLE calculation depending on the availability of the experimental values of the total mixture mole fractions z_i. In the case of data containing T, P and the values z_i the classical method of the three-phase flash calculation was used. For systems considered in this paper the data contain the equilibrium compositions of all three phases in addition to T and P and do not present the mole fractions z_i. To be able to use this data at all, the last values must be assumed. We can assume that the mole fractions z_i refer to the total mixture or to the total liquid phase. In the first case the mole fractions z_i correspond to the arithmetic mean values of the experimental mole fractions of individual components in all three phases. In the second case these mean values refer to both liquid phases only. It is obvious that both assumptions cause some inaccuracies in the material balance of each component. The last assumption seems to be much more reliable and it was used in the second approach of the VLLE calculation. When z_i values are computed as in the first case the flash calculations often do not converge.

For isobaric data the known values are represented by the pressure and mole fractions z_i of the total liquid phase. The experimental temperature is treated in calculations as an initial value. For the known values z_i and T the algorithm calculates the LLE (aqueous phase fraction in the total liquid and the compositions of both liquid phases). In the next step the VLE is calculated for both liquid phases. For known values of P and the mole fractions of the liquid phase the algorithm computes the mole fractions y_i of the gas phase and the boiling temperature. The values of T obtained for both liquid phases are compared to each other. If they differ by more than the value of 0.001 K, the organic phase temperature is taken as a new one for further calculations. In the next step again the LLE and the VLE for both liquid phases are computed. Iterations are continued until the difference between the temperatures in both gas phases is lower than 0.001 K. Subsequently the algorithm computes for the same substances the differences between the mole fractions y_i calculated for both liquid phases. If they are greater than the value of 0.0001, the new temperature is assumed and the algorithm returns to the LLE and the VLE computations for both liquid phases. If not, the VLLE is calculated. A detailed description of the algorithm is given elsewhere (Wyczesany, 2014).

3. CALCULATION OF NRTL EQUATION PARAMETERS

NRTL equation parameters were calculated by the minimization of the objective function OF given by Eq. 2.

$$OF = \sum_{i=1}^{NLLE}\sum_{j=1}^{Nc}\sum_{k=1}^{2}\left(x_{\exp,k,j,i} - x_{\mathrm{cal},k,j,i}\right)^2 + W1\sum_{i=1}^{NVLE}\sum_{j=1}^{Nc}\left(y_{\exp,j,i} - y_{\mathrm{cal},j,i}\right)^2 + W2\sum_{i=1}^{NVLE}\left(T_{\exp,i} - T_{\mathrm{cal},i}\right)^2 \tag{2}$$

This function uses $NLLE$ experimental points for the LLE. The data may refer to the VLLE and the LLE of the given system or its subsystems. The first term of the function OF refers to Nc components and both liquid phases. The second term of the minimized function uses $NVLE$ experimental points of the VLE and also includes Nc components. The data may refer to the VLLE and the VLE for the given system or its subsystems. The last term of the function OF applies the differences between the experimental and calculated temperatures and is calculated for *NVLE* experimental points. The values *W*1 and *W*2 are the weight parameters, which enable better fitting of the calculated values to the experimental data. For ternary mixtures the minimized objective function contains 9 parameters (A_{12}, A_{21}, A_{13}, A_{31}, A_{23}, A_{32}, α_{12}, α_{13}, α_{23}).

4. RESULTS OF CALCULATION AND THEIR DISCUSSION

In a previous work by the author (Wyczesany, 2014) the coefficients of the NRTL equation were calculated for 27 mixtures determined at nearly atmospheric pressure. In this work these parameters were fitted for four new systems and calculated again for the mixture of water - *n*-propanol - DNPE putting emphasis on the better fitting of the concentration and temperature of the ternary heteroazeotrope. Table 1 lists the investigated mixtures and Table 2 presents the calculated values of the NRTL equation parameters.

The values representing the accuracy criteria of correlation and prediction of the VLLE and the VLE are the following: Δx_i and Δy_i - absolute mean deviations between experimental and calculated equilibrium compositions of species *i* in the liquid and vapour phases, respectively and ΔT – absolute mean difference between experimental and calculated equilibrium temperatures. Additionally, two mean deviations ΔX and ΔY were defined (Eq. 5). The first one refers to all the components (*Nc*) in a given liquid phase, the second one to all the components in the gas phase.

$$\Delta x_i = \frac{1}{NLLE}\sum_{i=1}^{NLLE}\left|x_{\exp,i} - x_{\mathrm{cal},i}\right|, \qquad \Delta y_i = \frac{1}{NVLE}\sum_{i=1}^{NVLE}\left|y_{\exp,i} - y_{\mathrm{cal},i}\right| \tag{3}$$

$$\Delta T = \frac{1}{NVLE}\sum_{i=1}^{NVLE}\left|T_{\exp,i} - T_{\mathrm{cal},i}\right| \tag{4}$$

$$\Delta X = \frac{1}{Nc}\sum_{i=1}^{Nc}\Delta x_i\,, \qquad \Delta Y = \frac{1}{Nc}\sum_{i=1}^{Nc}\Delta y_i \tag{5}$$

Table 1. Experimental ranges of temperatures and pressures, number of the experimental points and references for the VLLE data of the considered systems

No.	System	*T*, K	*P*, bar	*Np*	Ref.
1	water – *n*-propanol – cyclohexane	340-341	1.013	23	Lee and Shen (2003)
2	water – *n*-propanol – isooctane	348-352	1.013	17	Pienaar et al. (2013)
3	water – *n*-propanol – DNPE	347-352	1.0	11	Lladosa et al. (2008)
4	water – *n*-propanol – DIPE	335-346	1.013	18	Pienaar et al. (2013)
5	water– n-propanol – *n*-propyl acetate	355-357	1.013	11	Pla-Franco et al. (2014b)

Table 2. Coefficients of the NRTL equation for the systems (1) – (5)

No.	A_{12}	A_{21}	A_{13}	A_{31}	A_{23}	A_{32}	α_{12}	α_{13}	α_{23}
1	914.09	160.78	1771.1	1396.3	344.24	712.49	0.4589	0.3174	0.5661
2	903.93	333.92	2617.6	1354.9	460.63	759.68	0.5684	0.3196	0.5940
3	918.53	169.50	1598.3	901.75	159.43	254.75	0.4729	0.2904	0.2644
4	883.85	259.42	1921.0	893.44	159.47	152.23	0.5299	0.3209	0.5289
5	929.17	194.07	1500.8	537.60	-14.243	232.84	0.4971	0.3446	0.1200

Table 3 presents deviations obtained during the parameter correlation referring to the VLLE of the ternary systems. The mean deviations ΔX do not exceed 1 mol% and are generally significantly lower for the aqueous phase. The mean deviations ΔY are in the range of 1.07 - 1.54 mol%, and the mean deviations ΔT only in two cases exceed the value of 0.3 K. The maximum deviations ($\Delta x_{i,aq,max}$, $\Delta x_{i,org,max}$, $\Delta y_{i,max}$ and $\Delta T_{i,max}$) refer usually to one experimental point.

Table 3. Mean and maximum deviations obtained during the parameter correlation referring to the VLLE of the considered systems

	System				
	1	2	3	4	5
ΔXaq	0.0015	0.0061	0.0059	0.0049	0.0033
$\Delta Xorg$	0.0062	0.0089	0.0086	0.0057	0.0094
ΔY	0.0154	0.0153	0.0127	0.0107	0.0114
ΔT	0.10	0.12	0.33	0.31	0.15
$\Delta x_{i,aq,max}$	0.0068	0.0229	0.0144	0.0723	0.0057
$\Delta x_{i,org,max}$	0.0208	0.0443	0.0660	0.0300	0.0452
$\Delta y_{i,max}$	0.0351	0.0406	0.0380	0.0410	0.0183
$\Delta T_{i,max}$	0.38	0.36	0.87	0.86	0.25

Table 4 presents deviations obtained during the parameter correlation referring to the VLE of the binary subsystems: water – *n*-propanol and *n*-propanol – entrainer (hydrocarbon, ether or ester). The accuracy of the description is quite good in spite of the fact that VLE temperatures often significantly differ from VLLE temperatures.

Table 4. Mean and maximum deviations obtained during the parameter correlation referring to the VLE of binary subsystems (water – alcohol and alcohol – entrainer).

		1	2	3	4	5
water *n*-propanol	Δy	0.0069	0.0122	0.0066	0.0089	0.0074
	$\Delta T/ref$	0.25[a]	0.50[a]	0.29[a]	0.37[a]	0.34[a]
	$\Delta y_{i,max}$	0.0260	0.0343	0.0267	0.0255	0.0311
	$\Delta T_{i,max}$	1.52	1.85	1.56	1.53	1.75
n-propanol entrainer	Δy	0.0057	-	0.0025	-	0.0017
	$\Delta T/ref$	0.21[b]	-	0.31[c]	-	0.09[d]
	$\Delta y_{i,max}$	0.0232	-	0.0115	-	0.0050
	$\Delta T_{i,max}$	0.70	-	0.60	-	0.21

[a] – Mączyński and Mączyńska (1981); [b] – Mączyński et al. (1982); [c] – Lladosa et al. (2006);
[d] - Mączyński et al. (1984)

Since the NRTL-VLL parameters can be used in a simulator for modelling *n*-propanol dehydration processes via heterogeneous azeotropic distillation, the model should accurately predict the composition, temperature and the type (homogeneous or heterogeneous) of the azeotropes. Table 5 presents the experimental and calculated compositions (in mole fractions) and temperatures of the azeotropes for the considered ternary systems and their binary subsystems. The necessary calculations were performed with ChemCAD. In most cases, the accuracy of the prediction is satisfactory. The best precision can be observed for the water - *n*-propanol – cyclohexane mixture. The least accuracy occurs for the water – *n*-propanol – DNPE system. If the system does not form any ternary azeotrope (mixture 4), the NRTL-VLL parameters correctly predict this fact. Remaining ternary systems listed in Table 5 form heteroazeotropes. The NRTL-VLL parameters correctly predict this phenomenon also.

Table 5. Comparison of experimental and calculated compositions (in mole fractions) and temperatures of ternary and binary azeotropes of the considered systems

	system	exp.	calc.	exp.	calc.	exp.	calc.	exp.	calc.
1	water	0.256	0.261	0.568	0.577	0.300	0.301	-[a]	-
	n-propanol	0.132	0.132	0.432	0.423	-[b]	-	0.240	0.238
	cyclohexane	0.612[a]	0.607	-[c]	-	0.700	0.699	0.760	0.762
	T, K	339.98	340.15	360.90	360.95	342.65	342.63	347.91	347.92
2	water	0.352	0.356	0.568	0.547	0.471	0.450	-[c]	-
	n-propanol	0.208	0.204	0.432	0.453	-[c]	-	0.453	0.433
	isooctane	0.440[c]	0.440	-[c]	-	0.529	0.550	0.547	0.567
	T, K	347.04	347.38	360.90	360.62	352.28	352.21	357.93	357.93
3	water	0.383	0.367	0.568	0.578	0.396	0.386	-[d]	-
	n-propanol	0.103	0.117	0.432	0.422	-[d]	-	0.334	0.341
	DNPE	0.514[d]	0.516	-[c]	-	0.604	0.614	0.666	0.659
	T, K	346.85	347.44	360.90	360.70	348.20	348.24	358.04	358.50
4	water	-	-	0.568	0.559	0.220	0.216		
	n-propanol	-	-	0.432	0.441	-[c]	-	-	-
	DIPE	-	-	-[c]	-	0.780	0.784	-	-
	T, K	-	-	360.90	360.74	335.35	335.09	-	-
5	water	0.525	0.507	0.568	0.577	0.520	0.520	-[e]	-
	n-propanol	0.081	0.095	0.432	0.423	-[e]	-	0.613	0.593
	n-propyl acetate	0.394[e]	0.398	-[c]	-	0.480	0.480	0.387	0.407
	T, K	355.36	355.53	360.90	361.08	355.55	355.93	367.63	368.03

[a] – Lee and Shen (2003); [b] – Horsley (1962); [c] – Pienaar et al. (2013); [d] – Lladosa et al. (2008); [e] – Pla-Franco et al. (2014b)

5. SIMULATIONS OF N-PROPANOL DEHYDRATION VIA HETEROGENEOUS AZEOTROPIC DISTILLATION

The NRTL-VLL parameters obtained in the presented works have been used in the simulation of dehydration processes of the mixtures: water - *n*-propanol via the heterogeneous azeotropic distillation. The calculations were performed with a ChemCAD simulator which contains numerical values of the coefficients of the NRTL equation for many binary systems in its database. They would correspond to the VLE parameters if the components are miscible completely. If the mixture exhibits a relatively small miscibility gap (as the water - *n*-butanol system), ChemCAD has usually two sets of parameters: for the VLE and the LLE. However, if the miscibility gap is large (as in the water - hydrocarbons systems) the NRTL equation parameters describe the LLE only. These coefficients taken from the database have been replaced by the NRTL-VLL parameters for the considered ternary systems. For comparison, in the case of the mixture with *n*-propyl acetate the simulations were also performed using the NRTL binary parameters taken from the ChemCAD database.

In the simulations of n-propanol dehydration the following entrainers were used: cyclohexane, isooctane, DNPE and *n*-propyl acetate. All simulations were performed using in the thermodynamic settings the following global phase option: "Vapor / Liquid / Liquid / Solid".

Figure 1 shows the flowsheet of this process (the numbers of streams are placed in squares and the numbers of unit operations in circles). Stream 1 contains 100 kmol/h of a mixture having the mole fractions of water and n-propanol equal to 0.5 and the vapour fraction equal to 0.5. It is separated in the distillation column 1 into water having a concentration of 99.9 mol% and the gaseous distillate which is an azeotropic mixture of water and n-propanol. This mixture is directed into the distillation column 2 which has not any condenser and is fed also by the organic phase from the decanter 3. Pure *n*-propanol (99.9 mol%) is obtained at the bottom of the column 2 and the top product of this column with a composition and temperature close to the ternary azeotrope is totally condensed at heat exchanger 4 and separated into two liquid phases in the decanter 3. The last unit can calculate the three-phase VLLE. In all performed simulations the flow of the gaseous stream 12 was equal to zero and the decanter calculated only the LLE. (ChemCad has a flash unit which always treats the first output stream as vapour. Therefore, if we want to calculate the separation of two liquids only we must use the LLV flash.) The aqueous phase from the decanter is directed into the distillation column 1. The device 6 is a controller which counts the losses of the third component in the streams 3 and 7. These losses are supplemented by the stream 9.

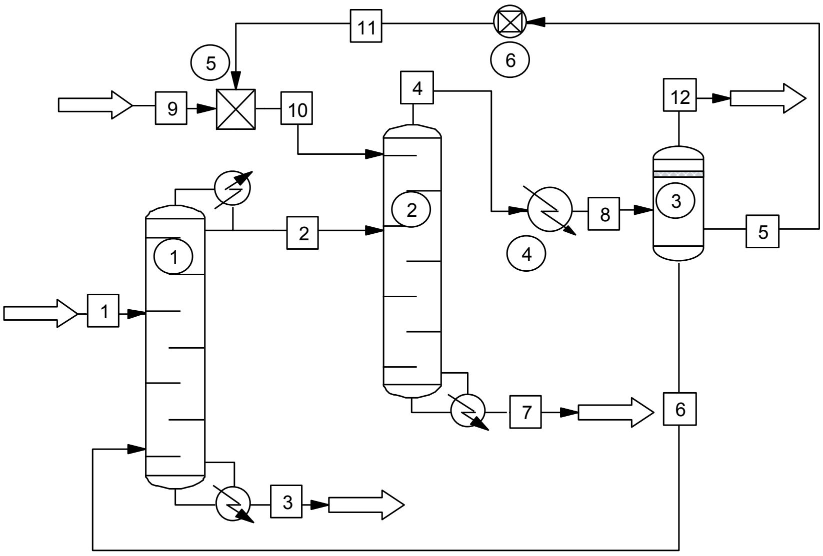

Fig. 1. Flowsheet of n-propanol dehydration

For all simulations carried out in the work the numbers of stages in columns have been established by trial method, so as the column was able to produce at the bottom water or alcohol of the assumed purity. The feed stage numbers of both columns were chosen also by trial method, based on conditions that the total heat delivered to the reboilers of both columns was the lowest. For the all performed simulation processes the reflux ratio at the top of the column 1 was fixed to 0.1.

Table 6 presents the total flow, composition and temperature of the streams 4, 5, 6 and 2 as well as the total number of stages and the feed stage numbers for both columns. For the mixtures with cyclohexane and DNPE Table 6 presents two solutions. For both mixtures in the first solution the top stream of the column 2 has the composition and the temperature close to the azeotrope. In the second solution these values are significantly different from those of the azeotrope. In the latter case, the streams 4 and 5 have significantly higher total flows, resulting in greater energy requirements for a given flowsheet.

Table 6. Total flow, composition and temperature of the streams 4, 5, 6 and 2. The total number of stages and the feed stage numbers for both columns. x_1, x_2 and x_3 – mole fractions of water, *n*-propanol and entrainer, respectively

		Stream					Column	
Entrainer		4	5	6	2		1	2
cyclohexane first solution	kmol/h	276.32	208.29	68.03	118.503	no of stages	10	13
	x_1	0.2598	0.0360	0.9449	0.5451	feed stg. str. 1	3	
	x_2	0.1324	0.1589	0.0513	0.4528	feed stg. str. 6	9	
	x_3	0.6078	0.8051	0.0037	0.0021	feed stg. str. 10		1
	T, K	339.82	339.69	339.69	360.67	feed stg. str. 2		3
cyclohexane second solution	kmol/h	330.99	262.14	68.84	118.84	no. of stages	10	13
	x_1	0.2637	0.0858	0.9409	0.5454	feed stg. str. 1	3	
	x_2	0.2283	0.2738	0.0552	0.4523	feed stg. str. 6	9	
	x_3	0.5080	0.6404	0.0039	0.0022	feed stg. str. 10		1
	T, K	345.38	339.72	339.72	360.67	feed stg. str. 2		3
isooctane	kmol/h	232.55	161.21	71.34	121.32	no. of stages	10	15
	x_1	0.3428	0.0976	0.8970	0.5277	feed stg. str. 1	3	
	x_2	0.2182	0.2700	0.1011	0.4712	feed stg. str. 6	9	
	x_3	0.4390	0.6324	0.0019	0.0011	feed stg. str. 10		1
	T, K	348.05	347.37	347.37	360.43	feed stg. str. 2		5
DNPE first solution	kmol/h	231.35	167.20	64.15	114.14	no. of stages	10	20
	x_1	0.3318	0.0885	0.9660	0.5433	feed stg. str. 1	2	
	x_2	0.1599	0.2101	0.0292	0.4540	feed stg. str. 6	9	
	x_3	0.5083	0.7014	0.0048	0.0027	feed stg. str. 10		1
	T, K	348.69	347.38	347.38	360.76	feed stg. str. 2		3
DNPE second solution	kmol/h	289.93	223.73	66.20	116.20	no of stages	10	20
	x_1	0.3403	0.1591	0.9526	0.5431	feed stg. str. 1	2	
	x_2	0.2533	0.3159	0.0418	0.4537	feed stg. str. 6	9	
	x_3	0.4064	0.5250	0.0056	0.0032	feed stg. str. 10		1
	T, K	351.01	347.65	347.65	360.75	feed stg. str. 2		3
n-propyl acetate	kmol/h	266.73	204.08	62.65	112.60	no of stages	10	28
	x_1	0.4908	0.3428	0.9730	0.5414	feed stg. str. 1	2	
	x_2	0.1527	0.1938	0.0189	0.4541	feed stg. str. 6	9	
	x_3	0.3565	0.4634	0.0081	0.0045	feed stg. str. 10		1
	T, K	355.66	354.27	354.27	360.80	feed stg. str. 2		12
n-propyl acetate NRTL coefficients ChemCAD	kmol/h	241.69	177.98	63.71	113.67	no of stages	10	25
	x_1	0.4918	0.3191	0.9741	0.5461	feed stg. str. 1	3	
	x_2	0.2248	0.2973	0.0225	0.4520	feed stg. str. 6	9	
	x_3	0.2834	0.3836	0.0034	0.0019	feed stg str 10		1
	T, K	356.13	354.61	354.61	360.27	feed stg. str .2		11

For a mixture with *n*-propyl acetate Table 6 shows also simulation results obtained for the NRTL equation coefficients taken from the ChemCAD database. The composition of the stream 4 differs here significantly from that of the azeotrope.

The vapour from the top of column 1 (stream 2) should have the composition and temperature close to the corresponding values for the binary azeotrope of water - *n*-propanol system. It can be seen that in all simulations this agreement is satisfactory.

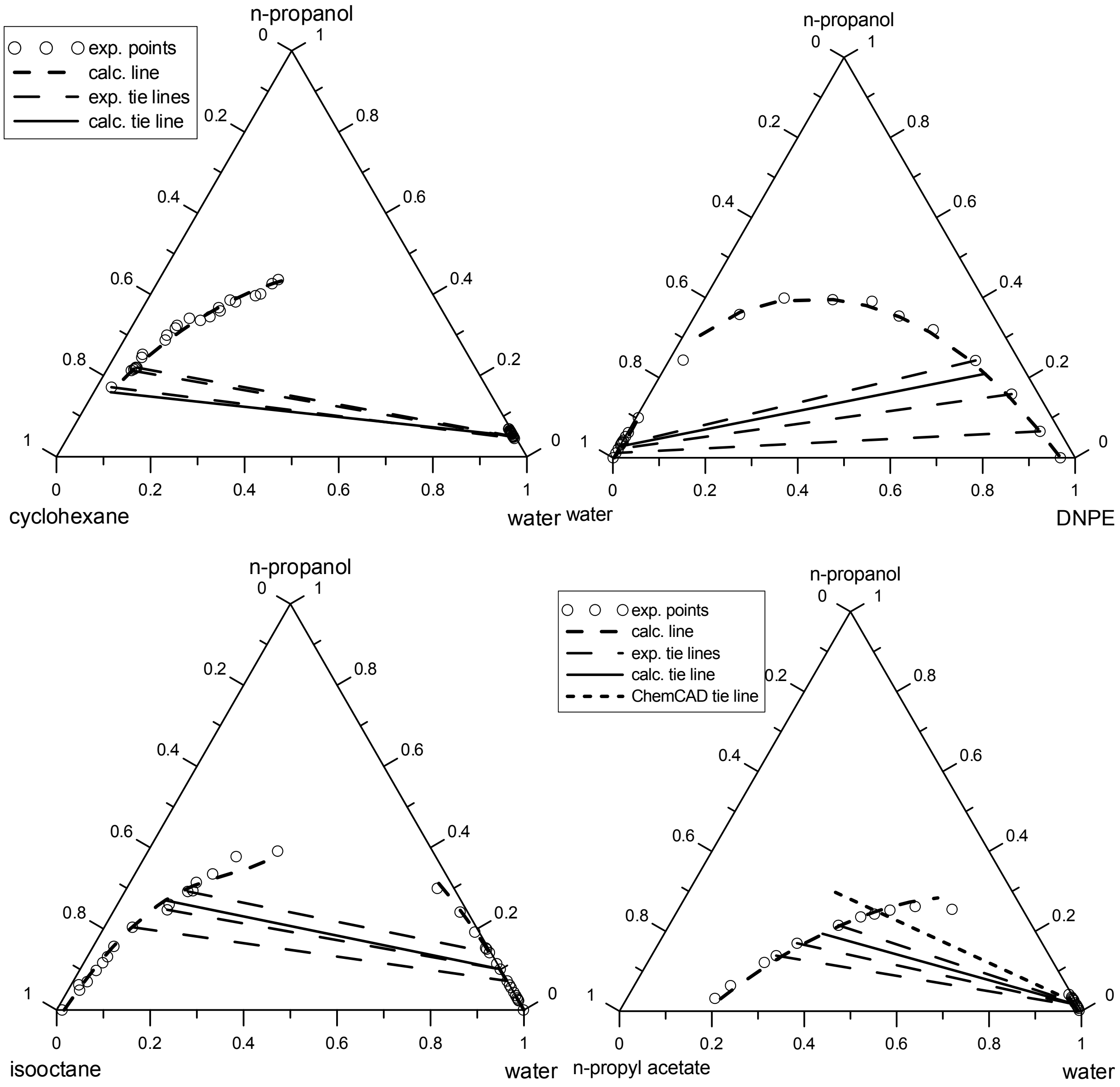

Fig. 2. The comparison of the concentrations of both liquid phases formed in the decanter with the experimental values of the LLE for the water – *n*-propanol – hydrocarbon (ether, ester) systems

The models describing the VLLE presented in the literature have the biggest problems with precise description of the LLE. Therefore, the agreement between the concentrations of both liquid phases formed in the decanter and the experimental LLE values is a very important factor that strongly affects the accuracy of the entire simulation. This agreement has been illustrated for the four considered systems in Fig. 2. It presents the experimental points of the LLE taken from the VLLE data, the lines describing these points by the NRTL-VLL parameters, tie lines drawn with a solid line on the base of the concentrations of the organic and the aqueous phases (respective streams 5 and 6) taken from the simulations and three experimental tie lines drawn with the dashed lines. In order to make the graphs clear, only three experimental tie lines closest to the tie line obtained from the simulation were placed on them. For the all four simulations, the line connecting the concentrations of the two phases obtained in the decanter fits very well into three experimental tie lines. In the case of mixtures with cyclohexane and DNPE the graphs were drawn for the first solution. For the system with *n*-propyl acetate the graph contains also the tie line plotted on the base of the simulation obtained using the NRTL equation coefficients taken from the ChemCAD database. This line differs significantly from the experimental LLE data. It has an impact on the results of the entire simulation through the values of the molar flow and concentrations of the streams 4 and 5, which are here significantly different from those obtained for the NRTL-VLL parameters. So, the original coefficients taken from the ChemCAD database are not suitable for simulation of heterogeneous azeotropic distillation.

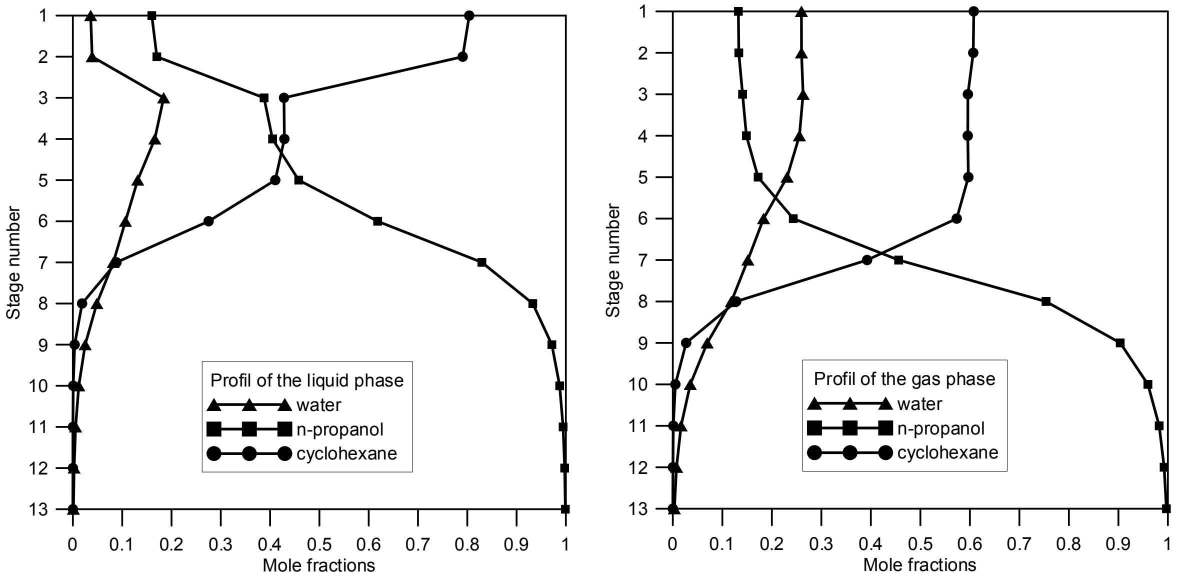

Fig. 3. Composition profiles of the liquid phase and the gas phase in the azeotropic column for the water - n-propanol - cyclohexane mixture.

Figure 3 presents the profile of the liquid phase and separately the profile of the gas phase in the azeotropic column for the water - n-propanol - cyclohexane mixture. For all simulations performed in the work only one liquid phase was present in the azeotropic column. No phase splitting was detected. The same phenomenon was observed for the simulation of ethanol dehydration with isooctane (Font et al., 2003) as well as in the experimental conditions of this process (Gomis et al., 2007b).

Table 7. Energy requirements for the investigated systems

Entrainer		col. 1	col. 2	ht. ex. 4	total
Cyclohexane first solution	Q-, MJ/h	-495.4	-	-9781.4	-10276.8
	Q+, MJ/h	3484.7	4840.2	-	8324.9
Cyclohexane second solution	Q-, MJ/h	-498.8	-	-12336.8	-12835.6
	Q+, MJ/h	3523.6	7360.5	-	10884.1
Isooctane	Q-, MJ/h	-509.0	-	-8853.4	-9362.4
	Q+, MJ/h	3606.7	3805.8	-	7412.5
DNPE first solution	Q-, MJ/h	-479.0	-	-8766.0	-9245.0
	Q+, MJ/h	3257.4	4034.7	-	7292.1
DNPE second solution	Q-, MJ/h	-487.7	-	-11344.7	-11832.4
	Q+, MJ/h	3353.6	6526.2	-	9879.8
n-propyl acetate	Q-, MJ/h	-472.4	-	-10602.6	-11075.0
	Q+, MJ/h	3149.5	5972.9	-	9122.4

Table 7 shows the energy requirements for each considered simulation. They take into account separately the heat duties in the column condensers and the coolers and the heat duties in the column reboilers. In the case of a mixture with cyclohexane and DNPE the first solutions have the lower total flows of the streams 4 and 5. These variants have also lower energy requirements. The simulations performed for the systems with isooctane and DNPE have lower energy requirements than the simulations with cyclohexane and n-propyl acetate.

6. CONCLUSIONS

For 5 ternary systems considered in this work calculation results showed that the NRTL equation can describe quite accurately the VLLE of ternary mixtures and the VLE of their binary subsystems if the binary parameters of this equation were fitted simultaneously to the three-phase and two-phase equilibrium data**.** The deviations ΔX do not exceed 1 mol % and they are usually lower for the aqueous phase. The deviations ΔY referring to the vapour phase are in the range of 1.07 - 1.54 mol%, and the differences ΔT only in two cases exceed the value of 0.3 K. The binary NRTL-VLL parameters describe the VLE of binary subsystems water – *n*-propanol and *n*-propanol – entrainer quite well despite the fact that VLE temperatures often significantly differ from VLLE temperatures. The NRTL-VLL parameters calculate the compositions and the temperatures of ternary azeotropes with good accuracy. The same conclusion refers to the binary subsystems of the considered ternary mixtures. The model also correctly predicts that the water – *n*-propanol – DIPE mixture does not form any azeotrope whereas the remaining ternary systems listed in Table 5 form heteroazeotropes. In the majority of simulations the top products from the azeotropic column have compositions and temperatures close to the corresponding experimental values of ternary azeotropes. The accuracy is very good for the mixtures: water - *n*-propanol – cyclohexane and water - *n*-propanol - isooctane. Examples referring to the water - *n*-propanol - cyclohexane and the water - *n*-propanol - DNPE mixtures indicate that if the top stream of the azeotropic column has the composition significantly different from that of azeotrope, then the recycle streams (especially organic phase) take higher values and the simulation results are energetically less favourable.

The top products from the first column are the mixtures having the compositions and temperatures close to the experimental values of the water - *n*-propanol azeotrope.

The accuracy of the entire simulation strongly depends on the correct prediction of the concentrations of both liquid phases formed in the decanter. Figure 2 shows that for all simulations (performed using the NRTL-VLL parameters) the lines connecting the concentrations of both liquid phases formed in the decanter fit very well to three closest experimental tie lines. For the simulation performed using the NRTL equation coefficients taken from the ChemCAD database the concentrations of the liquid organic phases obtained in the decanter differed very significantly from the experimental LLE data.

The energy requirements take into account for each simulation separately the heat duties in the column condensers, and coolers and separately the heat duties in the column reboilers. The simulations performed for the systems with isooctane and DNPE have the lowest energy requirements.

SYMBOLS

A_{ij}, A_{ji}	parameters of the NRTL equations, K
FC	objective function
$Q-$	heat duty in the column condenser or cooler, MJ/h
$Q+$	heat duty in the column reboiler or heater, MJ/h
T	temperature, K

ΔT	abs. mean deviation between experimental and calculated equilibrium temperature, K
$W1$, $W2$	weight factors
x, y	mole fractions in the liquid and the vapour phase, respectively
ΔX, ΔY	mean deviation defined in Eq. (5)
Δx, Δy	absolute mean deviation between experimental and calculated equilibrium composition in the liquid and the vapour phase, respectively
z	assumed mole fraction of component i in the entire mixture or in the entire liquid phase

Greek symbols

α_{ij}	parameter of the NRTL equation
γ_i	activity coefficient of species i

Subscripts

exp	experimental
cal	calculated
aq	aqueous phase
org	organic phase
max	maximum

REFERENCES

Arifin S., Chien I.L., 2007. Combined preconcentrator/recovery column design for isopropyl alcohol dehydration process. *Ind. Eng. Chem. Res.,* 46, 2535-2543. DOI: 10.1021/ie061446c.

Cairns B.P., Furzer I., 1990. A multicomponent three-phase azeotropic distillation. 3. Modern thermodynamic models and multiple solutions. *Ind. Eng. Chem. Res.*, 29, 1383-1395. DOI: 10.1021/ie00103a042.

Chang W.T., Huang C.T., Cheng S.H., 2012. Design and control of a complete azeotropic distillation system incorporating stripping columns for isopropyl alcohol dehydration. *Ind. Eng.Chem. Res.*, 51, 2997-3006. DOI: 10.1021/ie202021g.

Chemcad VI. Process Flowsheet Simulator, 6.4.0.5052 version, Chemctations Inc., Huston 2010.

Font A., Asensi J.C., Ruiz F., Gomis V., 2003. Application of isooctane to the dehydration of ethanol. Design of a column sequence to obtain absolute ethanol by heterogeneous azeotropic distillation. *Ind. Eng. Chem. Res.*, 42, 140-144. DOI: 10.1021/ie0204078.

Gomis V., Font A., Pedraza R., Saquete M.D., 2005. Isobaric vapor – liquid and vapor – liquid – liquid equilibrium data for the water + ethanol + cyclohexane system. *Fluid Phase Equil.*, 235, 7-10. DOI: 10.1016/j.fluid.2005.07.015.

Gomis V., Font A., Saquete M.D., 2006. Vapour – liquid – liquid and vapour – liquid equilibrium of the system water + ethanol + heptane at 101.3 kPa. *Fluid Phase Equil.*, 248, 206 – 210. DOI: 10.1016/j.fluid.2006.08.012.

Gomis V., Font A., Pedraza R., Saquete M.D., 2007a. Isobaric vapor – liquid and vapor – liquid – liquid equilibrium data for the water – ethanol – hexane system. *Fluid Phase Equil.*, 259, 66-70. DOI: 10.1016/j.fluid.2007.04.011.

Gomis V., Pedraza R., Frances O., Font A., Asensi J.C. 2007b. Dehydration of Ethanol Using Azeotropic Distillation with Isooctane. *Ind. Eng. Chem. Res.*, 46, 4572 - 4576. DOI: 10.1021/ie0616343.

Gomis V., Pedraza R., Saquete, M. D., Font A., García-Cano J., 2015. Ethanol dehydration via azeotropic distillation with gasoline fractions as entrainers: A pilot-scale study of the manufacture of an ethanol–hydrocarbon fuel blend. *Fuel*, 139, 568-574. DOI: 10.1016/j.fuel.2014.09.041.

Horsley L.H., 1962. Azotropic Data; *Advances in Chemistry Series Number 35*; American Chemical Society: Washington, DC.

Lee L.S., Shen H.C., 2003. Azeotropic behavior of a water + *n*-propanol + cyclohexane mixture using cyclohexane as an entrainer for separating the water + *n*-proponal mixture at 760 mmHg. *Ind. Eng. Chem. Res.*, 42, 5905 - 5914. DOI: 10.1021/ie0208220.

Lladosa E., Monton J. B., Burguet M.C., Munoz R., 2006. Isobaric vapor–liquid equilibria for the binary systems 1-propyl alcohol + dipropyl ether and 1-butyl alcohol + dibutyl ether at 20 and 101.3 kPa. *Fluid Phase Equil.*, 247, 47 - 53. DOI: 10.1016/j.fluid.2006.06.017.

Lladosa E., Monton J.B., Burguet M.C., de la Torre J., 2008. Isobaric (vapour+liquid+liquid) equilibrium data for (di-n-propyl ether+n-propyl alcohol+water) and (diisopropyl ether+isopropyl alcohol+water) systems at 100kPa. *J. Chem. Therm*., 40, 867-873. DOI: 10.1016/j.jct.2008.01.002.

Mączyński A., Mączyńska Z.,1981. *Verified vapour-liquid equilibrium data. Binary one-liquid systems of water and organic compounds*. PWN, Warszawa, Vol. 5, p. 102, data 8.

Mączyński A., Biliński A., Oracz P., Treszczanowicz T., 1982. *Verified vapour-liquid equilibrium data. Binary systems of C_{4+} hydrocarbons and alcohols*. PWN, Warszawa, Vol. 6, p. 106, data 9.

Mączyński A., Biliński A., Mączyńska Z., 1984. *Verified vapour-liquid equilibrium data. Binary systems of alcohols and oxygen compounds*. PWN, Warszawa, Vol. 8, p. 237, data 1.

Pienaar C., Schwarz C.E., Knoetze J.H., Burger, A.J., 2013. Vapour−liquid−liquid equilibria measurements for the dehydration of ethanol, isopropanol, and n-propanol via azeotropic distillation using DIPE and isooctane as entrainers. *J. Chem. Eng. Data*, 58, 537-550. DOI: 10.1021/je300847v.

Pla-Franco J., Lladosa E., Loras S., Monton J.B., 2014a. Thermodynamic analysis and process simulation of ethanol dehydration via heterogeneous azeotropic distillation. *Ind. Eng. Chem. Res.*, 53, 6084-6093. DOI: 10.1021/ie403988c.

Pla-Franco J., Lladosa E., Loras S., Monton J.B., 2014b. Isobaric vapour−liquid−liquid equilibria for the ternary systems ethanol + water + propyl acetate and 1-propanol + water + propyl acetate. *J. Chem. Eng. Data*, 59, 2054-2064. DOI: 10.1021/je500191j.

Wu Y.C., Chien I.L., 2009. Design and control of heterogeneous azeotropic column system for the separation of pyridine and water. *Ind. Eng. Chem. Res.*, 48, 10564-10576. DOI: 10.1021/ie901231s.

Wyczesany A., 2011. Wykorzystanie symulatora Chemcad do modelowania destylacji heteroazeotropowej mieszanin zawierających wodę i etanol. *Przem. Chem.*, 90, 1419-1424.

Wyczesany A., 2014. Calculation of vapour−liquid−liquid equilibria at atmospheric and high pressures. *Ind. Eng. Chem. Res*., 53, 2509-2519. DOI: 10.1021/ie403418p.

Young S., 1902. The preparation of absolute alcohol from strong spirit. *J. Chem. Soc., Trans.,* 81, 707-717. DOI: 10.1039/CT9028100707.

Received 28 July 2016
Received in revised form 16 February 2017
Accepted 22 February 2017

DE GRUYTER OPEN

Chemical and Process Engineering 2017, 38 (1), 177-191

DOI: 10.1515/cpe-2017-0014

INFLUENCE OF OXIDIZING REACTOR ON FLUE GAS DENITRIFICATION BY OZONATION AND POSSIBILITY OF BY-PRODUCT SEPARATION

Włodzimierz Kordylewski*[1], Adam Hałat[2], Dariusz Łuszkiewicz[1]

[1]Wroclaw University of Science and Technology, Faculty of Mechanical and Power Engineering, Wybrzeże Wyspiańskiego 27, 50-370 Wrocław, Poland

[2]Wrocław University of Science and Technology, Faculty of Chemistry, Wybrzeże Wyspiańskiego 27, 50-370 Wrocław, Poland

Results of laboratory scale research have been presented on the effects of an oxidizing reactor on ozone consumption and by-producs composition and separation of simultaneous NO_x and SO_2 removal from a carrier gas by ozonation method and absorption in an alkaline solution. The additional Dreschel washer added before two washers containing 100 ml of 0.1 molar NaOH solution played the role of an oxidation reactor. Its effect was investigated using an empty (dry or wetted) or filled with packing elements washer. The measured by-products in a scrubber and in the oxidizing reactor were SO_3^{2-}, SO_4^{2-}, NO_2^- and NO_3^- ions, respectively. It has been shown that use of oxidizing reactor improves NO_x removal efficiency reducing ozone consumption. Wetting of the oxidation reactor with water enables a preliminary separation of sulphur and nitrogen species between the oxidizing reactor and an alkaline absorber. Application of packing elements in the oxidizing reactor allows to retain 90% of nitrogen compounds in it. Some results were confirmed by tests in pilot scale.

Keywords: ozone, simulated flue gas, denitrification, desulphuration, by-products

1. INTRODUCTION

Oxidative methods for removing nitrogen oxides from flue gas, which consist of pre-oxidation of NO_x and absorption of oxidized components in alkaline solutions, are a promising alternative to the method of NO_x reduction, like SCR. Much research work has been carried out in many countries, such as U.S.A. (Carpenter, 2013), in Asia (Japan (Yamamoto et al., 2001), China (Zhang et al., 2014) and Korea (Mok, 2006)) and also in Europe (Poland (Krzyżyńska and Hutson, 2012) and Denmark (Stamate et al., 2006)). Much effort was devoted to the selection of an appropriate oxidant (Nelo et al., 1997), of which the most effective proved to be ozone (Jaroszyńska-Wolińska, 2009; Nelo et al., 1997).

In the U.S.A., LoTOx (Low Temperature Oxidation for NO_x Control) a method for cleaning exhaust gases from nitrogen oxides has been developed, which went through a commercial implementation. It involves the addition of ozone into exhaust gas duct, and then absorbing NO_x oxidation products in an alkaline absorber (Carpenter, 2013). In Denmark research on ozonation of the exhaust gas from a boiler powered by biomass and oil was conducted, oxidation products being captured in the water scrubber (Stamate et al., 2006). In Japan successful tests were conducted on exhaust gas from a Diesel engine. Moreover, ozone has proven to be helpful in regeneration of the ceramic particulate filter (Okubo et al.,

---

*Corresponding author, e-mail: wlodzimierz.kordylewski@pwr.edu.pl

2006). Fujishima et al. (2008) used the ozonation method to clean exhaust gas from oil combustion. Thanks to special design of an ozone probe they were able to inject ozone to the exhaust gas at the temperature of about 250 °C. Actually, there are about 30 industrial installations using the ozonation method for exhaust gas treatment in the world (Modern Power Systems, 2015).

The main object of further research is optimization of the ozonation method in order to improve its efficiency and reduce ozone consumption (Głomba and Kordylewski, 2014; Jędrusik et al., 2015). It was established that increasing the contact time between ozone and exhaust gas, improves efficiency of NO_x and Hg^0 removal (Dora et al., 2009). Interesting studies were performed by combining ozonation with addition of ethanol (Jie et al., 2016) and pyrolusite (Sun et al., 2011), and applying catalysts (cerium-titanium) (Jie et al., 2014). Results are promising, but the methods are still at the stage of laboratory tests. Different types of gas reactors were used to improve the effects. In case of experimental research of the $LoTO_x$ method an additional reactor to increase the residence time from 0.5 to 6 s was used (Omar, 2008). Zhang at al. (2014) used a stainless steel reactor to provide sufficient reaction time in gas phase and maintain constant temperature of the process.

Important elements of any emission control are its by-products (Carpenter, 2013). As a result of exhaust gas ozonation nitrates and nitrites and sulphites and sulphates are retained in the alkaline absorbent (Kuropka, 2012). Lower oxidized forms, i.e. nitrites and sulphites, are more dangerous for the environment, therefore more attention has to be paid to improve the organization of ozonation for obtaining more friendly by-products (Regulation of the Minister of Environment, 2009).

The aim of this study was to find the best solution for the oxidation reactor by improving its efficiency of the exhaust gas ozonation and subsequent by-product composition optimization. There was also another noteworthy effect of the oxidation reactor relies on the separation of nitrogen and sulfur species. This effect was significant only when the oxidation reactor was wetted. The possibility of separation of sulfur and nitrogen compounds is important from the point of view of their utilization. An attempt to explain the mechanisms of chemical reactions associated with the use of an oxidizing reactor was made. Tests were performed in a lab-scale, but some solutions developed in the lab were tested in a pilot plant.

2. THE MECHANISMS OF CHEMICAL REACTIONS OF NO_X AND SO_2 WITH OZONE

Because the main topic are by-products of nitrogen oxide removal from flue gas by ozonation and absorption in alkaline solutions, a discussion about mechanisms of chemical reactions will be helpful. The basic reaction scheme of NO_x oxidation by ozone in gaseous phase is as follows (Skalska et al., 2011):

$$NO+O_3 \rightarrow NO_2+O_2 \tag{1}$$

$$NO+NO_2=N_2O_3 \tag{2}$$

$$NO_2+O_3 \rightarrow NO_3+O_2 \tag{3}$$

$$NO+NO_3=2NO_2 \tag{4}$$

$$NO_2+NO_3=N_2O_5 \tag{5}$$

$$N_2O_5+H_2O \rightarrow 2HNO_3 \tag{6}$$

$$2O_3+M \rightarrow 3O_2 \tag{7}$$

The products of NO_x oxidation in gaseous phase are determined by the molar ratio O_3/NO in the temperature range of 20−100 °C. For $O_3/NO \approx 1$ the main nitrogenous component of flue gas after ozonation remains NO_2, because the reaction (1) is fast (Skalska et al., 2011) and the product of reaction (2) N_2O_3 is unstable. However, the role of N_2O_3 in the absorber cannot be overestimated, because N_2O_3 is well-soluble, while NO and NO_2 are only weakly-soluble (Sander, 1999). Dissolved N_2O_3 and NO_2 react with water to form nitrous and nitric acid according to:

$$N_2O_{3,aq}+H_2O_{,aq}=2HNO_{2,aq} \tag{8}$$

$$2NO_{2,aq}+H_2O_{,aq}=HNO_{2,aq}+HNO_{3,aq} \tag{9}$$

However, the efficiency NO_x capture in this way (8, 9) from flue gas is limited to about 60% due to the reactions of disproportionation of nitrous acid with release of NO (Joshi et al., 1985):

$$3HNO_{2,aq}=HNO_{3,aq} + 2NO_{aq}+H_2O_{aq} \tag{10}$$

$$2HNO_{2,aq}=NO_{aq}+NO_{2,aq}+H_2O_{aq} \tag{11}$$

Further increasing the molar ratio $O_3/NO > 1$ results in oxidation of NO_2 to NO_3 in reaction (3), which combined with NO_2 gives a very well-soluble dinitrogen pentoxide (N_2O_5) (Wang et al., 2015). In a solution N_2O_5 is converted into stable nitrate ions NO_3^-. In the exhaust gas N_2O_5 reacts with steam and gaseous HNO_3 is formed whose solubility is fivefold higher than that of NO_2 (Sander, 1999). In order to obtain more complete oxidation of NO_x to N_2O_5 longer residence time before the absorber is necessary, therefore an oxidizing reactor was applied in the experiment. The presence of SO_2 in flue gas has no visible impact on the mechanism of NO ozonation, since ozone practically reacts with SO_2 at temperature above 100 °C (Sun et al., 2014):

$$SO_2+O_3\rightarrow SO_3+O_2 \tag{12}$$

Moreover, at temperature > 100 °C thermal decomposition of ozone (7) begins to be of significance (Fridman, 2008). Theoretically, SO_2 could react with nitrogen dioxide:

$$SO_2+NO_2\rightarrow NO+SO_3 \tag{13}$$

However, due to high energy of activation (113 kJ/mol) this reaction could also be neglected (Zhang et al., 2014).

Chemistry of interaction between dissolved nitrogen oxides and sulphur dioxide is much more complicated and important for the by-products of ozonation. There is an old idea, that interaction between nitrogen dioxide and sulphur ions enhances simultaneous capture of these pollutants (Chen et al., 2002). The summary reactions in an alkaline solution are well known, for example for sodium hydroxide solution:

$$HNO_2+NaOH\rightarrow NaNO_2+H_2O \tag{14}$$

$$HNO_3+NaOH\rightarrow NaNO_3+H_2O \tag{15}$$

$$SO_2+2NaOH\rightarrow Na_2SO_3+H_2O \tag{16}$$

In an alkaline solution the absorption of NO_2 is similar to that of water (9), except that decomposition is prevented according to the reaction (14) (Thomas and Vanderschuren, 2000). Nitric acid instantaneously dissociates and leads to the formation of stable nitrate (15). The mechanism of SO_2 absorption in aqueous alkaline solutions could be represented by the following two equations (17, 18) (Hikita H. et al., 1977)

$$SO_2+OH^-=HSO_3^- \tag{17}$$

$$HSO_3^-+OH^-=SO_3^{2-}+H_2O \tag{18}$$

The rate and stoichiometry of SO_3^{2-} and NO_2 reaction have been studied by a number of researchers. Littlejohn et al., (1993) believe that nitrogen dioxide accelerates the catalytic conversion of sulphite ions to sulphate. Chen et al., (2002) suggested that the effectiveness of sodium sulphite (Na_2SO_3) aqueous solution for NO_2 absorption can be explained by the interactions between $NO_{2,aq}$ and SO_3^{2-} expressed by the overall reaction:

$$2NO_2 + SO_3^{2-} + H_2O = 2NO_2^- + 2H^+ + SO_4^{2-} \tag{19}$$

The presence of ozone in solution is an additional factor supporting the oxidation of sulphite ions according to the reaction:

$$SO_3^{2-} + O_{3,aq} \rightarrow SO_4^{2-} + O_{2,aq} \tag{20}$$

3. EXPERIMENTAL

3.1. Lab-scale investigations

Studies on a laboratory scale involved examining the impact of the use of an oxidation reactor on the efficiency of removing pollutants from a carrier gas by the method of ozonation and reaction products obtained in the absorber. A general scheme of the bench scale laboratory is demonstrated in Fig. 1.

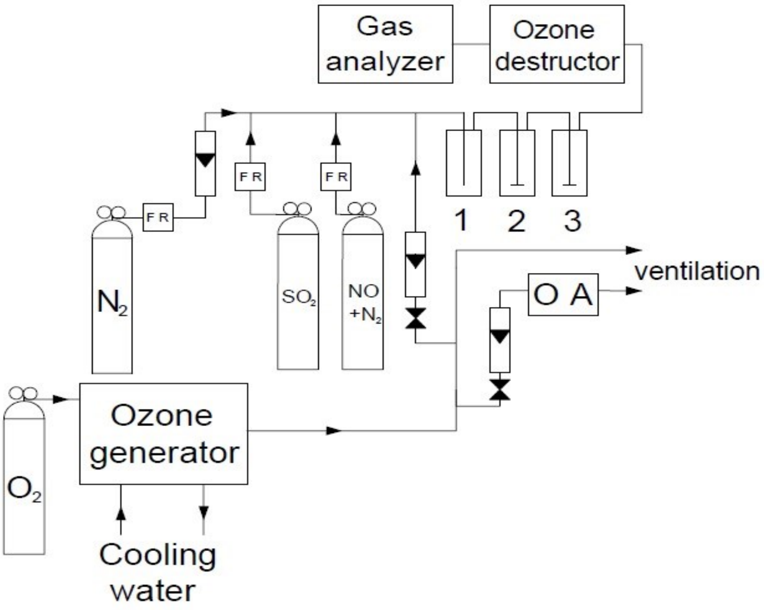

Fig. 1. Scheme of test stand, FR– flow controller, OA – ozone analyser,
1– oxidizing reactor (*OR*), 2, 3 – washers with 0.1 M NaOH solution

The carrier gas was technical nitrogen discharged from a steel cylinder (PN-EN ISO 14175 – N1, 99.5N_2, Air Products), whose flow rate was controlled by a flow controller ALBORG GFC 17. To the carrier gas sulphur dioxide (99.98% SO_2, Linde) and nitrogen oxide (10% NO in N_2, Linde) from a steel cylinder were added and controlled by flow regulators (NO - ERG 1000N_2; SO_2- ERG 100N_2). Ozone was generated in an ozone generator (OZAT CFS-2G) of DEGREMONT TECHNOLOGIES, which was fed by technical oxygen from a steel cylinder (PN-EN ISO 14175 - O1, 99.5% O_2, Air Products). The concentration of ozone was measured by an ozone meter BMT 964 of BMT Messtechnik GmbH.

The carrier gas was flowing through two Dreschel's washers 2, 3, each containing 100 ml of 0.1 M sodium hydroxide solution (POCH S.A.). Before the washers 2, 3 an additional washer 1 served as an oxidizing reactor (*OR*). The effect of oxidizing reactor was tested by the use of: “dry” (empty) and “wet” washer 1 (whose walls were wetted with about 30 ml of distilled water or filled with wet packing elements). Concentrations of contaminations in the carrier gas were measured by exhaust gas analysers (TESTO 350XL, TESTO 350S or Gasmet DX-4000). Due to sensitivity of the electrochemical sensors to ozone, prior to the gas analyser an ozone destructor was placed (Fig. 1). Basic installation test parameters were shown in Table 1. The governing parameter in these studies was the intensity of ozonation defined as the molar ratio X_{NO}:

$$X_{NO}=\frac{\mathrm{O_3}}{\mathrm{NO}},\quad \frac{\mathrm{mol\ O_3}}{\mathrm{mol\ NO}} \tag{21}$$

Table 1. Basic parameters

Parameter	Unit	Amount
Carrier gas volume flow rate	$\mathrm{dm^3/h}$	130
Ozone concentration	$\mathrm{g/Nm^3}$	7 - 50
$\mathrm{NO_x}$ concentration	ppm	400 - 500
$\mathrm{SO_2}$ concentration	ppm	700 - 800
Measurement time	h	0.5
Residence time of the oxidizing reactor	s	6

3.2. Pilot-scale investigations

The stand for pilot research for $\mathrm{NO_x}$ removal by ozonation method was shown in our earlier works (Głomba et al., 2016; Głomba and Kordylewski, 2014). The pilot plant was located in the Wrocław CHP (Combined Heat and Power), which provided the exhaust gas with volumetric flow rate of 200 $\mathrm{m^3/h}$ from OP 430 boiler. The same methods and equipment were used for measuring the concentration of contaminants. Before the absorber a “wet” oxidizing reactor (*OR*) was added, 200 $\mathrm{dm^3}$ in volume, which provided a residence time of about 6 s (Fig. 2). The exhaust gas temperature at the installation inlet was controlled by the cooler and it was in the range from 60 to 80 °C.

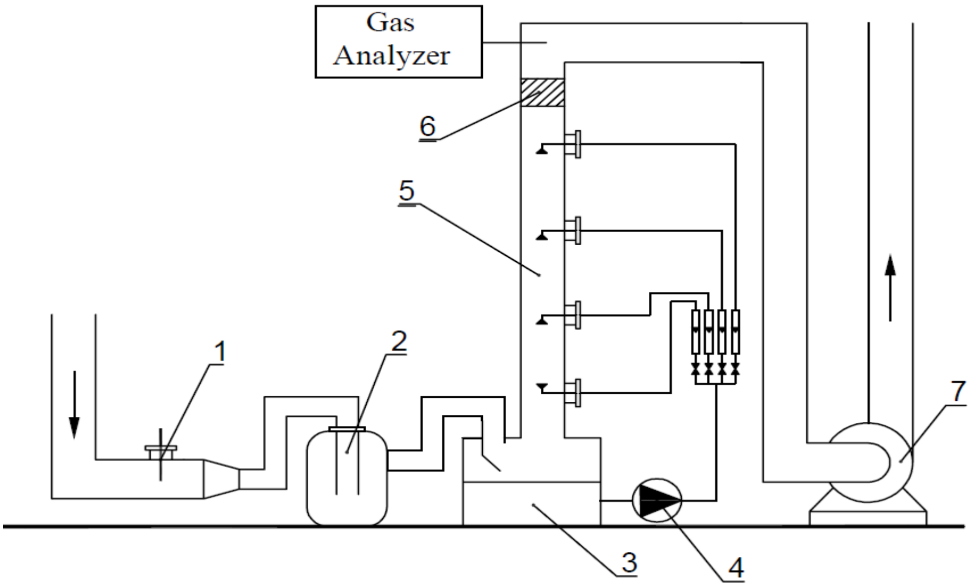

Fig. 2. Fragment of pilot installation for simultaneous $\mathrm{NO_x}$ and $\mathrm{SO_2}$ removal from flue gas, 1 – ozone injector, 2 – oxidizing reactor (*OR*), 3 – absorbent tank, 4 – absorbent pump, 5 – spray tower, 6 – demister, 7 – fan

3.3. Research methodology

Efficiency of nitrogen oxides removal from flue gas η_{NOx} was determined by measuring $\mathrm{NO_x}$ concentration after ozone destructor C^{out}_{NOx} referring these values to $\mathrm{NO_x}$ concentration on installation inlet $C^{\mathrm{int}}_{\mathrm{NOx}}$.

$$\eta_{NOx} = \left(1 - \frac{C^{out}_{\mathrm{NOx}}}{C^{\mathrm{int}}_{\mathrm{NOx}}}\right) 100\% \tag{22}$$

Samples of the sorption liquid collected from the absorber tank were analysed for the presence of nitrite, nitrate, sulphite and sulphate ions. Concentrations of nitrite and nitrate ions in NaOH solution were determined by adsorption spectrophotometry in UV range using spectrophotometer UV/Vis Cary 50 from Varian. Concentrations of sulphite ions were measured by iodometric method, while sulphate ions were measured by ion chromatography or plasma spectroscopy (ICP).

Based on the obtained results of concentration measurements of nitrate and nitrite ions the number of moles of nitrogen compounds in absorption liquid in the washers 2 and 3 $\left(n^{A}_{\mathrm{NO}_{(2,3)}}\right)$ and those collected from the oxidizing reactor $\left(n^{R}_{\mathrm{NO}_{(2,3)}}\right)$ were calculated. The fraction of nitrogen compounds captured in the oxidizing reactor δ was determined from the following relationship:

$$\delta = \frac{n^{R}_{\mathrm{NO}_{(2,3)}}}{n^{R}_{\mathrm{NO}_{(2,3)}} + n^{A}_{\mathrm{NO}_{(2,3)}}} \tag{23}$$

The degree of conversion of sulphite to sulphate ions (η_{SO4}) was determined by referring the number of $\mathrm{Na_2SO_4}$ moles (n_{SO4}) to the sum of sulphite (n_{SO3}) and sulphate moles in the absorption liquid:

$$\eta_{SO4} = \frac{n_{\mathrm{SO4}}}{n_{\mathrm{SO3}} + n_{\mathrm{SO4}}} \cdot 100\% \tag{24}$$

4. INFLUENCE OF OXIDIZING REACTOR ON EFFECTIVENESS OF NO REMOVAL AND BY-PRODUCT COMPOSITION

4.1. Oxidation reactor without filling

The investigations were conducted in the lab-scale setup (Fig. 1), wherein the carrier gas ($\mathrm{N_2}$) was doped only with NO, so that its concentration was about $C^{\mathrm{int}}_{\mathrm{NOx}} = 500$ ppm. The duration of a single measurement was 30 minutes. The molar ratio X_{NO} was varied from 0 to 2.0.

Dynamics of the process of NO ozonation was illustrated by measuring changes of NO, $\mathrm{NO_2}$ and $\mathrm{NO_x}$ concentrations with time for $X_{\mathrm{NO}} = 1.0$ after the ozone destructor (Fig. 3). The values of nitrogen oxide concentration were stabilized within approx. 10 minutes after the injection of ozone to the carrier gas. The use of the oxidizing reactor did not change the character of $\mathrm{NO_x}$ response to ozonation compared to the situation without oxidizing reactor (Kordylewski et al., 2013).

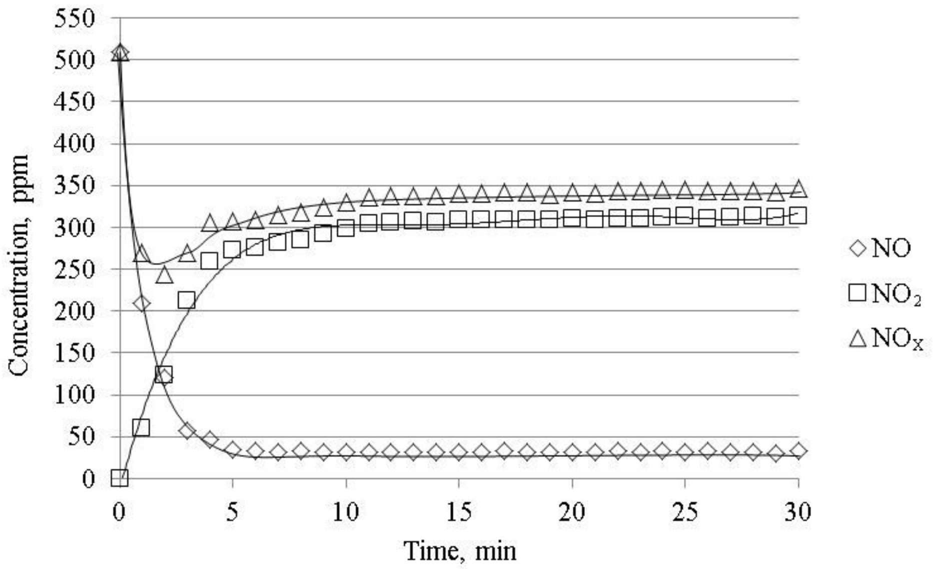

Fig. 3. Changes in NO, NO_2 and NO_x concentrations with time in the carrier gas after start of the ozone feed for $X_{NO} = 1.0$ ("dry" *OR*)

The impact of the oxidizing reactor (*OR*) on the efficiency of NO removal from the carrier gas for the molar ratio X_{NO} in the range of 1.0–2.1 is shown in Fig. 4. The oxidizing reactor improves the efficiency of NO_x removal. The best results were achieved for the "wet" oxidizing reactor, e.g. for $X_{NO} = 1.4$, NO removal efficiency was about 93%.

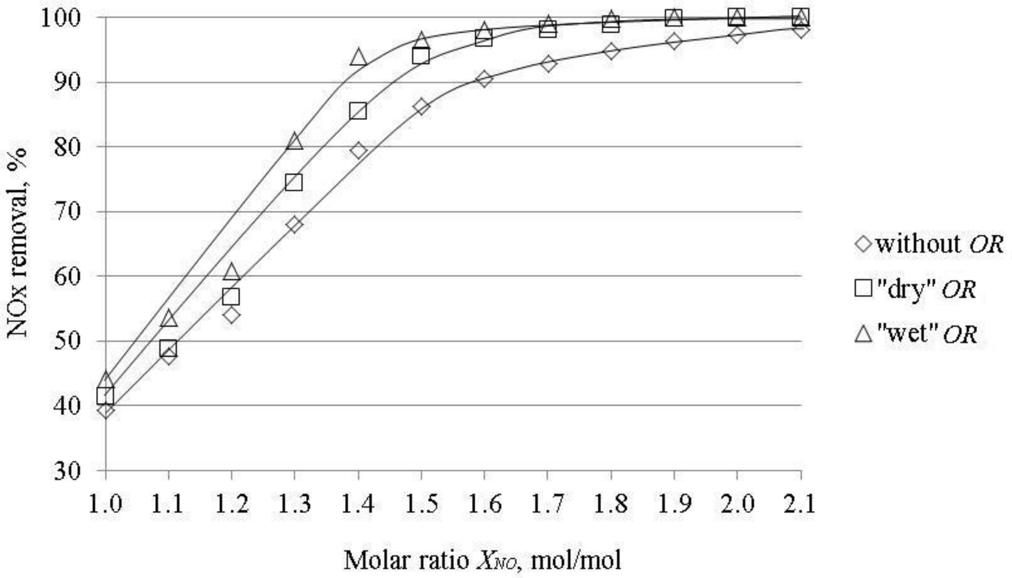

Fig. 4. The influence of the oxidizing reactor (*OR*) on the efficiency of NO_x removal from the carrier gas, ($C^{int}_{NOx} = 500$ ppm)

Solutions from the washers 2 and 3 and washings from the "wet" oxidizing reactor (*OR*) were analysed for the presence of nitrite and nitrate ions. Figure 5 shows how the number of moles of nitrate and nitrites ions varied vs. the molar ratio X_{NO}.

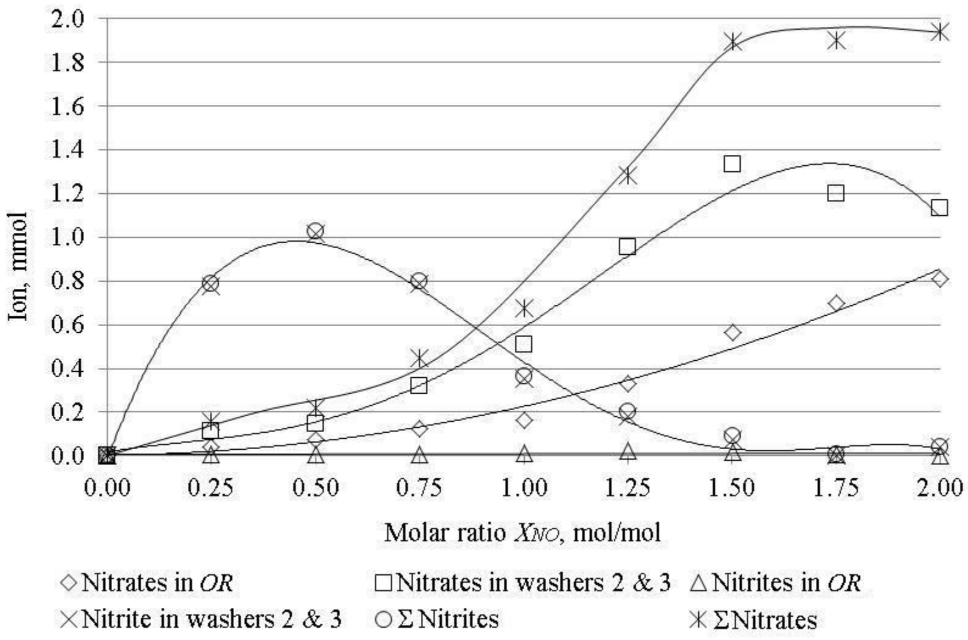

Fig. 5. The influence of intensity of ozonation (X_{NO}) on the composition of by-products in the liquids collected from washers 2&3 and "wet" *OR*

With increasing intensity of ozonation X_{NO}, the number of nitrate ions was increasing and the number of nitrite ions was decreasing in absorbent from the oxidizing reactor and the washers 2 and 3, respectively. Nitrogen in the inlet carrier gas and in the products (NO_x in the outlet carrier gas, nitrates and nitrites in the solutions) was balanced with error not exceeding 10%. The fractions of nitrogen compounds captured in the washers 2 and 3 and in the "wet" oxidizing reactor (*OR*) depending on the molar ratio X_{NO} are shown in Fig. 6.

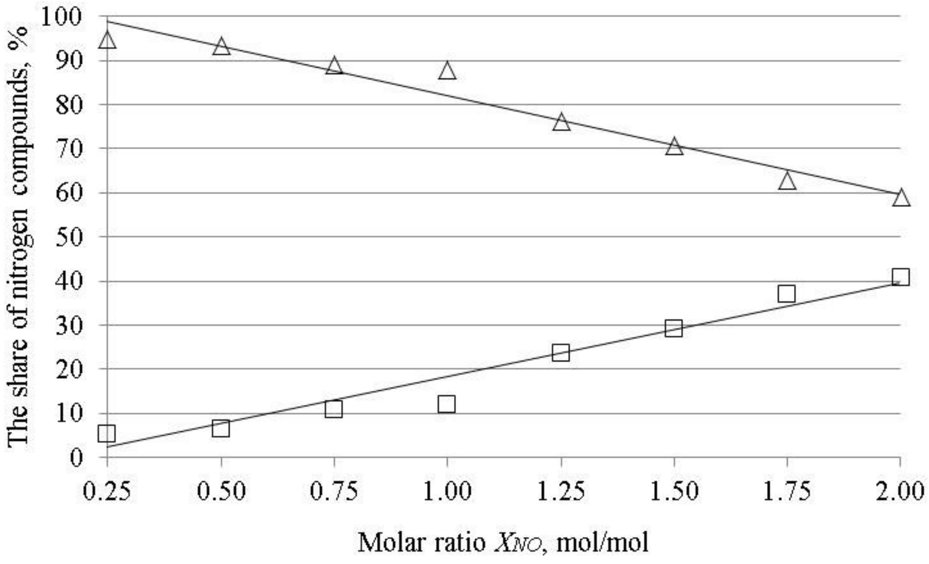

Fig. 6. The fractions of nitrogen compounds δ captured in (ΔΔΔ) washers 2&3 and (□□□) "wet" *OR* vs. the molar ratio X_{NO}

A part of the nitrogen compounds was retained in the "wet" oxidation reactor, and its share grew up with the ozone increasing intensity. For example, at $X_{\mathrm{NO}} = 2.0$ the amount of nitrate and nitrite ions measured in the "wet" oxidizing reactor constituted 40% of their total quantity retained in all washers 1, 2 and 3.

4.2. Oxidizing reactor with packing elements

In order to increase the fraction of captured nitrogen compounds in the oxidizing reactor, different packing elements of the oxidizing reactor were applied, which should enlarge the contact surface of N_2O_5 with water. As packing elements the Białecki's rings made of stainless steel (440 m^2/m^3) and the Rashig rings made of ceramic (243 m^2/m^3) and glass (253 m^2/m^3) were used (Wallas, 1988). The packing elements before measurements were wetted by about 30 ml of distilled water. The results of measurements are shown in Table 2.

The use of packing rings made of stainless steel resulted in retention of approx. 92% of nitrogen species in the oxidation reactor, which means a prominent improvement in relation to the reactor without packing elements. Moreover, the use of packing elements resulted in an increase in the efficiency of denitrification for $X_{NO} = 1.0$.

Table 2. Nitrate and nitrites ions in the washers 2 and 3 and in the oxidizing reactor (*OR*)

Packing elements/material	X_{NO}	NO_x inlet	NO_x outlet	Washers 2&3		*OR*		η_{NOx}	δ
				NO_2^-	NO_3^-	NO_2^-	NO_3^-		
		ppm	ppm	mmol	mmol	mmol	mmol	%	%
No	1.0	482	160	0.024	0.888	0.006	0.221	66.8	19.9
No	1.5	523	9	0.040	0.980	0.005	0.400	98.3	32.7
Yes/stainless steel	1.0	550	40	0.048	0.224	0.130	2.180	92.7	82.9
Yes/stainless steel	1.5	550	0	0.016	0.118	0.100	1.990	100	91.6
Yes/ceramic	1.0	450	78	0.044	0.230	0.050	0.770	82.7	79.0
Yes/ceramic	1.5	450	0	0.014	0.270	0.020	0.950	100	78.2
Yes/glass	1.0	508	72	0.182	0.306	0.020	0.722	85.8	66.9
Yes/glass	1.5	500	0	0.012	0.164	0.015	0.944	100	87.9

δ- fraction of nitrogen compounds captured in oxidizing reactor (see formula 22)

5. INFLUENCE OF OXIDIZING REACTOR ON EFFECTIVENESS OF SIMULTANEOUS REMOVAL OF NO AND SO_2 AND BY-PRODUCTS

5.1. Oxidizing reactor without packing elements

The investigations were conducted in the lab-scale setup (Fig. 1), but the carrier gas (N_2) was doped with NO and SO_2, to reach their initial concentrations of about 400 ppm and 800 ppm, respectively. The duration of a single measurement time was 30 minutes. The molar ratio X_{NO} was varied from 0 to 2.0.

The influence of the oxidizing reactor on the efficiency of NO removal depends on the molar ratio X_{NO} and is shown in Fig. 7. No remark is made on sulphur dioxide, because it was completely removed from the carrier gas in all measurements.

Dynamics of the process was very similar to that of NO removal, wherein absorption of sulphur dioxide in the NaOH solution took place immediately, while stabilization of nitrogen oxide concentrations followed by about 10 minutes. Comparison of the efficiency η_{NO} revealed a substantial difference between the experiments with and without the oxidizing reactor, again the highest efficiency was achieved for the "wet" oxidizing reactor.

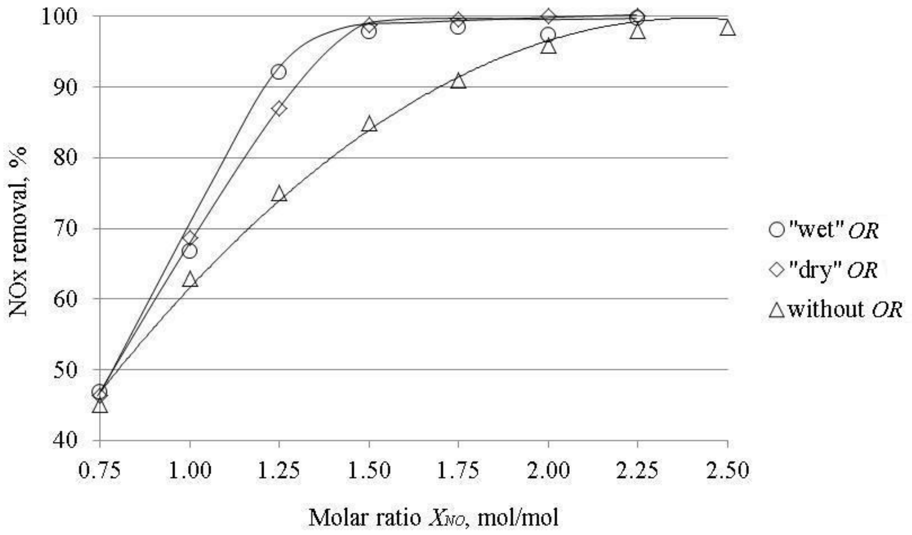

Fig. 7. The influence of oxidizing reactor on NO_x removal efficiency vs. molar ratio $X_{\rm NO}$ for initial concentration of approx. 400 ppm NO and 800 ppm SO_2

Figure 8 shows by-product composition (amount of ions measured in the washers 2 and 3, and the *OR*) vs. molar ratio $X_{\rm NO}$ when "wet" oxidizing reactor was used. With an increase of the ozonation intensity $X_{\rm NO}$ grew nitrates, while decreasing the amount of nitrites in the solution. The by-product composition for "dry" oxidizing reactor had the same character, only in this case nitrates were formed more slowly.

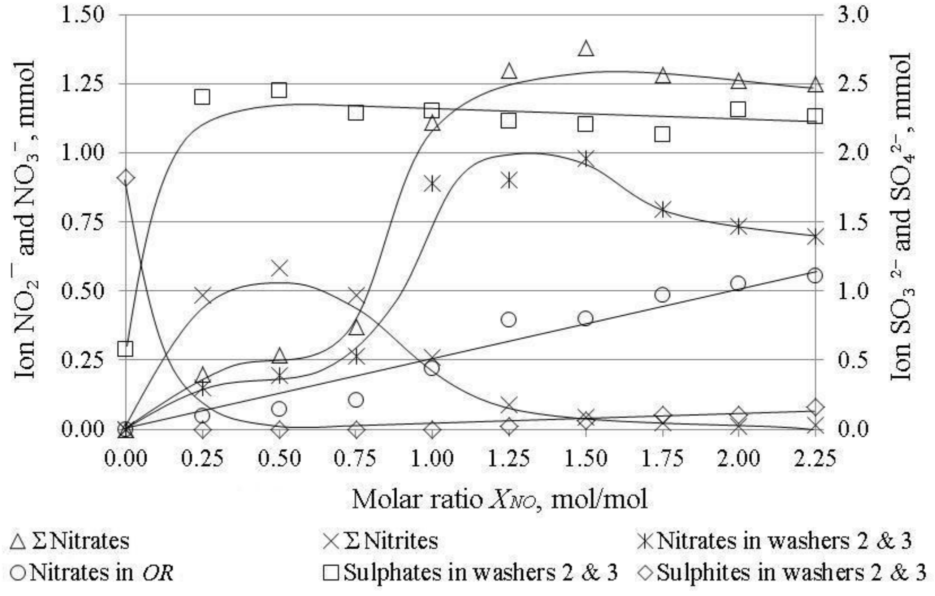

Fig. 8. Composition of by-products of simultaneous removal of NO and SO_2 vs. molar ratio X_{NO} when "wet" oxidizing reactor was used

In the earlier work (Głomba et al., 2016) it was demonstrated that ozonation of gas containing sulphur dioxide, promotes the conversion of sulphite to sulphate being absorbed in the alkaline solution although complete oxidation of sulphite required the ratio $\frac{O_3}{SO_2}$ of at least 2.0. In the case of ozonation of gas containing NO and SO_2 complete oxidation of sulphite occurred at much lower values, i.e. $\frac{O_3}{NO+SO_2} \approx 0.1$ for $\frac{NO}{SO_2} = 0.5$, which indicates there was another agent which stimulated this process.

The agent is nitrogen dioxide, which accelerates oxidation of SO_3^{2-} ions. Littlejohn et al. (1993) suggest that NO_2 acts catalytically in this process.

The fraction of nitrogen compounds captured in the washers 2 and 3 and in the “wet” oxidizing reactor *OR* is shown in Fig. 9. The obtained results also indicate that sulphur dioxide was not removed from the carrier gas in the oxidation reactor, the washings from the oxidizing reactor contained only nitrites and nitrates.

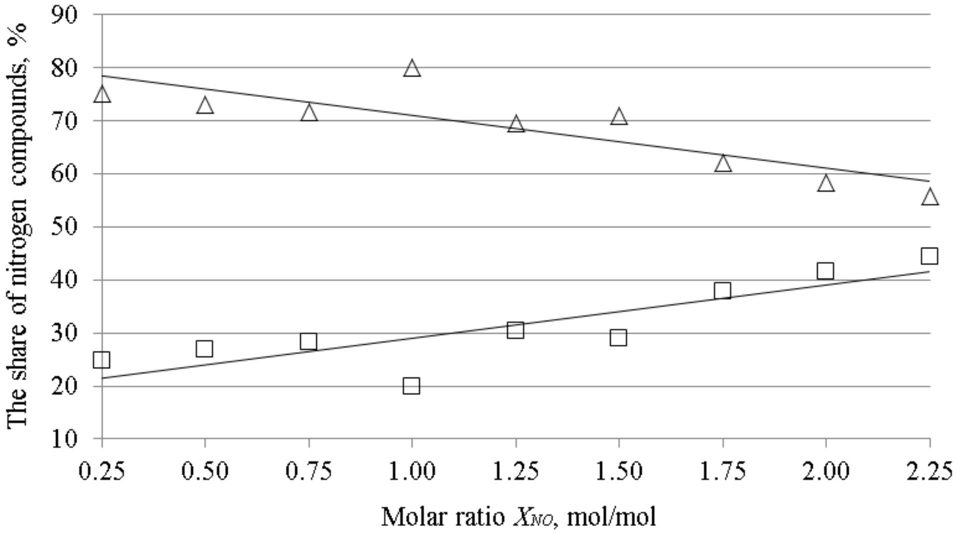

Fig. 9. The fractions of nitrogen compounds δ captured in (ΔΔΔ) washers 2&3 and (□□□) “wet” *OR* vs. the molar ratio X_{NO}

5.2. „Wet”oxidizing reactor with packing elements

The “wet” packed bed in the oxidizing reactor was used to maximize the fraction of contaminates captured in the reactor. The same packing elements were as those of NO_x removal from the carrier gas in Section 4.2. The results of measurements are summarized in Table 3.

Table 3. Results of analysis of absorbents from washers 2 and 3 and the oxidizing reactor (*OR*) for different filling materials

Packing elements /material	X_{NO}	Washers 2&3				*OR*			η_{NOx}	δ
		NO_2^-	NO_3^-	SO_3^{2-}	SO_4^{2-}	NO_2^-	NO_3^-	SO_4^{2-}		
		mmol	mmol	mmol	mmol	mmol	mmol	mmol	%	%
No	1.0	0.240	0.890	0.02	2.30	0.006	0.22	0.022	66.8	20
No	1.5	0.040	0.980	0.06	2.20	0.005	0.40	0.024	98.3	29
Yes/stainless steel	1.0	0.202	0.126	0.08	2.22	0.05	1.29	0.07	91.7	80
Yes/stainless steel	1.5	0.040	0.164	0.12	2.18	0.03	1.36	0.08	99.5	87
Yes/ceramic	1.0	0.256	0.192	0.09	1.99	0.04	1.12	0.06	88.9	72
Yes/ceramic	1.5	0.050	0.284	0.10	1.97	0.05	1.33	0.07	99.8	81
Yes/glass	1.0	0.244	0.170	0.10	2.10	0.023	0.72	0.10	89.6	64
Yes/glass	1.5	0.060	0.244	0.18	2.07	0.033	0.97	0.11	99.0	77

δ- fraction of nitrogen compounds captured in oxidizing reactor (see formula 22)

Also in this case increased effectiveness of NO_x removal from the carrier gas was noticed, especially significantly for $X_{NO} = 1.0$. In addition, approx. 80% of nitrogen compounds was retained in the oxidation reactor regardless of the packing material. The positive effect of packing elements was probably due to an increase in contact surface of N_2O_5 with the solution.

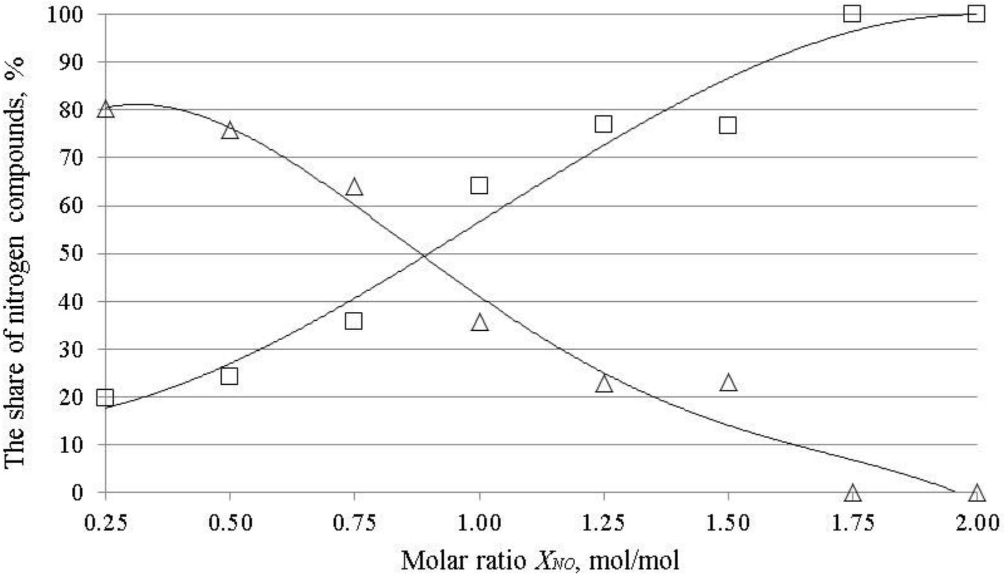

Fig. 10. Separation of the fraction of nitrogen compounds (NO_2^- and NO_3^-) δ between the (ΔΔΔ) washers2&3 and the (□□□) oxidizing reactor (*OR*) with glass packing elements vs. the molar ratio X_{NO}

More specifically, separation of nitrogen ions between the washers 2 and 3 and the oxidation reactor packed with Rasching rings are presented as a function of X_{NO} in Fig. 10. Starting from $X_{NO} > 1.75$ virtually almost all nitrogen (as nitrate) was retained in the oxidizing reactor. As for sulphur dioxide, a little was retained in the oxidation reactor; only 1 and 4% of initial content of SO_2 in the reactor without packing elements and with packing elements, respectively. These results should be considered as promising because they confirm the possiblity of nitrogen and sulphur compound separation.

5.3. Use of oxidizing reactor in pilot plant studies

Also in the pilot-scale investigations positive effects of the "wet" oxidizing reactor were found. For each molar ratio X_{NO} the efficiency of NO_x removal was higher from about 20 to 40% than that without the reactor. For example, for the molar ratio $X_{NO} \approx 1.7$ the efficiency of NO_x removal from flue gas reached practically 100% when the oxidizing reactor was in use (Fig. 11).

Unfortunately, not many results concerning by-products captured in the absorber were obtained, because difficulties were encountered in the analysis of nitrogen compounds by the spectrophotometric method. The difficulties were caused by the fact that the absorber was fed with water from Odra river containing some impurities (Głomba et al., 2016). This did not prevent analysis of sulphites and sulphates in the absorber. As in the laboratory in this case it has also been found that the ozone treatment of flue gas significantly improves the conversion efficiency of SO_3^{2-} to SO_4^{2-} (Table 4).

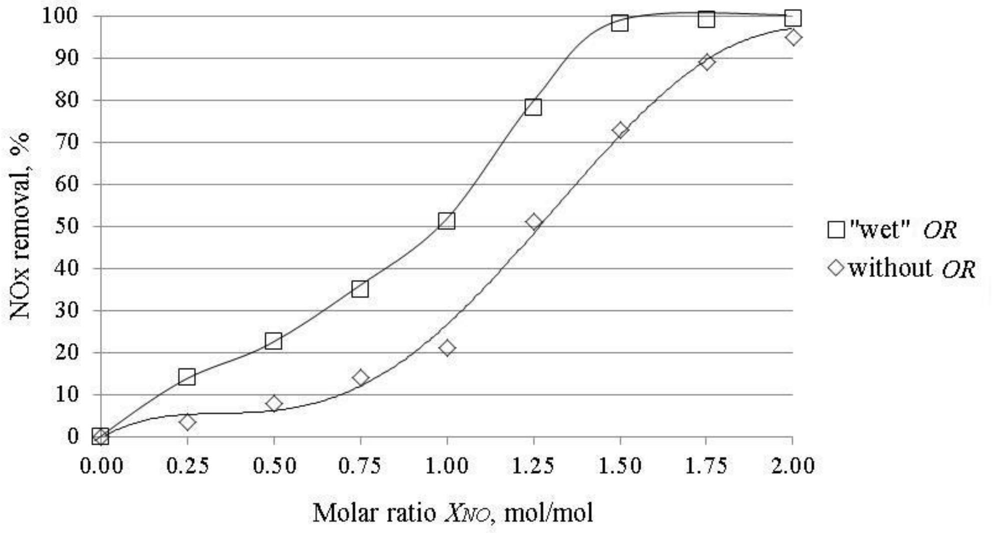

Fig. 11. Efficiency of NOx removal vs. the molar ratio X_{NOx} in the pilot-plant

Table 4. Influence of flue gas ozonation on the conversion efficiency (η_{SO4}) of SO_3^{2-} to SO_4^{2-}

X_{NO}	Initial SO_2 concentration	Scrubber			η_{SO4}
		SO_3^{2-}	SO_4^{2-}	$SO_3^{2-} + SO_4^{2-}$	
	ppm	mmol	mmol	mmol	%
1.0	136	99.3	512.4	611.7	83.8
2.0	207	80	2599	2679	97.0
2.25	203	0	2452	2452	100.0

6. SUMMARY

Investigations carried out in the lab- and pilot-scale enabled to draw the following conclusions:

- The oxidizing reactor improves the efficiency of denitrification, which reduces consumption of ozone.
- Denitrification is much more efficient in humid gas phase with packing elements than in an aqueous absorption solution.
- Wetting of the oxidation reactor with water enables a preliminary separation of sulphur and nitrogen compounds.
- Application of packing elements in the oxidizing reactor allows to retain 90% of nitrogen compounds in the reactor.

The results presented in this paper were obtained in the study financed by the National Centre for Research and Development under the Contract SP/E/1/67484/10- Strategic project- Advanced technologies energy generation: Development of technology for highly efficient "zero-emission" coal-fired units with integrated CO₂ capture from flue gas.

SYMBOLS

C	concentration, ppm
M	stable particle for energy carrying
n	number of moles

OR	oxidizing reactor
X_{NO}	molar ratio O_3/NO, mol O_3/mol NO

Greek symbols

δ	fraction of nitrogen compounds captured in oxidizing reactor, %
η_{NOx}	efficiency of NO_x removal, %
η_{SO4}	degree of conversion of SO_3^{2-} to SO_4^{2-}, %

Superscripts

A	amounts related to solution in washers
int	related to parameters at inlet
out	related to parameters at outlet
R	amounts related to oxidizing reactor

Subscripts

aq	liquid state
NO_x	sum of NO and NO_2
$NO_{(2,3)}$	sum of nitrites and nitrates,
SO3	sulphites
SO4	sulphates

REFERENCES

Carpenter A. M., 2013. Advances in multi-pollutant control. *IEA CLEAN COAL CENTRE*, CCC/227.

Chen L., Lin J.-W., Yang Ch.-L., 2002. Absorption of NO_2 in a packed tower with Na_2SO_3 aqueous solution. *Environ. Prog.,* 21, No.4, 225-230. DOI: 10.1002/ep.670210411.

Chirona R.J., Alshuter B., 1999. Chemical aspects of NO_x scrubbing. *Pollution Engineering*, 32, 33-36.

Dora J., Gostomczyk M.A., Jakubiak M., Kordylewski W., Mista W., Tkaczuk M., 2009. Parametric studies of the effectiveness of NO oxidation process by ozone. *Chem. Process Eng*., 30, 621–634.

Fridman A., 2008. *Plasma Chemistry*. Cambridge University Press, Cambridge.

Fujishima H., Kuroki T., Tatsumi A., Okubo M., Otsuka K., Yamamoto T., Yoshida K., 2008. Performance characteristics of pilot-scale NO_x removal from boiler emissions using plasma-chemical process. *11th International Conference on Electrostatic Precipitation*, Hangzhou, 644-648. DOI: 10.1109/08IAS.2008.120.

Głomba M., Hałat A., Kordylewski W., Łuszkiewicz D., 2016. Research on products of simultaneous removal of SO_2 and NO_x from flue gas by ozonation and alkaline absorption. *Environ. Prot. Eng.*, 42, 125-136. DOI: 10.5277/epe160208.

Hikita H, Asai S., Tsuji T., 1977. Absorption of sulfur dioxide into aqueous sodium hydroxide and sodium sulfite solutions. *AIChE J.*, 23, 538–544. DOI: 10.1002/aic.690230419.

Jaroszyńska-Wolińska J., 2009. *Investigations of the chemical reactions of nitrogen oxides with ozone generated in low-temperature plasma*. Instytut Chemii i Technologii Jądrowej, Warszawa.

Jędrusik M., Kordylewski W., Łuszkiewicz D., 2015. Removal of nitrogen oxides from flue gas by ozonation method. *Rynek Energii*, 6, 119-124.

Jie D., Heruijing C., Qin Z., Jiandong L., Junjun X., Shule Z., 2016. Selective denitrification of flue gas by O_3 and ethanol mixtures in a duct: Investigation of processes and mechanisms. *J. Hazard. Mater.*, 311, 218–229. DOI: 10.1016/j.jhazmat.2016.02.063.

Jie D., Qin Z., Shule Z., 2014. Simultaneous desulfurization and denitrification of flue gas by catalytic ozonation over Ce–Ti catalyst. *Fuel Process. Technol.,* 128, 449–455. DOI: 10.1016/j.fuproc.2014.08.003.

Joshi J.B., Mahajani V.V., Juvekar V.A., 1985. Absorption of NOx gases. *Chem. Eng. Com.*, 33, 1-92. DOI: 10.1080/00986448508911161.

Kordylewski W., Jakubiak M., Hardy T., 2013. Pilot plant studies on NOx removal via NO ozonation and absorption. *Arch. Environ. Prot.*, 39, 93-106. DOI: 10.2478/aep-2013-0025.

Krzyżyńska R., Hutson N.D., 2012. Effect of solution pH on SO_2, NO_x, and Hg removal from simulated coal combustion flue gas in an oxidant-enhanced wet scrubber. *J. Air Waste Manage. Assoc.*, 62, 2, 212-220. DOI: 10.1080/10473289.2011.642951.

Kuropka J., 2012. *Technologie oczyszczania gazów z dwutlenku siarki i tlenków azotu*. Oficyna Wydawnicza Politechniki Wrocławskiej, Wrocław.

Littlejohn D., Wang Y., Chang S-G., 1993. Oxidation of aqueous sulfite ion by nitrogen dioxide. *Environ. Sci. Technol.,* 27, 2162-2167. DOI: 10.1021/es00047a024.

Modern Power Systems, 2015. A pioneering NOx removal technology for the power industry. *Modern Power Systems*, 35(5), 32-33.

Mok S.Y., 2006. Absorption-reduction technique assisted by ozone injection and sodium sulfide for NO_x removal from exhaust gas. *Chem. Eng. J.*, 118, 63-67. DOI: 10.1016/j.cej.2006.01.011.

Nelo S.K., Leskela K.M., Sohlo J.J.K., 1997. Simultaneous oxidation of nitrogen oxide and sulfur dioxide with ozone and hydrogen peroxide. *Chem. Eng. Technol.*, 20, 40-42. DOI: 10.1002/ceat.270200108.

Okubo M., Kuroki T., Kitaura K. and Yamamoto T., 2006. Diesel engine emission control using pulsed corona plasma-chemical hybrid process. *J. Environ. Eng.,* 1, 29-38. DOI: 10.1299/jee.1.29.

Omar K., 2008. Evaluation of BOC's LotOx process for the oxidation of elemental mercury in flue gas from a coal-fired boiler. *Topical report for Linde Group and U.S. Department of Energy by Western Research Institute (WRI-08-RO10)*.

Regulation of the Minister of Environment on conditions to be met when introducing sewage into the water or soil and on substances particularly harmful to the aquatic environment (*Dz. U. 2009, nr 27, poz. 169*), (in Polish).

Sander R., 1999. *Compilation of Henry's Law constants for inorganic and organic species of potential importance in environmental chemistry*. Air Chemistry Department Max-Planck Institute of Chemistry, Germany.

Skalska K., Miller J.S. , Ledakowicz S., 2011. Kinetic model of NOx ozonation and its experimental verification. *Chem. Eng. Sci.*, 66, 3386-3391. DOI: 10.1016/j.ces.2011.01.028.

Stamate E., Jorgensen L., Jensen T. K., Chen W., Kristensen P. G., Tobiasen L., Simonsen P., Michelsen P. K., 2009. Pilot test and optimization of plasma based DeNOx. *Final Report PSO project No. 2006-1-6365*.

Sun W.Y., Ding S.L., Zeng S.S., Su S., Jiang W., 2011. Simultaneous absorption of NOx and SO_2 from flue gas with pyrolusite slurry combined with gas-phase oxidation of NO using ozone. *J. Hazard. Mater.*, 192, 124–130. DOI: 10.1016/j.jhazmat.2011.04.104.

Sun C., Zhao N., Zhuang Z.K., Wang H., Liu Y., Weng X., Wu Z., 2014. Mechanisms and reaction pathways for simultaneous oxidation of NO_x and SO_2 by ozone determined by in situ IR measurements. *J. Hazard. Mater.*, 274, 376–383. DOI: 10.1016/j.jhazmat.2014.04.027.

Thomas D., Vaderschuren J., 2000. Analysis and prediction of the liquid phase composition for the absorption of nitrogen oxides into aqueous solutions. *Sep. Purif. Technol.*, 18, 37-45. DOI: 10.1016/S1383-5866(99)00049-0.

Wallas S.M., 1988. *Chemical processes: Equipment selection and design.* Butterworth, Wobum, MA.

Wang H., Zhuang Z., Sun C., Zhao N., Liu Y., Wu Z., 2016. Numerical evaluation of the effectiveness of NO_2 and N_2O_5 generation during the NO ozonation process. *J. Environ. Sci.* (*China*). 41, 51-58. DOI: 10.1016/j.jes.2015.05.015.

Yamamoto T., Okubo M., Hayakawa K., Kitaura K., 2001. Towards ideal NOx control technology using a plasma-chemical hybrid process. *IEEE Trans. Ind. Appl.*, 37, 1492-1498. DOI: 10.1109/28.952526.

Zhang J., Zhang R., Chen X., Tong M., Kang W., Guo S., Zhou Y., Lu J., 2014. Simultanoeus removal of NO and SO_2 from flue gas by ozone oxidation and NaOH absorption. *Ind. Eng. Chem. Res.,* 53, 6450-6456. DOI: 10.1021/ie403423p.

Received 08 September 2016
Received in revised form 01 March 2017
Accepted 03 March 2017

Instructions for Authors

All manuscripts submitted for publication in Chemical and Process Engineering must comprise a description of original research that has neither been published nor submitted for publication elsewhere.

The content, aim and scope of the proposals should comply with the main subject of the journal, i.e. they should deal with mathematical modelling and/or experimental investigations on momentum, heat and mass transfer, unit processes and operations, integrated processes, biochemical engineering, statics and kinetics of chemical reactions. The experiments and modelling may cover different scales and processes ranging from the molecular phenomena up to production systems. The journal language is grammatically correct British English.

Chemical and Process Engineering publishes: i) full text research articles, ii) invited reviews, iii) letters to the editor and iv) short communications, aiming at important new results and/or applications. Each of the publication form is peer-reviewed by at least two independent referees.

Submission of materials for publication

The manuscripts are submitted for publication via email address *A.Bin@ichip.pw.edu.pl*. When writing the manuscript, authors should preferably use the template for articles, which is available on the *www.degruyter.com/view/j/cpe*.

Proposals of a paper should be uploaded using the Internet site of the journal and should contain:
- a manuscript file in Word format (*.doc, *.docx),
- the manuscript mirror in PDF format,
- all graphical figures in separate graphics files.

In the following paragraph the general guidelines for the manuscript preparation are presented.

Manuscript outline

1. Header details
   a. Title of paper
   b. Names (first name and further initials) and surnames of authors
   c. Institution(s) (affiliation)
   d. Address(es) of authors
   e. Information about the corresponding author; academic title, name and surname, email address, address for correspondence

2. Abstract – should contain a short summary of the proposed paper. In the maximum of 200 words the authors should present the main assumptions, results and conclusions drawn from the presented study.

3. Keywords – Up to 5 characteristic keyword items should be provided.

4. Text
   a. Introduction. In this part, description of motivation for the study and formulation of the scientific problem should be included and supported by a concise review of recent literature.
   b. Main text. It should contain all important elements of the scientific investigations, such as presentation of experimental rigs, mathematical models, results and their discussion. This part may be divided into subchapters.
   c. Conclusions. The major conclusions can be put forward in concise style in a separate chapter. Presentation of conclusions from the reported research work accompanied by a short commentary is also acceptable.

Figures: drawings, diagrams and photographs should be located in appropriate places in the manuscript text according to the template. Their graphical form should be of vector or raster type with the minimum resolution of 900 dpi. In addition, separate files containing each of the drawings, graphs and photos should be uploaded onto the journal Web site in one of the following formats: bmp, gif, tiff, jpg, eps. Due to rigid editorial reasons, graphical elements created within MS Word and Excel are not acceptable. The final length of figures should be intended typically for 8 cm (single column) or 16 cm in special cases of rich-detail figures. The basic font size of letters in figures should be at least 10 pts after adjusting graphs to the final length.

Figures: drawings, diagrams and photographs should be in gray scale. In case of coloured graphs or photo an additional payment of 300 PLN (72 €) per 1 page containing coloured figures on both sides, or 150 PLN (36 €) per page containing coloured figures on one side will be required.

Tables should be made according to the format shown in the template.

All figures and tables should be numbered and provided with appropriate title and legend, if necessary. They have to be properly referenced to and commented in the text of the manuscript.

5. List of symbols should be accompanied by their units

6. Acknowledgements may be included before the list of literature references

7. Literature citations

The method of quoting literature source in the manuscript depends on the number of its authors:

- single author – their surname and year of publication should be given, e.g. Marquardt (1996) or (Marquardt, 1996),
- two authors – the two surnames separated by the conjunction “and” with the publication year should be given, e.g. Charpentier and McKenna (2004) or (Charpentier and McKenna, 2004),
- three and more authors – the surname of the first author followed by the abbreviation “et al.” and year of publication should be given, e.g. Bird et al. (1960) or (Bird et al., 1960).

In the case of citing more sources in one bracket, they should be listed in alphabetical order using semicolon for separation, e.g. (Bird et al., 1960; Charpentier and McKenna, 2004; Marquardt, 1996). Should more citations of the same author(s) and year appear in the manuscript then letters “a, b, c, ...” should be successively applied after the publication year.

Bibliographic data of the quoted literature should be arranged at the end of the manuscript text in alphabetic order of surnames of the first author. It is obligatory to indicate the DOI number of those literature items, which have the numbers already assigned. Journal titles should be specified by typing their right abbreviations or, in case of doubts, according to the List of Title Word Abbreviations available at http://www.issn.org/2-22661-LTWA-online.php.

Examples of citation for:
Articles

Charpentier J. C., McKenna T. F., 2004. Managing complex systems: some trends for the future of chemical and process engineering. *Chem. Eng. Sci.*, 59, 1617-1640. DOI: 10.1016/j.ces.2004.01.044.

Information from books (we suggest adding the page numbers where the quoted information can be found)

Bird R. B., Stewart W.E., Lightfood E.N., 2002. *Transport Phenomena*. 2nd edition, Wiley, New York, 415-421.

Chapters in books

Hanjalić K., Jakirlić S., 2002. Second-moment turbulence closure modelling, In: Launder B.E., Sandham N.D. (Eds.), *Closure strategies for turbulent and transitional flows*. Cambridge University Press, Cambridge, 47-101.

Conferences

ten Cate A., Bermingham S.K., Derksen J.J., Kramer H.M.J., 2000. Compartmental modeling of an 1100L DTB crystallizer based on Large Eddy flow simulation. *10th European Conference on Mixing*. Delft, the Netherlands, 2-5 July 2000, 255-264.

8. Payments

Starting from 2014 a principle of publishing articles against payment is introduced, assuming non-profit making editorial office. According to the principle authors or institutions employing them, will have to cover the expenses amounting to 40 PLN (or 10 €) per printed page. The above amount will be used to supplement the limited financial means received from the Polish Academy of Sciences for the editorial and publishing; and in particular to increase the capacity of the next CPE volumes and to proofread the linguistic correctness of the articles. The method of payment will be indicated in an invoice sent to the authors or institutions after acceptance of their manuscripts to be published. In justifiable cases presented in writing, the editorial staff may decide to relieve authors from basic payment, either partially or fully.

All correspondence should be sent to Editor-in-Chief, Prof. Andrzej K. Biń, email address *A.Bin@ichip.pw.edu.pl*.

The Azoty Group is a future-oriented project. But this has always been the case. When in 1927 President Ignacy Mościcki decided to build the State-owned Nitrogenous Compounds Factory it was a vision of the future. A vision of Poland's grand chemical industry.

This vision, and the history of all the companies the Group put together give us the picture of one of the key capital groups in the European fertiliser-chemical sector.

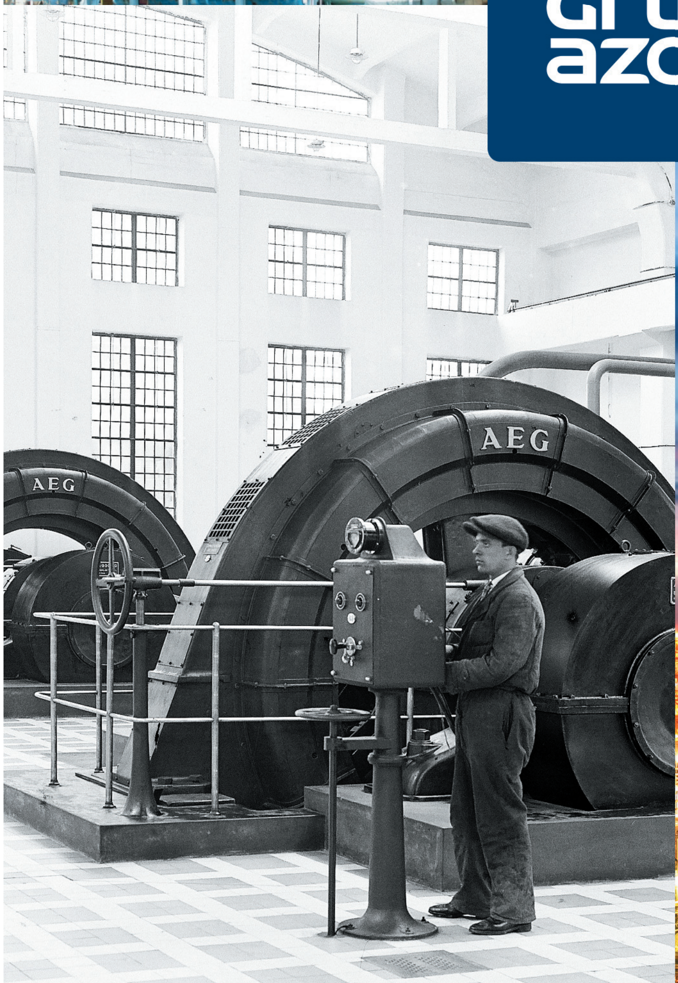

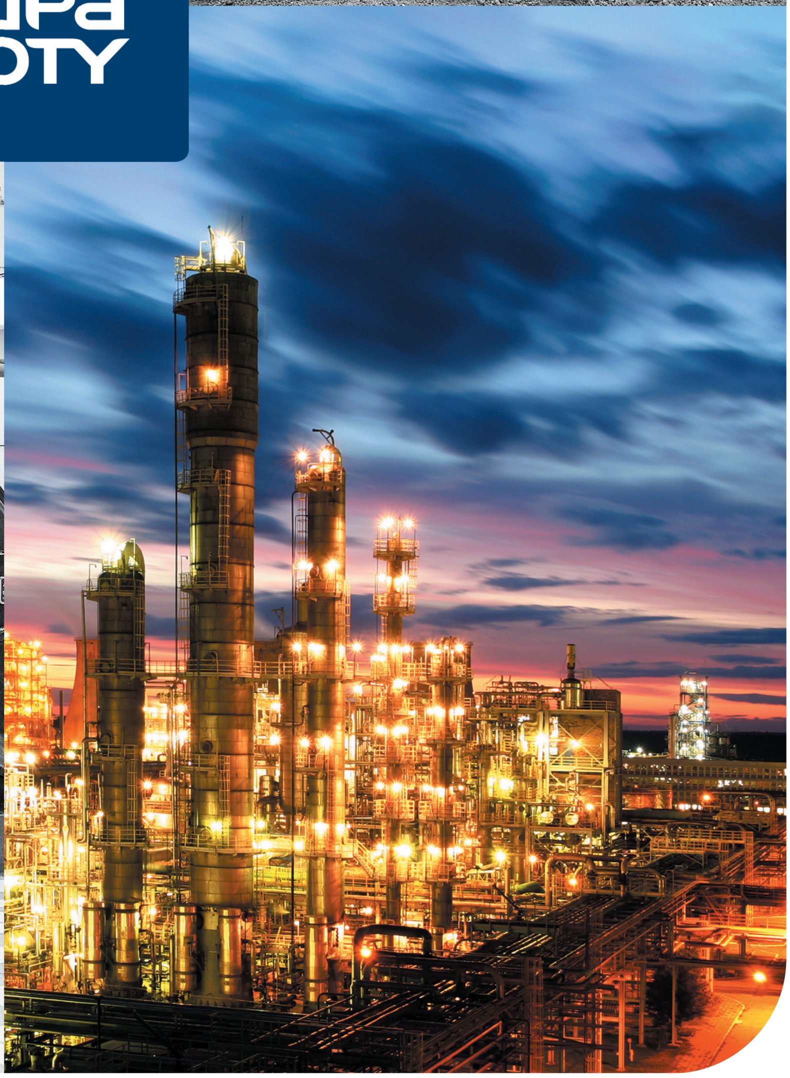

grupaazoty.com